Pure

Bangor University

DOCTOR OF PHILOSOPHY

# Electrical and spectral characterisation of inkjet printed poly(3,4-ethtylenedioxythiophene) : poly(4-styrenesulphonate)

Morris, David Jonathan

*Award date:*
2004

*Awarding institution:*
Bangor University

Link to publication

**General rights**
Copyright and moral rights for the publications made accessible in the public portal are retained by the authors and/or other copyright owners and it is a condition of accessing publications that users recognise and abide by the legal requirements associated with these rights.

- Users may download and print one copy of any publication from the public portal for the purpose of private study or research.
- You may not further distribute the material or use it for any profit-making activity or commercial gain
- You may freely distribute the URL identifying the publication in the public portal ?

**Take down policy**
If you believe that this document breaches copyright please contact us providing details, and we will remove access to the work immediately and investigate your claim.

Download date: 27. Apr. 2024

# Electrical and spectral characterisation of inkjet printed Poly(3,4-ethylenedioxythiophene):poly(4-styrenesulphonate)

David Jonathan Morris

Institute of Bioelectronic and Molecular Microsystems
School of Informatics
University of Wales, Bangor

A thesis submitted to the University of Wales for the degree of Doctor of Philosophy

August 2004

I'W DDEFNYDDIO YN Y LLYFRGELL YN UNIG

TO BE CONSULTED IN THE LIBRARY ONLY

U.W.B. LIBRARY P.C.B. LLYFRGELL

# SUMMARY

This thesis describes a pioneering investigation in which time resolved scanning Kelvin probe microscopy (SKPM) and Raman spectroscopy were combined to identify processes occurring at the interface of inkjet printed poly(3,4-ethylenedioxythiophene):poly(4- styrenesulphonate) (PEDOT:PSS) and aluminium and indium tin oxide (ITO) electrodes.

In order to undertake these measurements an experimental inkjet printing system was designed and constructed capable of robustly inkjetting polymer solutions with micron resolution suitable for inkjetting typical polymer device structures.

The main findings of the SKPM work showed; (i) that there was good charge transfer between ITO and polymer as indicated by the lack of a significant potential drop at the interface, however this was not the case with the aluminium electrodes where large potential drops were seen at the interface and (ii) that ionic impurities in the polymer migrated under an applied electric field to the electrodes where they were not discharged, resulting in a collapse of the potential across the bulk of the polymer. These mechanisms were likely to be those responsible for the $I \propto t^{-n}$ behaviour seen in potential step response measurements.

This behaviour was confirmed by the Raman spectroscopy which showed changes in the spectra in the range 1200 to 1600cm$^{-1}$ related to the structure of the conjugated polymer backbone and its doping levels.

The observed charge transfer and ionic migration results have significant implications for polymer devices including the efficiency and degradation of PLEDs and FETs and the operating mechanism of polymer memory devices.

CONTENTS

*Abstract* . . . . . ii

*Contents* . . . . . iii

*Glossary* . . . . . vii

*Acknowledgements* . . . . . ix

*Authors declaration* . . . . . x

*1. Introduction* . . . . . 1

*2. Literature review* . . . . . 6
2.1 Introduction . . . . . 6
2.2 PEDOT:PSS . . . . . 6
2.3 Electronic conduction in conjugated polymers . . . . . 7
2.4 Doping of conducting polymers . . . . . 9
2.5 Bulk charge transport . . . . . 11
2.6 Contacts . . . . . 12
2.6.1 The Schottky barrier . . . . . 12
2.6.2 Deviations from ideal behaviour . . . . . 16
2.7 Fabrication and inkjet printing . . . . . 18
2.7.1 Inkjet print systems . . . . . 19
2.7.2 Inkjetting of polymer solutions . . . . . 19
2.7.3 Device fabrication . . . . . 21
2.8 Scanning Kelvin Probe Microscopy (SKPM) . . . . . 24
2.9 Spectroscopy . . . . . 27
2.10 Concluding summary . . . . . 31

*3. Inkjet printing system* . . . . . 32
3.1 Introduction . . . . . 32
3.2 Inkjet print system requirements . . . . . 33
3.2.1 Aims . . . . . 33
3.2.2 Objectives . . . . . 33
3.3 *XY* stage . . . . . 36
3.3.1 Requirements of *XY* stage . . . . . 36

3.3.2 Construction . . . 38
3.3.3 Stepper motor control . . . 39
3.4 Inkjet print head . . . 40
3.4.1 Inkjet print head selection . . . 40
3.4.2 Droplet ejection accuracy . . . 42
3.4.3 Printhead construction . . . 43
3.4.4 Microdrop controller, *MD-E-201-H* . . . 44
3.4.5 Ink formulation . . . 47
3.4.6 Droplet ejection and maintenance . . . 47
3.5 Optical alignment . . . 48
3.5.1 Specifications . . . 48
3.5.2 Alignment . . . 49
3.5.3 Optics . . . 50
3.5.4 Lighting . . . 51
3.5.5 Future development . . . 52
3.6 GUI for system control . . . 53
3.6.1 Specifications . . . 53
3.6.2 Matlab GUI . . . 54
3.6.3 Future development . . . 55
3.7 Assessment of inkjet print system . . . 55
3.8 Concluding summary . . . 55

4. *Inkjet printing of polymers* . . . 57
4.1 Introduction . . . 57
4.2 Inkjet printing lines of droplets . . . 57
4.3 Cross-sectional analysis of lines . . . 59
4.4 Inkjet printing across electrode edges . . . 61
4.4.1 Gold electrodes . . . 62
4.4.2 Aluminium electrodes . . . 63
4.4.3 ITO electrodes . . . 64
4.5 Contact angle measurements . . . 65
4.6 Inkjet printing across electrode gaps . . . 67
4.7 Cross-sectional analysis of electrode-polymer-electrode structures . . . 70
4.8 Concluding summary . . . 71

5. *Experimental techniques for droplet characterisation* . . . 73
5.1 Introduction . . . 73
5.2 Electrode fabrication . . . 73
5.3 Sample preparation . . . 74
5.4 DC electrical measurements . . . 75
5.5 Atomic Force and Scanning Kelvin Probe microscopy . . . 76

5.5.1 Atomic force microscopy . . . 77
5.5.2 Scanning Kelvin Probe Microscopy . . . 77
5.6 Raman spectroscopy . . . 78
5.7 EDX . . . 79
5.8 Concluding summary . . . 81

*6. Results and discussion: Aluminium electrodes* . . . 82
6.1 Introduction . . . 82
6.2 Sample fabrication . . . 83
6.2.1 Sample 1 . . . 83
6.2.2 Sample 2 . . . 86
6.3 DC results . . . 87
6.3.1 Charging/discharging transients . . . 89
6.4 Cross-sectional analysis . . . 89
6.5 Computer modelling . . . 92
6.5.1 Sample without interfacial layer . . . 95
6.5.2 Sample with interfacial layer . . . 97
6.6 SKPM results . . . 98
6.6.1 Work function difference . . . 98
6.6.2 Potential distribution across sample . . . 100
6.6.3 Time resolved SKPM . . . 104
6.6.4 Additional SKPM work . . . 112
6.7 Raman spectroscopy and optical images . . . 112
6.7.1 Experimental sequence . . . 113
6.7.2 Raman spectra and optical images taken prior to injecting current . . . 114
6.7.3 Effect of injecting 2pA into the sample . . . 118
6.7.4 Effect of injecting 200pA into the sample . . . 118
6.7.5 Raman spectra and optical images after storing sample under zero electric bias for 16 hours under laboratory conditions . . . 120
6.7.6 Comparison of Raman spectra . . . 121
6.8 EDX results . . . 124
6.9 Concluding summary . . . 127

*7. Results on ITO electrodes* . . . 129
7.1 Introduction . . . 129
7.2 Sample fabrication . . . 129
7.3 DC results . . . 131
7.4 Cross-sectional analysis . . . 131
7.5 SKPM results . . . 132
7.5.1 Work function difference . . . 132

7.5.2 Potential distribution across the sample . . . 134
7.5.3 Time resolved SKPM . . . 137
7.6 Raman spectroscopy and optical images . . . 142
7.6.1 Experimental sequence . . . 142
7.6.2 Optical images . . . 143
7.6.3 Comparison of Raman spectra . . . 145
7.7 Concluding summary . . . 146

*8. Further analysis and discussion of I-t data* . . . 148
8.1 Introduction . . . 148
8.2 Steady state current due to DC conductivity . . . 148
8.3 $t^{-n}$ current decay . . . 151
8.4 Concluding summary . . . 152

*9. Conclusions and further work* . . . 153
9.1 Conclusions . . . 153
9.2 Further work . . . 156

*A. Electrode fabrication* . . . i
A.1 Aluminium electrodes . . . i
A.2 Gold electrodes . . . ii
A.3 ITO electrodes . . . iii

*B. Program for inkjet print system* . . . iv

*C. Cross-sectional area of inkjetted lines* . . . xx
C.1 Matlab m-file for calculating cross-sectional area of inkjet printed lines along their length . . . xx
C.2 m-file for calculating cross-sectional area of inkjet printed lines along their length that cross electrode gaps . . . xxi

*Bibliography* . . . xxiii

*Publications arising from work* . . . xxx

GLOSSARY

| Abbreviation | Details |
|---|---|
| AFM | Atomic Force Microscopy |
| Al | Aluminium |
| $Alq_3$ | Tris(8-hydroxy-quinoline) aluminium |
| ASCII | American Standard Code for Information Interchange |
| CAD | Computer Aided Design |
| CCD | Charge Coupled Device |
| CNC | Computer Numerical Control |
| DIC | Differential Interference Contrast |
| DPI | Dots Per Inch |
| EDX | Energy Dispersive X-Ray Spectroscopy |
| EFM | Electric Force Mircoscopy |
| GPIB | General Purpose Interface Bus |
| GUI | Graphical User Interface |
| HDPE | High Density Polyethylene |
| ITO | Indium Tin Oxide |
| LB | Langmuir-Blodgett |
| LED | Light Emitting Diode |
| MIS | Metal Insulator Semiconductor |
| MS | Metal Semiconductor |
| PA | Polyacetalene |
| PEDOT | Poly(3,4-ethylenedioxythiophene) |
| PI | Polyimide |
| p-Si | Poly Silicon |
| PSS | Poly(4-styrenesulphonate) |
| PTFE | Polytetrafluoroethylene |
| PVP | poly-4-vinylphenol |
| P3HT | Poly(3-hexylthiophene) |
| RBS | Rutherford Backscattering Spectrometry |
| RFID | Radio Frequency Identification |
| RGB | Red Green Blue |
| SAM | Self Assembled Monolayer |
| SKPM | Scanning Kelvin Probe Microscopy |

| | |
|---|---|
| TFT | Thin Film Transistor |
| TPI | Turns Per Inch |
| USB | Universal Serial Bus |
| UPS | Ultraviolet Photoelectron Spectroscopy |
| UPW | Ultra Pure Water |
| UV | Ultra Violet |
| UV-Vis-NIR | Ultra Violet-Visible-Near Infrared |
| XPS | X-ray Photoelectron Spectroscopy |

# ACKNOWLEDGEMENTS

I would like to take this opportunity to thank the people who have helped me through my Ph.D.

My thanks go to my supervisor, Professor D.M. Taylor, for supporting me in many ways throughout my Ph.D., his invaluable help in the preparation of my thesis and for many enlightening discussions.

I would like to show my appreciation to the EPSRC for their grant without which I would not have started. I would also like to thank Dr. Stephen Yeates of Avecia Ltd. for providing advice on inkjet printing and samples of ink.

I would like to thank all members of staff in the School of Informatics including John Cambridge for his continual help with the AFM/SKPM/Raman spectroscope and Iwan Jones for helping construct the inkjet printing system.

Dr. Andy Goater and Dr. Julian Burt deserve a big mention for the amount of time they spent assisting me, from microscope objectives to mongooses, nothing was beyond their bounds.

Finally I would like to thank my parents for, well, just doing what parents do, but doing it especially well. I'm sure they're glad I'm paying taxes now. And to Sian for so many things that I'd need an extra appendix to list them all, may we have many more happy years together.

On a far sadder note I would like to take a moment to remember John Tame who passed away as I finished this thesis. My first dealings with him were when I started my final year project back in 1999. His time and effort in helping me get to grips with the clean room and all of its intricacies certainly contributed to getting me to where I am today. His humour was legendary, coffee time discussions have lost their amusement without him. He will be sorely missed by all those who knew him.

# 1. INTRODUCTION

Anyone reading the electronic press will not have failed to notice the increasing attention given to smart tags, flexible displays and inkjet printed electronics. This interest has arisen from the advances made in elucidating the charge transport mechanisms and in the fabrication of commercially-viable electronic devices from organic materials, including polymers. In the early days of electrical engineering polymers such as polyethylene were utilised for their electrically insulating properties and high electrical breakdown strength. As the range of polymers expanded some found application in sensors and transducers.

We now know that the discovery of semiconduction in polyacetylene by Ito, Shirakawa and Ikeda [1] and the further discovery in 1977 that the conductivity could be increased controllably by doping [2] was the start of polymer electronics. These discoveries led to the Nobel Prize in Chemistry for 2000 being awarded to Heeger, Macdiarmid and Shirakawa.

About a decade later, the first field effect transistors (FETs) using a polymer as the active material was reported [3]. This was followed rapidly by reports of polymer Schottky diodes in 1987 [4] and light emitting polymer (LEP) diodes in 1990 [5].

One of the significant properties of polymers is their ability to be processed from a liquid solution which opens many different avenues of fabrication techniques. These include dip coating [6], Langmuir Blodgett (LB) films [7], spin coating [8], inkjet printing [9][10][11], stamping [12] and screen printing [13]. All of these methods are relatively easy to perform, require minimal equipment and have low development costs. As a result, the field of polymer electronics is open to a wide spectrum of research with minimal barriers to development [14].

The inorganic silicon industry presents a story of success starting in 1956 with the award of a Nobel prize in physics for the invention of the transistor by Bardeen, Brattain and Shockley. From that point the industry has pursued a path of decreasing feature size, increasing switching speed and device density. Today this provides massive processing power within the information technology (IT) industry. The development and fabrication costs of today's microchips is so great that the ability to produce small batches is prohibitive and results in a stifling of innovation.

The solution processing of polymers and the associated fabrication methods allow a great diversification in the devices that can be fabricated. The primary advantage is the size and type of substrates that can be used. Silicon wafer size, and the processing facilities used, currently sit at 300mm. To manufacture anything larger increases the cost prohibitively. On the other hand, commercially available inkjet printers are capable of continuous banner printing on flexible substrates 5 meters in width (Vutek UltraVu 5330) and there are minimal barriers to using this type of technology for the manufacturing of polymer devices.

Clearly plastic electronics should not attempt to compete with the inorganic silicon industry in terms of switching speed or small feature size, but should instead focus on its low development costs, ease of processing and large size flexible substrates. From this, an array of new applications can spring, some of the most promising being radio frequency identification (RFID) tags printed onto labels for security or for bar code free shopping [15], giant flexible displays capable of being hung from or wrapped around objects and rolled up for transportation [12] and full size digital image capture, which if combined with a phosphor converter allows x-ray imaging [16].

Given that electronic polymers are easily solution-processed, the most suitable device structures are formed from multiple layers of thin films (figure 1.1) as opposed to the monolithic structures found in inorganic fabrication. This presents a set of challenges relating to the formation of these layers and the physical, chemical and electronic interactions between them. While many of the materials used in polymer electronics are initially selected for their bulk properties (conduction, light emission etc) it is invariably the properties of the interfaces between the different materials which determine the overall performance of the fabricated device.

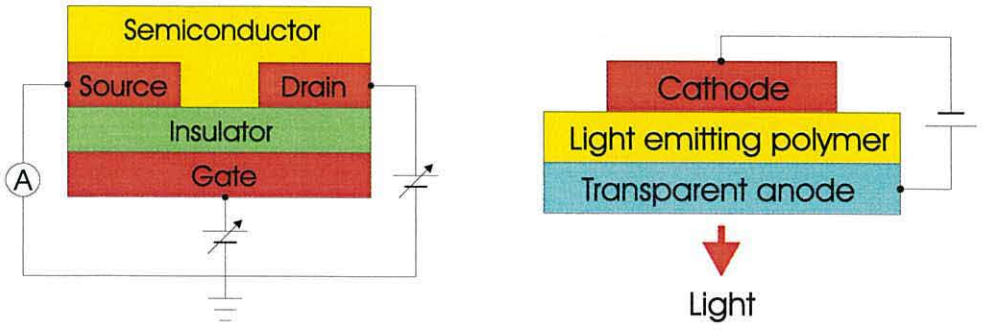


(a) Thin film FET structure.

(b) Light emitting polymer diode structure.

**Fig. 1.1:** Typical device structures in polymer electronics.

Generally, the polymeric layers are prepared by spincoating a solution of the

polymer onto a substrate. The quality of the final layer after solvent evaporation and/or subsequent thermal treatment, is dictated in large measure by the surface tension of the polymer and the surface energy of the substrate on which the film is formed. To produce a uniform thin film, a solution with a low surface tension and a substrate with a high surface energy is required. In some cases, such as inkjet printing, the aim is not to form a continuous film but to deposit discrete droplets of solution in specific locations. As an inkjetted droplet impacts with a substrate a balance is struck between the outward momentum of the spreading droplet and the forces due to surface energy. By careful manipulation of the surface energy and inkjetted solution the size and profile of the dried droplets can be controlled.

By patterning regions of high and low surface energy onto a substrate the coverage of a solution on a surface can be altered [17][18]. In combining surface energy patterning and inkjet printing it is possible to deposit specific quantities of polymer solution onto a substrate and then pattern the regions over which they extend [19].

In fabricating multilayer devices, successive layers are built up on top of each other. One of the problems this presents is "stack integrity", in which the solvent of a new top layer can dissolve or swell previous layers. This generally results in a degradation of the material properties. The solution to this problem is solvent selection, in which alternate layers in a stack are deposited from polar and non-polar solvents [19].

Another problem is that of chemical reactions between layers and their by-products diffusing into different layers. This has been seen in the interface between poly(3,4-ethylenedioxythiophene):poly(4-styrenesulphonate) (PEDOT:PSS) and indium tin oxide (ITO) where the acidic PEDOT:PSS solution can etch the ITO before drying or where moisture absorption causes hydrolysis of the polymer, again resulting in the etching of the ITO [20][21].

PEDOT:PSS was inkjetted onto and across thin films of three common electrode materials, aluminium, gold and ITO, in this thesis in an effort to investigate the physical behaviour of this process.

In any device, charge carriers must be injected from contacts and for multilayer devices, from one layer to another. The injection of charge carriers is determined by the height of the energy barrier due to the alignment of the carrier energy levels between different materials. For small barriers, charge is easily injected from one material to the other and the device current is purely limited by their bulk

transport properties. For larger barriers charge can be transported away from the contact at a greater rate than can be injected across the energy barrier. In this case the device is limited by the energy level alignment of the different materials [22]. This can be overcome by modification of the surface properties or by the inclusion of additional layers which facilitate the injection of charge between the layers it separates [23][24]. A good example of the addition of an extra layer to facilitate charge injection is the use of PEDOT:PSS, between the ITO electrode and the light emitting polymers [25][26].

PEDOT, a conducting thiophene derivative (1.2) was first synthesized in 1988 by chemists at Bayer AG. Using oxidative chemical or electrochemical polymerization PEDOT was found to be insoluble, a problem which was solved by using poly(styrene sulphonic acid) as a water soluble polyelectrolyte to produce PEDOT:PSS [27] or under its commercial name, Baytron P. Initially used as an antistatic coating in photographic films and on plastic components [28] its uses were expanded and developed to include conducting electrodes in capacitors [29], FETs [10][19] and LEDs [30] and, as mentioned previously, as a charge injecting layer in PLEDs [25][26]. The reader is referred to an excellent review of the progress of PEDOT by Groenendaal et.al. [31].

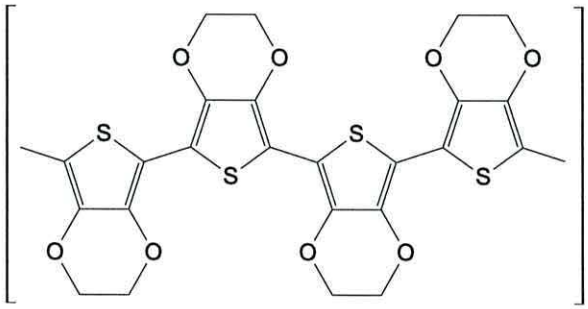


**Fig. 1.2:** Chemical structure of PEDOT.

As has been discussed, the field of polymer electronics has advanced considerably, producing processable and stable polymers for use in devices. Fabrication techniques and structures have been developed and adapted to allow simple and cheap manufacturing of devices on the laboratory scale. However, there is much still to be understood, particularly in the area of the interfacial effects relative to polymers.

While a range of techniques have been developed for studying/characterising the free surface of materials, very few of these can be applied to studying the interfaces within an actual device. Resort has to be made to artificial situations e.g. using low energy electron beam irradiation to stimulate current flow through a device

while studying it with X-ray photoelectron spectroscopy [32]. One solution to the problem is to create lateral rather than transverse devices structures, figure 1.3.

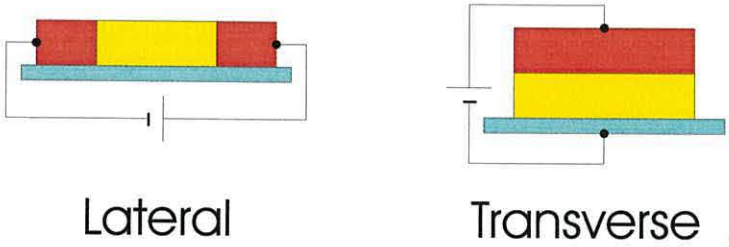


**Fig. 1.3:** Lateral and transverse structures.

If the active layer is thin enough, then the polymer/electrode interface is accessible to a wide range of investigative techniques. In this thesis we have applied atomic force microscopy (AFM), scanning Kelvin probe microscopy (SKPM) and Raman spectroscopy to study processes at these interfaces. AFM is a well established tool for the analysis of surfaces and has been adapted to allow electric force microscopy (EFM) and SKPM to be made [33][34][35]. The use of EFM/SKPM is limited primarily to the upper surface. However, by adopting the horizontal structure the potential distribution across interfaces can be determined.

Fourier transform infrared (FTIR) spectroscopy and Raman spectroscopy allow investigation of the structural properties of materials by the analysis of reflected or transmitted light from an illuminated sample [36][37]. While it is possible to probe through multilayer samples, the illumination and collection of light from the sample is via microscope lenses, limiting the resolution of analysis to the micron scale. Therefore it would be difficult to investigate the properties of thin films in vertical structures as the point of focus would extend through more than one layer. Again, the use of a horizontal structure allows each individual material to be viewed without interference from layers above or below it.

# 2. LITERATURE REVIEW

## *2.1 Introduction*

The aim of this chapter is to provide a review of the current literature pertinent to the work contained within this thesis. This is achieved by examining the electrical properties of polymers including one of the most commonly used ones to date, namely PEDOT:PSS. The main themes described are doping, conduction and contacts.

Also reviewed are some of the most common devices and structures in use today in polymer electronics and the fabrication techniques relevant to them.

Finally, given the need to further investigate electronic polymers and the way in which they behave in multilayer structures two methods, the scanning Kelvin probe and Raman spectroscopy, of probing their properties in-situ are described and discussed.

## *2.2 PEDOT:PSS*

PEDOT is a polythiophene derivative developed at Bayer AG in 1988 [38]. Originally processed by chemical or electrochemical methods, PEDOT was found to have good conductivity (circa $300 Scm^{-1}$) but was insoluble. While insolubility is unattractive in terms of ease of fabrication, PEDOT possessed many attactive properties such as optical transparency and high chemical stability [31].

In 1991 it was found that PEDOT could be doped with PSS, see figure 2.1. PSS is water soluble and dopes the PEDOT during polymerisation by acting as a counterion to the polythiophene chain resulting in a soluble conducting polymer [27]. Marketed commercially as Baytron P, the polymer fulfilled the requirement for ease of fabrication by being water soluble and forming good films while at the same time retaining its optical transparency, high chemical stability and good conductivity (circa $1 Scm^{-1}$).

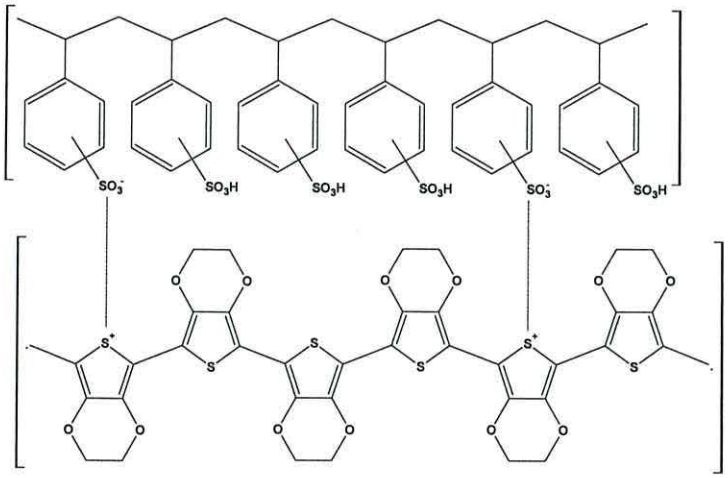


**Fig. 2.1:** Chemical structure of PEDOT doped with PSS.

## 2.3 *Electronic conduction in conjugated polymers*

Conjugated polymers possess a "backbone" of alternating single and double carbon-carbon bonds, figure 2.2, and it is to this that the electronic properties of PEDOT can be attributed. Carbon has an atomic number of 6 and has a ground state of $1s^2 2s^2 2p^2$.

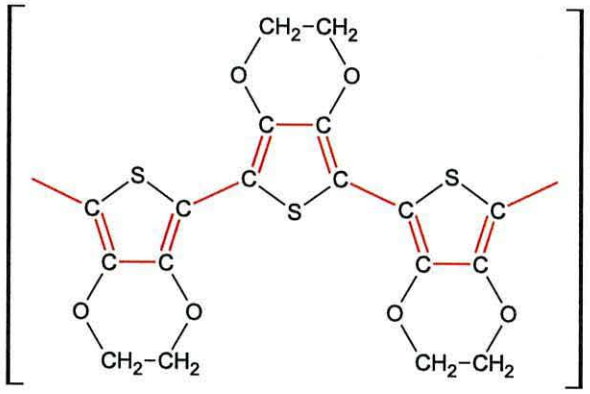


**Fig. 2.2:** Chemical structure of PEDOT showing conjugated backbone in highlighted in red.

If the carbon atoms which make up the backbone of the polymer are saturated then all four of the valence electrons are involved in chemical bonding which form $\sigma$ bonds. In this case the four valence atomic orbital form four identical $sp^3$ hybridised orbitals. As all of the electrons are involved in chemical bonding the polymer is an insulator.

In the case of unsaturated conjugated polymers only three of the four valence electrons are involved in chemical bonding and form 3 identical $sp^2$ hybridised orbitals aligned at 120° to each other. The remaining $2s$ electron is promoted into an empty $p_z$ orbital which is oriented perpendicularly to the plane of the $sp^2$

hybridised orbitals. This is shown in figure 2.3.

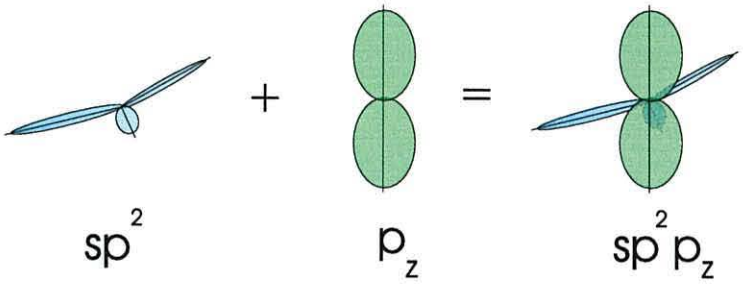


**Fig. 2.3:** Graphical representation of the orbitals in a $sp^2$ hybridised carbon bonding system.

Figure 2.4(a) shows how the 3 $sp^2$ hybridised orbitals overlap each other to form chemical $\sigma$ bonds while figure 2.4(b) shows how the $p_z$ hybridised orbitals overlap each other to form $\pi$ bonds. The $\pi$ bonds have a weaker interaction and allow the electrons within the orbitals to be delocalised over large portions of the chain, thus facilitating conduction of charge along the polymer. The $\sigma$ bonds form the "backbone" of the polymer chain while the $\pi$ bonds form the path for conduction along it.

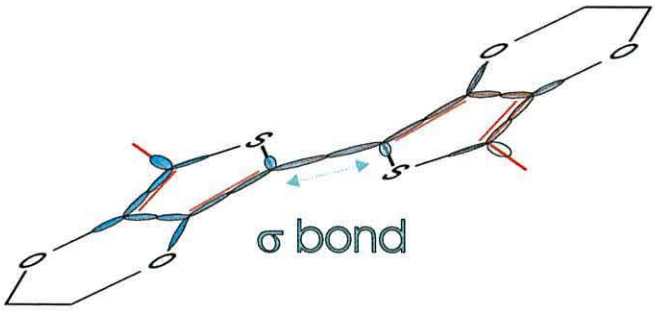


(a) Chemical structure of PEDOT with the $sp^2$ hybridised orbitals overlaid showing the $\sigma$ bonding system.

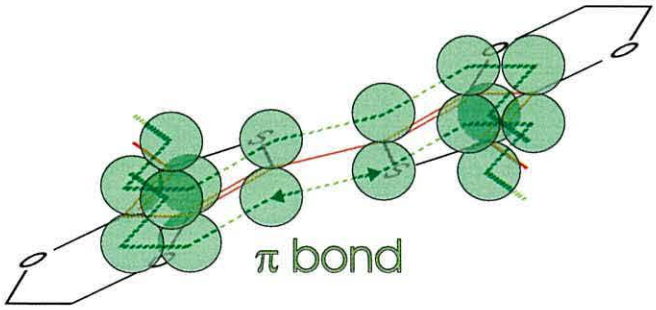


(b) Chemical structure of PEDOT with the $p_z$ hybridised orbitals overlaid showing the $\pi$ bonding system.

**Fig. 2.4:** $\sigma$ and $\pi$ bonds in PEDOT.

## 2.4 *Doping of conducting polymers*

Usually the intrinsic conductivity of a conjugated polymer chain is relatively low in the range $10^{-10}$ to $10^{-5} Scm^{-1}$ but can be increased to the "metallic" range of approximately 1 to $10^{4} Scm^{-1}$ by doping. This can be achieved by four different methods, i) chemical, ii) electrochemical, iii) space charge injection and iv) photo doping. In all cases, charge is either added or removed, p-doped or n-doped respectively, from the $\pi$ system resulting in an increased ability to transport charge along the conjugated polymer backbone.

Chemical and electrochemical doping involves redox reactions in which electrons are added to (reduction) or removed from (oxidation) the $\pi$ system of the conjugated polymer while charge balance is maintained by the presence of counter ions. By adjusting the doping concentration, the conductivity of the polymer can be varied. Providing the electron or hole has sufficient energy to overcome the binding energy between it and its counter ion it can contribute to current flow in the polymer. It can be difficult to control the level of doping in the chemical doping process. This is overcome in electrochemical doping in which the charge on the polymer is supplied by an electrode with ions moving in or out of the polymer from the electrolyte to maintain charge balance. The doping concentration is therefore controlled by the difference in potential between the electrode and the electrolyte.

Charge injection and photo-doping involve no counter ions. In charge injection doping, the amount of charge in the $\pi$ system is altered by the accumulation of charge within the polymer due to an electric field. In metal/semiconductor (MS) structures, the injection of charge across the interface into the semiconductor can locally alter the doping of the polymer at the interface.

The process can also occur in metal/insulator/semiconductor (MIS) structures where the charge distribution in a semiconductor is altered by the application of an electric field across the insulator. This results in a surface layer of charge forming in the semiconductor at the semiconductor/insulator interface changing the amount of charge on the polymer in that region.

In photo-doping electron-hole pairs are created in the polymer by photo-absorption during irradiation. This creates free charges which exist for the duration of the applied irradiation but which disappear due to recombination when the irradiation is removed. If a potential is applied during irradiation then the electron-hole pairs separate and photoconductivity is observed. As a result of photo-absorption the polymer is locally oxidized and reduced by the presence of the hole and electron respectively resulting in an alteration of the charge in the $\pi$ system.

The addition of an electron or hole to the $\pi$ system of the conjugated polymer in turn generates a structural relaxation in the molecule which shifts the energy levels of the charge to a lower energy. Therefore as the electron or hole moves along the conjugated backbone so too does the structural deformation it creates.

If the interchange of the single and double carbon bonds within a conjugated polymer results in no change in the total energy of the system then the system is a degenerate ground state system. If the interchange results in a higher ground state energy then the system is a non-degenerate ground state system.

In non-degenerate ground state systems (such as in PEDOT) the combination of the electron or hole and the structural deformation it creates is known as a polaron. This results in two polaronic states in the bandgap, symmetrically located above and below the valence and conduction bands respectively.

If a further electron or hole is added to the $\pi$ system of the conjugated polymer a second polaron is created. Both polarons can exist independently of each other or they can combine to form a bipolaron. The formation of polarons and bipolarons is dependent on the doping levels. In thiophenes the structural deformation of the polaron/bipolaron causes the benzene ring to change from a benzenoid to a quinoidal configuration (figure 2.5). The structural arrangement and doping scheme is shown in figure 2.6.

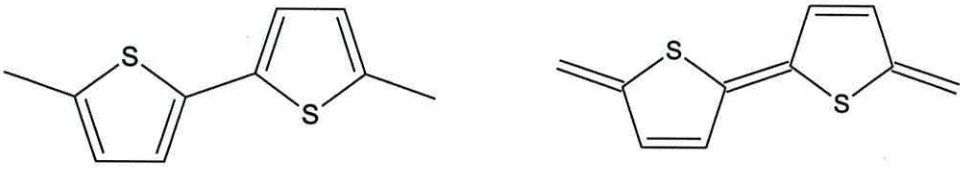


(a) benzenoid. (b) Quinoid.

**Fig. 2.5:** Bonding arrangement in polythiophene.

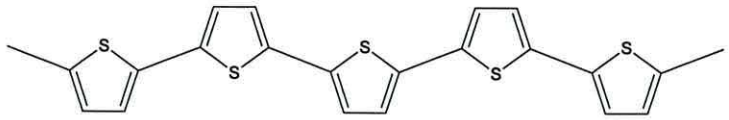

(a) Neutral polythiophene.

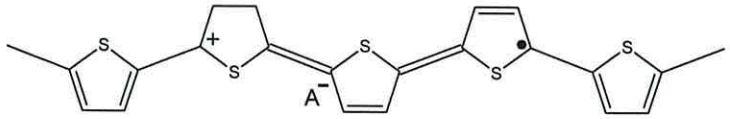

(b) Polaron.

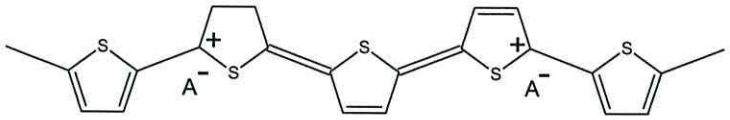

(c) Bipolaron.

**Fig. 2.6:** Structural arrangement in polythiophene.

The reader is directed to two excellent articles by A.J. Heeger [39] and A.G. MacDiarmid [40], which include discussion of doping in conjugated polymers.

## 2.5 *Bulk charge transport*

The linking of $\pi$ orbitals along a conjugated polymer chain allows the movement of charge along that chain (intrachain transport). However, in a bulk polymer the chains often lie in a disordered state so a charge moving through the polymer will not traverse a single conjugated chain, but will have to move along many different chains (interchain transport). The ability of a charge to hop from one chain to another is dependent on how well the $\pi$ orbitals of each chain align and any difference in energy levels between the conduction bands [41][42].

In the case of PEDOT:PSS, the polymer is a blend of two polymers, conducting PEDOT and its charge balancing dopant PSS. X-ray and ultraviolet photoelectron spectroscopy studies have shown that the distribution of PEDOT and PSS throughout a film is not uniform, rather, there is a greater percentage of PSS at the surface. AFM studies of the surface of spin coated films show a grain-like appearance, which combined with the spectroscopic results indicate that the films consist of individual grains, with each grain having a centre rich in PEDOT and a surface rich in PSS [43][44].

One of the methods to increase the conductivity of PEDOT:PSS films is to

increase the molecular order within the films thereby increasing the overlap of the $\pi$ orbitals of different chains. This can be achieved by the addition of polyalcohols such as sorbitol and glycerol to the PEDOT:PSS solution prior to spin coating. The polyalcohols interact with the PEDOT:PSS in such a way as to reduce interchain interactions during spin coating allowing greater orientational relaxation, therefore increasing the molecular order. Following the evaporation of the solvents, including the sorbitol, the films exhibit higher conductivities than those spun from sorbitol-less solutions even though there is no sorbitol remaining [41][44].

## *2.6 Contacts*

It is necessary to make contacts from devices to external circuits or between individual devices. This invariably requires the formation of a contact between a metal and a semiconductor. It is desirable that this contact is ohmic. By this we mean that there is good transport of electrons and holes across the junction such that there is little potential drop across the junction and that the current through the device is determined by the bulk conductivity of the semiconductor rather than the properties of the contact.

In many instances the contact between a metal and a semiconductor is rectifying such that when current flows in one direction through the junction there is minimal potential drop across it, but in the opposite direction there exists a large potential drop across it. An example of a rectifying contact is the Schottky barrier.

### *2.6.1 The Schottky barrier*

The behaviour of a semiconductor-metal contact can be predicted by an examination of the electron energy band diagrams of the two materials. Figure 2.7 shows the electron energy band diagrams for a metal and a p-type semiconductor. The energy $q\Phi_M$ is the energy required to remove an electron at the Fermi level to the vacuum outside the metal surface and is known as the work function of the metal, $\Phi_M$. Similarly the work function, $\Phi_S$, of the semiconductor is determined by the energy difference between the Fermi level of the semiconductor and the vacuum level where the Fermi level lies in the energy gap, $E_G$, between the valence, $E_V$, and conduction, $E_C$, bands of the semiconductor.

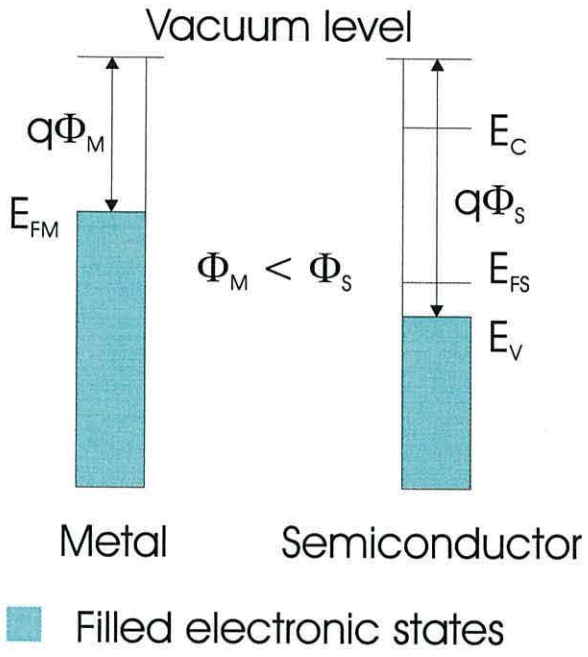


**Fig. 2.7:** Electron energy band diagrams for a metal and a p-type semiconductor.

When the metal and semiconductor are brought into contact charge transfer occurs until the Fermi levels of the two materials align (shown in figure 2.8). Holes from the semiconductor diffuse into the metal to recombine with the electrons there resulting in the semiconductor charging negatively with respect to the seminconductor. As a result a depletion region is formed in the semiconductor next to the interface. This creates an internal potential which acts to limit the charge transfer between the materials. At equilibrium this potential is known as the contact potential and is the difference between the work function potentials $\Phi_M - \Phi_S$.

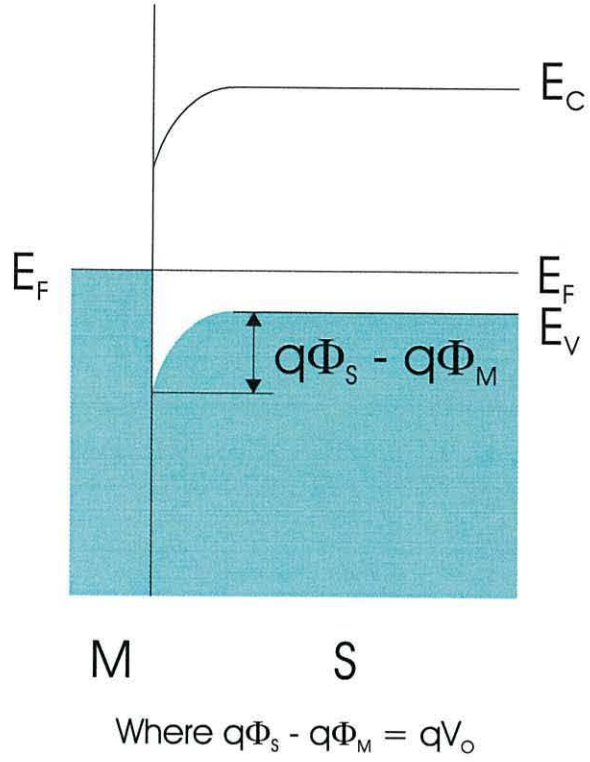


**Fig. 2.8:** Electron energy band diagram of a metal and a p-type semiconductor in contact.

When an electric field is applied to the junction the contact potential between the two materials can be varied and gives rise to the Schottky effect (shown in figure 2.9). If the metal is made positive with respect to the semiconductor by an applied voltage then the barrier to a hole moving from the valence band of the semiconductor into the metal is reduced by the applied potential. This will increase the rate of conduction of holes across the barrier. If the metal is made negative with respect to the semiconductor, the barrier to hole flow will be increased, thus reducing hole transport.

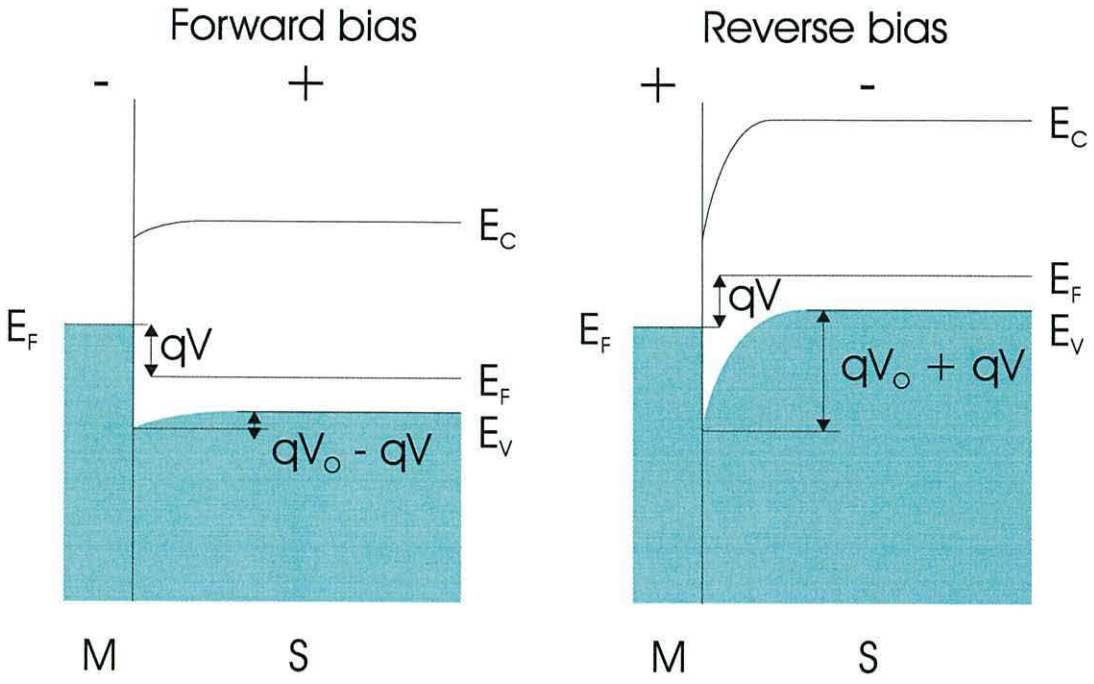


**Fig. 2.9:** Electron energy band diagrams for a metal and p-type semiconductor junction under forward and reverse bias.

The description of the Schottky barrier above relates to the case where $\Phi_S > \Phi_M$. Where $\Phi_M > \Phi_S$ an ohmic contact is formed. When the Fermi levels of the two materials align the majority carriers do not diffuse into the metal so no depletion region is formed as holes are transfered to the semiconductor. In this case the barrier to hole flow between the metal and the semiconductor is small and easily overcome. As a result the contact conducts holes well across the junction regardless of the polarity of an applied potential.

The use of materials of different work functions can be seen in polymer light emitting diodes, where for optimum efficiency an equal number of electrons must be injected from a cathode into the light emitting polymer as holes from the anode. Therefore the cathode needs to be of low work function while the anode of high work function [22].

Metals such as calcium and magnesium have low work functions so make good electron injectors, however both are environmentally reactive so are less desirable. Aluminium makes a more appropriate electrode, however its work function is not sufficiently low to provide highly efficient electron injection. This can be modified by the inclusion of an intermediate layer of lithium fluoride between the light emitting layer and the aluminium providing increased electron injection and the required environmental stability [45].

The structure of polymer light emitting diodes consists of a light emitting

polymer sandwiched between an anode and a cathode. In order for light to escape one of the electrodes needs to be optically transparent. Indium tin oxide is a widely used anode due to it being conductive and transparent. However, the work function of ITO is highly variable and is dependent on the surface condition of the material [46][47]. This can be due to different deposition methods or down to atmospheric conditions or adsorbed species. Again, the inclusion of an intermediate layer, this time of PEDOT:PSS, improves the hole injection efficiency of the electrode [24][26].

### *2.6.2 Deviations from ideal behaviour*

The contacts described in the previous section are ideal cases based on an examination of the electron energy band diagrams of the two materials. Metals and conjugated polymers have a weak interaction and it would be expected that they would conform to the predicted behaviour. However, studies using photoemission spectroscopy have shown that organic/organic [48] and organic/metallic [49][50] contacts do not behave as expected, requiring consideration of surface states and interface dipoles. When the different materials are brought together chemical interactions between them may form new chemical species which can alter the electronic structure and hence behaviour of the junction.

The presence of a dipole layer at an organic/metallic interface can alter the charge injection barrier. An interface dipole in which the organic layer is charged negatively and the metallic layer positively reduces the work function of the metal having the effect of reducing (increasing) the hole (electron) injection barrier. An oppositely directed dipole will have the reverse effect on the hole/electron injection barrier [51]. The formation of interface dipoles is governed by the adsorption of the organic molecules onto the surface of the metal.

Koch et.al. [50] compared the energy level alignment of electrodes of gold and PEDOT:PSS to a variety of conjugated organic molecules using UPS. The aim of the investigation was to compare electrodes of two fundamentally different materials but of similar work functions. Even though the work functions of gold and PEDOT:PSS are similar the injection barrier for holes into the conjugated organic layer was found to be significantly larger for the gold electrode than the PEDOT:PSS electrode. In metals there is a contribution to the work function from the surface dipole which is modified by the adsorption of the conjugated organic molecules on its surface. When the conjugated organic molecule was deposited onto the surface of the gold the work function of the gold decreased due to a smaller contribution from the surface dipole resulting in a greater barrier to hole injection. The work function of PEDOT:PSS is determined by the charge transfer

between the PEDOT and PSS units and has minimal contribution from surface dipoles. As a result, the adsorption of conjugated organic molecules on the surface of PEDOT:PSS has little effect on its work function resulting in a smaller barrier to hole injection than for gold.

Metallic electrodes are generally evaporated under vacuum. If the metal is deposited onto an organic film then the hot metal atom will have sufficient energy to break the weak van der Waals bonds of the organic solid and diffuse into the film. If, on the other hand, the organic material is deposited on top of the metal there is less likelihood of diffusion as the surface of the metal provides a stable surface for the lower energy organic molecules. As a result the interface between the materials is either diffuse or abrupt depending on the deposition process and can result in significantly different contacts [52].

Many metals readily form a thin oxide layer on their surfaces which can form an insulating barrier between the metal and subsequently deposited semiconductors. Aluminium is a commonly used electrode material and reacts with oxygen to form an oxide layer during evaporation. If the layer is sufficiently thin, electrons and holes can tunnel through. However as the thickness increases the metal-semiconductor device behaves more like a metal-insulator-semiconductor device.

Work by Lazzaroni et.al. produced theoretical modelling and x-ray and ultraviolet photoelectron spectroscopy (XPS, UPS) on the interaction of aluminium vacuum evaporated onto films of polyacetylene and polythiophene [53]. They showed that the evaporated aluminium molecules interacted strongly with carbon in the conjugated backbone. This resulted in a significant disturbance to the $\pi$ system of the chain, significantly reducing the conjugation length. The bonding between the aluminium and carbon atoms leads to a charge transfer between them with the aluminium atom becoming more positive. The charge transfer should not be considered as a doping/dedoping process as the charges are localised on the polymer backbone so cannot contribute to conduction.

As mentioned earlier, ITO is a commonly used anode material in polymer light emitting diodes with PEDOT:PSS as a hole transport layer to improve the injection of holes into the light emitting polymer. However it was found that the interface between ITO and PEDOT:PSS was not chemically stable [20]. PEDOT:PSS solutions typically have a pH of between 1 and 2 and $In_2O_3$ has a high solubility in acid therefore it is presumed that the PEDOT:PSS has the ability to dissolve the ITO. Using Rutherford backscattering spectrometry (RBS) it was found that the indium content of the PEDOT:PSS varied with time and conditions.

The indium content was low immediately after spin coating (from an aqueous solution) and remained relatively low even after prolonged heating in a dry nitrogen atmosphere. However, upon exposure to air for several days the indium content of the PEDOT:PSS increased to a maximum of 1.2at.%. It was proposed that atmospheric moisture was absorbed by the PSS forming acidic $H_3O^+$ byproducts capable of etching the ITO and allowing indium to diffuse into the film. It was also found that the indium content of the PEDOT:PSS was uniform across the full thickness of the 150nm thick film.

Separate work found that a self-assembled monolayer (SAM) of alkylsiloxanes between the ITO and the PEDOT:PSS was sufficient to prevent the diffusion of indium into the polymer film [21]. The SAMS were deposited onto the ITO by immersion and produced ultrathin (≈0.3-0.5nm) and uniform layers allowing uniform charge transport across it.

## *2.7 Fabrication and inkjet printing*

Electronic polymers are generally solution processable allowing a variety of fabrication methods including dip coating, LB films, spin coating, inkjet printing, stamping and screen printing. The primary principle underlying these technologies is the deposition of a solution in which a polymer is dissolved and upon evaporation of the solvent the polymer remains.

Inkjet printing lends itself well as a method for depositing polymer solutions providing the solution is within the handling capabilities of the inkjet printer. The primary factors affecting the printability of a solution are its viscosity and surface tension, both of which can be modified with additives. Inkjet printing is an additive process so there is minimal waste which contrasts with the photolithographic process. The process is non-contact and with suitable mechanical control can be applied to 3D surfaces and allows the use of flexible substrates. The process of depositing polymers is data-driven with the required pattern commonly generated by computer aided design (CAD) packages which means that small batches can be produced or even individual circuits.

It should be noted that inkjet printing is not limited to polymer solutions but can include ceramic precursors, sol-gels, nano-particles, metallic dispersions and biologically laden solutions to name but a few. The reader is directed to three articles reviewing fabrication and in particular inkjet printing in the field of microfabrication [11][54][55].

One of the aims of inkjet printing in polymer electronics is to develop the capability to inkjet print all-polymer devices on a reel-to-reel production allowing individual device fabrication. This could allow the realisation of large area, flexible displays, for example, or RFID tags as an alternative to bar codes [10][15][56][57][58].

### *2.7.1 Inkjet print systems*

Inkjet print systems can be classified under two broad types, continuous inkjet printers and drop-on-demand inkjet printers. A continuous inkjet printer has a piezo-electric printhead which employs a small piezo-electric crystal bonded to a reservoir of ink. As the crystal changes shape it sends a pressure wave from the reservoir to the print nozzle which ejects a droplet from the nozzle. The nozzle continuously ejects droplets at a frequency of around 1KHz and imparts an electric charge onto each droplet. The droplets then pass between two pairs of electrode plates oriented at 90° to each other which can deflect the trajectory of the flying droplet. The electrodes are then used to pattern the deposition of ink on a stationary or moving substrate or, if no droplets are required, the ink is directed into a catchment reservoir for recycling.

Drop-on-demand printers do not eject droplets continuously instead moving the printhead (or substrate) so that the printhead can eject a droplet onto the desired location. Once in position a single droplet (or multiple if required) is ejected using a variety of methods. The two primary methods are piezo-electric and thermal. As described earlier the piezo-electric method uses the change in shape of a piezo-electric crystal to generate a pressure wave in the ink to eject it from the nozzle. The thermal method, also known as bubble jet, uses tiny heaters to generate high temperatures which boil the ink and create a bubble of steam which forces the ink ahead of it out of the nozzle. Generally piezo-electric systems are deemed more suitable for polymer inks as the vaporisation of the ink in thermal inkjetting may have a detrimental effect on the polymer.

### *2.7.2 Inkjetting of polymer solutions*

The formation of droplets on ejection from the inkjet nozzle is dependent on the viscosity and surface tension of the ink used, typically up to 2cP and above $35\text{mNm}^{-1}$ respectively [11]. Polymer chemists have worked towards solution processable electronic polymers for many years and as a result many different materials can be inkjetted. Solutions can be modified by the addition of additives such as methanol, ethanol, isopropanol or acetone [19].

The resolution of printing is determined by a number of factors including the accuracy with which a droplet can be placed on a substrate and on the size of the remaining polymer deposit. The accuracy of droplet placement is dependent on three factors; nozzle jetting, nozzle to substrate separation, nozzle to substrate alignment. The size, shape and position of the polymer deposit is dependent on droplet volume, polymer concentration in the solvent, interaction between the droplet and the surface and evaporation rate of solvent. The reader is directed to an article by Creagh et.al. for further discussion into the accuracy of inkjetting [59].

Once a droplet has been ejected from the print nozzle it will continue on a straight flight path until it impacts with the substrate (unless air currents are present). If a nozzle ejects a continuous train of droplets onto a substrate it would be expected that each droplet would exactly overlay the previous one. However this is not the case due to statistical variations in the ejection process which cause slight deflections in the flight of a droplet. It is difficult to minimise this since it occurs during the formation of the droplet as it breaks the meniscus across the face of the nozzle.

The flight of the droplet can also be deflected as it leaves the nozzle by either nozzle imperfections or nozzle contamination. Imperfections in the nozzle can add an additional error to the flight of the droplet, though this error is constant from droplet to droplet so can be corrected by re-alignment of the nozzle. This is more difficult if the nozzle is one of many in a fixed array. Dried ink deposits or wetting of ink on the face of the nozzle can also deflect the flight of the droplet. This cannot be corrected for but can be avoided by (1) regular cleaning of the nozzle and its face, (2) formulating the ink, (3) coating the face such that it becomes hydrophobic, and hence is not wetted by the ink.

Given that the droplet continues in straight flight once it leaves the nozzle, minimising the nozzle to substrate separation will reduce any errors in the point of impact on the substrate. The ability to reduce the separation depends on the mechanical structure of the printer but can be limited by the flatness of the substrate. Typical separations are in the order of 0.3-1mm.

The accuracy of the alignment of the nozzle over the substrate will clearly have a direct effect on the accuracy of the point of impact of a droplet on a substrate. This can be overcome by the use of high quality movement stages and stiff construction methods.

As a droplet impacts with a surface it spreads out across the substrate finally limited by the surface tension of the liquid and the surface energy of the substrate. The surface tension of the ink can be considered constant and is determined by the modification of the polymer solution for jetting. Substrates with different surface energies can be used to modify the size of the "wet" impacted droplet prior to evaporation. In addition, regions of different surface energy can be used to modify the spreading of an impacting droplet. However this approach can have a detrimental effect on printing resolution on substrates where the surface energy is poorly defined [10].

The concentration of polymer in solution is determined by the formulation of the ink required to provide an acceptable viscosity and surface tension. The volume of the droplet can be minimised so as to increase the resolution of printing, however there is a limit due to the physical instability of very small droplets. Typical volumes are in the order of 5 to 30pL with a droplet to droplet volume variation in the order of 1%.

Evaporation of the solvent from the "wet" droplet leaves polymer deposit on the substrate. While it may be expected that the remaining polymer would have a similar profile to that of the "wet" droplet this is not the case. The outer edge of the droplet is fixed. As solvent evaporates from the edges an outward flow from the centre is set up. This results in a greater deposition of polymer at the outer edge than in the centre, a process which is governed by the evaporation rate of the solvent [58].

### *2.7.3 Device fabrication*

Two of the most significant applications for inkjet printing in polymer electronics are the fabrication of all-polymer, printed FETs and for patterning light emitting polymers. Sirringhaus et.al. succeeded in inkjet printing all-polymer FETs and integrated them into logic circuits although the fabrication process did involve a photolithographic step [10][19]. One of the important factors in the performance of thin film FETs is the length of the channel between the source and drain electrodes. In order to achieve sufficient drive current and fast switching a channel shorter than $10\mu m$ is necessary. Although inkjet printing is achieving smaller droplet volumes and greater deposition accuracy, the resolution of printed electrodes still falls short of that required for fabricating parallel source and drain electrodes with a separation of less than $10\mu m$ and no short circuit between them.

Sirringhaus et.al. overcame this problem by the use of surface energy patterning. A 50nm thick layer of polyimide (PI) was deposited on a glass slide and covered by

a photolithographically patterned photoresist. The unprotected PI was then etched using an $O_2$ plasma and the photoresist removed leaving $5\mu m$ wide strips. This resulted in hydrophilic glass with regions of hydrophobic PI on its surface. Upon inkjet printing an aqueous solution of PEDOT:PSS onto the glass close to the PI strips the ink droplets spread out until they reached the PI which then repelled the ink. This method of surface energy patterning allowed a pair of conducting PEDOT:PSS electrodes to be printed with a separation of $5\mu m$ where the resolution of the channel edges was governed not by the inkjet printing process but by the hydrophobic PI strip.

The inkjet printed source and drain electrodes were then followed by spin coated layers of semiconductor and gate dielectric before an inkjet printed gate electrode was deposited (without need of patterned PI). In order to fabricate circuits with multiple FETs it is necessary to be able to connect the gate of one to the source or drain of another and requires interconnects through different layers of the thin film structure. This was achieved by the creation of via holes through the gate dielectric and semiconducting layer using a novel inkjet printing process. It was found that if a droplet of solvent (for the layer to be penetrated) was deposited on the surface of a film it would partially dissolve the film and then redistribute the film solute towards the edge of the droplet upon evaporation. This is the same effect as found with an evaporating droplet on a surface as discussed earlier. Upon repeated deposition of solvent the film is progressively dissolved and migrates outwards to form a via hole. Providing the layer below is insoluble in the inkjetted solvent then the via hole will not progress any deeper and by changing the solvent for conducting ink a conducting interconnect can be made.

Their work presented a significant step towards all-polymer printed circuits but was limited by the photolithographic patterning of the surface energy of the substrate. This was later overcome by the use of a laser patterning technique to modify the surface energy of the substrate to a resolution of $5\mu m$. A substantial review of the aspects affecting inkjet printed FETs can be found in Burns et. al. [57].

One of the greatest restrictions on the use of inorganic semiconductors in the field of light emitting displays is the size of the substrate that the associated fabrication techniques can handle. As discussed previously, inkjet printing is essentially unlimited in the size of substrate it can handle. Therefore there is the option to fabricate large displays using light emitting polymers as the active elements. The two significant factors governing the use of inkjet printing in light emitting displays are the lateral resolution of the display element and the uniformity of the thickness of the deposited polymer.

For basic monochrome 150 dots per inch (dpi) displays, inkjet deposited droplets of light emitting polymer of $100\mu m$ in diameter are sufficiently small to form the individual pixels of the display. Multi-colour displays are more complex, with each pixel requiring red, green and blue light emitting elements, with each colour being capable of variable light intensity output. Therefore each pixel requires at least three patterned light emitting elements. In order to fabricate these into a high resolution display the light emitting elements may require a higher degree of patterning, a problem that has been addressed in the fabrication of inkjet printed FETs.

This was demonstrated by Shimoda et. al. who fabricated a pixelated display using a polysilicon thin film transistor (p-Si TFT) backplane for driving the light emitting elements [58]. In order to allow RGB (red green blue) colour each pixel comprised three columns of sub-pixels, with each column containing three sub-pixels thereby allowing four grey scales for each of the three colours. Therefore each pixel comprised 9 sub-pixels. In order to obtain a high enough resolution for the display each pixel was designed to be no larger than $200\mu m$. This was achieved by having a 3x3 grid of sub-pixels per pixel, with each sub-pixel being $30\mu m$ in diameter and $40.5\mu m$ apart. In order to achieve the level of accuracy required, a $3\mu m$ layer of PI was placed on top of an ITO electrode and patterned so as to remove a $30\mu m$ diameter circle of the polymer. Upon inkjet printing the light emitting polymers onto the substrate, the droplets self-aligned by collecting in the base of the circular holes providing accurate patterning and location of the light emitting elements.

Inkjet printing is capable of depositing accurate quantities of polymer inks to specific locations on a substrate. However the evaporation of the solvent has a significant effect on the remaining deposit of polymer solute. As a result inkjet printing can produce variable results when used for fabricating displays [58]. The solution to this problem is primarily one of tailoring the solvent evaporation conditions.

As discussed earlier, inkjet printing produces polymer deposits of variable thickness. The vertical structure of polymer light emitting diodes applies an electric potential across a thin film of a light emitting polymer sandwiched between electrodes. Any pin holes in the emissive layer will create a short circuit between the electrodes while any variations in thickness will locally alter the electric field across the layer which could eventually lead to its breakdown [60].

One solution to the problem of pinholes was presented by Yang et. al. who used a spin coated buffer layer in conjunction with inkjet printing [61][62][63].

The buffer layer is a spin coated layer which is either applied before or after the inkjet printed polymer and effectively seals any pinholes in the inkjetted layer thus preventing short circuits between the anode and cathode. A secondary function of the buffer layer is to act as a charge injection layer. Either the buffer layer can be the charge injection material and the inkjetted material the electroluminescent polymer or vice versa. If the potential applied to the electrodes is lower than the injection barrier for the electroluminescent polymer without the charge injection layer, but higher than that with the layer, then only those regions will emit light.

A similar use of a buffer layer was demonstrated by Hebner et. al. in which fluorescent dyes were introduced into spin coated films of a light emitting polymer to alter the wavelength of emitted light [9][64].

## 2.8 *Scanning Kelvin Probe Microscopy (SKPM)*

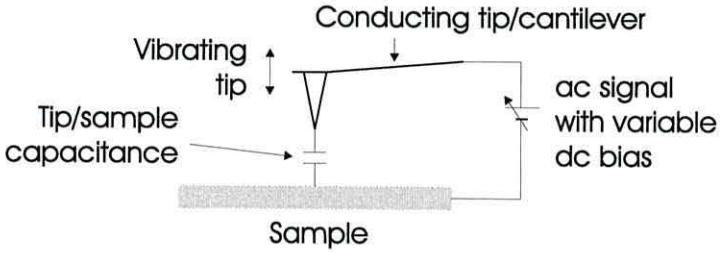


**Fig. 2.10:** Modification of AFM for SKPM using a conducting tip with an applied dc potential.

The Kelvin probe is a widely used technique for determining the contact potential difference between conducting materials [65]. It utilises a vibrating electrode above a conducting sample where the contact potential between the electrode and sample charges the air capacitance formed between them. As the electrode vibrates the distance between it and the sample varies resulting in a change in the capacitance between them and a measurable alternating current.

If the contact potential, i.e. the potential difference between the electrode and sample is zero then the alternating current generated by the vibrating electrode will tend to zero. Using this principal, if a DC bias is applied to the electrode such that the alternating current tends to zero, then the DC bias will equal the contact potential between the electrode and sample.

The Scanning Kelvin Probe Microscope (figure 2.10) utilises this effect by applying an AC signal to a conducting AFM tip vibrating just below its resonant frequency. Due to long-range Coulomb forces, the tip will oscillate with respect to

the surface in relation to this AC signal. Simultaneously, a DC bias is applied to the tip such that when the physical oscillations of the tip tend to zero, the contact potential between the tip and sample is equal to the DC bias applied to the tip.

This can be shown mathematically. If an oscillating voltage;

$$V_{AC}sin(\omega t) \tag{2.1}$$

is applied to the tip, a resulting oscillating electrostatic force, $F$, will be felt, the amplitude given by;

$$F = \frac{1}{2}V^2\frac{\delta C}{\delta z} \tag{2.2}$$

where $V$ is the potential between the tip and substrate, $C$ the tip-substrate capacitance and $z$ the tip-surface separation.

The potential between the tip and the substrate is the sum of the surface potential, $V_S$, the DC bias, $V_{DC}$, and the applied ac signal, $V_{AC}sin(\omega t)$, giving;

$$F = \frac{1}{2}(V_S + V_{DC} + V_{AC}sin(\omega t))^2\frac{\delta C}{\delta z} \tag{2.3}$$

Equation 2.3 can be expanded to give a fundamental component;

$$F(\omega) = (V_S + V_{DC})V_{AC}sin(\omega t) \tag{2.4}$$

Therefore as $V_S + V_{DC}$ tends to zero so to will the amplitude of the oscillation of the tip. By adjusting $V_{DC}$ so as to null the tip vibration $V_S + V_{DC} = 0$ so the sample potential can be determined by the applied DC bias.

In order to generate a two dimensional map of surface potential the sample is moved in one horizontal plane in which it obtains the height data using TappingMode AFM. The same line is then scanned again using a method known as LiftMode in which the tip is lifted a preset distance above the sample and scanned across a second time, maintaining a constant sample/tip separation (the lift height). On this second trace the surface potential is determined using the Kelvin probe method. Hence the SKPM generates two matrices of data where each matrix location relates to the same position. One matrix contains height data, the other contains surface potential data.

In a polymer device, charge needs to be injected from one electrode and extracted from another. In order to obtain optimum efficiency in the device barriers to charge transport need to be kept to a minimum. SKPM provides a method for investigating the potential distribution across devices and identifying points of

high potential drops, thereby indicating barriers to charge transport. The primary limitation of SKPM is that it can only provide the surface potential of a device. Therefore the potential distribution in vertical multilayer structures, as used in polymer light emitting diodes, cannot effectively be examined using SKPM.

SKPM has been used to produce plots of the surface potential across the channel of operating organic FETs. Both Burgi et.al. [66] and Nichols et. al. [35] used the same bottom contact structure of FET shown in figure 2.11(b) using P3HT and pentacene as the active materials respectively while Puntambekar et. al. [67] compared both the top and bottom contact structures using pentacene. In all of the bottom contact devices significant potential drops were seen at the electrode edges. In the comparison of the top and bottom contact devices it was shown that there was a significant difference in the behaviour of the two structures, with a near-linear potential drop between the electrodes edges of the top contact device, indicating efficient charge injection in this case.

The use of SKPM provides the ability to identify contact resistances at the source and drain electrodes and observe the effect of different electrode polarisations (injecting/extracting), electrode materials and top/bottom electrode contacts on these contact resistances.

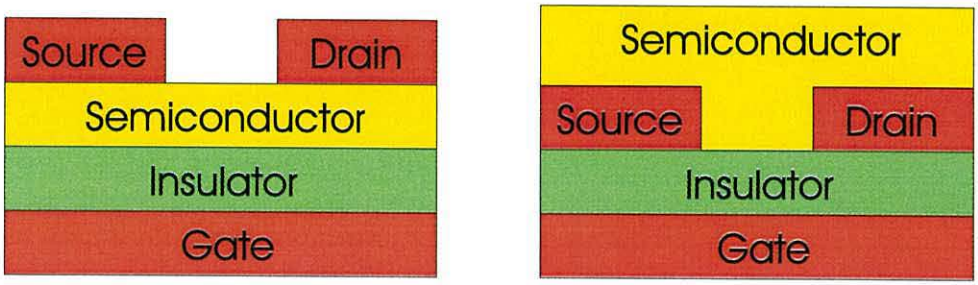


(a) Top contact FET.

(b) Bottom contact FET.

An alternative method for probing of the potential distribution in devices is to make point contacts to the devices and measure the potential at that point using an electrometer. This technique has been applied to Al/P3HT/Au Schottky diodes and a sexithiophene based FET [68][69] and provided measurements of the contact resistances at the organic-metal interface.

While capable of high resolution potential mapping the contact method has disadvantages over the scanning Kelvin probe method. The point contact may physically damage the film it is contacting. Damage can also be caused by current flowing through the point contact causing local Joule heating and break down of the electrical properties of the film. Furthermore data can only be taken at a series

of discrete points rather than in a continuous profile.

The resolution of SKPM data is nominally 100nm in the horizontal plane and 50mV for the surface potential measurement [66][67]. In principle, the Kelvin probe relies on the electrostatic interactions between the tip and a sample. However, the geometry of the tip and the cantilever which supports it have a significant effect on those electrostatic interactions and on the resulting surface potential map. As the tip vibrates above the surface of the sample the capacitance between them varies and by the nulling of the DC bias applied to the tip the sample potential can be determined. The measured potential therefore is not an exact measure of the potential below the tip but a weighted average of all surface potentials over the sample where the weighting factors are governed by the derivatives of the capacitive interactions between the tip and cantilever and the sample surface. Therefore to achieve the greatest resolution the interactions between the area directly under the tip need to be maximized while those between the sample and the side of the tip and the cantilever need to be minimized. This can be attained by having a long tip supported by a cantilever of minimal area so as to reduce its interactions with the surface while the tip itself should be slender with a slightly blunt end. The reader is directed to two papers by Koley et.al. and Jacobs et.al. for further discussion on SKPM resolution [70][33].

A further effect on the resolution of the SKPM can be due to adsorbed water on the surface of the sample shielding the surface potential. This can be reduced by ensuring films are dehydrated and that the atmospheric humidity is low during the measurement [71].

## *2.9 Spectroscopy*

Raman spectroscopy can be used for investigating the structure and chemistry of molecules within a sample. When monochromatic light is shone upon a transparent sample most of the light will pass through unchanged while some will be scattered by the molecules of the material. Of this scattered light some will have been scattered elastically (also known as Rayleigh scattering) and some inelastically. Light scattered elastically will retain its original frequency, $\nu$, while light scattered inelastically will have shifted in frequency.

Raman spectroscopy is based on the analysis of these inelastically scattered photons. These photons of light, lose or gain some energy when they interact with the vibrating molecules of the sample. This change in energy is measured as a shift in frequency of the light scattered back from the sample, either $\nu - \nu_1$ or $\nu + \nu_1$,

known as the Stokes and anti-Stokes shifts respectively. The frequency shift is characteristic of the molecule and its bonds allowing a qualitative and quantitative analysis of the structure and chemistry of the sample.

As discussed in section 2.4, doping polythiophenes alters the structure of the alternating single-double bonds of the conjugated backbone resulting in the benzene ring changing from a benzenoid to quinoid configuration (figure 2.5). The change in the bonding structure changes the resonant properties of the molecule resulting in a detectable change in the Raman spectrum.

Electrochemical doping of PEDOT allows the amount of charge on the polymer chain to be controlled accurately by the potential between the electrode and the electrolyte. Therefore by combining an electrochemical cell with a Raman spectroscope, the spectra can be determined for different stages of doping.

In 1999 Garreau et.al. published work in which Raman spectra of PEDOT were taken in situ during electrochemical doping [36] and was followed by two more papers on the same theme in 2002 [72][37].

Prior to taking the Raman spectra they took optical absorption spectra in the UV-vis-NIR (Ultra Violet - visible - Near InfraRed) range. From this they could determine that in the neutral state the PEDOT had a large absorption peak around 600nm but as the doping increased the 600nm peak decreased while a broad band grew in the range 800 to 1800nm. Therefore different excitation wavelengths for the Raman spectroscopy would be in resonance with the different doping states of the polymer.

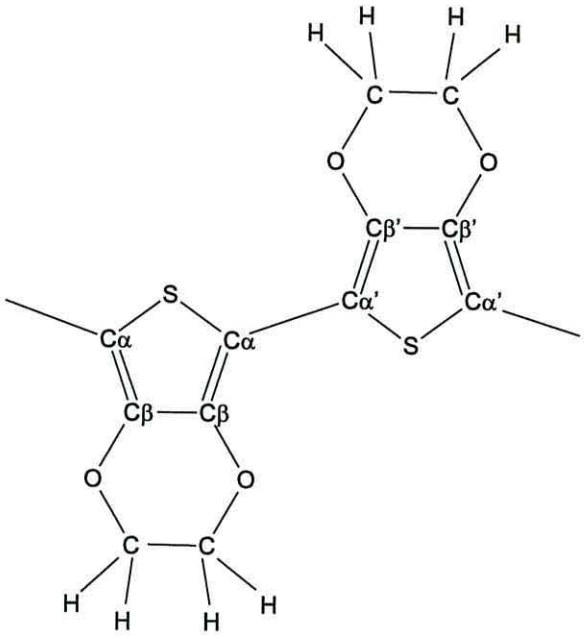


**Fig. 2.11:** Bond assignments for PEDOT.

Figure 2.11 shows the bond assignments for the PEDOT polymer. As the polymer changes from a benzenoid to quinoid configuration the bonds along the conjugated back bone change. These bonds are assigned the following vibrational modes; symmetric $C_\alpha$=$C_\beta$ stretching, asymmetric $C_\alpha$=$C_\beta$ stretching, $C_\beta$=$C_\beta$ stretching and $C_\alpha$-$C_{\alpha'}$ inter-ring stretching. Following symmetrized dynamic matrix modelling (see ref. [36] and references therein) these vibrational modes were assigned predicted wavelengths and are shown in table 2.1.

| Calculated ($cm^{-1}$) | Description |
|---|---|
| 1509 | asymmetric $C_\alpha$=$C_\beta$ stretch |
| 1444 | symmetric $C_\alpha$=$C_\beta$ stretch |
| 1366 | $C_\beta$=$C_\beta$ stretch |
| 1267+1228 | $C_\alpha$-$C'_\alpha$ (inter-ring) stretch |

**Tab. 2.1:** Vibrational assignments for doping effected PEDOT bonds.

The cyclic voltammetry was carried out between -0.1V and +0.8V and showed two oxidation peaks at -0.1V and +0.55V. In polythiophenes polarons appear after the first oxidative peak and bipolarons after the second. The intensity of the Raman spectra taken with an excitation wavelength of 514nm decreased with increasing cell potential confirming that as the polymer became doped it moved out of resonance with the 514nm excitation wavelength. The Raman spectra taken with an excitation wavelength of 1064nm did not decrease in intensity with doping confirming that the doped polymer was in resonance with the 1064nm excitation wavelength.

At the excitation wavelength of 1064nm they made the following observations:

*Asymmetric $C_\alpha$=$C_\beta$ stretch;* At -1.0V it is split into two bands at 1503 and $1545cm^{-1}$, after the first oxidative peak they shift to 1528 and $1562cm^{-1}$ respectively, after the second oxidative peak only one broad peak is observed at $1539cm^{-1}$.

*Symmetric $C_\alpha$=$C_\beta$ stretch;* At -1.0V it is at $1423cm^{-1}$ and shifts down to $1411cm^{-1}$ before the first oxidative peak, after which it shifts to $1431cm^{-1}$, and $1450cm^{-1}$ after the second oxidative peak.

*$C_\beta$=$C_\beta$ stretch;* No change.

*$C_\alpha$-$C'_\alpha$ (inter-ring) stretch;* At -1.0V two bands occur at 1238 and $1271cm^{-1}$. The $1238cm^{-1}$ peak broadens and shifts to $1249cm^{-1}$ before the first oxidative peak, after which it shifts to $1263cm^{-1}$. Following the second oxidative peak three peaks occur at 1239, 1268 and $1289cm^{-1}$.

From the behaviour of the band associated with the $C_\alpha$=$C_\beta$ stretch, the neutral polymer was deduced to have an intermediate structure which changed to a quinod configuration after the first oxidative step and benzenoid after the second. This behaviour is different to polythiophenes where the structure changes from benzenoid to quinoid upon doping.

In 2002 Garreau et.al. [72] included Raman spectra taken with an excitation wavelength of 674nm of PEDOT electrochemically doped in an aqueous medium. At this wavelength the polymer was more resonant in its neutral rather than doped form, however spectral peaks could still be resolved as the polymer was doped.

Raman spectra taken at cell potentials of -0.7 and -0.3V show peaks at 1222, 1267, 1366, 1423 and $1515cm^{-1}$ which correspond to the vibrational modes listed in table 2.1. As the cell potential increased to +0.5 and +0.7V the following changes were observed:

*Asymmetric $C_\alpha$=$C_\beta$ stretch;* Replaced by two peaks at 1528 and $1568cm^{-1}$.

*Symmetric $C_\alpha$=$C_\beta$ stretch;* Broadened to include two or more peaks at 1423 and $1442cm^{-1}$.

*$C_\beta$=$C_\beta$ stretch;* No change.

*$C_\alpha$-$C'_\alpha$ (inter-ring) stretch;* Replaced by one broad peak at $1262cm^{-1}$.

From the above spectral observations they showed that the neutral PEDOT had an intermediate form changing to a benzenoid one upon doping in an aqueous

medium.

Lapkowski et.al. performed similar spectral observations under electrochemical oxidation of PEDOT [73]. Under an excitation wavelength of 1064nm they took Raman spectra at different cell potentials. Analysis of the cyclic voltammetry and the Raman spectra showed that the neutral polymer displayed a band at $1415cm^{-1}$ due to the symmetric $C_\alpha$=$C_\beta$ stretch. Upon doping this band was joined initially by a second at $1449cm^{-1}$ and at higher doping levels a third at $1478cm^{-1}$ with the $1415cm^{-1}$ band decreasing at the expense of the higher two. This they suggested indicated that the polymer was quinoid in nature in its neutral state and benzenoid in its doped state.

## *2.10 Concluding summary*

This chapter gives detail of the current state of research in certain fields of polymer electronics. Special attention was given to PEDOT:PSS as it is one of the most commonly used electronic polymers. It can be seen that while the electronic properties of polymers are exceedingly important so too are the interactions between polymers and different materials when they are contacted.

One of the significant advantages of polymers over inorganic technologies is the ease of fabrication. Attention must be given to the advent of inkjet printing as a means for depositing polymers. This allows the additive deposition of discrete quantities of polymer to specific places on exceptionally large or non-planar substrates.

Methods of investigating some of the properties of polymers were discussed. Advances have been made in the utilisation of conducting AFM tips for SKPM which allows the surface potentials across device structures to be displayed highlighting possible charge transport barriers at interfaces. In addition Raman spectroscopy can be used to indicate the stage of doping of PEDOT:PSS within an electrochemical cell.

Therefore the work in this thesis shall combine SKPM and Raman spectroscopy as a method for investigating the electrical characteristics of inkjetted PEDOT:PSS and its interface with electrodes of ITO, gold and aluminium.

# 3. INKJET PRINTING SYSTEM

## *3.1 Introduction*

The work reported in this thesis is concerned with investigating inkjet printed materials used in electronics. A prerequisite for this work therefore was the construction of an inkjet printing system and developing an understanding of inkjetting so as to allow such materials to be deposited in the required structures.

This chapter describes the realisation of the inkjet printing system shown in figure 3.1 capable of printing polymer solution-based inks between electrodes of gold, aluminium and ITO with alignment to substrate features and good positional accuracy.

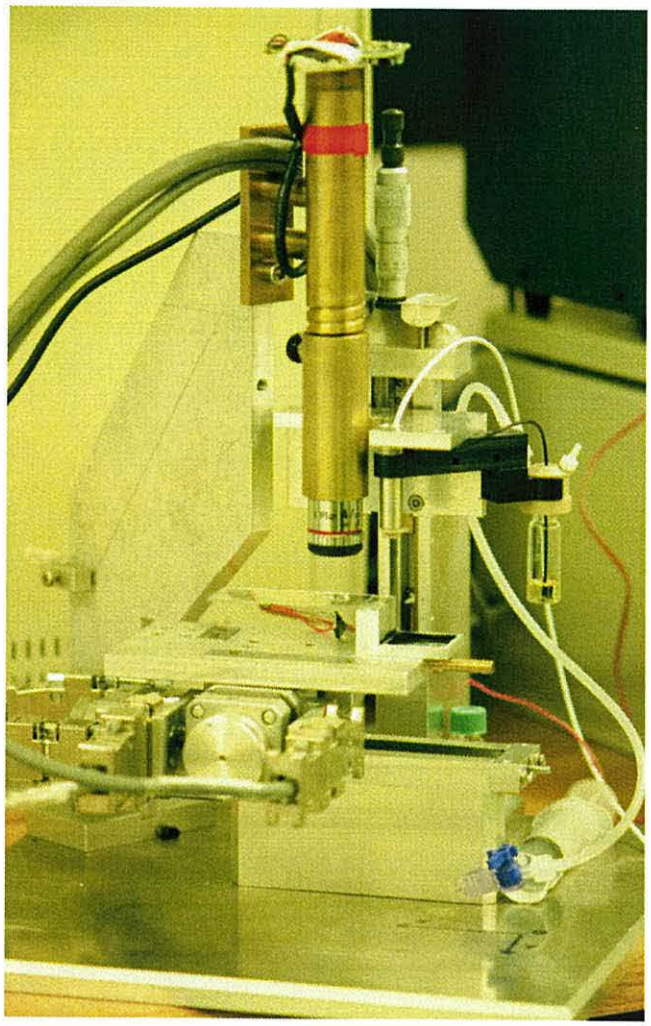

**Fig. 3.1:** Photo of inkjet print system.

## *3.2 Inkjet print system requirements*

### *3.2.1 Aims*

Two primary factors govern the specification of the inkjet printing system required for performing the experimental work undertaken here. Firstly the types of polymer solutions to be printed and secondly the resolution of patterning required. In addition a form of alignment was required such that droplets could be deposited at specific locations with relation to surface features or previous droplets. The aim therefore was to realize such a system in accordance with the objectives listed below.

### *3.2.2 Objectives*

- Typical polymer solutions used in electronic devices include PEDOT:PSS, P3HT and PVP which are soluble in a variety of solvents including water, xylene, chloroform and isopropanol. Any inkjet print system developed should be

able to deposit single droplets of such solutions reliably and without degrading either the ink or the print-head.

- The resolution required in polymer electronic devices depends on the type of device being fabricated. Light emitting displays require pixels in the region of $30\mu m$ in diameter and with a separation of $40\mu m$ [58]. Polymer transistors require parallel electrodes separated by less than $5\mu m$ wide and with no chance of the channel being bridged. While it was known that it was not possible to deposit individual droplets with the resolutions mentioned above, the movement and alignment system needed to be capable of operating to such micron scales.

- In order to align droplets accurately a magnifying optical system was required with the ability to locate surface features and transparent polymer droplet deposits. A reliable method for depositing droplets with respect to these features with suitable accuracies was necessary.

From the specifications above an outline for the system was formed and is shown in figure 3.2. It consisted of three main sections, (i) a computer controlled, motorised $xy$ stage, (ii) an inkjet print head mounted on a $z$ slide and (iii) an optical alignment system based on a microscope objective and CCD camera in a fixed position relative to the $xy$ stage. The camera and printhead were mounted in fixed $xy$ positions on a solid baseplate with the substrate being moved below them on the $xy$ stage. Once the $xy$ distance between the center of the camera and print nozzle was determined it was then possible to position features on the substrate directly below the print nozzle.

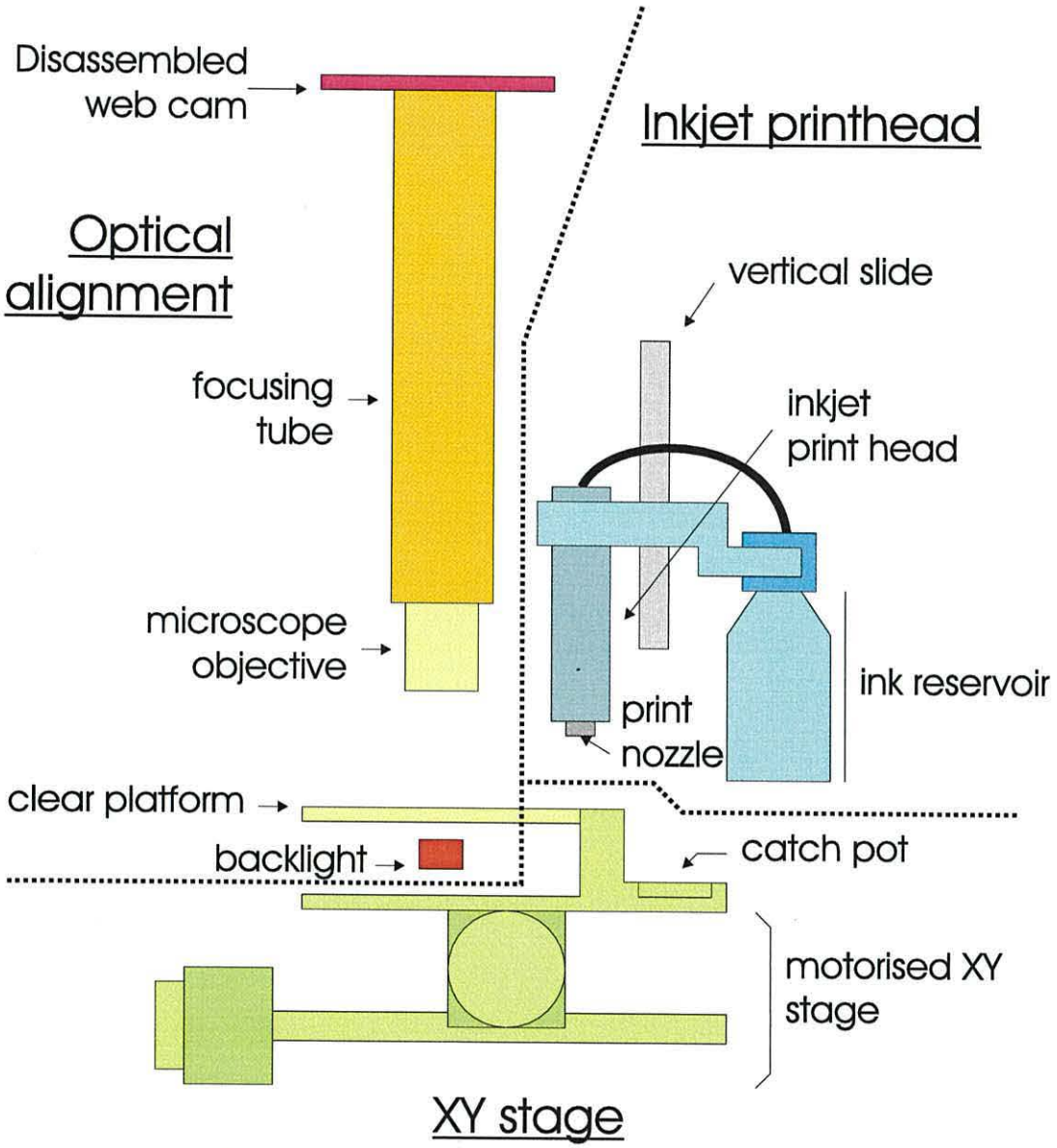


**Fig. 3.2:** Outline of inkjet print system showing the $xy$ movement stage, inkjet printhead and optical alignment system.

## *3.3 XY stage*

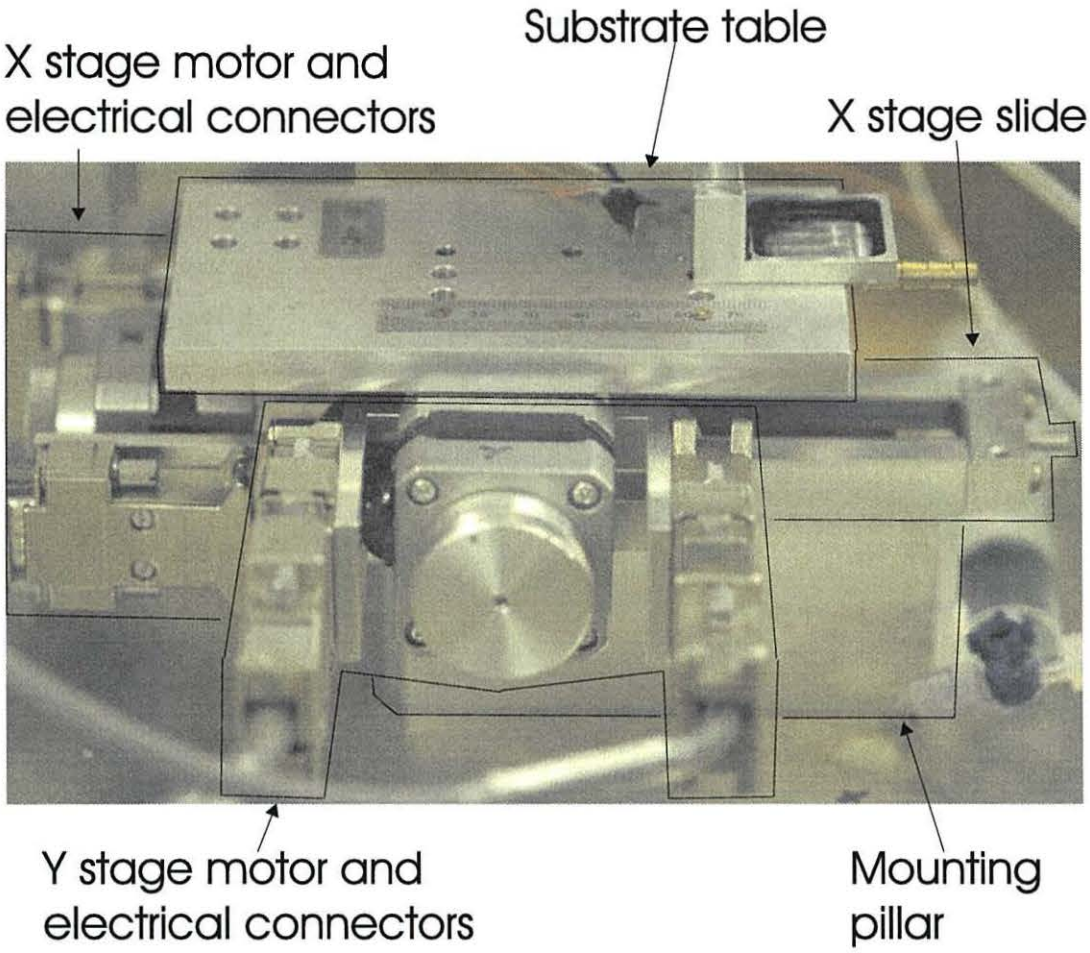


**Fig. 3.3:** Photo of $XY$ stage.

### *3.3.1 Requirements of XY stage*

The $xy$ stage shown in figure 3.3 was responsible for moving a substrate in the horizontal plane below a fixed printhead so as to deposit ink in specific locations. The requirement for the movement range of the $xy$ stage was difficult to quantify. One of the advantages of inkjet printing as a fabrication technique is the potentially unlimited substrate size. In specifying the range of movement required, the size of typical substrates available and the likely device size was taken into account. A typical substrate used was a 76 x 26mm glass microscope slide, however these were often cut to much smaller dimensions, approximately 12 x 7mm, to allow it to fit under the AFM/SKPM. Due to the necessity for offsetting the microscope from the print head (therefore reducing the available print area) and possible increases in device complexity and size, an $x$ stage length of 80mm was selected with 25mm for the $y$ stage. This would guarantee a definite printable area of 25mm by 25mm. A larger stage range was not selected as it was not felt that devices or groups of

devices would exceed that size. An additional factor was the increase in cost with size and of increased inaccuracy due to greater weight and size.

An important factor when considering the driving of the stages was the problem of the timing of droplet deposition and of physical movement of the stage introducing error. When inkjet printing lines the solvent from the droplets dry at a specific rate which can affect the formation of the dried film/line. Therefore the time delay between successive droplets is an important factor in the movement of the stage. Another issue is the drying of the ink solvent in the nozzle of the print head. For these reasons it was decided to drive the $xy$ stages with stepper motors controlled by a computer rather than manually adjusted micrometer screws. This then enables a faster movement of the stage preventing drying on the nozzle and allowing precise control of the droplet to droplet solvent interactions. It also prevents hand adjustment of the micrometer from introducing error in the movement of the stages.

Having chosen a stepper motor drive for the $xy$ stage, the resolution of movement had to be considered. A stepper motor works by using a series of individually energized electromagnetic coils. This allows the motor to not only rotate continuously but also to pause at a specific position. The angle between individually addressed positions can be in the order of a few degrees. By connecting the stepper motor to a drive rod with a worm screw the rotational movement of the motor could be converted into a horizontal stage drive. The finer the pitch of the drive rod and the smaller the stepping angle of the stepper motor the smaller the distance the stage can be moved with a single step of the motor. Using a 4000-step stepper motor and a drive rod of 4mm pitch (the rod moves 4mm per single revolution) a stage movement of $1\mu m$ was attainable.

### *3.3.2 Construction*

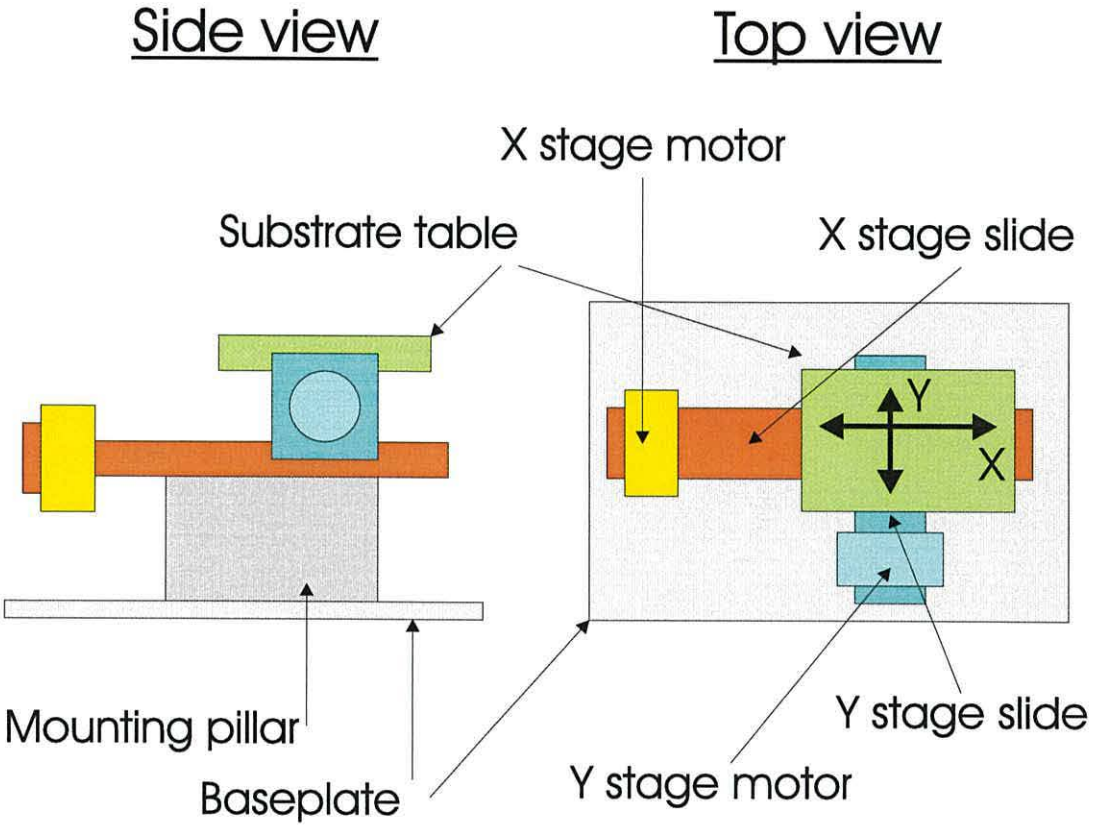


**Fig. 3.4:** Diagram showing $XY$ stage.

Two Unislide A1500 dovetail slides were supplied by Time and Precision Industries Ltd. and mounted as an $xy$ stage, one with 80mm of travel and the other 25mm. Each stage was fitted with a stepper motor capable of micro stepping up to 4000 steps per revolution. Steel M4 allen bolts were used in mounting the stages on top of a solid metal pillar on a large (300mm by 300mm) square metal baseplate. The purpose being to provide weight and rigidity to the design. This is shown in figure 3.4.

resulting in a slight negative pressure on its face. The purpose being to prevent ink from flowing freely from the nozzle. This posed problems as it brought it below the level of the table of the $xy$ stage. This problem was overcome by mounting the bracket at a 45° angle in the horizontal plane to the $xy$ stage allowing it to remain outside of the range of movement of the table. For systems capable of printing onto larger substrates either a longer feed line from the ink reservoir or a different arrangement would be required.

### 3.4.4 *Microdrop controller,* MD-E-201-H

**Fig. 3.9:** Front panel of *MD-E-201-H* Microdrop controller.

The piezo electric print head was sent control waveforms from the Microdrop controller shown in figure 3.9. The primary function of the controller was to generate a square wave pulse for the piezoelectric actuator. The pulse potential and duration could be varied using the controller until the correct ejection of droplets was obtained. The controller had 3 modes of operation; manual trigger, external trigger, external block trigger and continuous operation. In the manual mode a specified number of droplets could be deposited on pressing a button on the front panel. The same applied in the external mode except the trigger was from an external input. In the continuous mode droplets were ejected continuously at a specified frequency. The number of droplets deposited per block could be set using the block length setting.

The continuous mode was used to characterize the droplet ejection. The frequency of the ejection could be varied between approximately 100Hz and 2.3Khz. An additional output for a strobed LED was provided. The delay between the ejection of the droplet and the triggering of the strobe diode enabled the droplet ejection process to be captured at any stage.

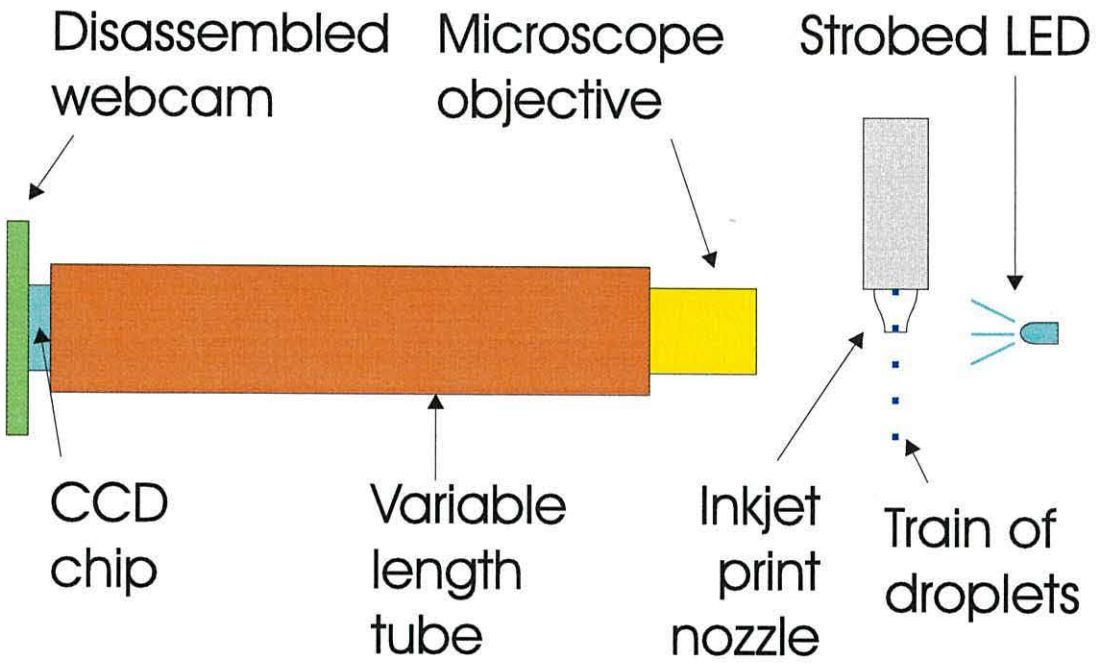


**Fig. 3.10:** Diagram showing method for viewing droplet formation.

In order to examine and evaluate the formation of droplets by the print head the optical assembly described in section 3.5.3 was mounted so as to view the nozzle from the side (shown in figure 3.10). The system consisted of a 5 times multiplication microscope objective, an adjustable length light-tight tube and a disassembled web camera (Creative Video Blaster Webcam 3) mounted on a temporary *xyz* stage. The inkjet print nozzle was back lit with an LED connected to the delayed strobe LED output of the *MD-E-201-H* Microdrop controller.

The delay between ejection and strobing was varied in $20\mu s$ increments, with images being captured at each stage. These images were then cropped and arranged as the single sequence shown in figure 3.11. It should be noted that the same droplet is not imaged at $20\mu s$ intervals, but different droplets. From the regular shape and path of the droplets it can be concluded that there is minimal variation between successive droplets.

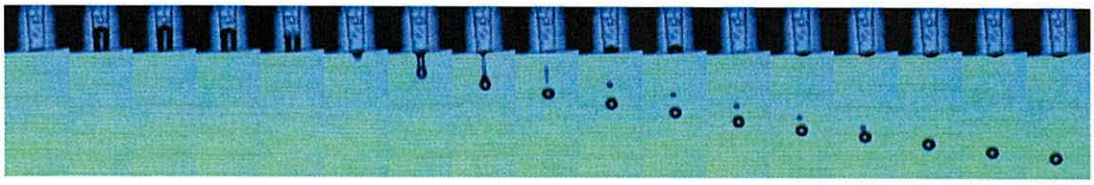

**Fig. 3.11:** Sequence of strobed images showing droplet formation. The delay between images is $20\mu s$.

One of the issues involved with printing is the square wave pulse used to drive the piezoelectric actuator which in turn generates the pressure wave for ejection.

The pulse could be viewed using an oscilloscope via an external output from the controller. This allowed an exact measure of the pulse amplitude and duration to be taken. These were varied while ejecting droplets in the continuous mode and the resulting train of droplets viewed using the side viewing camera. Using this method the pulse was varied until a steady stream of droplets was obtained then used to optimise the droplet ejection in terms of droplet size and reliability of droplet production, especially for single droplet ejection. Typical values for the pulse amplitude and duration were 110V and $90\mu s$ respectively.

Two effects were encountered, the first was unreliable droplet ejection due to reducing the droplet volume, the second being satellite droplets. While no exact measure of the droplet volume could be made, the internal diameter of the print nozzle is clearly visible and was used as a reference for the droplet diameter. From the estimate of the droplet diameter it was then possible to calculate the volume of the droplet using equation 3.1;

$$V = \frac{4}{3}\pi r^3 \tag{3.1}$$

Where V is the volume of the sphere (L) and r is the radius of the sphere (m).

It was found that pulses of lower potential and shorter duration produced droplets of lower volume. However problems were encountered when switching from continuous mode ejection to single droplet ejection. This effect could be seen when the droplet volume was minimised at an ejection frequency of 2.3KHz and then the ejection frequency decreased to 100Hz. In some instances the droplet train tended to break up and form a meniscus of wetted ink over the face of the nozzle. In order to simulate the condition of depositing single droplets at discrete time intervals, the droplet characterisation was performed at the lowest ejection frequency, approximately 100Hz. Care was taken to ensure that it was possible to deposit single droplets in a repeatable fashion before the side viewing camera was removed.

The second problem was that of the tail of the droplet broke up as it left the meniscus of the print head, forming a secondary satellite droplet. This satellite then travelled off in a slightly different direction and at a different speed. This is shown in figure 3.12. Clearly, having two droplets travelling in different directions and at different speeds is undesirable. Careful manipulation of the drive waveforms allowed satellite droplets to be eliminated or as shown in figure 3.11, allow it to catch up with the main droplet and be reabsorbed.

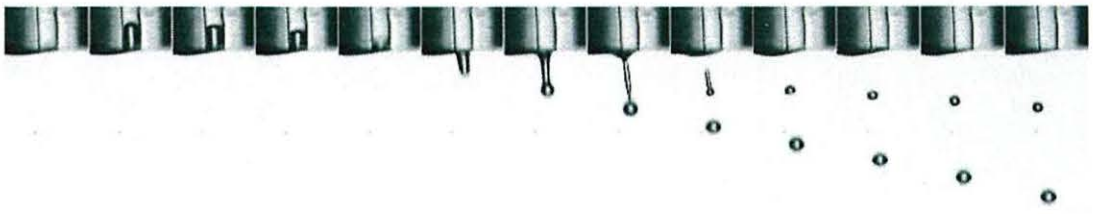

**Fig. 3.12:** Sequence of images showing a satellite droplet forming from the tail of the main droplet.

### *3.4.5 Ink formulation*

The polymer solution used in this investigation was PEDOT:PSS and is available as an aqueous dispersion from Bayer AG under the name Baytron P. Two variants of Baytron P are available, Baytron P AI4083 and Baytron P CH8000. These are known as "electronic grade" and were developed as an interfacial layer on ITO in organic or polymer light emitting diodes. They have a reduced particle size and less gel particles in comparison to standard Baytron P. The CH8000 variant was developed with a lower conductivity for matrix array based devices where cross-talk between closely spaced devices is a problem. Table 3.1 shows the conductivities of the different grades.

| Grade | Conductivity ($Sm^{-1}$) |
|---|---|
| Baytron P | 100 |
| AI4083 | 0.1 |
| CH8000 | 0.001 |

**Tab. 3.1:** Conductivities of different grades of Baytron P.

The viscosity and surface tension of the solution to be inkjetted is important for droplet ejection. This was outside the bounds of this investigation so a sample of Baytron P modified for inkjet printing using the Microdrop print nozzle was obtained from Avecia. This PEDOT:PSS was then known as m:PEDOT:PSS. Due to the commercial interests of Avecia the exact composition of the m:PEDOT:PSS was not known except that it was based on CH8000. However methanol, ethanol, isopropanol or acetone are likely to have been added [19].

### *3.4.6 Droplet ejection and maintenance*

One of the problems associated with inkjet printing is the drying of the solvent on the face or just inside the print nozzle resulting in blockages. This was found to happen with m:PEDOT:PSS. Two glass vials were kept, one containing m:PEDOT:PSS, the other isopropanol. When not in use isopropanol was passed through the system by applying a positive pressure to the ink reservoir using a

syringe. The polymer solution was driven from the head in a jet and collected as waste. Once the jet from the head ran clear, the positive pressure was removed and the head capped leaving the system clean of polymer. A similar procedure was used to re-charge the printhead with m:PEDOT:PSS ready for printing.

It was found that it took just over 4s for the ink to dry on the nozzle such that droplets could not be ejected. However applying only a slight positive pressure caused ink to well up on the nozzle face where it could be dabbed off with low lint tissue (Kimberly-Clark Kimwipes Lite 100). This had to be performed immediately before printing. If the printhead was left to dry for longer periods of time (longer than 10 minutes) then slight positive pressure was often not enough to clear the blockage. In this case isopropanol was dabbed onto the face of the nozzle using low lint tissue or the print nozzle lowered into a small container of isopropanol.

Due to the small number and simplicity of devices fabricated in this investigation the above processes were acceptable for purging and cleaning the nozzle. If a larger number of more complex devices were to be fabricated an automatic system for cleaning/purging the print nozzle should be developed. This could include, (i) a motorised pump for applying positive pressure to the ink reservoir, (ii) multiple reservoirs switched to feed the same nozzle allowing automatic purging of the nozzle with solvent, (iii) an area of the $xy$ stage equipped with soft rubber or fabric wipers and a solvent bath and (iv) a catch pot in the $xy$ stage to allow droplets to be ejected periodically to keep the head blockage free.

## *3.5 Optical alignment*

### *3.5.1 Specifications*

The computer controlled stepper motor drive of the $xy$ stage allows the position of the stage to be known at any time. Therefore, when building up patterns of droplets for devices, the stage is moved below the print nozzle and ink deposited in the desired locations. Neglecting errors in the flight of the droplet, in the stage movement and from interactions between the incident droplets and the substrate, droplets can be accurately aligned with respect to each other with no optical system required.

If the substrate is moved with respect to the stage or if droplets need to be aligned with respect to surface features then some means of aligning the print nozzle to the substrate is needed. Given the likely dimensions of the droplets and the relevant surface features, and the transparency of the materials used, a form of magnification was needed along with an appropriate light

source. As with the $xy$ stage movement, operating the system manually was deemed unsuitable as this could introduce errors in stage alignment, so a camera was needed.

### *3.5.2 Alignment*

Two methods for viewing the surface were considered. The first was to mount the camera such that it was able to view the point of impact of each drop as it was developed. This could be achieved by mounting the camera at an angle beside the print nozzle and focusing it on the substrate below it. However due to the construction of the print nozzle housing and the necessity to minimise the nozzle to substrate distance to 0.5mm this method was deemed impractical. Alternatively the camera could be mounted below the substrate looking upwards though it. The limitation with this method was that the substrate had to be transparent. An additional problem would be the alignment of the print nozzle and viewing system. This would require extra precision movement stages controlling their position.

For these reasons it was decided to mount the camera vertically beside the print head on its own bracket so that while the print head could be moved up and down the camera remained focused on the substrate. Then, provided the distance between the print nozzle and the center of the field of view was known the stage could be moved to align the print nozzle over the same location as viewed with the camera. This avoided problems with focusing due to the camera being angled to the substrate. It also viewed from above so substrates did not need to be transparent.

In order to align the camera with the print nozzle, a droplet was deposited on the substrate and the position recorded. The stage was then moved to find the droplet in the center of the camera's field of view. The second position of the stage was recorded and the required offset calculated. This process was repeated a number of times and the offset averaged. Typical figures for the $x$ and $y$ offset were 24.9 and 1.3mm respectively. Unless the optical viewing system and the inkjet printhead were moved in relation to each other the offset remained unchanged. However, if the web cam CCD sensor, microscope objective and printhead were moved (due to cleaning, disassembly etc) then the offsets had to be remeasured. This method removed the need to accurately align the camera with respect to the print nozzle as the alignment was performed by the stage movement.

### *3.5.3 Optics*

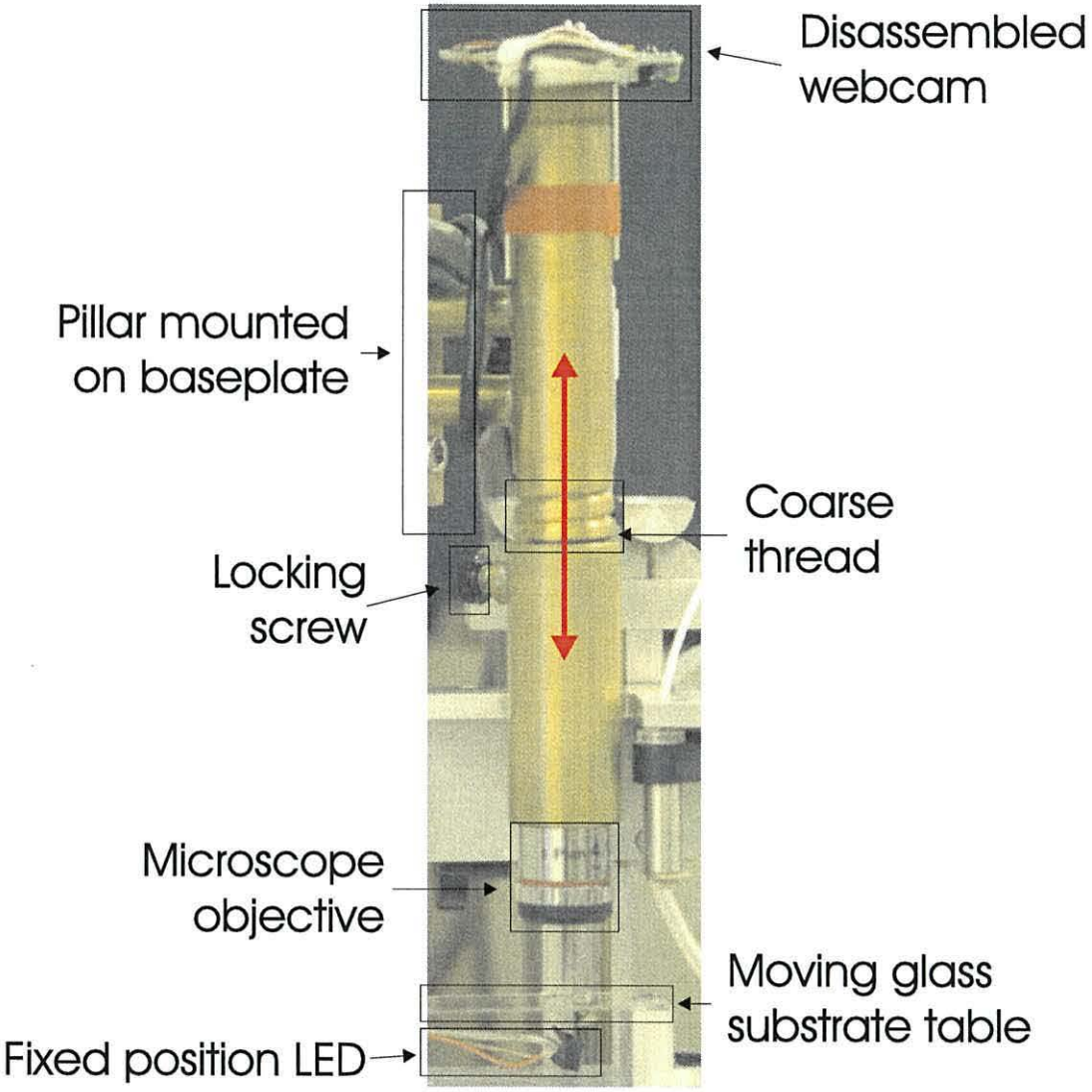


**Fig. 3.13:** Optical system based on disassembled webcam, variable length tube and microscope objective.

Figure 3.13 shows the system used for viewing the substrate. The optical system was based on a microscope objective mounted at one end of an optically sealed tube. On the other end a disassembled web camera (Creative Video Blaster Webcam 3) was mounted. This was the same system as used to view the nozzle sideways for droplet formation shown in figure 3.10. The camera was then connected to the USB port of a computer. The camera and microscope objective were mounted on either end of a tube. This tube was then fixed by a solid metal bracket to the baseplate upon which the $xy$ stage was mounted. In order to focus the microscope objective the tube was in two parts, one of lesser diameter than the other so that it could slide inside the other. The inner, fixed to the bracket, had a coarse pitch thread cut to its outside while the outer was equipped with a fine tipped bolt protruding into the inside. This allowed the outer tube to be moved up or down

with respect to the substrate by rotating it, the bolt tip being located within the coarse thread translating the rotational movement into linear movement for focusing.

On the upper end of the inner tube the web camera was mounted facing vertically downwards. A rubber 'O' ring was placed between the CCD chip and the top of the tube to provide, (i) mechanical protection to the glass face of the chip and (ii) a light-tight seal. The lower outer section of tube had a standard 0.8 inch x 36 TPI microscope objective thread cut into it. Due to the dimensions of the deposited droplets being approximately $100\mu m$ a field of view of around $500\mu m$ was required. A 5 times multiplication microscope objective provided this, however a 20 times objective was also used if greater magnification of individual droplets was required.

### *3.5.4 Lighting*

Lighting is an important aspect of optical microscopy. Given the optical transparency of PEDOT:PSS (and many other polymer solutions) and the ITO electrodes, special attention had to be paid to illuminating them so as to be able to image them with the camera. Differential Interference Contrast (DIC), or Nomarski, lighting is well known for its ability to give a good optical section to an image, highlighting relief in the sample. However, a set of polarized filters and expensive prisms is required to achieve this. A combination of oblique illumination and dark field illumination can be used to similar effect, highlighting edges in a sample. Given that the printed polymers are not deposited as continuous uniform films but as discrete droplets or lines, this method of illumination was found to work well.

The method by which the lighting was achieved can be seen in figure 3.13. An LED was mounted on the same bracket as the camera below a transparent supporting table. This allowed the substrate to be moved with respect to the print nozzle and camera but keeps the light source in the same position with respect to the camera. A glass microscope slide acted as the transparent supporting table 20mm above the surface of the $xy$ stage table. This provided enough space for the LED which was covered by black tape except for a small slit. By carefully adjusting the position and angle of the LED, its light could be made to approach the substrate from any angle, recreating the oblique illumination effect. Figure 3.14 shows two ITO electrodes and an inkjet printed line of m:PEDOT:PSS illuminated with the oblique technique. It can be seen that the edges of the features are clearly highlighted. This method however, does not cater for non-transparent substrates or electrodes. In such cases a similar method was used with a second LED mounted

above the transparent supporting table shining downwards. This provided oblique illumination from above. This technique was not so successful as the LED had to be positioned so as not to obscure the light path up to the microscope objective. However, the results were satisfactory enough to allow successful alignment.

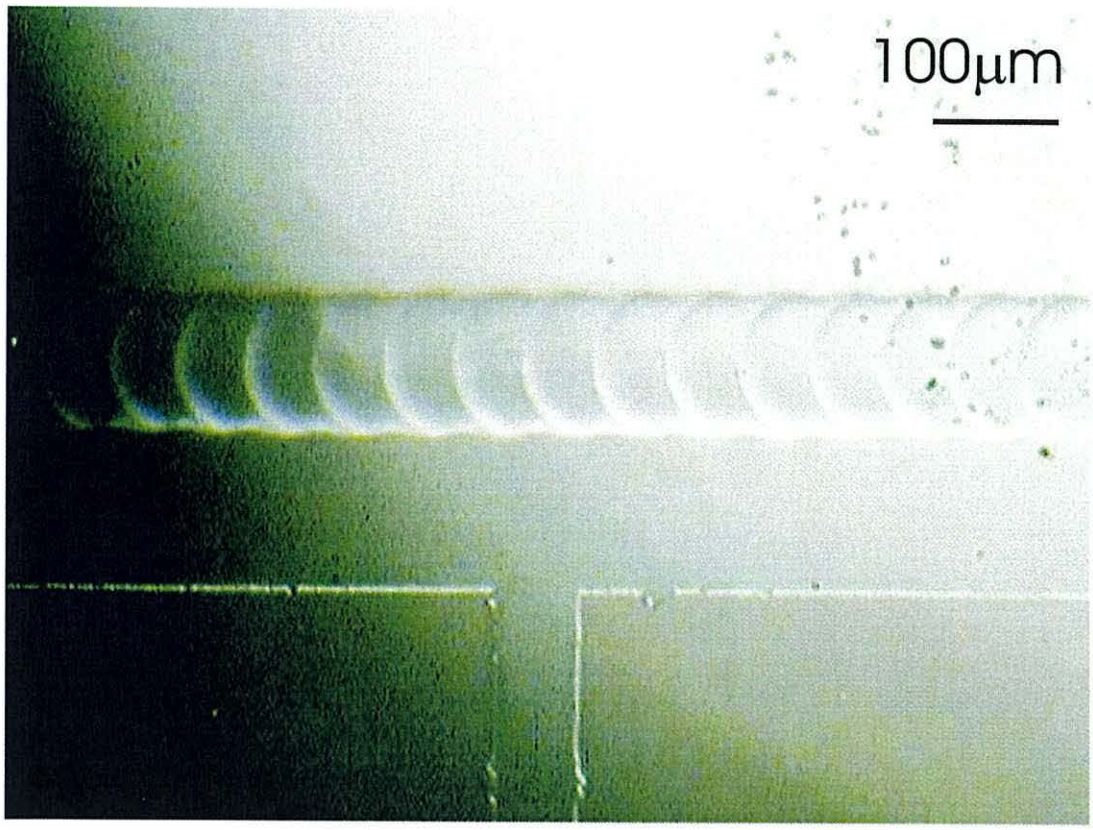


**Fig. 3.14:** Inkjet printed m:PEDOT:PSS and ITO electrodes imaged with oblique illumination.

### *3.5.5 Future development*

While the system describe above provided satisfactory results, the illumination was the most critical aspect. Adjusting the LED so as to highlight the necessary features on the substrates was difficult. A development of this would be to provide a more accurate method for mounting the LED and a better filter for covering the LED. Adding a reticule to the system so as to provide cross-hairs and a scale to the image would make aligning droplets with the substrate more accurate.

The video from the web camera was displayed using the software provided by Creative. It is possible to use Matlab (the program used for controlling the stage motors) to capture the video stream from the USB port. Matlab has a powerful image processing capability which, initially, could allow simple displaying of the video from the camera. If more complex devices were to be produced, Matlab could

be used to identify registration marks on the substrate and provide a higher degree of automation to the fabrication of devices.

## 3.6 GUI for system control

### 3.6.1 Specifications

As described in the previous sections, it was important not to disturb the inkjet print system by manual operations as this could introduce errors into the stages. For this reason a camera was used to capture images of the substrate for alignment and stepper motors were used to drive the $xy$ stages. As described above the video from the web camera was displayed using the software provided by Creative and the stepper motors controlled by EASI commands sent via the serial port.

The L25 system was supplied with a basic program allowing EASI commands to be sent to the serial port. These commands operated at a very low level and it was not possible to control the stage with respect to $x$ and $y$ positions in mm or $\mu m$. A GUI was required which would allow intuitive control of the stages and print nozzle and allow structures such as lines to be generated automatically. A list of necessary functions is shown below.

- Homing buttons allowing the stages to return to zero and recalibrate their position.
- Coordinate boxes allowing movement to exact positions to be specified.
- An eject button allowing single droplets to be ejected.
- Nudge buttons allowing the stage to be moved by $100\mu m$, $500\mu m$ or 1mm steps.
- Line printing buttons allowing lines with a specified number of droplets, deposition pitch and droplet deposition delay to be printed.
- A button allowing a specified piece of code to be run e.g. print a test pattern.

### *3.6.2 Matlab GUI*

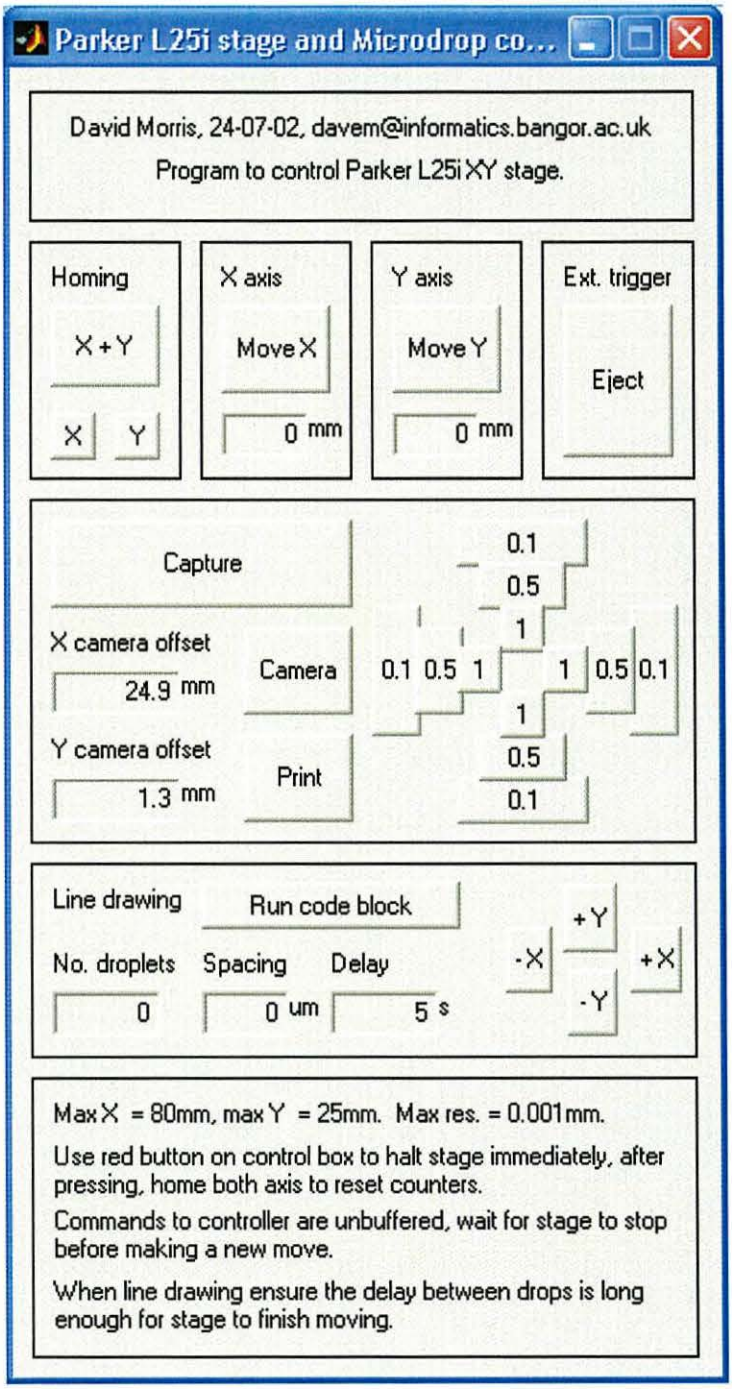


**Fig. 3.15:** Graphical user interface for inkjet print system.

Matlab V6.5 was used to develop the GUI shown in figure 3.15. Matlab was selected for three reasons, firstly existing experience in programming with Matlab and C (which Matlab uses extensively). Secondly Matlab supported serial port communications and thirdly Matlab contained GUIDE, an interface for easy generation of GUIs. A detailed description of the development of the GUI software has not been included here, however the code along with comments denoted by %

is listed in appendix B.

### *3.6.3 Future development*

When developing the GUI, it was anticipated that the most complicated structure to be deposited was a line of connected droplets. The development of the GUI is open ended allowing functions to be added. Typically this could include the ability to print films by printing a series of lines next to each other. For more complex devices such as transistor source and drain electrodes, instead of printing a series of connected lines to form the pattern a converter for G-code could be written. G-code is a language used to control CNC machines and many CAD packages are capable of exporting it. This would enable complex patterns of droplets to be developed in commercial CAD packages then exported to G-code which could then be run by the inkjet print system. Given the ability of Matlab to interface with the web camera, its image processing capabilities could be used to read alignment features on the substrate.

## *3.7 Assessment of inkjet print system*

No formal assessment of the final inkjet print system was carried out. Its development was an ongoing process in which many minor features were modified and updated so as to improve its performance. However, with respect to the aims and objectives outlined earlier in this chapter, it can be confirmed that the inkjet print system was capable of printing solutions of PEDOT:PSS (though no others were tried). The accuracy of the system was more than adequate for the devices that are shown in the following chapters and was capable of imaging the electrodes and polymer deposits for alignment and assessment.

## *3.8 Concluding summary*

This chapter gives details of the construction of the experimental apparatus for inkjet printing polymer solutions. A set of aims and objectives were set out at the beginning of the chapter, giving the requirements of the system. The body of this chapter has systematically dealt with each aspect and shown that they have been met satisfactorily. The development of the system was an ongoing process and possible future modifications to the system have been outlined.

An important aspect of micro-fabrication are the accuracies of the processes

involved. Within the relevant sections of this chapter the accuracies and resolutions of the inkjet print system have been discussed.

# 4. INKJET PRINTING OF POLYMERS

## *4.1 Introduction*

The previous chapter detailed the development, construction and assessment of an inkjet printing system and describes the process by which the reliable formation of droplets in flight can be observed. This chapter deals with the stage following this, in which the falling droplets impact with a substrate in order to manufacture devices.

An experimental understanding of the process that occurs as a falling droplet interacts with a substrate, and subsequently dries, is required. The factors involved are many and include the kinetic energy of the falling droplet, the surface energy and temperature of the substrate and the evaporation rate of the drying droplet.

Further investigation was required in the case where a series of droplets are deposited to form continuous lines. Previous droplets can affect the morphology and surface energy of the substrate while successive droplets can redissolve previous ones [74] [15]. This situation was then complicated when printing continuous lines of droplets from one area of substrate with one surface energy to another of different surface energy.

## *4.2 Inkjet printing lines of droplets*

One of the most basic structures required in inkjet printed devices is that of a continuous line of polymer material. This allows connections to be made between different regions, allows source and drain electrodes to be fabricated and is a start point for forming printed films of polymer.

The inkjet print system was used to deposit lines of individual droplets of m-PEDOT:PSS on to the surface of a cleaned glass microscope slide (for cleaning procedure see appendix A). The GUI controlling the inkjet printing system included a line printing function with three variables; (i) the number of droplets deposited, (ii) the distance the stage is moved between each droplet (known as the pitch) and (iii) the time delay between each droplet being deposited.

Initial attempts at printing lines used a delay of 1s between droplets. The results from this were poor and unpredictable, mainly due to subsequent droplets being deposited while previous ones were still fluid and mobile. The lines displayed significant pooling of ink at the start point of the line and included "bleeding" of wet ink between closely spaced lines. For this reason all subsequent lines were printed with the longest possible time delay without the ink drying and blocking the nozzle. This was found experimentally to be 4s.

6 different lines of droplets were printed in which the pitch of the droplets was different for each line. The line pitches were 20, 40, 60, 80, 100 and 120$\mu m$. After printing, the substrates were placed on a hotplate (IKA Ikamag) for 1 minute at 100°C in air to remove any remaining solvents that had not evaporated under normal laboratory conditions. The resulting lines were then examined using tapping mode AFM and are shown in figure 4.1.

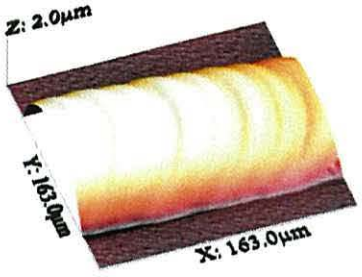


(a) 20$\mu m$ line pitch.

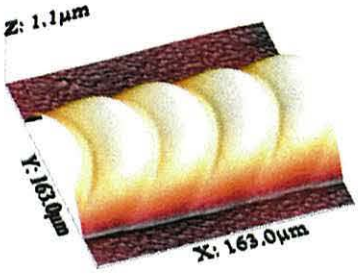


(b) 40$\mu m$ line pitch.

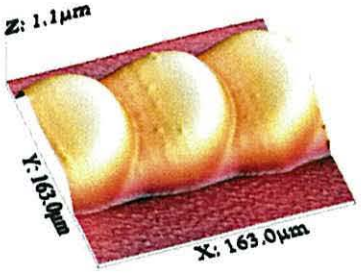


(c) 60$\mu m$ line pitch.

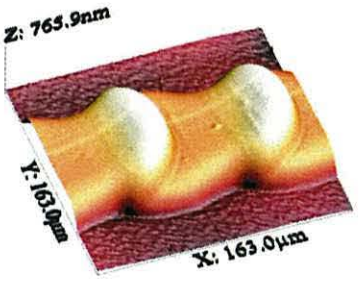


(d) 80$\mu m$ line pitch.

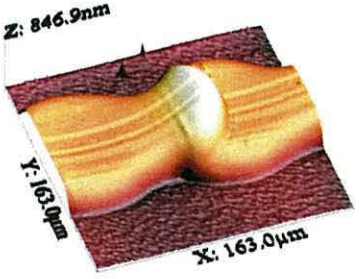


(e) 100$\mu m$ line pitch.

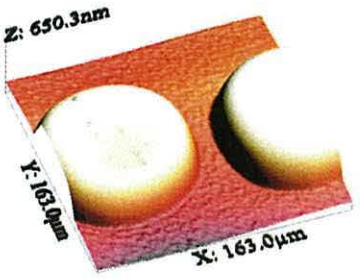


(f) 120$\mu m$ line pitch.

**Fig. 4.1:** AFM images of printed m:PEDOT:PSS droplets with varying line pitch.

Figures 4.1(d) and 4.1(e) show the effect of depositing droplets on or near to

other droplets. While it could be expected that successive droplets would simply overlay previous droplets this is not the case. When successive droplets are deposited such that part of the wet droplet contacts a previous, dry droplet, the wet droplet interacts with it in such as way as cover a greater area than if it had not. Figure 4.2 shows the outline size of a single droplet, in green, overlaid on a line a droplets with a pitch of $100\mu m$. In addition to slight spreading over the substrate in the overlay region, a significant proportion of the wet droplet migrated along the dry droplet.

When lines were printed with a 1s delay, the resulting structures were smoother along their length and with less distinct boundaries between individual droplets. However, the overall width of the lines was greater and displayed a pooling effect at the start of the line. For this reason successive experiments used lines printed with a 4s delay as this provided more regular lines with less spread and pooling.

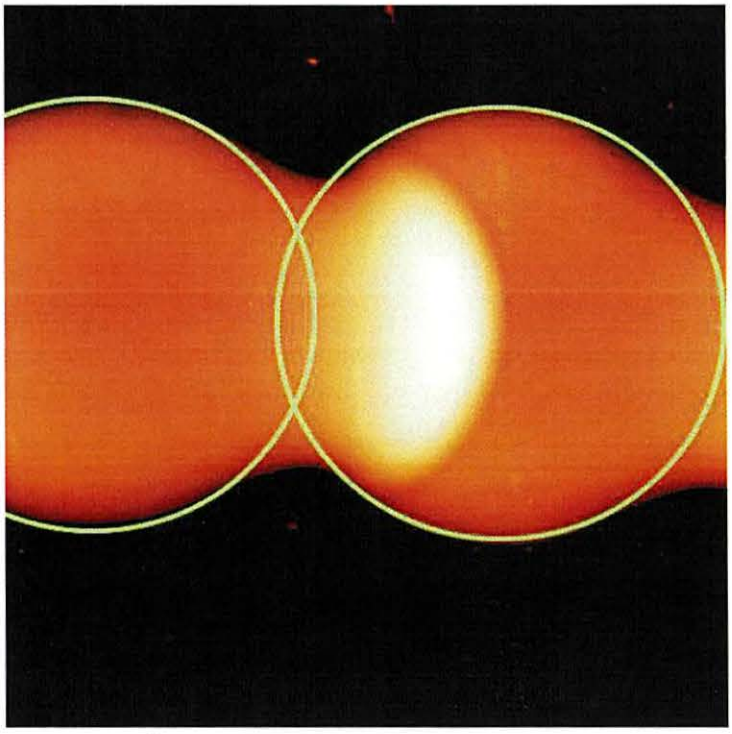

**Fig. 4.2:** Printed line with pitch of $100\mu m$ overlaid in green with the outline of a single droplet (image 163x163$\mu m$).

## 4.3 *Cross-sectional analysis of lines*

The lines in figure 4.1 show a large variation in width and height. Given that the lines are of conducting material and are intended for carrying current, the cross-sectional area of the lines is important. Determining the overall resistance of the printed lines is difficult due to the complex three dimensional geometries, however

an important factor governing the resistance will be the smallest cross-sectional area.

AFM data can be obtained not as the rendered images shown in 3 and 2 dimensions in figures 4.1 and 4.2 but as a matrix of height data where the rows and columns correspond to the $x$ and $y$ position, the value in each cell being the height. This data was exported from Nanotec Electronica S.L. WSxM version 4 software as an ASCII matrix file which was then imported into Matlab.

Given that the printed lines were aligned along the rows of the matrix, the cross-sectional area for each column of the matrix was calculated. However this included the area of some of the glass substrate too. A mean value for the height of the glass substrate was determined and the area of the substrate calculated then subtracted from the total area of each matrix column. This then gave a value for the cross-sectional area of the polymer for each column of the matrix. This data was then plotted against the horizontal distance along the line. The m-file code has been included in appendix C. Additional lines of code can be added to the m-file so as to report the least cross-sectional area of each line. Plots for all six lines in figure 4.1 are shown in figure 4.3.

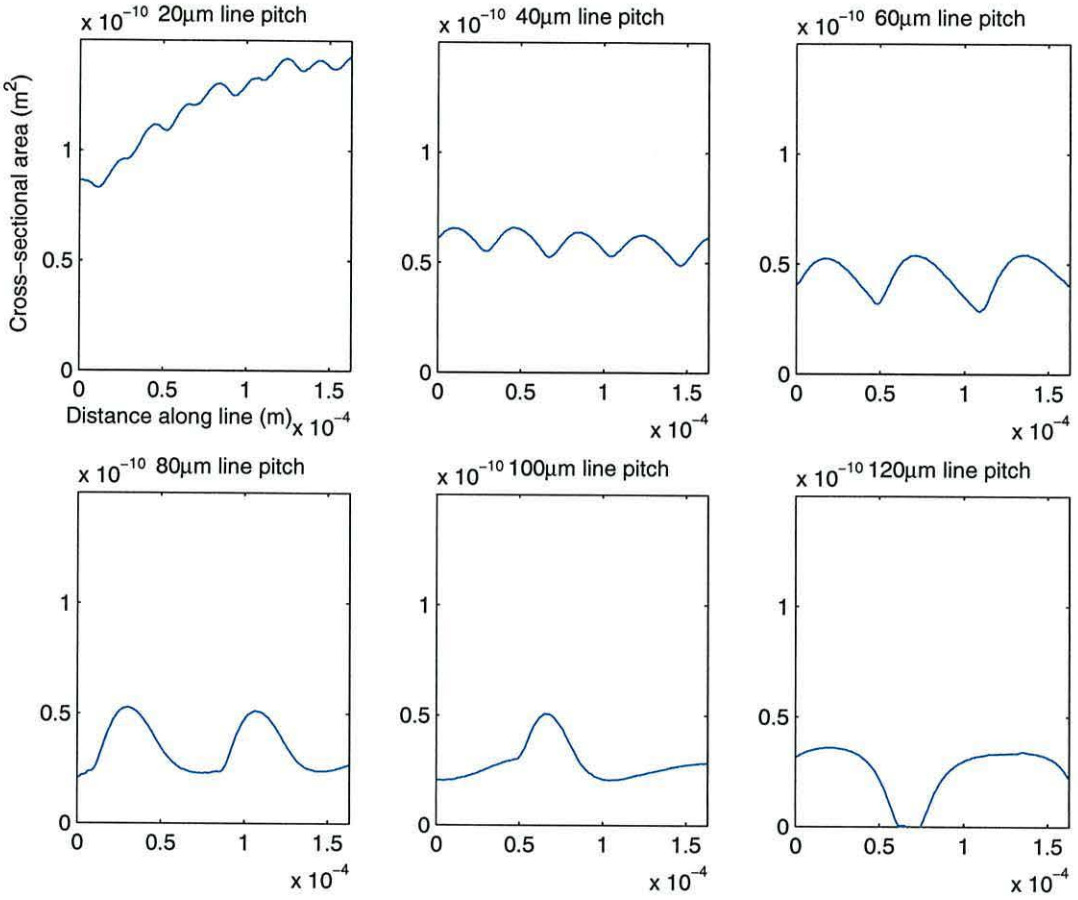


**Fig. 4.3:** Plots of cross-sectional area along lines printed with different pitch.

It should be noted that when making assessments of the resistance of such printed lines, that it is based on the assumption that the material forming individual droplets links chemically and or electrically to provide a continuous conducting medium.

## *4.4 Inkjet printing across electrode edges*

The importance of inkjet printed lines has been discussed above. However, to make use of the line it has to be able to make electrical contact with other materials. In the investigations in this thesis, the materials include gold, aluminium and ITO.

When depositing droplets across electrode edges or between two narrowly separated electrodes the differing surface energy and physical height change of the regions had to be considered. Problems were encountered in printing over the electrode edges and between pairs of electrodes, mainly due to the electrode surface having a lower surface energy than that of the underlying glass.

The primary assessment for the success of inkjet printing between/over electrodes edges was whether a complete physical join occurred between the conducting line and the electrode and hence an electrical connection was made. Further investigations could then be made as to the electrical properties of the interface between the polymer and the electrode.

### *4.4.1 Gold electrodes*

Lines of m:PEDOT:PSS were printed with a delay of 4s and varying pitches over substrates with gold electrodes (see appendix A for fabrication method). Figure 4.4 shows the case where lines have been printed from glass onto the gold electrode with a pitch of $60\mu m$. It can be seen that the droplet diameter when deposited on the gold electrode is considerably smaller than that of the droplets on glass. It can also be seen that no physical contact between the printed lines on glass has been made to the gold electrode which is typical of the gold electrodes.

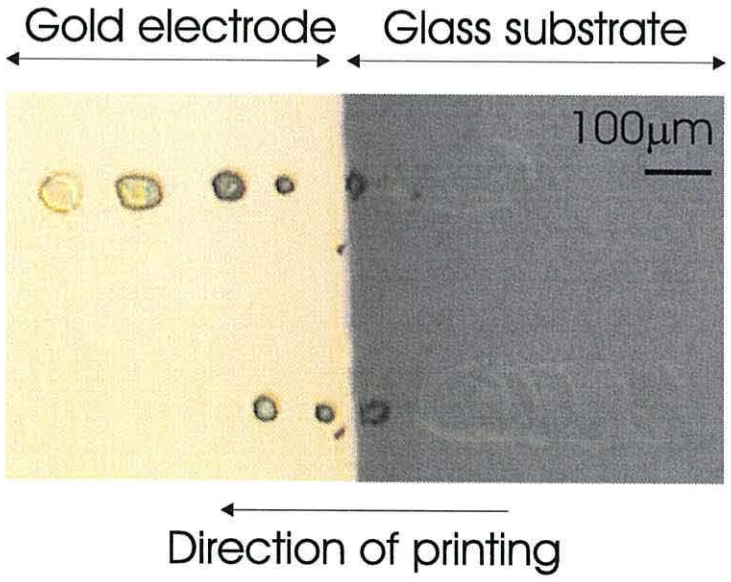


**Fig. 4.4:** Top lit microscope image showing inkjet printed lines of m:PEDOT:PSS printed on glass and gold.

An attempt was made to alter the surface of the gold electrode so as to enable the printing of polymers across its surface. Glass substrates fabricated with gold electrodes identical to those used above were passed through the flame of a bunsen burner until they glowed pink. The procedure was carried out in complete darkness in order to see the change in colour of the metal. Immediately after the change in colour was observed the substrates were removed from the flame and allowed to cool for 10s in air. The samples were then quenched in UPW at ambient room temperature.

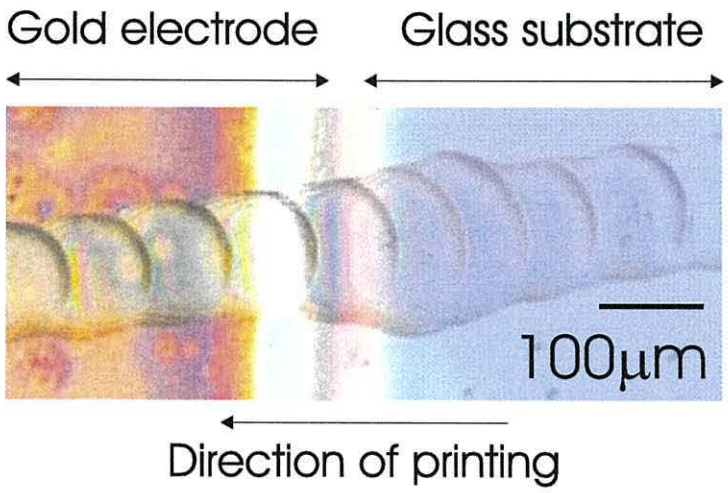


**Fig. 4.5:** DIC lit microscope image showing inkjet printed lines of m:PEDOT:PSS printed on glass and flame modified gold.

m:PEDOT:PSS was then printed across the electrode edges as above. Figure 4.5 shows a microscope image using DIC lighting which highlights edges and height changes in samples. It can be seen that a continuous line of polymer crossed from the glass onto the gold surface without interruption. The surface of the gold had a significantly different appearance to that of the gold in figure 4.4. No analysis of the gold after flaming was performed, however investigations into the electrical, chemical and surface energy properties of the gold before and after flaming could be valuable.

This method of modifying the surface of the gold electrode was not pursued as the flaming of the glass followed by water quenching caused the glass to crack. This could be remedied by allowing longer cooling times prior to quenching or the use of glass with a low modulus of expansion.

### *4.4.2 Aluminium electrodes*

The same printing process was then repeated with aluminium electrodes on glass, the results are shown in figure 4.6. Due to the bottom lighting of the microscope image it is not possible to show the evolution of the lines over the aluminium electrode in the images. The effect of the aluminium on the inkjet printed line is different to that of gold. Examinations of the lines using a top lit microscope revealed that the reduction in size of the droplets on the aluminium electrode was less pronounced in comparison to the case using gold electrodes. While lines A, B and C in figure 4.6 clearly do not make a physical connection with the aluminium electrode, line D does appear to, although severe pinching of the line occurs. Attempts were made to adjust the printing parameters so as to increase the likelihood of the lines making contact. It was found that by printing with a pitch

of $20\mu m$ the chances were greatly increased.

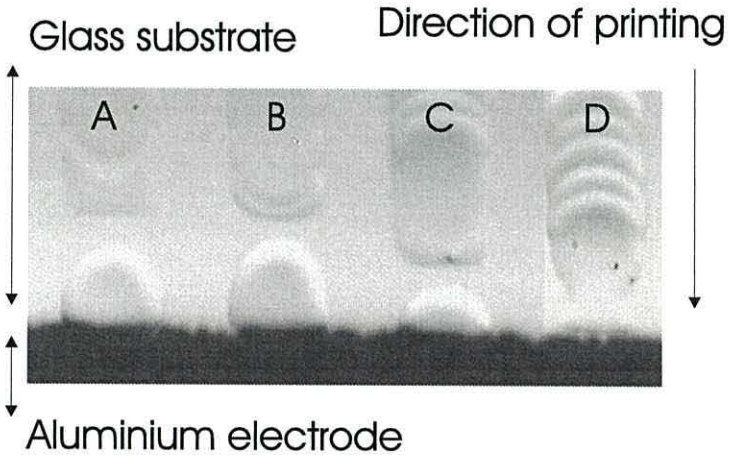


**Fig. 4.6:** Bottom lit microscope image showing inkjet printed lines of m:PEDOT:PSS printed on glass and aluminium (line width approximately $110\mu m$).

The effects seen in figures 4.4, 4.5 and 4.6 can be attributed to the differences in surface energy of the metal electrodes.

### *4.4.3 ITO electrodes*

Lines were printed over ITO electrodes in the same way as for the gold and aluminium electrodes. The successful formation of a physical connection between the polymer on the glass and the polymer on the electrode was observed. The line continued onto the surface of the ITO and did not break up into a line of discrete droplets. Figure 4.7 shows two images, the printing parameters are identical and the microscope magnification remains unchanged. The only difference was the substrate onto which they were printed, glass or ITO. It can be seen that the overall width of the line is narrower on ITO indicating that the surface of the ITO has a slightly lower surface energy than the glass.

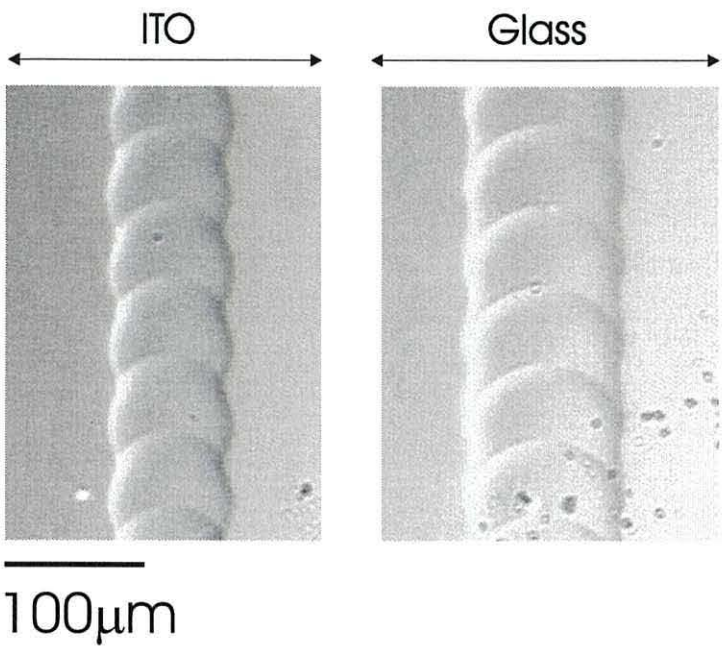


**Fig. 4.7:** Bottom lit microscope images, one showing m:PEDOT:PSS printed on glass, the other on ITO.

## *4.5 Contact angle measurements*

Surface tension can be considered as the force that holds a liquid together. The tension is an effect of the forces of attraction that hold the individual molecules of the liquid together. A surface tension exists between any boundary of a liquid be it with a gas, another liquid or a solid.

For a solid, the molecules of which it comprise are held together by forces of attraction too. Different materials will have different strengths of force holding its molecules together. If a droplet of liquid with weak forces of attraction between its molecules is placed on the surface of a material with strong forces of attraction between its molecules then the forces of the solid will overcome those of the liquid and the liquid will spread out across its surface. If the situation is reversed and the forces of attraction of the solids molecules are weaker than those of the liquids then the liquid will not spread out but bead up on the surface.

By placing a droplet of a liquid onto a surface and measuring the contact angle the three forces of interfacial tension can be related (see figure 4.8) by equation 4.1;

$$\gamma_{LV} \cos\theta = \gamma_{SV} - \gamma_{SL} \tag{4.1}$$

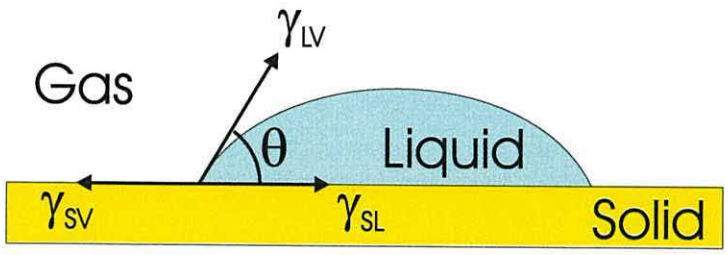


**Fig. 4.8:** Contact angle, $\theta$, formed by a liquid at the interface of a liquid, solid and gas.

A KSV Instruments Ltd. CAM 200 Optical contact angle and surface tension meter was used to determine the static contact angle of m:PEDOT:PSS on the different substrate materials providing an indication of the differing surface energies of the materials. The CAM 200 measures static contact angle by using a camera to view a droplet of liquid on a surface from the side, as shown in figure 4.9. The droplet it placed on the substrate using a syringe and illuminated from behind. The camera, substrate and syringe are all mounted on separate *xyz* stages which allow accurate positioning. Once an image of a droplet on the substrate has been captured image processing is used to identify the angle of the substrate and trace an outline of the droplet. The outline of the droplet is then intersected with the surface of the substrate and the contact angle measured.

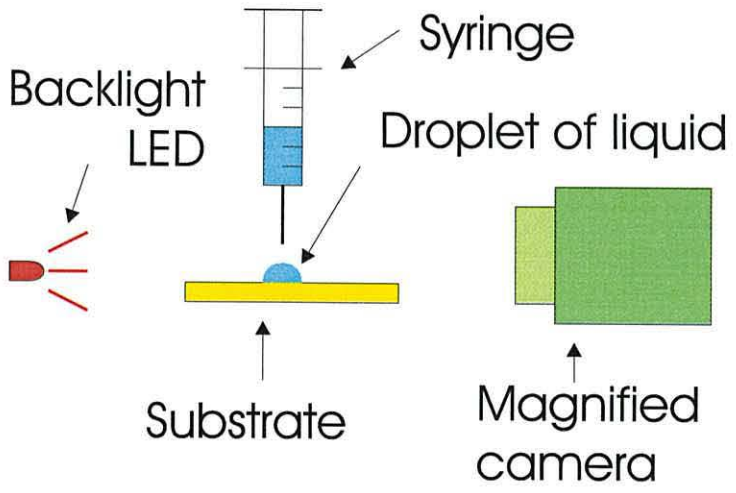


**Fig. 4.9:** Diagram showing principal of KSV Instruments Ltd. CAM 200 Optical contact angle and surface tension meter.

Droplets of m:PEDOT:PSS were deposited on to the same substrates as used in section 4.4 with the exception of flame treated gold. All experiments were conducted on the same day under the same ambient laboratory conditions. The contact angles for the different materials are shown in table 4.1 below (see appendix A for material details).

| Material | Contact angle (°) |
|---|---|
| Cleaned glass | 7.34 ±0.25 |
| Gold | 88.06 ±2.28 |
| Aluminium | 38.51 ±4.03 |
| ITO | 32.74 ±2.37 |

**Tab. 4.1:** Contact angles of m:PEDOT:PSS on different materials (error calculated to one standard deviation).

If a material has a high surface energy, i.e. it is hydrophylic, then a liquid is likely to spread out across its surface. As a result the contact angle with the surface will be low. If on the other hand the material has a low surface energy the liquid will not spread out so much across the surface resulting in a higher contact angle. Figures 4.4 to 4.7 in section 4.4 clearly show that m:PEDOT:PSS printed on the electrode materials form smaller droplets or narrower lines than on the glass. In addition the lines or droplets formed on gold are smaller/narrower than those on aluminium or ITO, which had similar sizes/widths.

Pure metals are infinitely polar so should have a very high surface energy, however in atmospheric conditions, the surfaces of metals can become modified resulting in a change in their energy. Gold is oleophilic so attracts hydrocarbons to its surface. The forces holding hydrocarbons together are low resulting in the surface of gold having a low surface energy. The process of flaming the surface removes the hydrocarbon layer from its surface, and providing the sample is used quickly, allows printing onto a surface of higher energy. Aluminium reacts with atmospheric oxygen forming an oxide layer on its surface decreasing its energy slightly.

This behaviour is confirmed by the contact angle measurements in table 4.1. They show that gold has a high contact angle of nearly 90° indicating that printed droplets would tend not to wet its surface as they do on glass which has a low contact angle of 7°. Aluminium and ITO have similar contact angles around 35° indicating that printed lines are more likely to spread out across their surfaces than with gold, but that some reduction in the deposited droplet should occur.

## *4.6 Inkjet printing across electrode gaps*

Parallel electrodes with a separation in the region of $50\mu m$ were used so as to allow the SKPM to examine the complete surface potential distribution across a pair of electrodes. Therefore the ability to inkjet print polymers from one electrode to another so as to make a continuous physical connection was required.

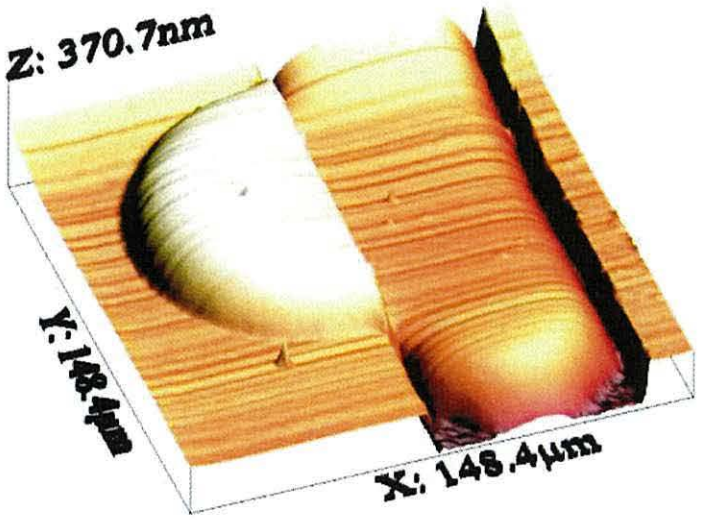


**Fig. 4.10:** Tapping mode AFM image showing a single m:PEDOT:PSS droplet deposited between two ITO electrodes.

Given that a single droplet on glass had a diameter of approximately $110\mu m$ it could be expected that a single droplet deposited over the center of the gap between the electrodes would be able to span them. Figure 4.10 shows a tapping mode AFM image of a single droplet deposited between two ITO electrodes. The droplet was aligned as accurately as possible over the center of the channel but clearly has only covered the left hand electrode. The process was repeated a number of times, with the alignment of the system being check and recalibrated. However, the droplet always had the tendency to mount only one of the electrodes.

The extent of the physical contact between the droplet and the right hand electrode is difficult to assess. The AFM tip could have been too wide to probe the interface at the right electrode. However, even if the droplet had made some form of contact, it is clear that this point would have a very high resistance in comparison to the rest of the structure due to the small cross-sectional area of contact.

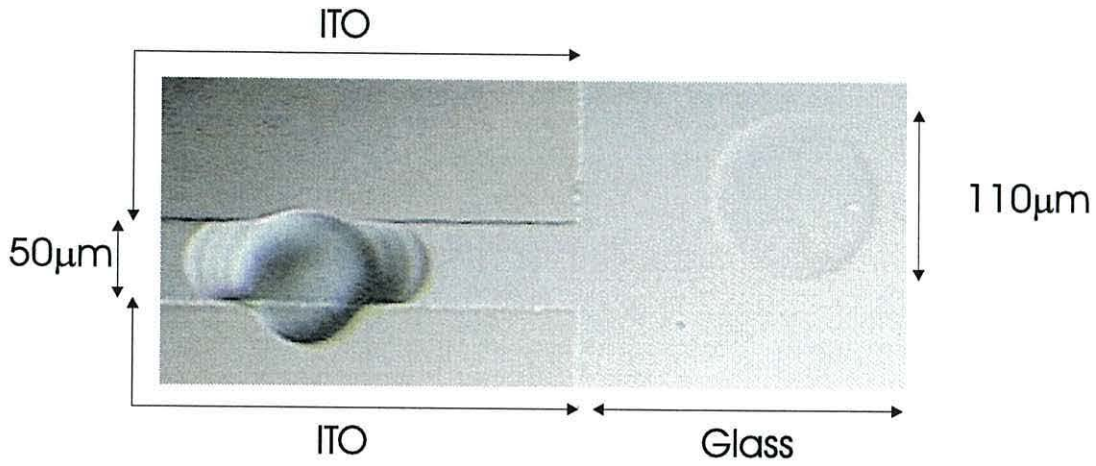


**Fig. 4.11:** Microscope image showing six m:PEDOT:PSS droplets deposited between two $50\mu m$ separated ITO electrodes. The droplet to the right shows the $110\mu m$ droplet diameter on glass.

The same process was repeated with droplets repeatedly deposited until an obvious physical contact had been made between both electrodes. After each droplet had been deposited the stage was moved and the alignment microscope used to observe the resulting structure. Figure 4.11 shows the final optical image where six droplets were deposited until both electrodes were contacted.

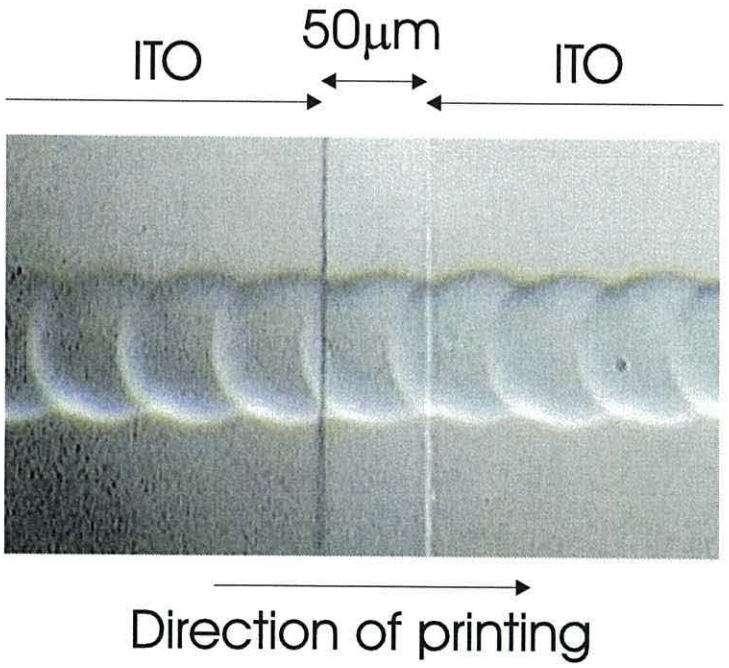


**Fig. 4.12:** Optical image of printed line across two ITO electrodes separated by $50\mu m$.

It was found that rather than printing a single droplet to bridge the electrode gap, a continuous line starting and ending in the middle of the electrodes far away from the electrode gap had a greater chance of making a complete physical

connection between the electrodes. In most cases the line crossed with minimal change in its regular morphology or with only slightly greater spreading of the material in the channel but no interruption of the conduction path. This is shown in figure 4.12. When investigating the effects of printing with different line pitches and delays over electrodes of differing materials it was found that printing lines with a pitch of $60\mu m$ and at 4s intervals was the most successful.

Most success was achieved using ITO electrodes and the method described above. ITO electrodes bridged by polymer could be fabricated with 100% reliability. It was possible to repeat the process with aluminium, however the likelihood of success was small while gold electrodes could not be bridged at all as expected from the results in section 4.4.

## *4.7 Cross-sectional analysis of electrode-polymer-electrode structures*

The method of producing cross-sectional area plots for inkjet printed polymer lines in section 4.3 was employed to produce the same data for lines printed across electrodes. The m-file code (included in appendix C) prompted the user to locate the electrode edges manually then produced a plot of cross-sectional area along the length of the line as it crossed from one electrode to the other. Figure 4.13 shows a cross-sectional area plot for an inkjet printed line across two ITO electrodes.

The plot was marked with the electrode edges, the electrode separation and the point of least cross-sectional area. This then allows an estimate of the resitivity of the material if the resistance between the electrodes can be determined.

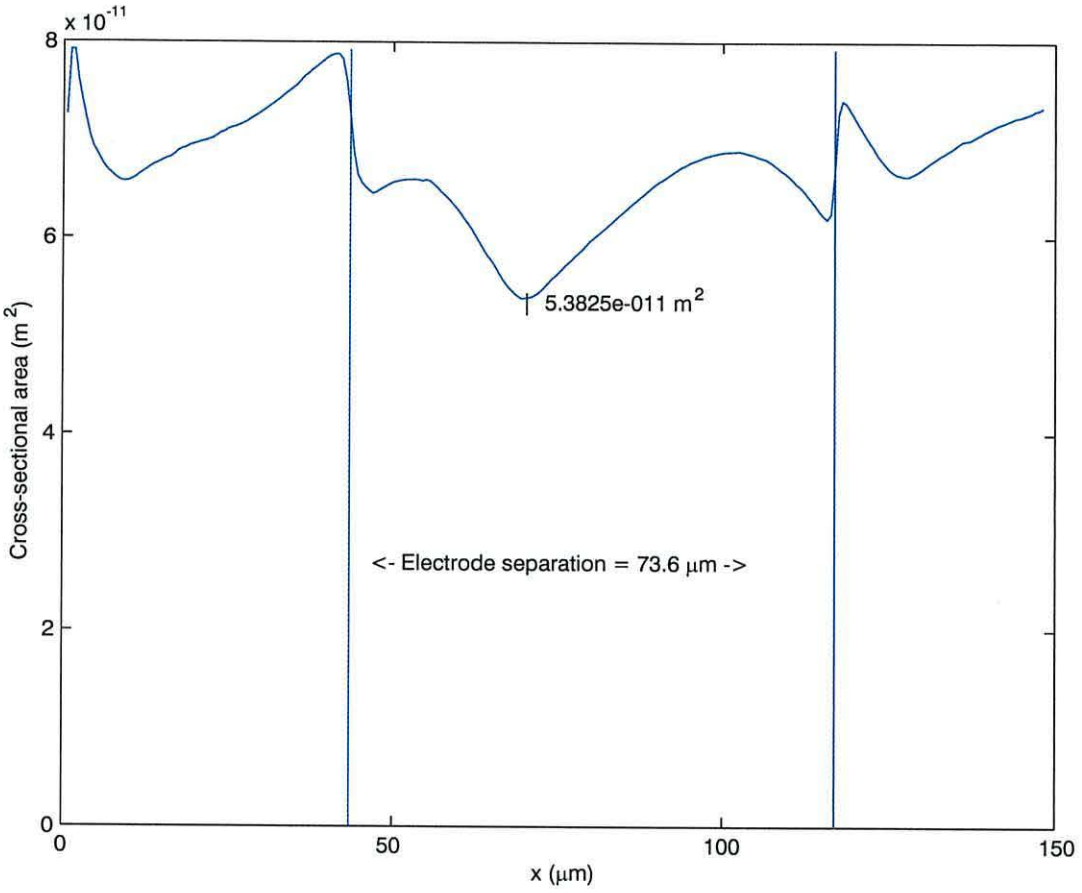


**Fig. 4.13:** Plot of cross-sectional area along length of printed line.

## *4.8 Concluding summary*

This chapter provides details of the use of the inkjet printing system for inkjet printing polymer solutions of m:PEDOT:PSS. An analysis of the printing of simple lines of polymer is given. This is followed by an analysis of the printing of lines between electrodes. The effects of the varying surface energies was considerable and limited the electrode materials to aluminium and ITO. The hydrophobic nature of the fabricated gold electrodes repelled the polymer solution from its edges and prevented electrical contact from being made A method for varying the surface energy of the gold was used and allowed successful contact to the gold however as a result of damge to the glass during the process it was not pursued.

ITO was identified as the most reliable electrode material for making a physical contact from one electrode to another using inkjet printed m:PEDOT:PSS. It was found that inkjet printing a continuous line across the electrode gap with a pitch of $60\mu m$ and delay of 4s produced the most regular results.

A method for producing cross-sectional area plots of the fabricated lines and devices was given based on AFM data. This will allow basic estimations of

resistance or conductivity to be made.

# 5. EXPERIMENTAL TECHNIQUES FOR DROPLET CHARACTERISATION

## *5.1 Introduction*

This chapter outlines the methods by which electrodes were fabricated and, following the deposition of inkjetted PEDOT:PSS, mounted for examination by AFM/SKPM. The chapter then describes the different methods used to characterise the electrical and spectral properties of the PEDOT:PSS.

Initially DC electrical measurements were performed providing basic information on the behaviour of the samples. Subsequently an AFM furnished with a conductive tip and operating in its SKPM mode was used, thus allowing the potential distribution across the samples to be ascertained. Raman spectroscopy was then used to reveal chemical and structural changes in the polymer in different regions of the samples. Finally EDX was used to give an indication of the likely ion content of the PEDOT:PSS in solution.

## *5.2 Electrode fabrication*

In order to make electrical contact to the droplets, electrodes were formed on the surface of a glass microscope slide, and the droplets deposited on top of the slide. Three electrode materials were used, gold, aluminium and ITO. The gold and aluminium was thermally evaporated onto glass under vacuum (gold including a chrome adhesion layer) while ITO coated glass was purchased from Delta-technologies Ltd. Photolithography was used to pattern a layer of photoresist with the image shown in figure 5.1. The unwanted electrode material was then removed using a suitable etch.

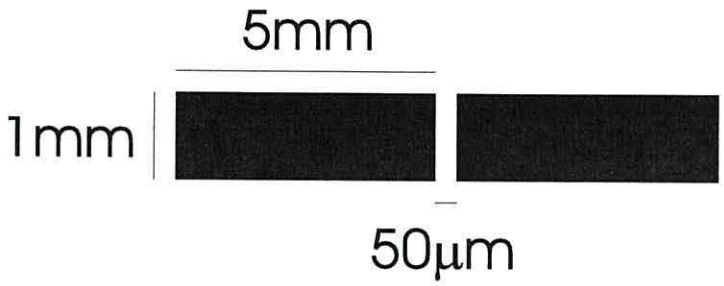


**Fig. 5.1:** Photolithographic mask

The electrode separation of $50\mu m$ was chosen based on the maximum scan range of the AFM which was $150\mu m$. With this separation, $50\mu m$ of each electrode could also be examined with the AFM/SKPM providing good reference points. If the channel was greater in length, the evolution of the potential on each electrode could not be observed completely.

The complete fabrication procedure for each electrode material is listed in appendix A.

## *5.3 Sample preparation*

The glass substrates containing electrode pairs were cut into approximately 12 by 7mm squares enabling them to fit onto the metal disks used in locating the samples in the AFM. Lines were then printed from one electrode to the other with a line pitch of $60\mu m$ and a delay of 4s. In order to ensure continuity of the line across the electrode gap, the line was started well away from the electrode gap, continued across the gap and far on to the other electrode. This was achieved by depositing 20 droplets to form a line of approximately 1.2mm in length. The samples were then baked on a hotplate (IKA Ikamag) for 1 minute at 100°C in air to remove any remaining solvents.

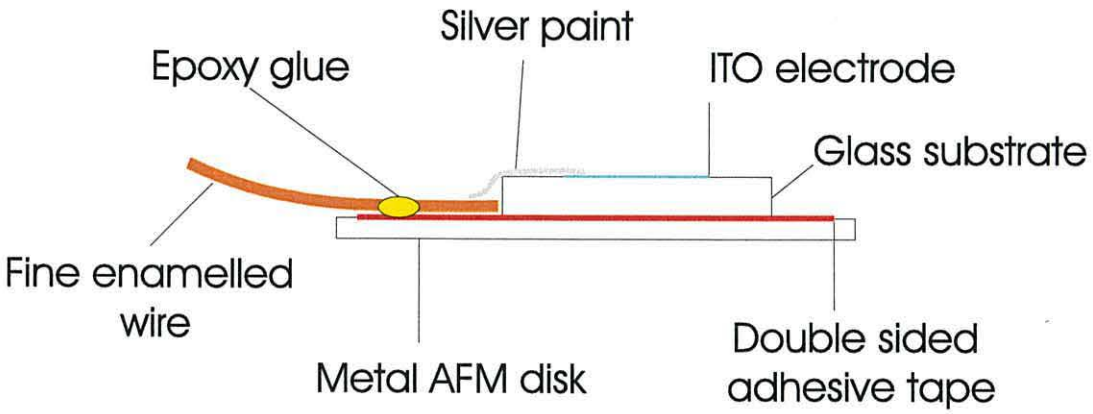


**Fig. 5.2:** Sample mounted on AFM disk.

Figure 5.2 illustrates the method by which the glass substrates with electrodes and printed polymer were mounted for subsequent analysis. A small slip of double sided tape was applied to the top surface of a metal AFM mounting disk and the cut glass substrate pressed onto it. Fine gauge enamelled wire was attached using non-conducting epoxy adhesive to the tape covered top surface of the metal puck. Fine gauge wire with an insulating enamel coating was used as the light weight and flexibility of the wire allowed the piezoelectric AFM stack to move unhindered. Additionally it was important that the wire was thin enough that it did not protrude too far above the surface of the electrodes and catch against the AFM tip holder.

Once firmly glued, the top surface of the enamelled wire was scratched using a sharp blade to remove a small amount of the insulating coating. Silver paint was then carefully applied so as to make a continuous conducting connection between the top of the wire and the electrode on the surface of the glass. As there were two separate electrodes on the samples, this process was repeated such that two wires, one to each electrode, were attached and connected. For consistency, the cut samples were mounted on the AFM disks and contacts made in the same way irrespective of whether DC electrical analysis, SKPM or Raman spectroscopy was to be performed.

## *5.4 DC electrical measurements*

DC electrical measurements were taken using a Keithley 237 high voltage source-measure unit. The primary functions of the 237 were to either apply a potential difference while measuring the corresponding current or source a current while measuring the potential difference. It was capable of sourcing voltage from 100V to 1100V, and current from 100fA to 100mA. It was able to measure voltage from 10V to 110V and current from 10fA to 100mA. The applied poten-

tial difference or current could be a constant dc value or varied in a stepwise fashion.

The 237 was set up to communicate with a computer via a GPIB connection. A personal computer was fitted with a GPIB card and connected to the 237 using a standard GPIB cable. Visual Basic was then used to write programs which allowed the specific potential or current sequences to be applied while the measured currents or potentials were collected and saved in a text file. Following this, the text file could be read with a variety of programs such as Microsoft Excel or Matlab. The individual potential or current sequences applied in taking the measurements have been listed in the relevant locations in the results chapters.

The DC measurements were taken under three different conditions. In the first case, in which the DC characteristics of the samples were determined, samples were placed in an electrically and light screened steel chamber. Due to the low potentials and currents involved in the measurements this provided a low electrical noise environment in which to take the readings. Triaxial leads were used to connect the Keithley 237 to the chamber for added electrical screening. The other two conditions relate to those pertaining to the SKPM and Raman microscopy measurements which are described below.

## 5.5 *Atomic Force and Scanning Kelvin Probe microscopy*

The use of inkjet printing in the deposition of conducting polymers allows specific quantities of material to be deposited at well defined locations. The aim is to build up conducting structures such as electrodes, interconnecting lines, interfaces to other materials or continuous films. Due to the discrete droplet fabrication method of inkjet printing the resulting conducting structures can have highly irregular morphologies. In comparison to, for example, photolithographically patterned gold films. This adds a third dimension when considering the resistances of the aforementioned conducting structures.

AFM and the associated SKPM enables accurate measurement of both morphology and surface potential respectively. The primary restrictions in the use of AFM and SKPM are that the dimensions of the structures and the measured potentials are within the operating ranges of the equipment. A Digital Instruments Nanoscope 3A was used for all AFM and SKPM measurements. The limits of the equipment were an $x$ and $y$ range of $150\mu m$ and a $z$ range of $5\mu m$. For SKPM measurements the surface potential was limited to a range of $\pm 10$V.

### *5.5.1 Atomic force microscopy*

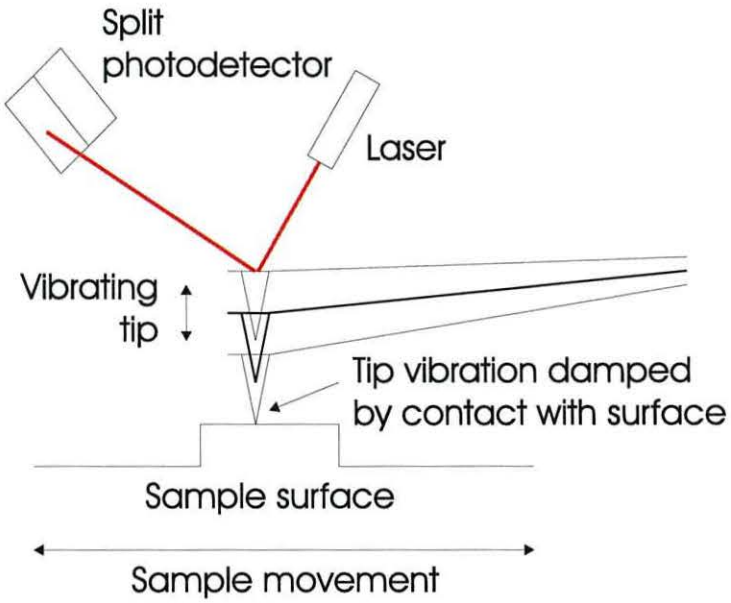


**Fig. 5.3:** AFM tip measuring sample height.

Figure 5.3 shows how a tip mounted on a cantilever can be used to measure surface height of a sample. All AFM images were taken using TappingMode AFM. This operates by lightly tapping the surface of a sample with a probe tip oscillating at its resonant frequency. As the tip approaches the surface of the sample the oscillation of the tip is damped and the height at that point recorded. A laser beam is shone onto the top of the cantilever, which is then reflected up onto a split photodetector. As the cantilever flexes the point on the photodetector at which the laser shines, changes. Therefore by measuring the difference in signal between the two sides of the detector, the height of the cantilever, and hence the tip, can be determined. An advantage of TappingMode AFM over ContactMode (where the tip is slid across the surface) is the reduction in damage to the sample and the elimination of lateral forces which can reduce image resolution. The sample is mounted on top of a column which can be bent using piezoelectric actuators. This enables the sample to be moved in three dimensions below the tip. Using this, the tip can be scanned across the sample surface, line by line, determining the height, building up a two dimensional matrix of height data. Image processing then enables the data to be projected in three dimensions and analysed for cross-section data, surface roughness etc.

### *5.5.2 Scanning Kelvin Probe Microscopy*

The principles behind the SKPM have been discussed in chapter 2. When performing SKPM measurements ideally the samples should be housed under the same

conditions as those when performing the DC electrical measurements. However, due to the configuration of the equipment it was not possible to enclose the sample in a screened chamber or to seal out all light. Neither was it possible to heat or cool the sample or to place it in a vacuum either. Hence, all measurements were made under ambient laboratory conditions.

## 5.6 *Raman spectroscopy*

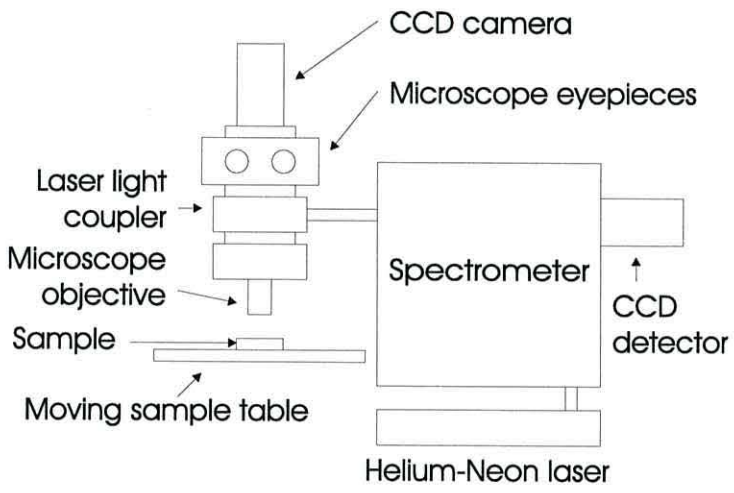


**Fig. 5.4:** Renishaw system 1000 Raman microscope.

A Renishaw System 1000 Raman microscope (figure 5.4) was used to capture spectra using the 180° illumination method where a laser beam impinges on the sample from the same direction as the collection optics. The laser beam was focused, and the reflected photons collected, using a microscope objective. Three objectives of x5, x20 and x50 magnification were available. When using the x50 magnification it allowed the region of collection to be reduced to a cube of 4 by 4 by $4\mu m$. A helium-neon laser of 633nm wavelength was used for all measurements.

A CCD camera was also coupled to the microscope objective. Using this it was possible to align its point of focus over specific areas of the sample. This allowed optical video of the sample to be viewed in real time although the software of the system only allowed still images to be captured.

A Raman spectrum is based on captured light of different frequencies scattered back from a sample illuminated by a monochromatic laser. The Renishaw System 1000 was controlled by computer software with a variety of settings for the capture of the spectrum. These included the frequency range over which light was captured (measured in wavenumbers ($cm^{-1}$)), the length of time for which light was captured

and the number of times this was repeated. Two filters were provided, the first a physical filter in the path of the laser which attenuated the intensity of the light incident on the sample. The second, a software filter, which enabled the effect of cosmic rays to be eliminated by capturing additional spectra prior to the main run and comparing them to see if peaks due to cosmic rays were present. If so they were filtered out of the main spectra.

As with the SKPM measurements the Raman microscope imposed limitations on the conditions under which the experiments could be performed. It was not possible to enclose the sample in an evacuated screened chamber nor heat or cool it. The equipment was located in a dark room which allowed complete darkness for the experiments.

## 5.7 EDX

Scanning Electron Microscopy (SEM) and Energy Dispersive X-Ray Spectroscopy (EDX) utilise thermionic emission of electrons from a metal accelerated by electric fields in a vacuum so as to collide with a conducting sample. The incident electrons can interact with the sample in four different ways; (i) it can pass straight through the sample without interacting in any way, (ii) it can scatter elastically (change its direction but not its energy), (iii) it can scatter inelastically (in interacting with one of the orbital electrons of an atom it loses some of its energy to that electron) and (iv) it can be scattered elastically and inelastically many times as it passes through the sample.

When inelastic scattering occurs an electron is excited out of the orbital of an atom in the sample and leaves the atom in an ionised state. This secondary electron can escape if near enough to the surface of the sample. The detection of these escaped secondary electrons forms the basis of SEM. Alternatively the secondary electron can fill one of the vacant orbital sites of another atom in an excited state. This atom then changes from an excited state to a normal low energy site giving off energy in the process. One of the ways that this energy can be given off is as X-rays in which the wavelength of the radiation, $\lambda$, corresponds to the difference in the energy, $\Delta E$, of the two states as in equation 5.1;

$$\lambda = \frac{hc}{\Delta E} \tag{5.1}$$

where $h$ is Plancks constant and c is the velocity of light. Different elements emit X-rays of different wavelengths so an analysis of the wavelengths of emitted radiation provides information regarding the elements within a sample and provides

the basis for EDX.

SEM uses an electron gun, usually a heated tungsten filament, to emit electrons which are then accelerated and then focussed to a point 5-10nm in diameter using condenser lenses. Deflector coils are then used to scan the focussed beam of electrons across the surface of the sample in a raster fashion. As the beam of electrons is incident on the sample at any one point the number of emitted secondary electrons is counted by a detector. This is shown in figure 5.5. Using this method an image illustrating the intensity of emitted electrons across the surface of the sample is produced. The electron beam can be scanned across areas smaller than $10\mu m x \mu m$ producing magnifications in excess of 10000 times.

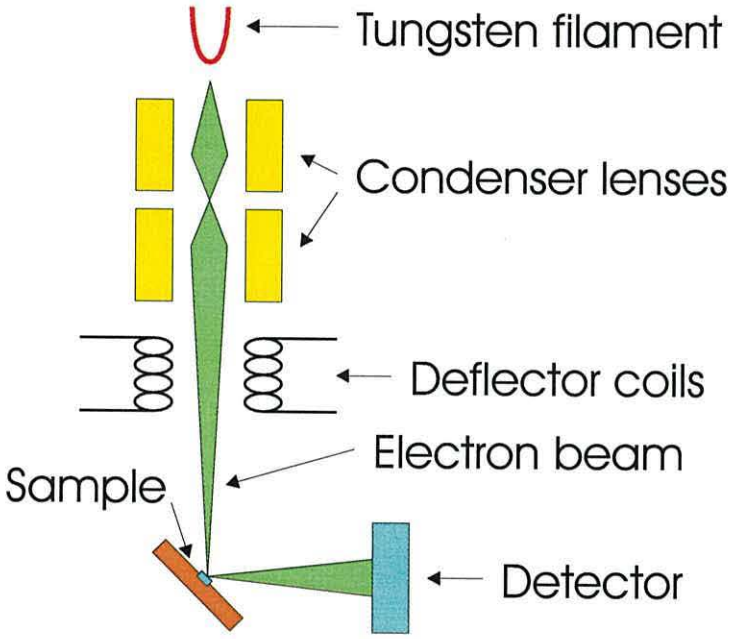


**Fig. 5.5:** Illustration of the principle behind the operation of SEM/EDX.

If the electron beam is instead focussed on a single point, measurement of the wavelengths of the emitted X-rays provides information as to which elements are present at that point while measurement of the rate of X-ray emission at a particular wavelength will give the quantity of an element at that point. EDX uses a liquid nitrogen cooled semiconductor sensor (usually silicon) to detect the incoming X-rays which excite electrons into the conduction band of the silicon resulting in electron-hole pairs. If an electric field is applied to the semiconductor the electron-hole pair will separate and each X-ray absorbed will generate a current pulse proportional to its energy. A multi-channel analyser can then produce a histogram of X-ray energies.

An Oxford Instruments Isis 3 was used to produce the EDX spectra. Samples were then exposed to a 14KeV electron beam for 30s while the resulting spectrum

of X-rays was captured using a Multi Channel Analyser (MCA).

## *5.8 Concluding summary*

In this chapter, an overview of the various experimental techniques and apparatus has been given. When undertaking the experiments the conditions under which the results were obtained and the fine adjustment of the equipment parameters had to be varied. The specific experimental conditions have been included in the following results chapters particularly where different equipment settings are pertinent to explaining the data obtained.

# 6. RESULTS AND DISCUSSION: ALUMINIUM ELECTRODES

## *6.1 Introduction*

This chapter presents results taken from samples consisting of coplanar aluminium electrodes connected by a region of m:PEDOT:PSS. The electrodes were vacuum evaporated aluminium on glass, patterned with photolithography and etched using either aqua regia or a mixture of phosphoric and nitric acid as described in chapter 5. The two different etches produced electrode separations of $80\mu m$ and $45\mu m$ respectively.

DC analysis of the sample was performed by applying a single square wave pulse of potential and measuring the current evolution with respect to time.

AFM was used to determine the topography of the sample and the data used to produce a 2 dimensional computer model to predict the expected surface potential distribution across the droplet.

SKPM was used to take correlated height and surface potential plots of the sample. The SKPM plots were taken with zero potential applied to the sample to determine the work function differences of the materials. The measurement was repeated with a potential difference applied to the electrodes to determine the potential gradient across the droplet. The potential difference was then reversed to eliminate electrode dependent effects. The slow-scan axis of the SKPM was subsequently disabled allowing time resolved plots of surface potential across a single cross-sectional line of the droplet to be observed.

Raman spectroscopy was used to investigate structural and chemical changes in the sample under the application of electrical bias while a CCD camera attached to the system was used to capture optical images at the same time.

## 6.2 Sample fabrication

### 6.2.1 Sample 1

Aluminium was vacuum evaporated onto a glass microscope slide then patterned and etched using photolithography and aqua regia. Due to the aggressive nature of aqua regia as an etch for aluminium the result was over etching of the aluminium and an electrode separation of $80\mu m$ (as determined by optical microscopy).

Tapping mode AFM was used to determine the thickness of the aluminium electrodes. The data was saved by the Nanoscope IIIA controller and then opened and interpreted using Nanotec Electronica S.L. WSxM version 4. The data was also exported from WSxM as an ASCII matrix file for importing into Matlab V6.5 for further analysis.

Figure 6.1 shows an AFM image taken of the edge of the aluminium electrode. The AFM data was flattened using a 2nd order fit based on the exposed glass substrate. Additionally, a spot cleaner was used to remove excessively large spikes in the image due to extraneous particles. Cross-sectional profiles were taken of the electrode edge and the thickness of the aluminium determined to be 20nm $\pm$2nm.

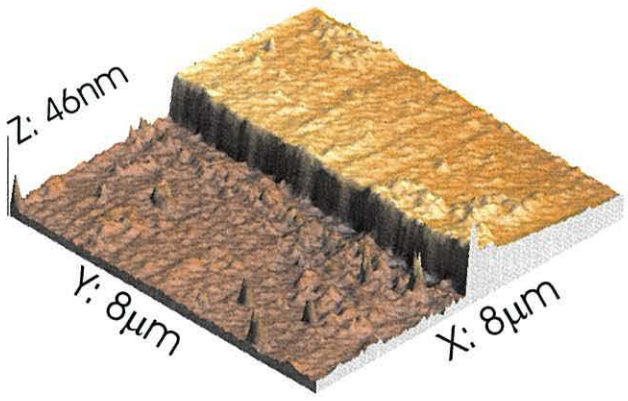


**Fig. 6.1:** AFM image of aluminium electrode edge.

m:PEDOT:PSS was printed as a line of droplets across the electrode gap starting on one electrode, well away from the electrode gap, passing over the gap and crossing far onto the other electrode. The line was printed with 20 droplets at a pitch of $60\mu m$ and with a delay of 4s between each droplet. The sample was then mounted on an AFM puck as described in chapter 5. Only one sample was fabricated by this method (designated Sample 1).

Figures 6.2 and 6.3 show the AFM images of such an inkjet printed island

of m:PEDOT:PSS bridging between two aluminium electrodes in 2D and 3D respectively. The AFM data was flattened using a 2nd order fit based on the exposed glass substrate and a spot cleaner was used to remove excessively large spikes in the image due to extraneous particles. The horizontal scale of the image is $150\mu m$ while the vertical scale is 670nm.

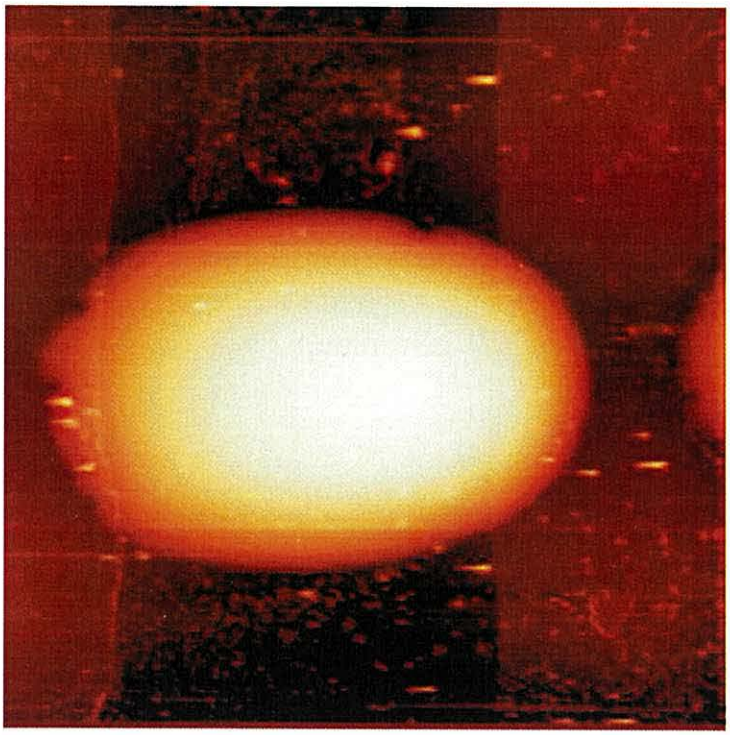

**Fig. 6.2:** 2D AFM image of inkjet printed m:PEDOT:PSS bridging two aluminium electrodes.

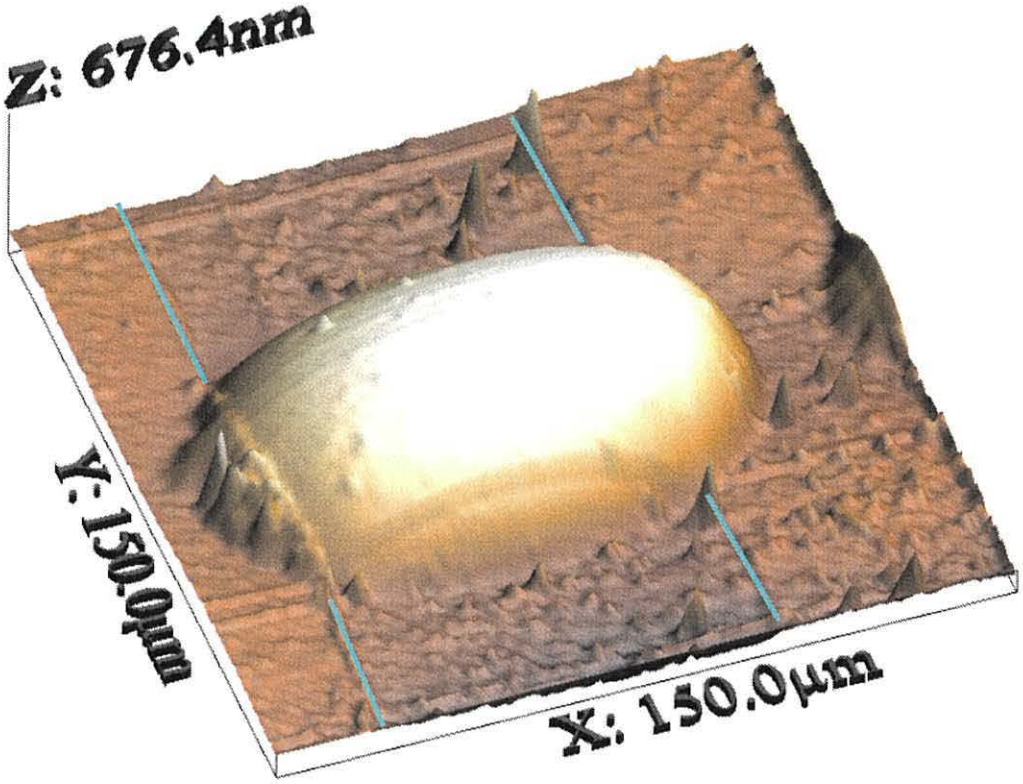


**Fig. 6.3:** 3D AFM image of inkjet printed m:PEDOT:PSS bridging two aluminium electrodes. The blue lines indicate the electrode edges.

Due to the low surface energy of the aluminium electrode the line of droplets did not form a continuous band of material but separated into a discontinuous line of polymer islands. The volume of these islands was greater than that of a single deposited droplet. The separate islands of polymer formed a regular line with a constant section length and separation. This indicated that the polymer solution had formed a continuous band while still in its liquid state but that it then broke up into islands before it had dried. It is likely that this was a continuous process, with a "drying edge" following the "leading edge" of the newly printed droplets and the polymer breaking into islands somewhere in between. There was no indication from AFM of any residue between the sections so their formation is assumed to have occurred prior to drying.

In figures 6.2 and 6.3 the edge of a second region of m:PEDOT:PSS can be seen on the right hand side. A second AFM image was taken which showed the region to the left hand side of the droplet bridging the electrode gap. From this, two estimates of the pitch (the distance from the start of one region to the start of the next) of the polymer islands were derived to be 130 and 133$\mu m$. By dividing the pitch of the separated islands by the pitch at which the individual droplets were deposited, the number of deposited droplets that goes to make up each section was calculated to be between 2.17 and 2.22.

### *6.2.2 Sample 2*

A second set of samples was then fabricated with an attempt made to increase the thickness of the aluminium electrode by increasing the amount of aluminium wire loaded for evaporation. The electrodes were again patterned using photolithography but the etch changed to a mixture of phosphoric and nitric acid to produce a more reliable etching process. The electrode separation was found to be $45\mu m$ by optical microscopy. From cross-sections taken from tapping mode AFM data the thickness of the aluminium electrode was found to be 40nm±4nm.

m:PEDOT:PSS was then printed as a line of droplets across the electrode gap and mounted on an AFM puck using exactly the same procedure as used in the first sample. This process was more reproducible with multiple near-identical samples being fabricated. One of these samples (designated sample 2) was used for the data collection.

Figure 6.4 shows an optical image of the inkjet printed sample taken using the CCD camera coupled to the Raman spectroscope. It can be seen that the printed line crosses from one electrode to the other forming a continuous band of polymer. This was not seen in the first sample. Given that the second set of electrodes were fabricated from aluminium vacuum evaporated at a different time to that of the first sample it is possible that the surface energy of the second aluminium electrodes was different. Alternatively, aqua regia was used to etch the electrodes for the first sample which was then changed to a phosphoric/nitric acid mixture for the second set, again resulting in a difference in the surface energy. The surface energy of the substrate on to which the polymer solutions were printed had a significant effect on the resulting polymer structures. Therefore, it is likely that the second set of aluminium electrodes had a higher surface energy allowing the polymer solution to spread more across its surface, forming a continuous band.

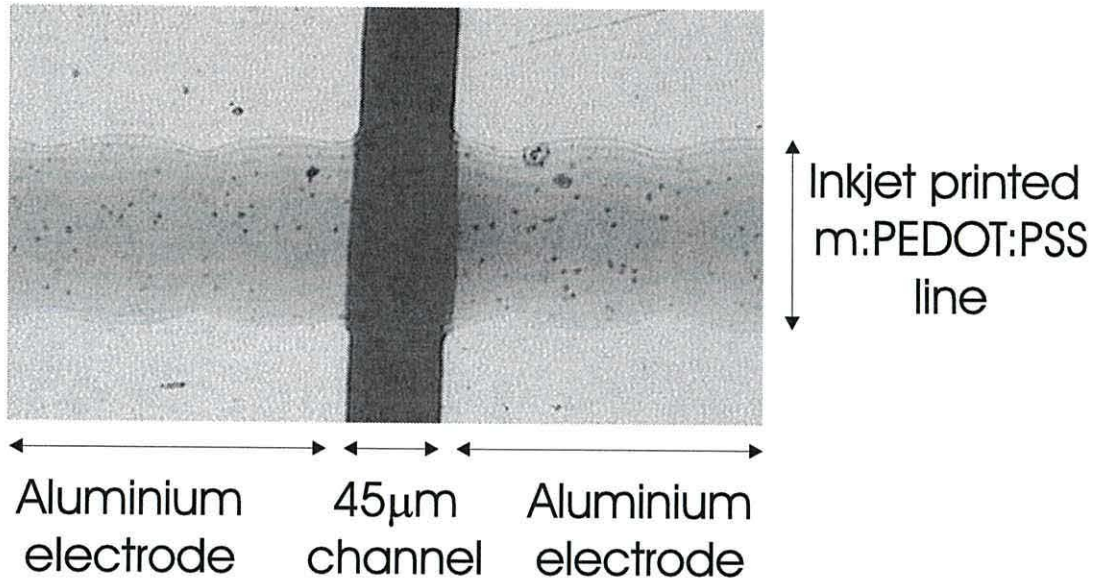


**Fig. 6.4:** Optical microscope image of the inkjet printed sample on aluminium electrodes taken using a x20 microscope objective. The width of the image is approximately $350\mu m$ and the height approximately $200\mu m$

## *6.3 DC results*

A Keithley 237 high voltage source-measure unit was used to apply a potential step of 5V to each sample while measuring the current over time. The potential step was applied from t=0s to t=200s. The results for sample 1 (comprising the isolated island of m:PEDOT:PSS bridging the electrodes) are shown in figure 6.5.

The I-t plot shows a charging current peak superimposed on a steady state current followed by a discharging current when the potential was removed. The steady state current can be used to determine the conductivity of the sample and was measured as $5x10^{-12}$A for sample 1. The I-t plot for sample 2 (comprising a continuous line bridging the electrodes) showed the same characteristics but with the steady state current of $1.4x10^{-10}$A. Taking these steady state currents the resistances of the samples were calculated using Ohms law to be $1x10^{12}\Omega$ for the first sample and $36x10^{9}\Omega$ for the second.

It should be noted that as successive measurements were made the steady state current decreased thereby indicating that there was some form of degradation to the sample under the application of an electric potential. The decrease in steady state current was not seen if the sample was simply left under atmospheric conditions confirming that the effect was due to the application of the electric field rather than exposure to the atmosphere.

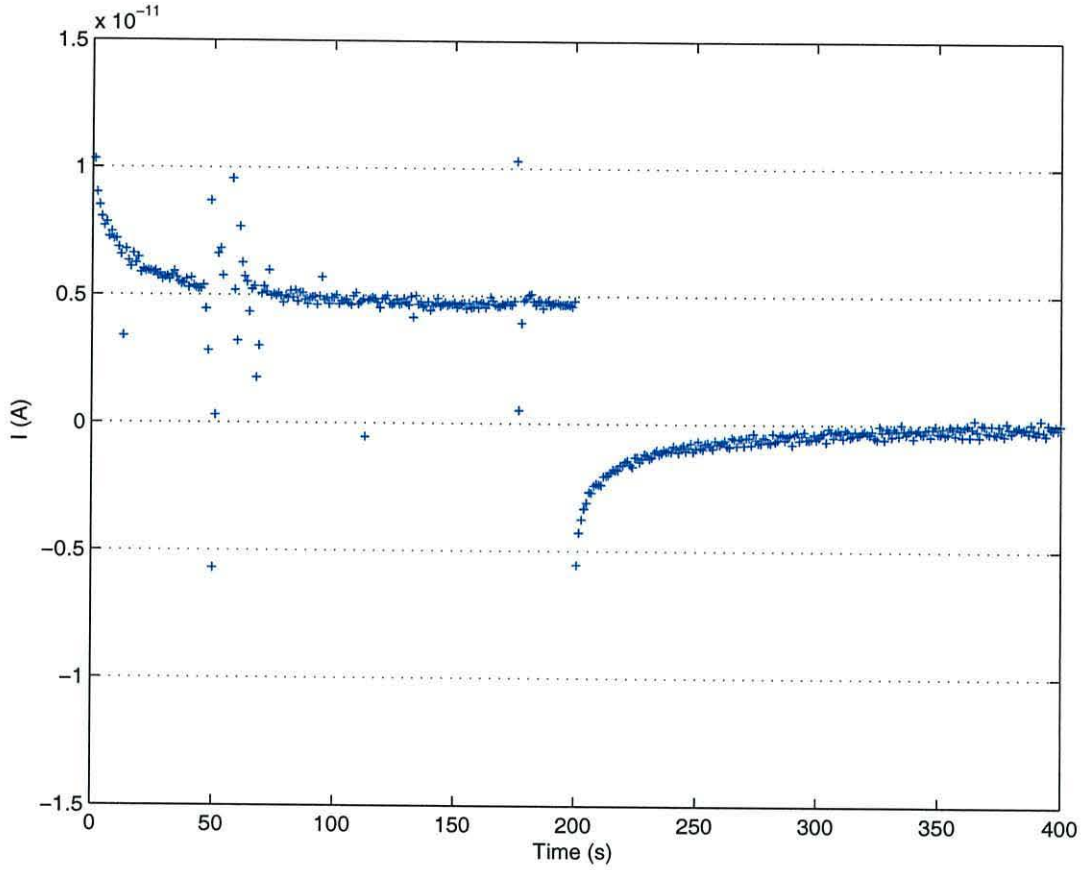


**Fig. 6.5:** I-t plot for applied 5V potential between t=0s and t=200s.

It is difficult to make direct comparisons between the resistances of the two samples as three factors change between the two of them; (i) the contact area between the polymer and the electrodes, (ii) the electrode separation and (iii) the topology (and hence cross-sectional area) of the lines.

If the resistance of the samples was entirely due to the bulk resistivity of the polymer and both lines had a similar topology then a reduction of the electrode separation by a factor of approximately 2 would result in an decrease in the resistance of the sample by the same amount. However the difference in the steady state currents is a factor of 28 so the electrode separation cannot account for the difference.

Figures 6.2 and 6.4 show that there is a significant difference in the contact area between the polymer and the electrodes in the two different samples. Given the likely presence of some form of insulating interfacial layer between the aluminium and polymer the resistance of the sample will not be simply determined by the bulk conductivity of the polymer but by a series combination of it and the resistances of the interfacial layers at either electrode. Reducing the contact area as occurs in the first sample would result in a similar reduction in the steady state current. The difference in the contact areas of the two samples has not been measured

however, a factor of 28 difference between the two is possible (see figures 6.2 and 6.4). A cross-sectional area analysis of the samples is further explored in section 6.4.

The effect of contact area could be examined further by printing lines across electrodes with varying separations and observing the effect on the steady state current. The contact area can be varied by printing lines with different numbers of droplets (and therefore different lengths) centered on the electrode gap. Using optical microscopy and the image processing toolbox within Matlab the contact area for the different line lengths could be quantified and compared with measured values of steady state current.

### *6.3.1 Charging/discharging transients*

The likely explanation for the charging/discharging transients seen in the I-t plot is that of electrode polarisation. When the potential is applied to the sample ions migrate within the bulk of the polymer to the electrodes where they cannot discharge. On application of the potential the charging transient results due to the movement of the ions through the polymer. On removal of the potential the ions migrate back into the bulk of the polymer and the discharging transient results.

Secondly, as the ions migrate to the electrodes under the applied field they generate a polarisation field in the bulk which opposes the applied field. As a result the field across the bulk of the polymer collapses thereby reducing the field acting on the holes flowing through the sample.

## *6.4 Cross-sectional analysis*

Chapter 4 details the method for the cross-sectional analysis of electrode-polymer-electrode structures. This was performed on the data from the AFM image shown in figures 6.2 and 6.3 and the results are shown in figure 6.6. The edges of the electrodes have been marked on the plot by lines and the point of least cross-sectional area between the electrodes by an X.

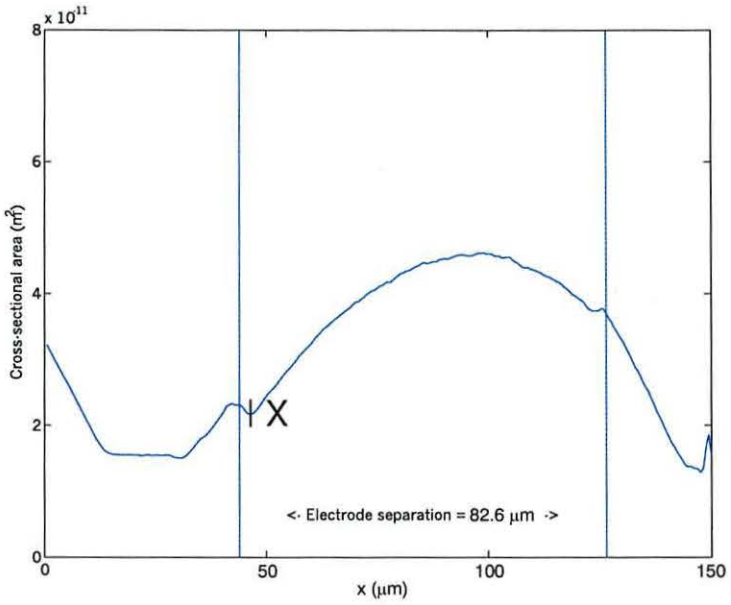


**Fig. 6.6:** Plot of cross-sectional area against distance along the length of the polymer bridge.

The point of minimum cross-sectional area for sample 1 was $2.17\text{x}10^{-11}m^2$. An exact measure of the cross-sectional area for sample 2 was not taken, however samples fabricated in an identical manner were analysed and found to have a cross-sectional area of $5\text{x}10^{-11}m^2$. This factor of 2.5 difference in area cannot account for the factor of 28 difference in the steady state currents, confirming the likelihood of there being a contact resistance at the aluminium-polymer interface.

Neglecting the contact resistance effects at the interface an estimate of the resistivity of the polymer was made. This is complicated by the complex 3D geometry of the sample, however an attempt was made based on the point of minimal cross-sectional area between the electrode edges. Figure 6.7 shows a column of material linking the electrodes whose cross-sectional area corresponds to the minimum cross-sectional area between the electrodes. The resistivity, $\rho$ ($\Omega m$), of the polymer is given approximately by:

$$\rho = \frac{RA}{l} \tag{6.1}$$

where R is the resistance ($\Omega$), A is the cross-sectional area ($m^2$) and l is the length of the column (m).

The data is presented in table 6.1.

| | Sample 1 | Sample 2 |
|---|---|---|
| Electrode separation ($\mu m$) | 82.6 | 45 |
| Steady state current (A) | $5x10^{-12}$ | $1.4x10^{-10}$ |
| Calculated resistance ($\Omega$) | $1x10^{12}$ | $36x10^{9}$ |
| Measured area ($m^2$) | $2.17x10^{-11}$ | $5x10^{-11}$ |
| Calculated resistivity ($\Omega m$) | $262x10^{3}$ | $43x10^{3}$ |

**Tab. 6.1:** Table summarizing the results of electrical and topological measurements on two samples based on aluminium electrodes.

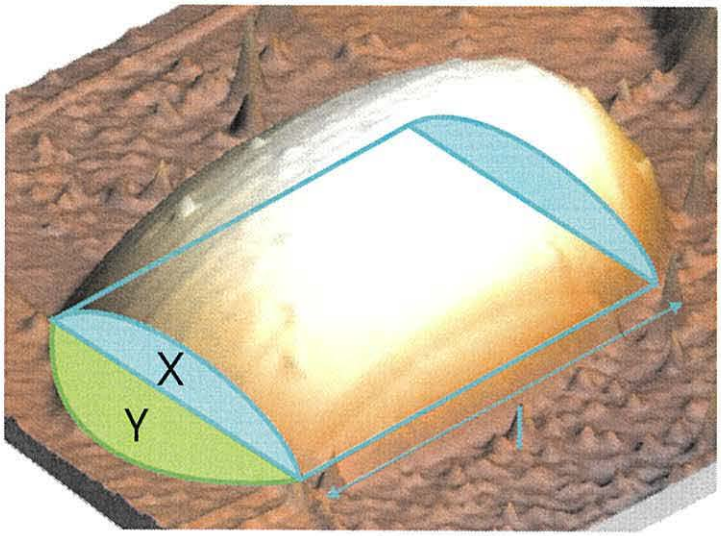


**Fig. 6.7:** Figure showing method for estimating the resistivity of the polymer.

The resistivity of sample 1 was found to be 262K$\Omega$m while sample 2 was 43K$\Omega$m. The Bayer data sheets list the resistivity of Baytron P as 0.01$\Omega$m and Baytron P CH8000 as 1K$\Omega$m. As discussed in chapter 3 modifications were made to the Baytron P CH800 to allow successful inkjet printing of the polymer solution. As the exact nature of the added solvents is not known it is not possible to comment on the possible changes in the conductivity of the modified Baytron P CH8000. However Jonsson et.al. [44] found that the conductivity of aqueous PEDOT:PSS could be increased by a factor of 600 by the addition of sorbitol.

Attempts were made to spin coat the inkjet modified m:PEDOT:PSS onto glass so as to provide a 4-point probe measurement of its conductivity. However, due to the lowered viscosity and surface tension required for inkjet printing, it was not possible to obtain a uniform film for analysis.

Further limitations to the accuracy of the calculation above are introduced by the simplification of the geometry of the droplet to that of a column of uniform cross-sectional area of length determined by the electrode gap. The area of the column is given by the minimum cross-sectional area of $2.17x10^{-11}m^2$, however this

increases to a maximum of approximately $4.47\text{x}10^{-11}m^2$. As a result the estimated value of resistivity will be higher than the actual value due to the increased ability to carry current in the central part of the droplet.

In the simplified geometry electrical contact is made to the vertical end face of the column (X in figure figure 6.7) at the edge of the electrode. Again this is not true to the actual geometry which is complicated by the existence of an interfacial layer. However, by making the contact to the end face X rather than the bottom face Y the estimated resistivity would be reduced in comparison to the actual value.

## *6.5 Computer modelling*

In order to resolve some of the issues regarding the accuracy of the calculations of the resistivity of the polymer and to provide predicted surface potential profiles for comparison with SKPM data a computer model of the electrode-polymer-electrode structure in sample 1 was developed based on actual AFM data.

An initial attempt was made using a supplementary program for Matlab called Femlab V2.3. This program was integrated into the Matlab environment and allowed the interchange of data between the two programs. As described in section 4.3 it was possible to import the AFM data from the Nanoscope IIIA via WSxM into Matlab as a 256x256 matrix of height data. Using a simple command ($A = surf(B)$) it was possible to place a bounding surface on to the AFM data. Following this a bounding box was placed on the under side of the AFM surface to form a complete volume describing that of the inkjetted line. A similar procedure was used to identify the position of the electrodes and to define separate entities for them.

This geometry then formed the basis for a computer model in which Laplace's equation was solved for a selection of boundary and volume conditions providing such data as current density and surface potential.

Unfortunately there were limitations to the process revolving around the inability of the Windows XP operating system to allocate more than 2Gb of virtual memory, even though more memory was available on the hard disk drives. This was partially overcome by reducing the resolution of the AFM data matrix from 256x256 to 10x10 so that less memory was required. A second problem due to the aspect ratio of the data was encountered. Prior to solving the geometry a tetrahedral mesh was placed within the volume across which Laplace's equation was solved. Given that the topology data was typically no more than $0.5\mu m$ high each tetrahedron was limited to sizes that could fit into that height. When spread across

a matrix of 150x150$\mu m$ this increased the number of tetrahedra to an excessively high number and again presented problems due to memory restrictions.

As a result it was decided that Femlab V2.3 was unsuitable for modelling the complex 3D data from the AFM. A second computer modelling package was used called CFD-ACE. The following describes the process for forming a 2D model based on the AFM data.

The AFM data was saved by the Nanoscope IIIA controller and then opened and exported from WSxM as an ASCII matrix file which was then imported into Matlab V6.5. An m-file was then written to take a cross-section through the data. The AFM data consisted of a 256x256 matrix. Following the cross-section, this was reduced to a single line of data that was 256 points long. Due to computing limitations the cross-section was rescaled from 256 to 64 data points in length. The data was then cropped to the length of the droplet and the locations of the electrode edges noted. The data was then written to a tabulated $XYZ$ data file.

The tabulated $XYZ$ data was imported into a CFD-GEOM geometry file and scaled so as to obtain a 1:1 aspect ratio. 20nm thick electrodes were then applied to the underside of the imported data, positioned using the locations noted when the cross-section was produced in Matlab. The electrodes were extended by 23.4$\mu m$ to either side of the droplet edges, this was an arbitrary value which was convenient for the meshing process and provided a reference point on each electrode. Applying the electrodes to the underside of the imported data rather than embedding them into the cross-section of the polymer droplet was not an exact representation of the sample, however it simplified the modelling process and was felt not to impact significantly on the accuracy of the model. A second geometry was formed, based on the first one, which included a 20nm thick interfacial layer between each electrode and the polymer. Both geometries were then filled with a triangular mesh. The first meshed geometry for the model without interfacial layers is shown in figure 6.8 while figure 6.9 shows the detail of an interfacial layer on the left hand electrode (the right hand electrode is the same) of the second meshed model.

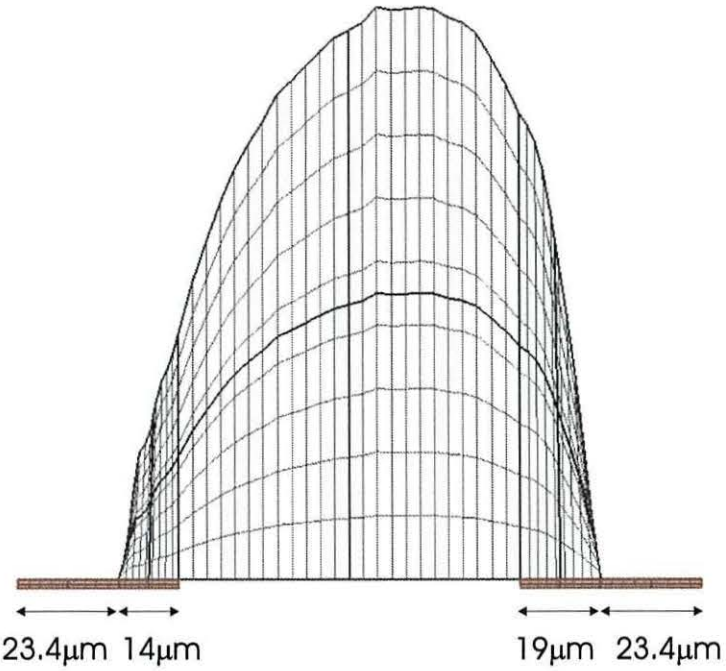


**Fig. 6.8:** Figure showing 2-D meshed geometry of sample taken from AFM data. The electrode regions are highlighted in red. The aspect ratio of the image is 50:1.

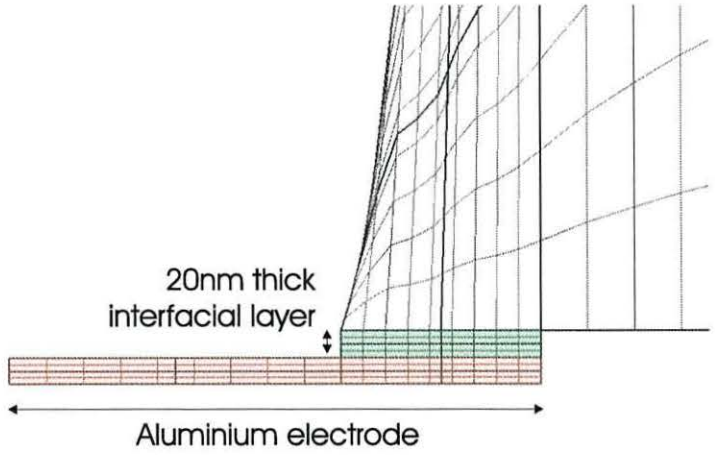


**Fig. 6.9:** Figure showing detail of interfacial layer on left hand electrode in the CFD geometry. The electrode regions are highlighted in red, the interfacial layer in green. The aspect ratio of the image is 50:1.

Once meshed the geometries were saved as .dtf files then opened in CFD-ACE. The modelling conditions were then applied including the volume and boundary conditions. In all of the models the boundary conditions were kept the same, 0V was applied to the end face of the left hand electrode while +1V was applied to the end face of the right hand electrode. The conductivity of each region of material was set by defining the volume conditions of the region. The model was then solved and the data opened in CFD-View which allowed a variety of plots to be presented from the solved data. Of most relevance was a plot of surface potential with respect to horizontal distance along the cross-section as this allowed direct comparison with data provided by the SKPM.

### *6.5.1 Sample without interfacial layer*

In order to solve the models, values for the conductivities of the polymer and electrodes were needed. Rather than use measurements of the conductivities of the materials, standard values were looked up in the literature. A value for the bulk conductivity, $\sigma_{Al}$ of aluminium of $37\text{x}10^{6}\text{Sm}^{-1}$ was found on the Goodfellows website. The conductivity, $\sigma_p$, of Baytron P CH8000 was listed as $1\text{x}10^{-3}\text{Sm}^{-1}$ in the Bayer data sheets. The value for the conductivity of the polymer, $\sigma_p$, was taken from the data sheets rather than the value measured in section 6.4 as it was believed the measured value did not represent the true conductivity of the polymer.

The values were entered into the respective volume conditions and the model then solved. Figure 6.10 shows the resulting plot of surface potential along the surface of the cross-section from one electrode to the other. Marked on the plot are the edges of the electrodes in red and the extent of the droplet in green.

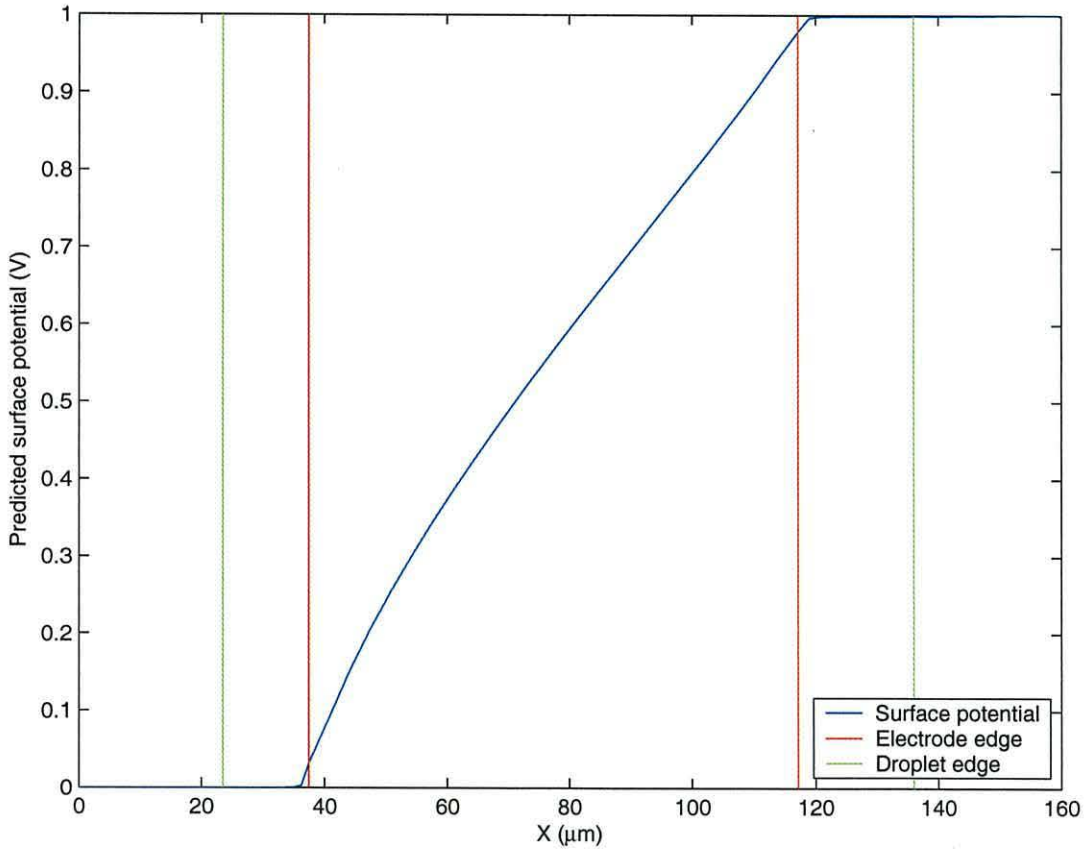


**Fig. 6.10:** Plot of predicted surface potential against distance along cross-section assuming $\sigma_{Al}$=$37\text{x}10^{6}\text{Sm}^{-1}$ and $\sigma_p$=$1\text{x}10^{-3}\text{Sm}^{-1}$.

There are three significant points which should be highlighted in figure 6.10; (i)

there is negligible potential dropped along the length of the aluminium electrodes, (ii) the significant potential drop is across the region of the polymer between the electrode edges and (iii) the potential drop across the polymer bridge is near-linear.

Given the 9 orders of magnitude difference between the conductivities of the aluminium and polymer the entire potential was expected to appear across the polymer in the inter-electrode gap as seen in the calculated results.

The near-linear potential drop from one electrode edge to the other was not expected as the cross-sectional area of the droplet between the electrodes varied by a factor of 2. However, the gradient of the potential drop is highest at the point of minimum cross-sectional area and lowest at the point of maximum cross-sectional area, as would be expected.

There is scope for further computer modelling of the potential gradients along the inkjet printed lines in figure 4.1. It would be possible to derive the resistance per unit length of the inkjetted lines and compare this with the volume of polymer deposited per unit length giving an indication of the current carrying efficiency of the different topologies of printed lines.

In order to investigate the effect of the conductivity of the polymer on the potential distribution across the sample, the conductivity of the polymer was changed to that of basic Baytron P while the conductivity of the aluminium electrodes remained unchanged. The conductivity of Baytron P was listed as $100Sm^{-1}$ in the Bayer data sheets. The model was re-solved and the potential distribution across the sample plotted. As expected, given the significant difference in the conductivities of the aluminium and polymer the change in the conductivity of the polymer had no effect, the results were indistinguishable from figure 6.10 where the conductivity was $1x10^{-3}Sm^{-1}$ (Baytron P CH8000).

As indicated above the conductivity of the electrodes was taken to be that for bulk aluminium. Figure 6.1 shows that the thickness of the electrodes was 20nm. At this thickness it is possible that the conductivity of the electrodes was less than that of bulk aluminium. The conductivity of the polymer was therefore changed back to that of Baytron P CH8000 and the conductivity of the aluminium reduced by 3 orders of magnitude from $37x10^{6}$ to $37x10^{3}Sm^{-1}$ and the model re-solved. The resulting potential distribution across the sample remained indistinguishable from that using the conductivity of bulk aluminium shown in figure 6.10. The conductivity of the aluminium was then reduced by 6 orders of magnitude from $37x10^{6}$ to $37Sm^{-1}$ and the model re-solved. This again had no effect on the

potential distribution across the sample. It can safely be assumed therefore that the conductivity of the aluminium electrode has no effect on the potential distribution.

### *6.5.2 Sample with interfacial layer*

A 20nm thick layer was inserted between the aluminium electrode and the polymer to investigate the possible effects of a low conductivity interfacial layer on the surface potential distribution. The thickness of the layer was chosen arbitrarily and only existed between the polymer and aluminium, not covering the entire surface of the electrode. The mesh for the left hand electrode is shown in figure 6.9, the right hand electrode is identical.

The original values for the conductivities of aluminium and Baytron P CH8000 were reinstated ($\sigma_{Al}$=37x10$^{6}$Sm$^{-1}$ and $\sigma_{p}$=1x10$^{-3}$Sm$^{-1}$) while the conductivity of the interfacial layer was varied between 1x10$^{-6}$ and 1x10$^{-9}$Sm$^{-1}$. The resulting surface potential plots are shown in figure 6.11.

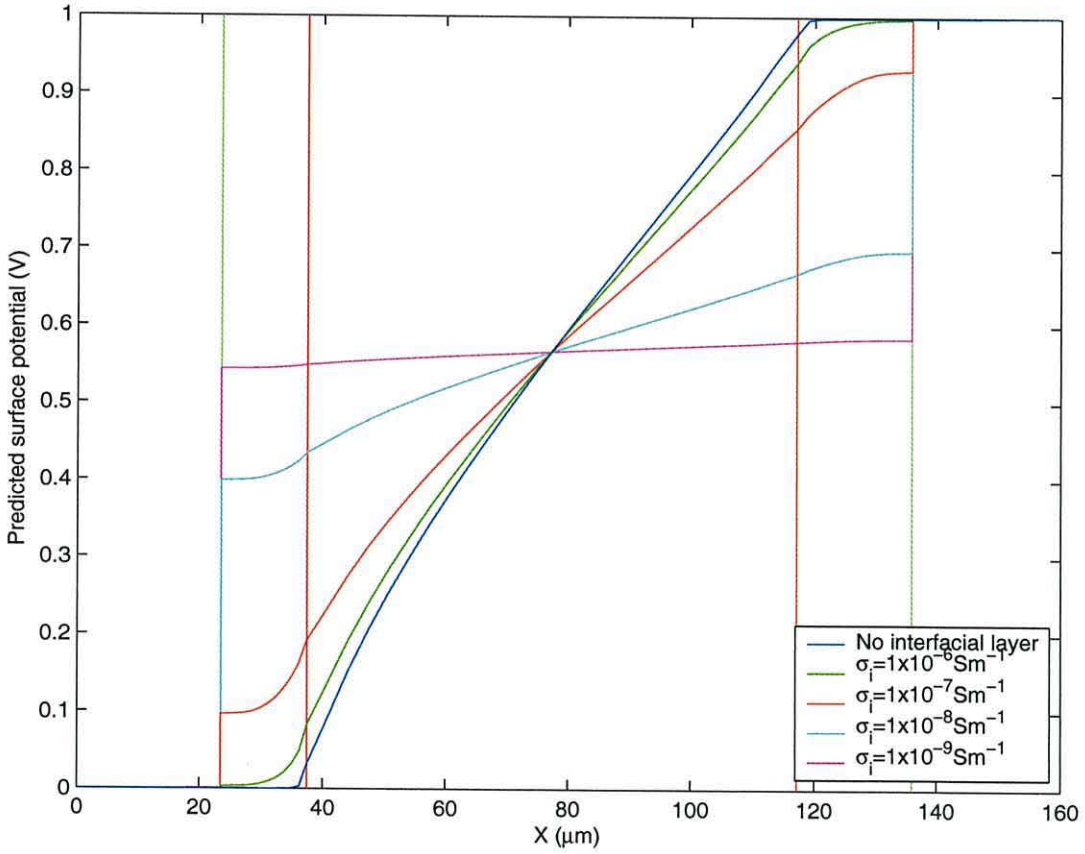


**Fig. 6.11:** Plot of predicted surface potential against distance along cross-section, showing the effect of an interfacial layer of varying conductivity.

With the inclusion of a low conductivity interfacial layer the potential dropped across the polymer between the electrodes decreases at the expense of the potential

dropped across the interfacial layer. Given the geometry of the sample the potential drops across the interfacial layers appear across a very narrow region in the surface potential plots. It is significant that the potential gradient appears not solely between the electrode edges but stretches from the outer boundary of the polymer deposit.

## *6.6 SKPM results*

### *6.6.1 Work function difference*

The SKPM utilises a conducting AFM tip to measure the surface potential of a sample using a variation on the Kelvin probe method. The original use of a Kelvin probe was to measure the contact potential or work function difference between two different materials [65]. When measuring the surface potential of a single material at zero bias with a SKPM, there will exist a potential difference between the material and the tip due to the work function difference between the material and the SKPM tip (unless they are of the same material).

If measuring the surface potential of a sample consisting of two materials, both at zero bias, then two different potential differences will appear between the tip and the two materials. This will result in a sample consisting of more than one material presenting regions of different surface potential even though there is zero bias applied to the sample.

Therefore when taking SKPM surface potential images of samples consisting of multiple materials, it is important to take a SKPM image of the sample with zero bias applied so as to determine the differing regions of work function.

A tapping mode AFM image was taken, with SKPM data taken on a second trace at a lift height of 500nm with both electrodes grounded. The AFM height image was identical to that shown in figures 6.2 and 6.3 so has not been repeated here. The surface potential image is shown in figure 6.12. Lighter colours indicate higher surface potential. A cross-section was taken from the data to provide a plot of surface potential distribution across the highest point of the polymer droplet from one electrode to the other and is indicated by the blue line.

The plot of surface potential distribution across the sample is shown in figure 6.13. The AFM height data was used to locate the boundaries of the main polymer droplet which were then marked on the plot with green lines.

**Fig. 6.12:** Image showing surface potential of sample with both electrodes grounded (image 150x150$\mu m$). The blue line indicates the path of the cross-section shown in figure 6.13.

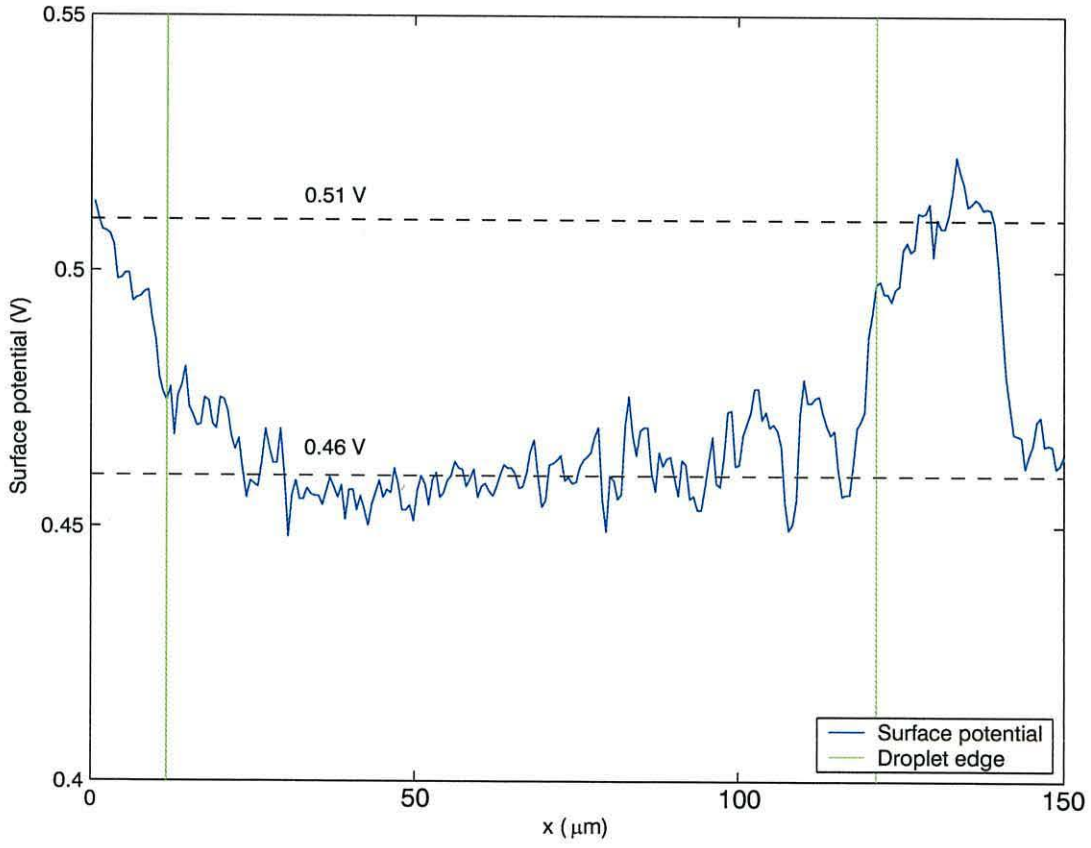


**Fig. 6.13:** Plot of surface potential against distance along cross-section for sample with both electrodes grounded.

The surface potential data shown in this section was saved such that an offset value was subtracted from the data set. As a result taking point potential readings from the data does not yield the true value of potential at that point instead allowing comparative measurements to be taken at different points on the surface.

Given that both electrodes were grounded, any differences in surface potential should be attributable to the difference in work function between the vacuum evaporated aluminium and the m:PEDOT:PSS. The cross-section in figure 6.13 shows two regions of aluminium and two regions of m:PEDOT:PSS. An average value for the surface potential of the polymer between the two green lines (the main polymer droplet) was measured as 0.46V and a value for the surface potential of the aluminium electrode was taken from the region to the right of the main droplet as 0.51V. Therefore the work function of m:PEDOT:PSS was found to be 0.05V higher than that of the aluminium.

The reported values of work function for aluminium and PEDOT:PSS vary by significantly more than 0.05V depending on measurement method, fabrication or storage conditions [75], therefore it is difficult to relate the potential difference seen in the SKPM image to those values found in the literature.

Given the data shown above, it should be possible to correct subsequent SKPM images by subtracting the zero bias SKPM image. However, it can be seen that the data shown in figure 6.12 does not present two distinct regions of differing work function corresponding to the polymer and aluminium. Therefore subtracting the raw data would introduce errors into subsequent data. This could be solved by using the image processing capabilities of Matlab to reduce the SKPM data (with zero bias applied to the sample) into regions of two distinct surface potentials, exactly 0.46V over the polymer and 0.51V over the aluminium.

It was decided not to use this method as it was difficult to determine the precise boundaries of the different materials. Instead the data was viewed more qualitatively than quantitatively and any corrections for work function were made when taking values at specific points in the image rather than over the image as a whole.

### *6.6.2 Potential distribution across sample*

The same measurements were then repeated with +5V applied to the right hand electrode while the left hand electrode remained grounded. The DC results in section 6.3 showed that the samples polarised on application of a potential

difference. Therefore a delay of 5 minutes was left between applying the potential and taking the SKPM measurement so as to ensure that the sample was in its steady state. The resulting surface potential image is shown in figure 6.14. The blue line indicates the path of a cross-section taken from one electrode to the other through the highest point of the droplet. The surface potential cross-section is shown in figure 6.15. The green lines indicate the edges of the main droplet while the red lines indicate the electrode edges.

**Fig. 6.14:** Image showing surface potential of sample with the left hand electrode grounded and the right hand electrode at +5V (image 150x150$\mu m$). The blue line indicates the path of the cross-section shown in figure 6.15.

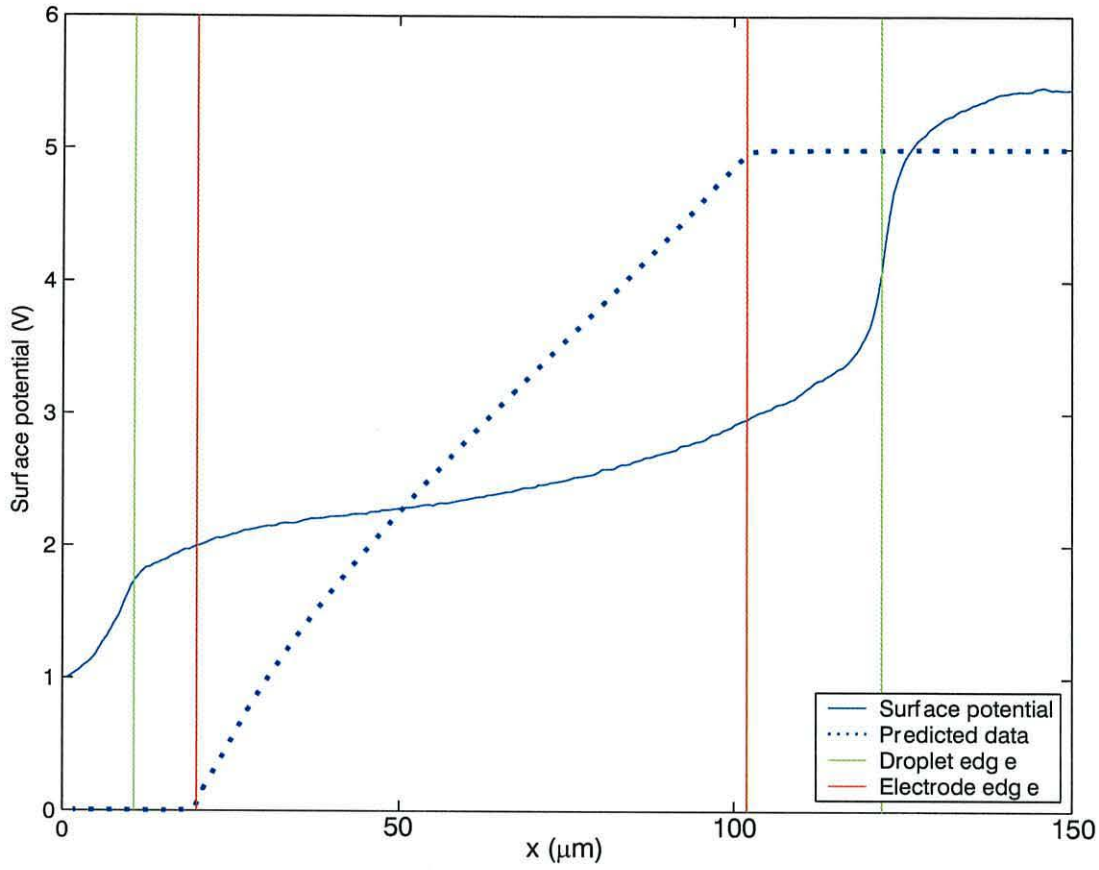


**Fig. 6.15:** Plot of surface potential against distance along the sample cross-section with the left hand electrode grounded and the right hand electrode at +5V.

Both electrodes were then grounded for 5 minutes then +5V applied to the left hand electrode while the right hand electrode remained grounded. In between taking the SKPM measurements the puck on which the sample was mounted was accidentally moved in the AFM. This explains the change in position of the droplet and electrodes in the SKPM data and plots, otherwise the surface potential profiles for the two potential orientations could be overlaid in direct comparison.

The resulting surface potential image is shown in figure 6.16. The blue line indicates the path of a cross-section taken from one electrode to the other through the highest point of the droplet. The surface potential cross-section is shown in figure 6.17. The green lines indicate the edges of the main droplet while the red lines indicate the electrode edges.

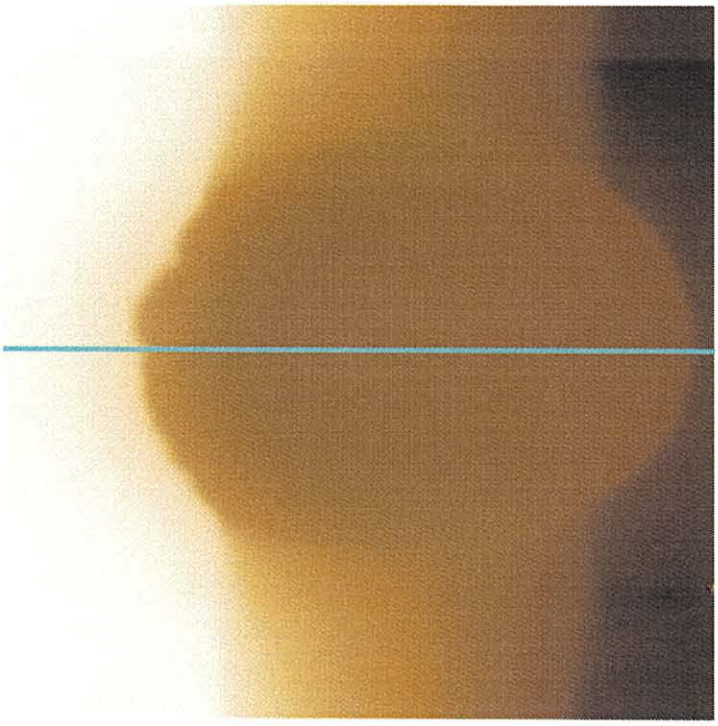

**Fig. 6.16:** Image showing surface potential of sample with the left hand electrode at +5V and the right hand electrode grounded (image 150x150$\mu m$). The blue line indicates the path of the cross-section shown in figure 6.17.

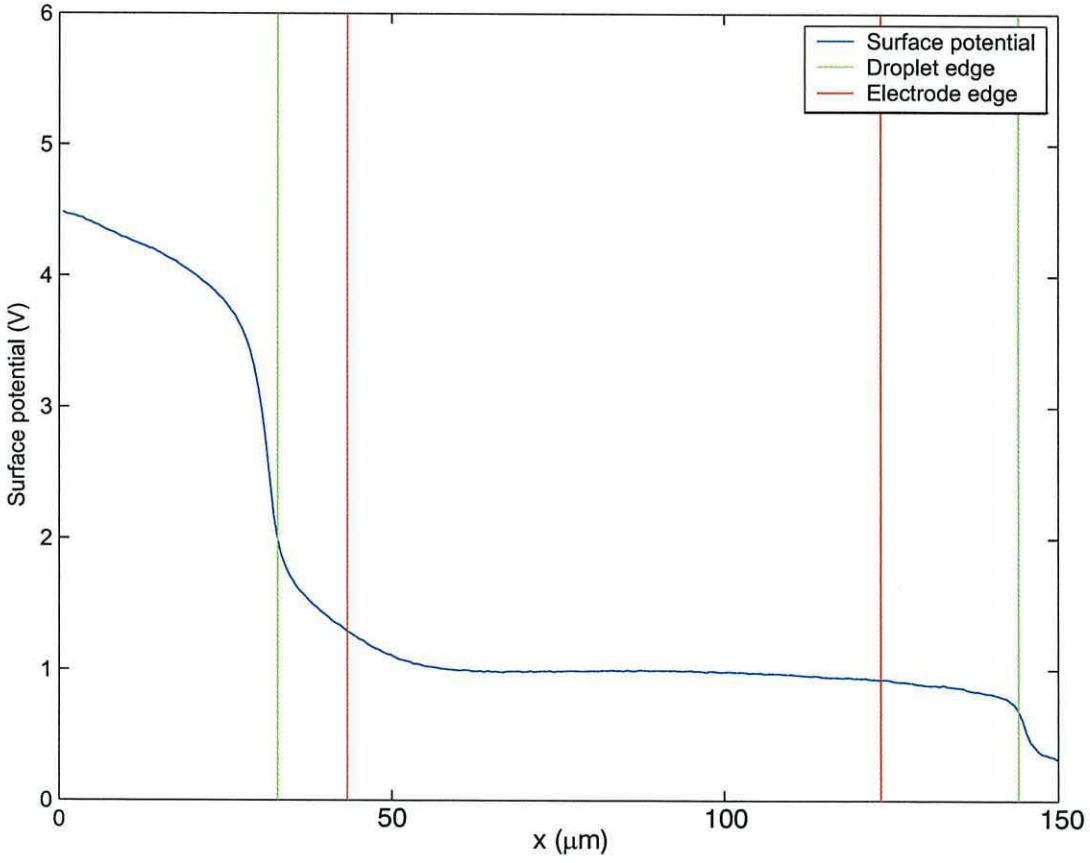


**Fig. 6.17:** Plot of surface potential against distance along cross-section for sample with the left hand electrode at +5V and the right hand electrode grounded.

Figures 6.15 and 6.17 show the potential distribution across the sample for the two bias polarities.

Given that the measured difference in work function between the m:PEDOT:PSS and vacuum evaporated aluminium was 0.05V while the overall potential drop across the sample was 5V, it was decided not to attempt to make any corrections to the data to account for work function difference.

The first thing that is apparent from the results is that the potential distribution across the sample does not conform to the near linear drop between the electrode edges predicted by the computer modelling (figure 6.10). Instead two significant potential steps appear, located at the edges of the polymer droplet (indicated by the green lines in the plots). Comparatively a greater potential is dropped across the electrode-polymer interfaces than is across the length of the conducting polymer between the electrodes. For both bias polarities the potential step at the anode is greater than that at the cathode.

Secondly it can be seen that the most significant potential drops occur not at the edges of the electrodes but at the outer boundary of the polymer deposit. This confirms that the potential drop occurs across the electrode-polymer interface rather than as a result of the change in conductivities of the electrode and polymer. This effect was illustrated in section 6.5.

The results shown above are comparable to the work by Burgi et.al. [66], Nichols et.al. [35] and Puntambekar et.al. [67] in which the injection properties of contacts to polymer films were examined using SKPM. In their work they fabricated field effect transistors using thin-film structures. They then examined the potential distributions across the FETs for different source-drain potentials and gate biases and showed the presence of potential drops at the source-drain electrodes due to charge transfer inefficiencies.

### *6.6.3 Time resolved SKPM*

Given the time dependence of the current in the I-t results shown in section 6.3 the time evolution of the surface potential distribution was then examined. In the previous section a delay of 5 minutes was allowed between the application/removal of the voltage to ensure the potential distribution could reach a steady state, as indicated by the I-t data.

In order to examine the time evolution of the surface potential across the sample

the SKPM tip was centered across the highest point of the droplet and the slow scan axis of the AFM disabled. This resulted in a time resolved surface potential plot from one electrode to the other across the highest point of the polymer droplet. The fast scan axis frequency then determined the repetition rate of the potential profiling.

A pulsed potential difference was applied to the sample using a Keithley 237 high voltage source-measure unit. Figure 6.18 shows the 5V pulse sequence applied to the right hand electrode (the left hand electrode remained grounded) and the period of time over which the SKPM data was captured. Each pulse lasted for 116s and the mark-space ratio was 1:1.

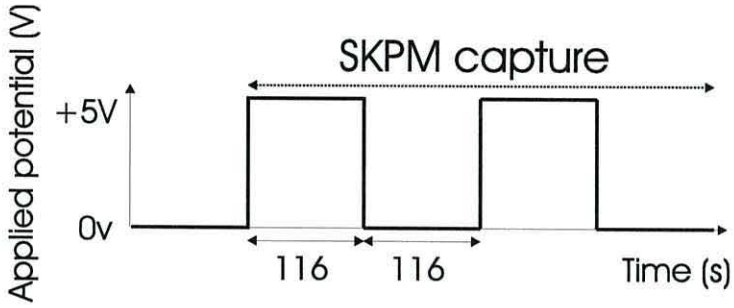


**Fig. 6.18:** Diagram showing applied potential with respect to time for the time resolved SKPM.

Figure 6.19 shows the surface potential image for the time resolved SKPM. The SKPM measurement settings remained unchanged with the exception that the slow scan axis was disabled and the fast scan axis frequency was 1Hz. Each line of the image represents the surface potential along the same height cross-section but at different times. The top of the image shows the first line scanned, successive lines show later times.

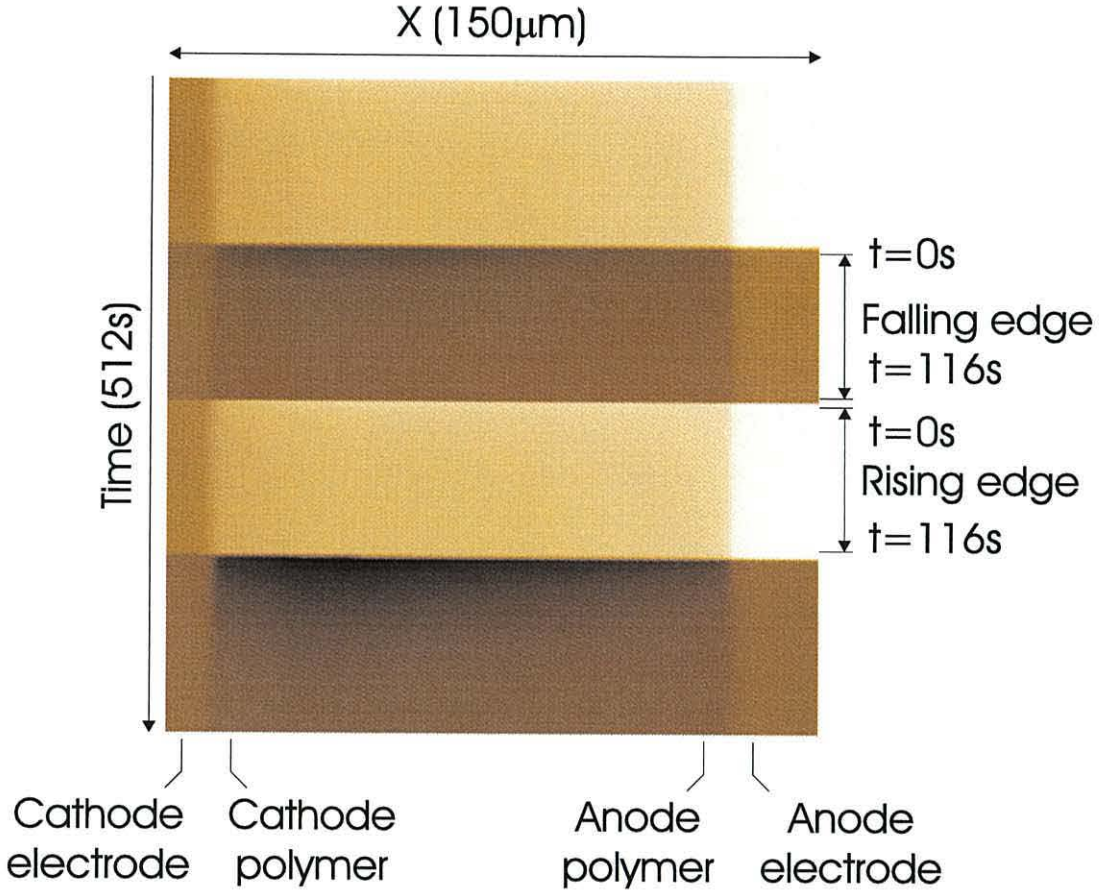


**Fig. 6.19:** Image showing time resolved surface potential of sample with the left hand electrode grounded and a pulsed potential applied to the right hand electrode (image 150$\mu m$x512s).

When collecting data the SKPM takes a topography scan followed by a surface potential scan. Each scan consists of a trace and a retrace with the data only presented for the trace. Therefore, while the fast scan axis frequency was 1Hz the topography scan required 1s to complete, with the trace data being recored in the first 0.5s and the surface potential scan requiring 1s to complete, with the trace data being recorded for the first 0.5s. Therefore each line of the SKPM image only took 0.5s to acquire but included a 1.5s delay between each line. As a result the SKPM line repetition period was 2s and as 256 lines were scanned the entire image required 512s to acquire.

One of the limitations of the slow measurement speed is that as each individual potential profile was being acquired, the actual potential distribution across the sample was changing. Therefore the horizontal surface potential profiles to not represent an entirely accurate depiction of the potential distribution across the sample. While it was possible to increase the fast scan axis frequency to 2Hz so as to reduce the time it took to acquire each individual line, this was limited by the ability of the SKPM to accurately track the surface of the sample. Some success

was had with scanning at 4Hz but the results showed some topographic break though as the tip was not following the surface of the sample at the exact lift height.

This to some extent was compounded by the high structures which the SKPM had to follow. It was found possible to set the gain controls of the SKPM to track accurately across the electrode area of the sample (which were in the order of 20-40nm high). Then when the SKPM tried to track across the inkjetted line (sometimes up to $1\mu m$ in height) the gain controls had to be adjusted again. Therefore the gain controls had to be adjusted to a compromise to allow accurate tracking across both height ranges.

The topography/surface potential and trace/retrace of the AFM/SKPM affects the labelling of the time resolved SKPM data and is seen in the next section. The first line after the application (or removal in the case of the falling edge profiles) of a potential is labelled as "t=0s". However as each potential line only requires 0.5s to capture but is separated by 1.5s, labelling the data as being that observed at 0s is incorrect as it may have occurred up to 1.5s after the application of the potential. Nevertheless this notation was used since it provided the best representation of the data.

#### *6.6.3.1 Cross-sections taken with respect to lateral position*

Two pairs of horizontal cross-sections were taken from the time resolved SKPM image. The cross-sections represented the surface potential with respect to horizontal distance across the sample, from one electrode to the other through the highest point of the droplet.

One pair was taken after the falling edge, the other after the rising edge. When acquiring the SKPM data, the captured image did not include the first rising edge (in figure 6.18) so the cross-sections were taken from the second one. The first falling edge was captured which is why the results for the falling edge precede the results for the rising edge. Each pair of cross-sections consisted of one taken immediately after the potential had changed and one 116s later.

The aim of this was to show the potential distribution across the sample at the instant the potential was applied (marked as t=0s), and then at some time after it had achieved steady state (t=116s). These are shown for the falling and rising edges in figure 6.20.

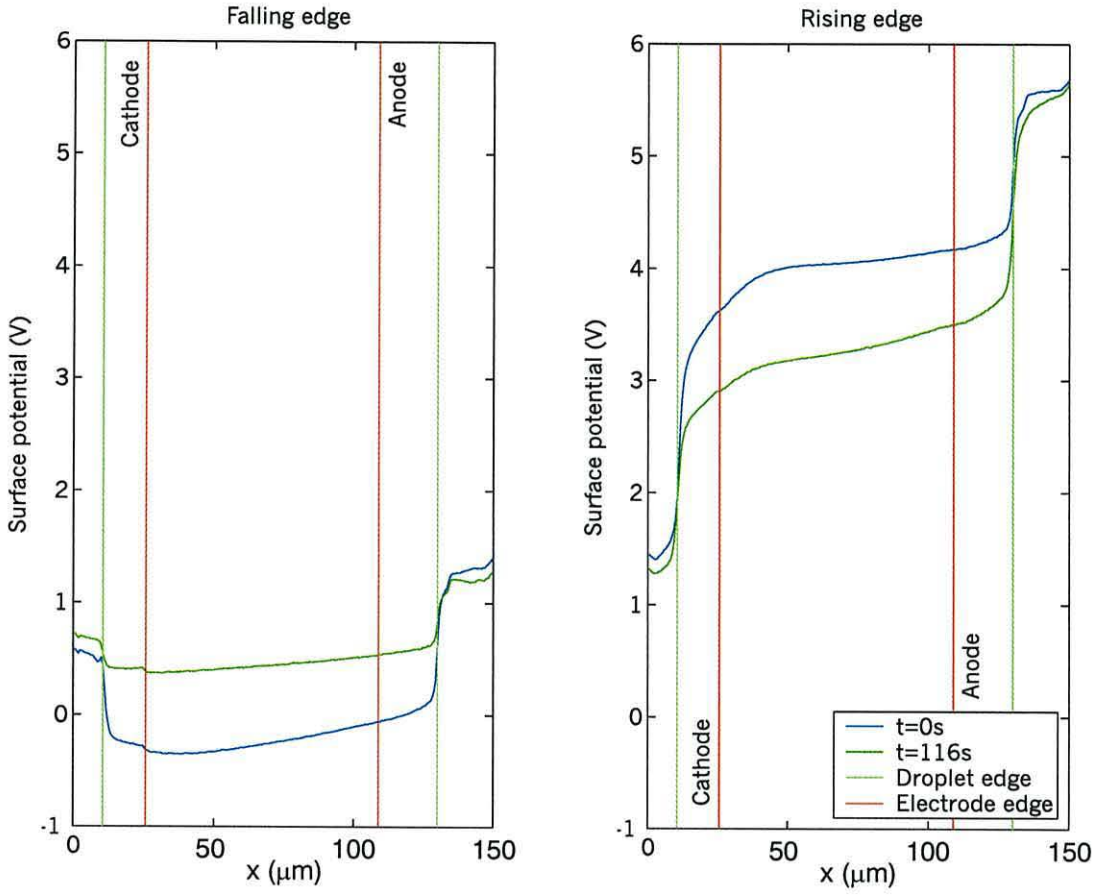


**Fig. 6.20:** Surface potential profiles of falling and rising edges obtained immediately after the voltage change (t=0s) and 116s later.

An analysis of the time resolved SKPM provides information as to the electronic and ionic process within the sample. As discussed earlier, the use of the SKPM is limited to a 2Hz scan rate. As a result the data acquired over times scales in the order of tens to hundreds of seconds.

The mobility, $\mu$, $(m^2V^{-1}s^{-1})$ of charge within a medium can be calculated using;

$$\mu = \frac{distance\ travelled}{transit\ time \times electric\ field} \tag{6.2}$$

As a rough approximation the initial electric field can be given by the identity: *applied potential* $\div$ *electrode separation*. The following equation can then be used to determine the transit time, t, of a charge between the electrodes;

$$t = \frac{d^2}{\mu \times V} \tag{6.3}$$

where d is the electrode separation and V the applied potential.

For a hole mobility, $\mu_h$, in PEDOT:PSS of $1x10^{-5}m^2V^{-1}s^{-1}$ [76] this gives a hole transit time of $1.28x10^{-4}$s. Therefore any effects due to the redistribution of

holes within the polymer will be too fast for the SKPM to capture. Ionic mobility is dependent on the type of ion and the medium through which it travels. No values for the mobility of different ions in PEDOT:PSS could be found, however typical values in the region of $1x10^{-10}$ to $1x10^{-15} m^2V^{-1}s^{-1}$ were found for the mobilities of ions in solids giving transit times of between 12.8 and $1.28x10^6$s [77]. Therefore these types of ionic processes are more likely to be seen using the SKPM. Interestingly, Moller et.al. found the electron mobility, $\mu_e$, of PEDOT to be $1.7x10^{-10} m^2V^{-1}s^{-1}$ which may indicate ions rather than electrons as the basis for that result [76].

An examination of the potential distribution across the sample immediately following the application of a potential to the sample (see figure 6.20, rising edge, t=0s) shows that large potential drops occur at both electrode-polymer interfaces, with the drop at the cathode larger than the drop at the anode. Given that this data was captured within the first 2s of the application of the potential the distortion to the potential distribution cannot be due to ionic accumulation at the electrodes.

The potential drops at the interfaces at early times are indicative of poor charge injection/extraction at the electrodes. In this case holes are being transported through the bulk of the polymer to the cathode more efficiently than they can be extracted across the interface into the cathode. At the anode holes are being injected more slowly than they can be transported away through the bulk of the polymer. As a result holes accumulate at the cathode creating an electric field which opposes the applied field producing the larger potential step at the cathode. Due to the mobility of holes in PEDOT:PSS this process will occur faster than can be captured by the SKPM so the time evolution of the holes cannot be viewed.

Following the application of the potential to the sample, positive and negative ions within the polymer will migrate under the electric field to the cathode and anode respectively even though that field has, to an extent, been collapsed by the accumulation of holes at the cathode. Unlike holes, the ions cannot be discharged at the electrodes and so accumulate there giving rise to further distortion of the potential across the sample.

The lower mobilities of ions in the polymer allow this process to be viewed using SKPM. The potential distribution across the sample following the ionic migration to the electrodes (see figure 6.20, rising edge, t=116s) show that while the majority of the potential dropped across the sample is still across the anodic and cathodic interfaces, the respective sizes of these drops has altered. The result be-

ing that the drop across the anode is slightly larger than the drop across the cathode.

As the ions migrate to the electrodes the electric fields they create will further distort the potential distribution across the sample. Their contribution to the potential distortion at the electrode interfaces will alter the charge injection properties of the electrodes. As a result the potential distribution across the sample will alter to that determined by the ionic accumulations rather than by charge transfer across the interfaces. As the ions accumulate at the interfaces the sample charges negatively as can be seen by the downward shift of the potential across the bulk of the polymer as time progresses (see figure 6.20, rising edge).

On removal of the applied potential the negative charge can be seen distributed across the sample (see figure 6.20, falling edge, t=0s). The accumulation of charge at the interfaces due to the interfacial charge transfer efficiencies (see figure 6.20, rising edge, t=0s) decay on a sub-second timescale so their effect on the potential distribution across the sample cannot be seen on the SKPM. However the negative charge accumulated as a result of the downward shift of the potential across the bulk of the polymer due to the movement of ions to the electrodes will decay as the ions migrate back into the bulk to assume an even distribution across the sample. The accumulation of negative charge indicates that some of the positive ions may have been lost.

Therefore two effects are seen which affect the potential distribution across the sample. The first fast one shows holes accumulating at the interfaces due to charge transfer inefficiencies and results in a distortion of the electric field across the sample. As a result of the higher mobility of holes these processes cannot be resolved on the timescale of the SKPM. The second slower effect shows the accumulation of ions at the electrodes under the influence of the applied electric field. This further distorts the potential distribution across the sample resulting in the accumulation of a net negative charge in the polymer.

These effects are further discussed in relation to the I-t results in chapter 8.

#### *6.6.3.2 Cross-sections taken with respect to time*

Four vertical cross-sections were also taken from the time resolved SKPM image. The cross-sections represented the surface potential with respect to time at specific locations in the sample; (i) on the aluminium cathode, (ii) on the polymer droplet over the cathode, (iii) on the polymer droplet over the anode and (iv) on the aluminium anode.

The four plots have been grouped into two pairs, one showing the electrode behaviour (i and iv) the other the behaviour of the polymer over the electrodes (ii and iii) and are shown in figure 6.21.

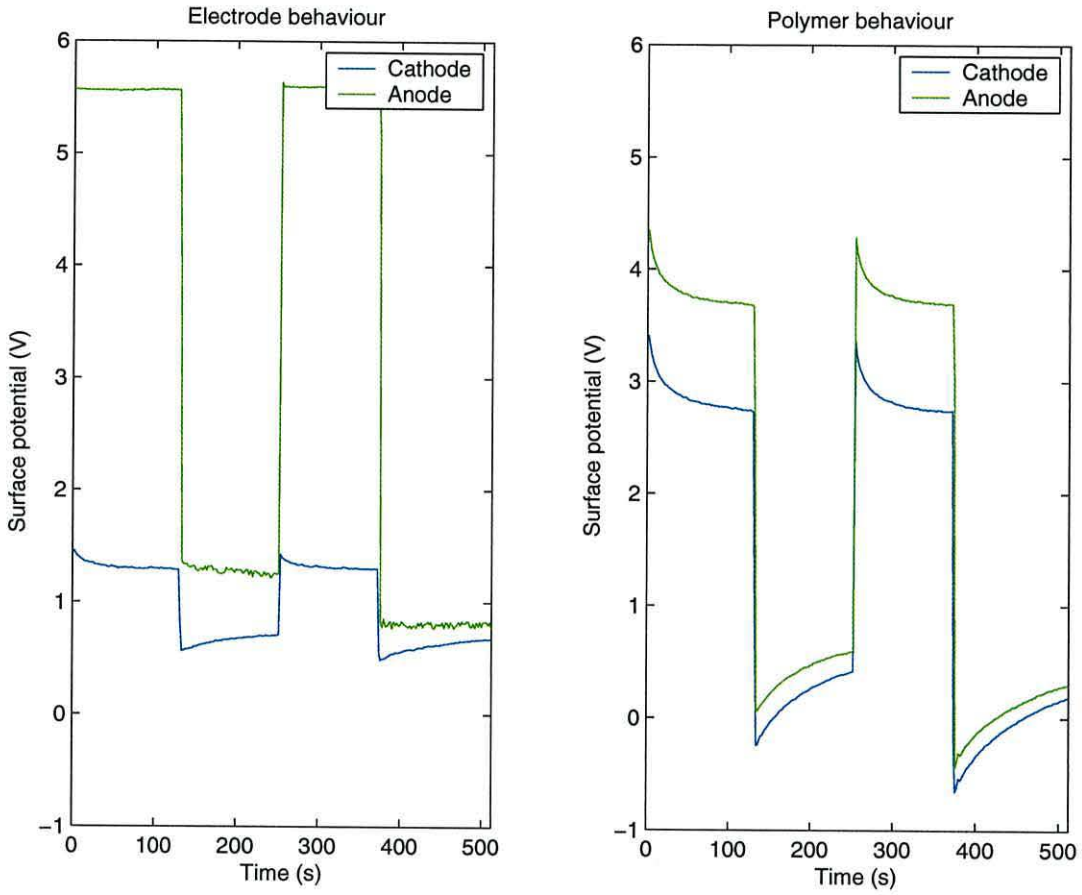


**Fig. 6.21:** Time evolution of the surface potential on the aluminium electrodes (i and iv) and on the polymer over the electrodes (ii and iii).

The cross-sections taken with respect to time provide an analysis of the time evolution of the surface potentials at different locations on the sample. The potentials on the anode and cathode (see figure 6.21, electrode behaviour) do not behave as would be expected. The potential on the cathode should remain at 0V while the potential on the anode should switch from 0V to +5V on application of the potential to the sample. The potential on the cathode should remain at 0V but shows an increase upon application of the potential, thus indicating a resistive element between the cathode electrode and the Keithley 237.

This can be explained by the presence of a current limiting resistor in the SKPM circuit. The purpose of this is to limit the current that might flow between the SKPM tip and the sample if the two were accidentally contacted while taking measurements and therefore damage the tip and/or sample. It can be seen that the potential on the cathode has charging/discharging transients similar to those in the

I-t plot of figure 6.5. This is explained by the fact that the limiting resistor has a constant resistance therefore the potential dropped across it will be proportional to the current flowing through it.

The time evolution of the surface potential of the polymer over the anode and cathode (see figure 6.21, polymer behaviour) confirms that seen in figure 6.20 but provides further detail of the potential transients. Most importantly it shows that the potential across the sample is always distorted so that minimal potential is dropped across the bulk even prior to the movement of ions to the electrodes. Therefore the charging/discharging transients seen in the I-t plot (figure 6.5) are not due to electrode polarisation depleting the field across the bulk of the sample but are more likely as a result of the ions moving through the polymer.

As mentioned above, the static SKPM results are similar to those shown by Burgi et.al. [66], Nichols et.al. [35] and Puntambekar et.al. [67]. However their work did not show the surface potentials time resolved as has been shown above. The ability to produce time resolved surface potential plots provides an extra means to analyse the processes underlying the potential drops seen at the electrode-polymer interfaces.

### *6.6.4 Additional SKPM work*

The previous SKPM experiments were then carried out on samples in which a continuous line was printed across the electrode gap (as in sample 2) in order to exclude the effects of contact area. These results included static and time resolved SKPM. This data confirmed the minimal influence of electrode-polymer contact area on the significant potential drops appearing at the interfaces.

## *6.7 Raman spectroscopy and optical images*

Raman spectroscopy provides a method for examining the structure and chemistry of molecules within a sample. The I-t and SKPM results indicate the movement of ions within the polymer and the accumulation of electronic charge at the interfaces. These effects can possibly alter the structure of the polymer, therefore it was decided to investigate the polymer using Raman spectroscopy.

The Raman spectroscope had a CCD camera coupled to it so optical images were captured at the same time as Raman spectra.

### *6.7.1 Experimental sequence*

Following the SKPM data collection on sample 1 it was at some stage exposed to higher potentials or current densities resulting in a permanent breakdown of the polymer as evidenced by higher than expected currents. In addition the polymer appeared darker than normal, especially at the electrodes. The conditions under which this occurred were not recorded therefore no comment can be made as to the nature of the breakdown phenomenon. As a result, Raman spectra were only taken from sample 2.

Sample 2 was placed on the substrate table of the Raman spectroscope and connected to the Keithley 237 high voltage source-measure unit. Optical images and Raman spectra were taken at different locations on the sample prior to passing current through the sample.

Initially 2pA was injected into the sample and optical images and Raman spectra taken while the sample was under bias. The current was then raised to 200pA and again, optical images and Raman spectra taken while under bias. The current was then removed and the sample left for 16 hours under laboratory conditions before taking a final set of optical images and Raman spectra.

Figure 6.22 shows the locations at which the different Raman spectra were taken. Listed below are the locations and their descriptions:

*a* On the polymer well onto the anode.

*b* On the polymer close to the anode edge.

*c* On the polymer in the middle of the electrode gap.

*d* On the polymer close to the cathode edge.

*e* On the polymer well onto the cathode.

*f* On a dark spot in the polymer close to the cathode edge.

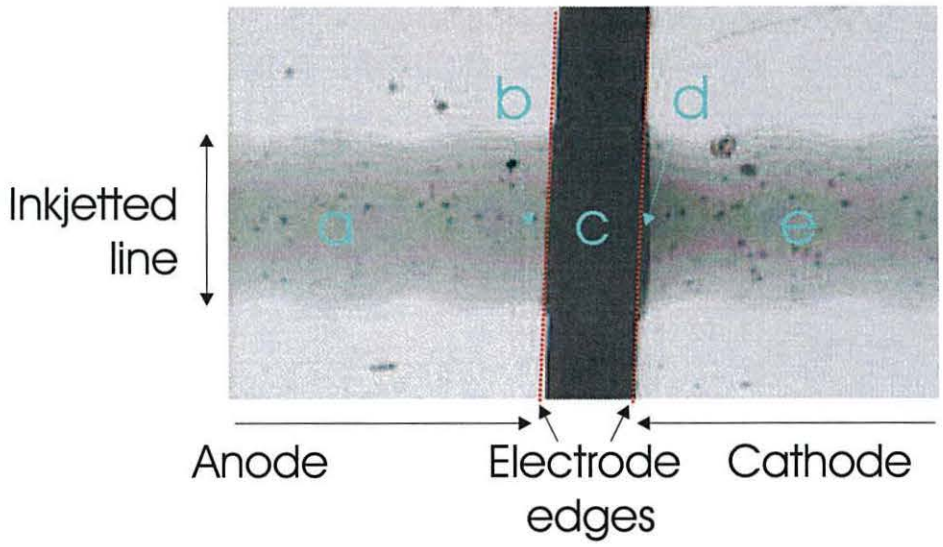


**Fig. 6.22:** Optical microscope image of sample identifying the locations at which Raman spectra were taken. The width of the image is approximately $350\mu m$ and the height approximately $200\mu m$.

As shall be described later, optical changes occurred in the polymer over the electrode close to the electrode edge. It is for this reason that Raman spectra were taken at two different locations on each electrode, one close to the electrode edge (within the region of change) and one further away from the electrode edge (greater than $50\mu m$ away).

### *6.7.2 Raman spectra and optical images taken prior to injecting current*

Figure 6.23 shows the Raman spectrum (10 accumulations of 10 seconds) of inkjet printed m:PEDOT:PSS on glass between two electrodes (location c, figure 6.22) prior to the application of an electric current. In this and all subsequent spectra the cosmic ray filter was on and a 50% filter used.

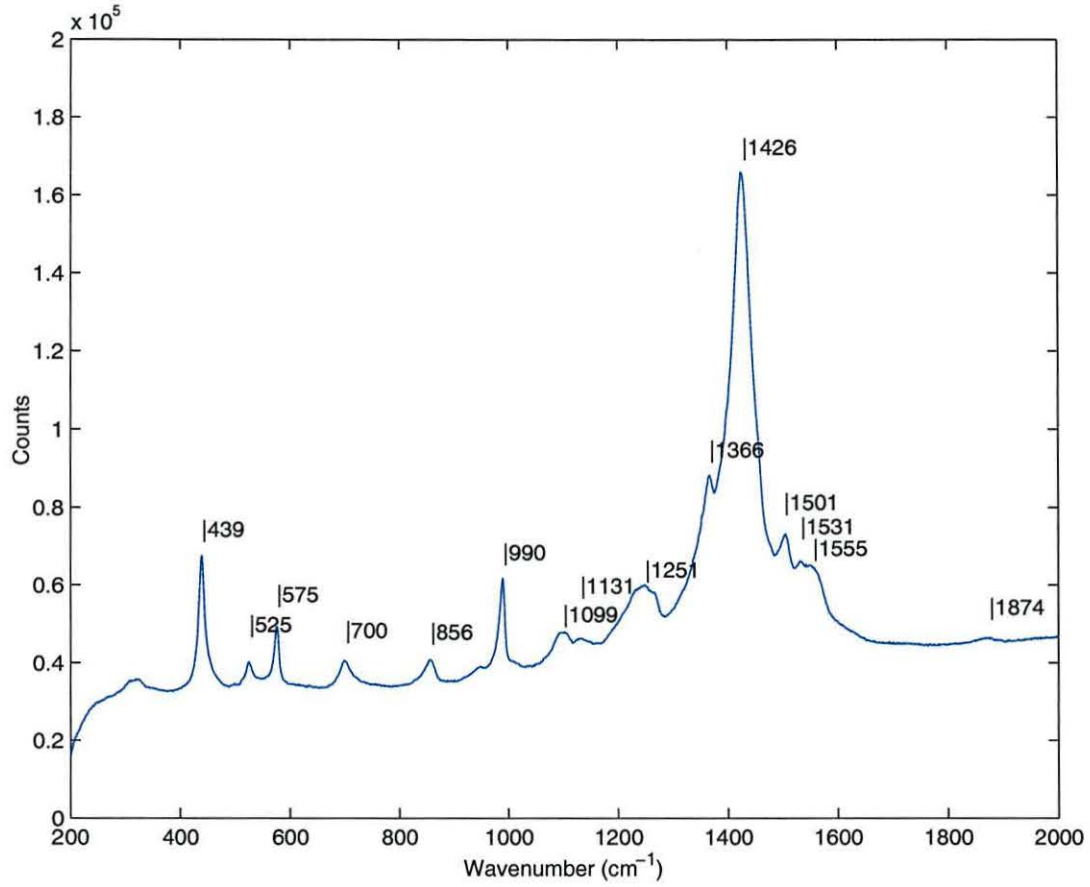


**Fig. 6.23:** Raman spectrum of inkjet printed m:PEDOT:PSS in the channel. The sample was not under electric bias nor had been prior to the collecting the spectrum.

The reader is referred to chapter 2, section 2.9 in which the effects of doping on the Raman spectra of PEDOT:PSS are discussed in full. Table 6.2 lists the bonds and the calculated vibrational assignments produced by Garreau et.al. [36] and compares the values to those found in figure 6.23. Figure 6.24 shows the chemical structure of PEDOT and the bonds referred to in table 6.2.

It can be seen that there is generally a good agreement between the peaks found by Garreau et.al. [36] and those found for the inkjetted m:PEDOT:PSS in this investigation.

| Calculated ($cm^{-1}$) | Experimental ($cm^{-1}$) | Assignment |
|---|---|---|
| 2931 | Off scale | $CH_2$ |
| 1509 | 1501 + 1531 + 1555 | asymmetric $C_\alpha$=$C_\beta$ stretch |
| 1444 | 1426 | symmetric $C_\alpha$=$C_\beta$ stretch |
| 1366 | 1366 | $C_\beta$-$C_\beta$ stretch |
| 1267 | 1251 | $C_\alpha$-$C'_\alpha$ (inter-ring) stretch |
| 1228 | 1251 | $C_\alpha$-$C'_\alpha$ (inter-ring) stretch + $C_\beta$-H bend |
| 1110 | 1131 | C-O-C deformation |
| 1061 | 1099 | C-O-C deformation |
| 988 | 990 | oxyethylene ring deformation |
| 964 | | oxyethylene ring deformation |
| 806 | 856 | oxyethylene ring deformation |
| 691 | 700 | symmetric C-S-C deformation |
| 577 | 575 | oxyethylene ring deformation |
| 486 | 525 | oxyethylene ring deformation |
| 440 | 439 | oxyethylene ring deformation |

**Tab. 6.2:** Vibrational assignments for PEDOT, calculated values are from Garreau et.al. [36] while the experimental values were obtained from figure 6.23, location c.

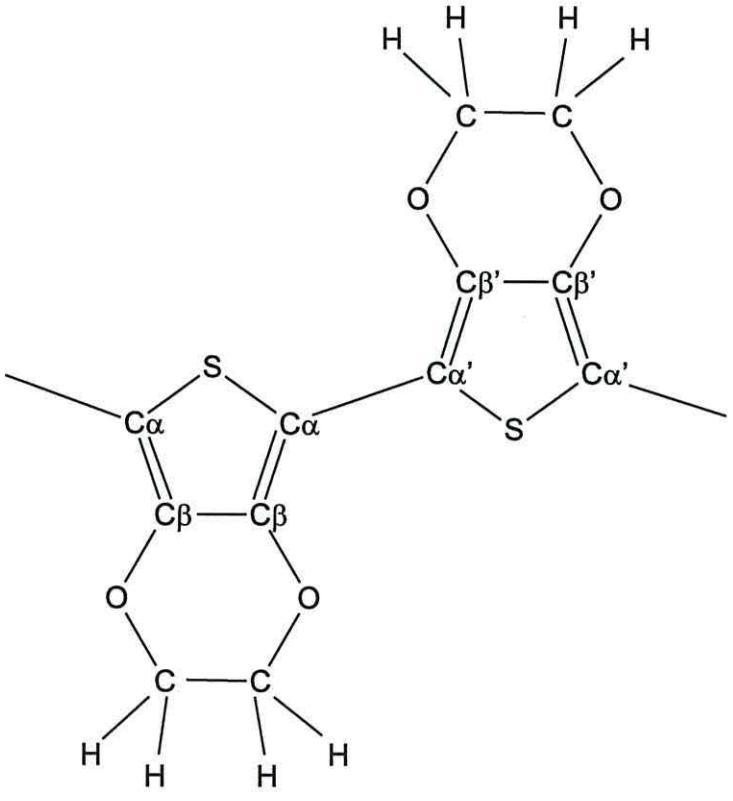


**Fig. 6.24:** Bond assignments.

A set of Raman spectra were taken (10 accumulation of 10 seconds) at the different locations on the sample as listed above and are shown in figure 6.25.

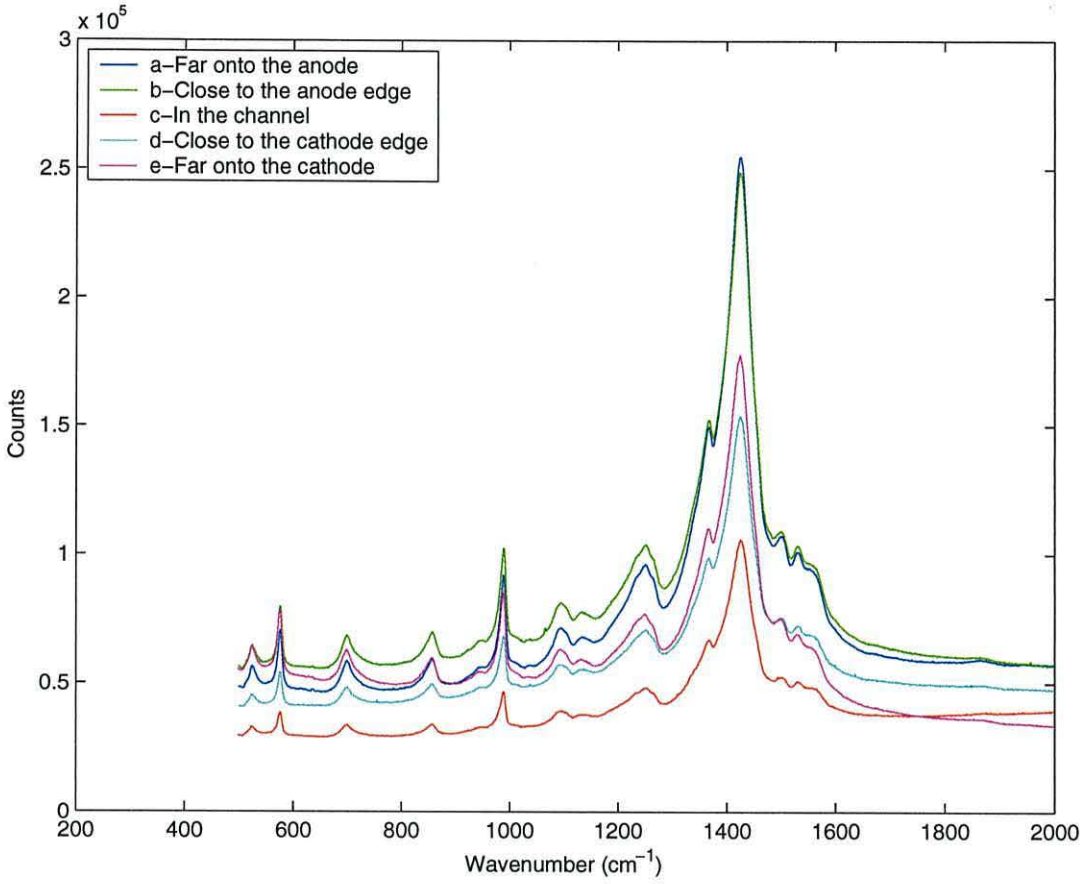


**Fig. 6.25:** Raman spectra of inkjet printed m:PEDOT:PSS at different locations on the sample. The sample was not under electric bias nor had been prior to the collection.

It can be seen that while there are differences in the individual spectra, the locations of the peaks remain constant irrespective of the acquisition location. The differences in baseline level and peak magnitudes is thought to be due to the focussing of the Raman spectroscope. The laser is focussed on the sample using an optical microscope. Initially the optical image is viewed and adjusted for a sharp image. The laser light is then coupled into the optical system and fine adjustment is made to the focus so as to minimise the size of the observable laser dot. Clearly this is a subjective process and the point at which the laser beam is focussed will have an effect on the captured spectrum.

A comparison of the spectra taken from the polymer on top of the aluminium electrode and on top of the glass shows no difference in the location of any of the peaks, indicating that the aluminium has no effect on the structure or doping of the polymer. However, any reactions between the aluminium and polymer are likely to take place at the interface and may form a very thin layer. The focussed collection

point of the Raman spectroscope forms a cube of side $4\mu m$. Therefore the spectral response from a layer possibly only in the region of tens of nanometers thick would be masked by the spectral response of the unaffected polymer in the rest of the measurement volume and would have little visible effect on the resultant spectrum.

Another factor which could vary the spectra is the effect of the focussed laser on the polymer. This could heat the polymer thereby affecting its chemical structure resulting in variations in the Raman spectra depending on the duration and degree of focus of laser illumination. Efforts were made to minimise this effect by exposing the polymer to as little focussed laser radiation as possible prior to capturing the spectra.

An optical image was then taken using the CCD camera coupled to the Raman spectroscope and a x20 microscope objective and has been shown previously in figure 6.4. The image shows the two aluminium electrodes separated by the channel and the inkjetted line of m:PEDOT:PSS crossing horizontally from one electrode to the other. The sample was top lit therefore the channel appears dark while the electrodes appear light. Small dark imperfections can be seen where the polymer lies on top of the aluminium. It is difficult to tell whether these are due to the polymer affecting the aluminium electrode or if it is an optical effect in which the clear polymer highlights the existing imperfections.

### *6.7.3 Effect of injecting 2pA into the sample*

A current of 2pA was then injected into the sample and optical images and Raman spectra obtained. Initially a potential drop of 0.7V was measured across the sample, increasing to 2.2V over the time taken to obtain the Raman spectra. No differences were observed in either the optical image or the Raman spectra between the zero current case and when 2pA was passing through the sample.

### *6.7.4 Effect of injecting 200pA into the sample*

The current was then increased to 200pA and optical images and Raman spectra obtained. Initially a potential drop of 22V was measured across the sample, increasing to 80V which was the maximum potential that could be dropped while 200pA was applied using the Keithley 237.

Although no change was observed in the optical image immediately after increasing the current to 200pA changes were observed later during the collection of the Raman spectra but were not recorded at the time.

Raman spectra (10 accumulation of 10 seconds) were taken at the different locations on the sample and are shown in figure 6.26. An artefact of the Raman spectrum capture software is that if the number of counts exceeds the range of the capture, it caps the data at that point. The effect of this can be seen on the main peak in the Raman spectrum taken at location b in figure 6.26.

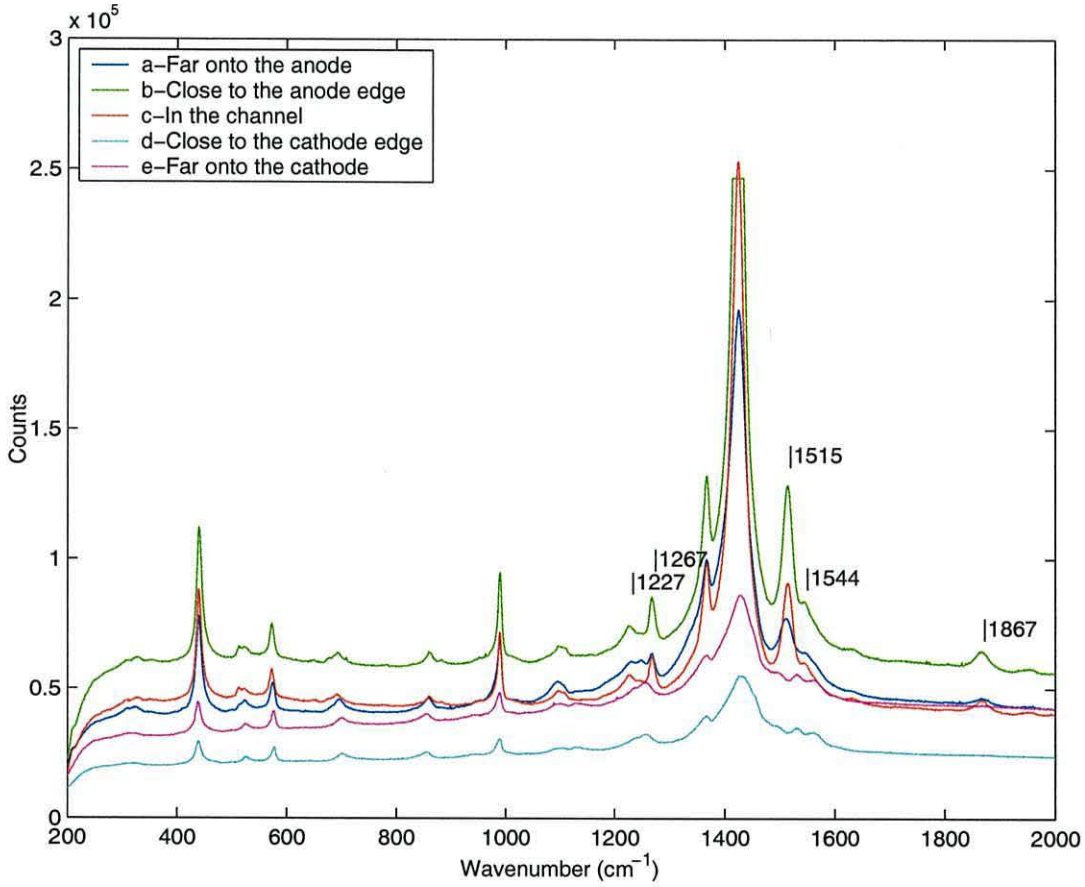


**Fig. 6.26:** Raman spectra of inkjet printed m:PEDOT:PSS at different locations on the sample. The sample was under an applied electric current of 200pA during the collection of the Raman spectra.

It can be seen that there is a significant difference in the Raman spectra of the sample when 200pA is passed through it, depending on the location at which the spectrum was taken. The Raman spectra taken on the cathode (locations d and e) showed:

i the main peak broadened and shifted up from 1426 to 1431cm$^{-1}$.

ii the peaks at 1501, 1531 and 1555$^{-1}$ showed no change.

The spectra taken on the anode and channel (locations a, b and c) showed 2 significant changes:

i the broad peak at 1251cm$^{-1}$ splits into three at 1227, 1251 and 1267cm$^{-1}$.

ii the three peaks at 1501, 1531 and 1555cm$^{-1}$ change to two peaks at 1515 and 1544cm$^{-1}$.

These effects shall be discussed in section 6.7.6.

### *6.7.5 Raman spectra and optical images after storing sample under zero electric bias for 16 hours under laboratory conditions*

The Keithley 237 was set to source zero current and the sample left under laboratory conditions for 16 hours before an optical image was taken, as shown in figure 6.27. The changes seen at the electrode edges in figure 6.27 were observed during the collection of the Raman spectra. The changes did not occur the instant 200pA was applied but were more gradual. It can be seen that in comparison to the image of the sample under zero bias (figure 6.4) the regions of polymer over the electrode but directly next to the electrode edges (locations b and d) appear considerably darker. The dark region on the cathode appears to be very narrow and has a distinct edge. The dark region on the anode is much wider and has a far more diffuse edge.

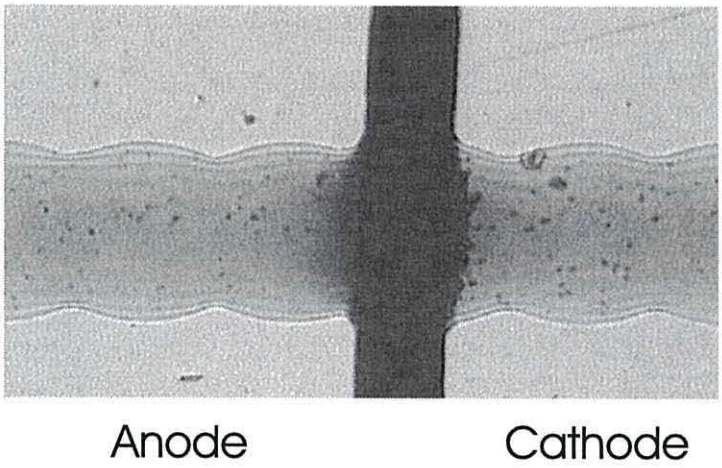


**Fig. 6.27:** Optical image of the sample taken under zero electric bias and after 16 hours under laboratory conditions. The width of the image is approximately 350$\mu m$ and the height approximately 200$\mu m$.

Raman spectra of the sample after being left under laboratory conditions for 16 hours returned to the same appearance as those taken of the virginal sample shown in figure 6.25. This evidence suggests that the changes in the Raman spectra are due to either the accumulation of ions which are seen to relax back into the bulk on removal of the potential, or charge transfer inefficiencies which will only be apparent under the applied potential.

The optical changes could be due to chemical changes in the polymer arising from the accumulation of the ions at the electrodes. Different ions would be attracted to the anode and cathode thereby reacting differently with the polymer and accounting for the different appearance of the anode and cathode. The optical changes are permanent while it would be expected that the accumulated ions would migrate back into the bulk of the polymer. As noted in section 6.3 the steady state current decreased with successive runs indicating that the polymer was degraded by the application of the electric field. The presence of the permanent optical changes could be related to the degradation of the sample. It is possible that under the application of the electric field a fraction of the accumulated ions at the interfaces reacted chemically with the polymer so as to dedope it slightly. On removal of the applied field the ions could remain chemically bonded to the polymer and not move back into the bulk. This would then result in the permanent optical changes seen and the decrease in the steady state currents. Additionally, the time resolved SKPM in figure 6.20 showed that the sample charged negatively indicating that the positive ions (or holes) were being lost. This is confirmed by the optical changes which occurred at the cathode, the location at which the positive ions accumulated.

Similar optical changes were seen by Rep et.al. [78] in which P3HT was spin coated across electrodes on glass and electrically stressed. Under, and following, the electrical stress, white patches appeared at the cathode. They attributed this to the migration of $Na^+$ ions from the glass substrate into the polymer where they were attracted by the electrical field to the cathode.

### *6.7.6 Comparison of Raman spectra*

The electrically induced changes in the Raman spectra shown in figure 6.26 occurred primarily in the wavenumber range, 1200 to 1600cm$^{-1}$. Figure 6.28 shows two plots over this wavenumber range for two different locations on the sample under a bias of 200pA. These plots show more clearly the changes induced by current.

Under the application of current the Raman spectra taken from the polymer showed one of two peak patterns. The polymer anywhere on the anode and in the channel showed one set of characteristic peaks while the polymer anywhere on the cathode showed another.

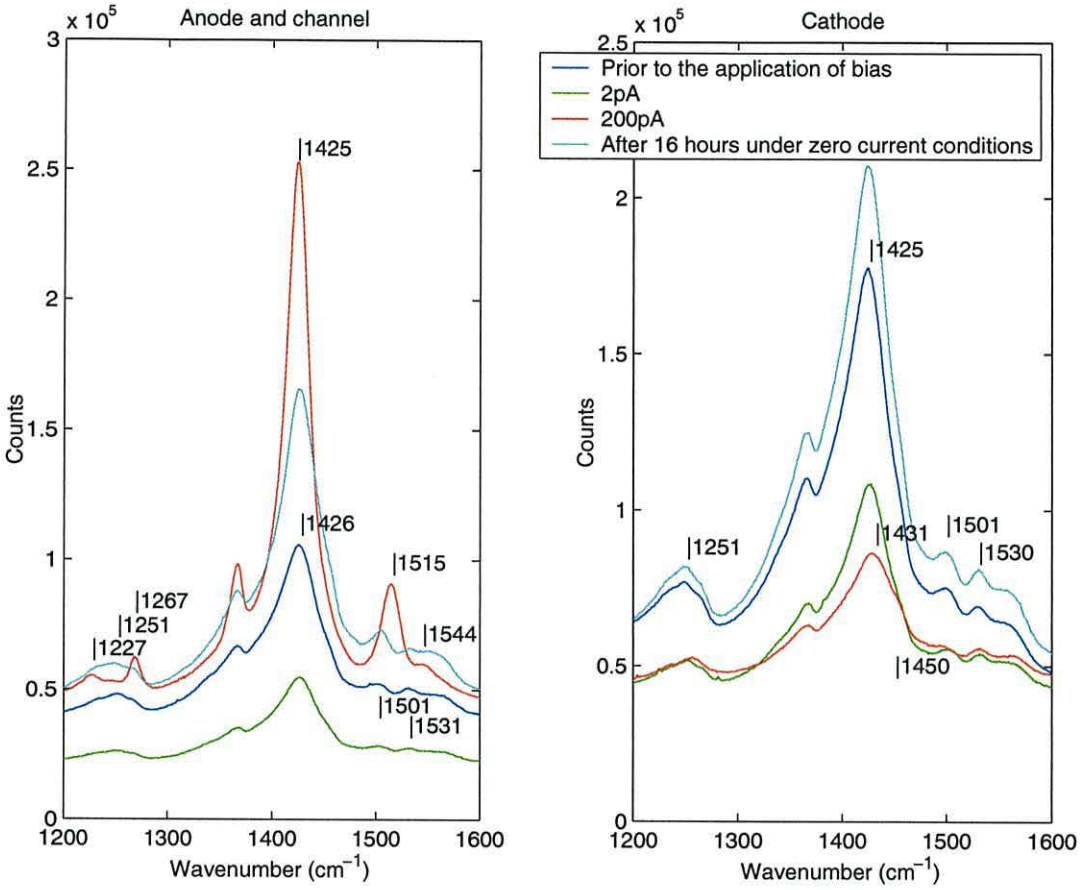


**Fig. 6.28:** Current induced changes in Raman spectra over the range 1200 to 1600cm$^{-1}$ for (i) the anode and channel and (ii) the cathode.

The work by Garreau et.al. [36][72][37] and Lapkowski and Pron [73] is based upon taking Raman spectra of PEDOT at different stages of doping within an electrochemical cell. The advantage of the electrochemical cell is that the amount of charge on the $\pi$ system of the polymer is governed by the potential between the electrode and electrolyte. Therefore the characteristic peaks of the Raman spectra can be related to the levels of charge on the $\pi$ system of PEDOT.

In one of their papers published in 2002 Garreau et.al. [72] presented Raman spectra of electrochemically doped PEDOT in an aqueous medium with an excitation wavelength of 676.4nm. The excitation wavelength is an important factor as the optical absorption spectra of PEDOT changes with doping therefore different excitation wavelengths will be resonant at different stages of doping. The excitation wavelength of 676.4nm was resonant primarily with the neutral form of the polymer, however was sufficiently resonant with the doped polymer that adequate spectra were produced throughout the doped states. The spectra presented in this thesis were taken with an excitation wavelength of 633nm. This should allow a comparison to be made between the data presented by Garreau et.al. at a wavelength of 676.4nm. Table 6.3 summarises their observations at an

excitation wavelength of 676.4nm. Similar observations and conclusions were found by Lapowski and Pron [73] so have not been listed.

| Bond assignment | Peak location ($cm^{-1}$) | |
|---|---|---|
| | Neutral polymer | Doped polymer |
| Asymmetric $C_\alpha$=$C_\beta$ stretch | 1515 | 1528 + 1568 |
| Symmetric $C_\alpha$=$C_\beta$ stretch | 1423 | 1423 + 1442 (broad) |
| $C_\beta$=$C_\beta$ stretch | 1366 | 1366 |
| $C_\alpha$-$C'_\alpha$ (inter-ring) stretch | 1222 + 1267 | 1262 (broad) |

**Tab. 6.3:** Summarised observations of Garreau et.al. [72] of electrochemically doped PEDOT and doping related bonds by Raman spectroscopy.

By comparing the observations in table 6.3 with the experimental data presented in figure 6.28 four observations can be made; (i) under zero bias the polymer at all locations exhibits the characteristic peaks of doped PEDOT, (ii) on application of 200pA to the sample the polymer at the anode and channel exhibits the characteristic peaks of neutral PEDOT, (iii) as the peaks in the spectra at the anode and channel change position to indicate the neutral polymer the magnitudes of the peaks increase, (iv) under the same conditions the polymer at the cathode shows no significant changes in the characteristic peaks although the primary peak at 1425$cm^{-1}$ shows a minor shift towards higher wavenumbers indicating even higher doping and (v) as the peaks in the spectra at the cathode change position to indicate the more doped polymer the magnitudes of the peaks decrease.

The inkjetted polymer, PEDOT:PSS is chemically doped by the PSS therefore it would be expected that the polymer under zero bias would produce spectra indicating that it was doped, as is seen.

The change in characteristic peak locations at the anode and channel under the application of 200pA and the increase in peak magnitudes is evidence for the polymer in these regions returning to its neutral form. In p-type doping of the polymer electrons are removed from the $\pi$ system introducing holes on to the chain. As the polymer becomes more neutral it shows that electrons are being added back into the $\pi$ system at the anode and channel.

Similarly, at the cathode, the slight shift of the primary peak to higher wavenumbers and the decrease in the peak magnitudes is evidence for the polymer becoming even more highly doped. This shows that even more electrons have been removed from (holes have been added to) the $\pi$ system at the cathode.

If the bulk polymer is able to transport holes injected by the anode more efficiently than the anode can inject them then the polymer at the anode will

have a lower than average hole concentration. Similarly, if the bulk polymer can transport holes to the cathode more efficiently than they can be extracted then the polymer at the cathode will have a higher than average hole concentration. The result of this is that space charges accumulate at the electrodes distorting the potential distribution across the sample. This confirms the data seen in the time resolved SKPM which, prior to the migration of ions, shows large potential drops at the electrodes (see figure 6.20, rising edge, t=0s).

## *6.8 EDX results*

The synthesis of Baytron P can leave a residual sodium ($Na^+$) and sulphate ($SO_4^{2-}$) content in the polymer solution (see section 3.4.5). This could be a possible source of mobile ionic charges within PEDOT:PSS. It is also possible that sodium can diffuse from glass into the polymer [78].

Four different samples of PEDOT:PSS were examined using EDX and are listed with their storage conditions in table 6.4. As described in section 3.4.5 PEDOT:PSS can be obtained from Bayer AG in different forms. The basic form is Baytron P, most commonly used as an anti-static coating. "Electronic grade" PEDOT:PSS is obtainable as Baytron P AI4083 and Baytron P CH8000. These variants are designed for use in electronic devices such as OLEDs and have lower conductivities (to reduce cross-talk in matrix devices), lower particulate content and size and lower ion content.

| Sample | PEDOT:PSS grade | Storage conditions |
|---|---|---|
| 1 | Baytron P | High Density Polyethylene (HDPE) bottle |
| 2 | m:Baytron P (CH8000) | Brown glass bottle |
| 3 | m:Baytron P (CH8000) | Brown glass bottle then glass vial |
| 4 | m:Baytron P (CH8000) | HDPE bottle |

**Tab. 6.4:** PEDOT:PSS samples and storage conditions.

A small amount of each of the four PEDOT:PSS samples was placed on the surface of adhesive carbon tape stuck to an SEM puck. The puck was then loaded into the chamber of the Oxford Instruments Isis 3 and exposed to 14KeV electrons for 30s while the resulting X-ray spectrum was captured using a Multi Channel Analyser (MCA). EDX was used to examine the possible ion content of the PEDOT:PSS by examining the emission of X-rays with wavelengths/energies characteristic of carbon, oxygen, sodium and sulphur. Table 6.5 lists the X-ray energy ranges corresponding to carbon, oxygen, sodium and sulphur.

| Element | Range (KeV) |
|---|---|
| Carbon | 0.188 - 0.368 |
| Oxygen | 0.428 - 0.627 |
| Sodium | 1.928 - 1.148 |
| Sulphur | 2.188 - 2.428 |

**Tab. 6.5:** X-ray energy ranges for selected elements.

Figure 6.29 shows the EDX spectrum for Baytron P which had been supplied and stored in a HDPE bottle. The energy bands corresponding to each of the four elements listed in table 6.5 have been marked on the spectrum in red.

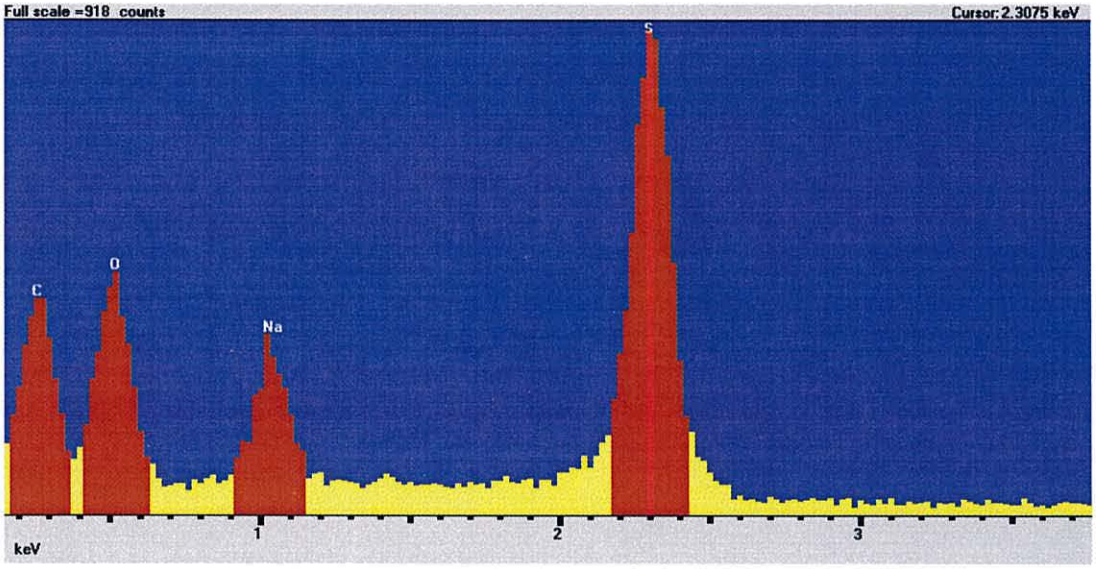


**Fig. 6.29:** EDX spectrum for Sample 1, Baytron P stored in a HDPE bottle.

In addition to the spectral peaks due to the interband transitions, the deceleration of the primary electrons produces a background radiation known as *white radiation* or *Bremsstrahlung radiation*. This is shown in yellow on figure 6.29. The analysis of the spectrum produces a count of the number of electron-hole pairs generated in the energy band for each element. From this a number of counts due to the white radiation is subtracted resulting in the net number of counts due to each specific element. These are listed in table 6.6 for each of the four samples.

| Sample | Carbon | Oxygen | Sodium | Sulphur |
|---|---|---|---|---|
| 1: Baytron P (HDPE) | 1271 | 1645 | 1044 | 4523 |
| 2: CH8000 (brown glass bottle) | 1895 | 2440 | 1158 | 7269 |
| 3: CH8000 (brown glass and vial) | 2213 | 2600 | 1276 | 8486 |
| 4: CH8000 (HDPE) | 1805 | 2159 | 581 | 6949 |

**Tab. 6.6:** Net number of counts for each of the four elements for the four different PEDOT:PSS samples.

The net number of counts for each element in a sample were then totalled and each element calculated as a percentage of the total for the four elements selected. These are shown in table 6.7.

| Sample | % Carbon | % Oxygen | % Sodium | % Sulphur |
|---|---|---|---|---|
| 1: Baytron P (HDPE) | 15.0 | 19.4 | 12.3 | 53.3 |
| 2: CH8000 (brown glass bottle) | 14.8 | 19.1 | 9.1 | 57.0 |
| 3: CH8000 (brown glass and vial) | 15.2 | 17.8 | 8.8 | 58.2 |
| 4: CH8000 (HDPE) | 15.7 | 18.8 | 5.1 | 60.5 |

**Tab. 6.7:** Elements in different samples.

The two ions noted in the Bayer information as likely to be present in PEDOT:PSS are sodium ($Na^+$) and sulphate ($SO_4^{2-}$). PEDOT:PSS contains sulphur and oxygen within the PEDOT chain therefore it is difficult to quantify the effect of the sulphate ions on the EDX spectra as some contribution to the sulphur and oxygen counts in the EDX data will be due to those from the PEDOT while some will be due to the sulphate ions. Sodium, on the other hand, is not present in PEDOT:PSS therefore the sodium counts in the EDX data will be entirely as a result of contaminant sodium which can be attributed to ions.

It can be seen that the sodium content of the standard grade Baytron P is higher than that of Baytron P CH8000 regardless of the container it was kept in. This is to be expected as the CH8000 variant was supposed to have a lower ion content (see section 3.4.5).

The analysis shows that the sodium content of the CH8000 depends on storage conditions. The CH8000 kept in the brown bottle or in the brown bottle then glass vial show similar sodium content while the same variant of PEDOT:PSS kept in a HDPE container had a distinctly lower sodium content. The implication of this is that sodium can diffuse out of the glass container in which the polymer is kept into the solution. The sodium content of the CH8000 that had been in contact with the glass bottle was approaching that of the standard grade PEDOT:PSS, Baytron P.

The results presented here showed the sodium content of PEDOT:PSS in its solid state, where the sodium content was assumed to have diffused into the solution in its liquid state while stored in glass containers. Rep et.al. [78] showed that sodium diffused out of (sodium rich) glass into P3HT under the application of an electric bias in similar structures to those used in the work present here. This is clearly a different experimental situation to that presented for the EDX results, however similar conclusions can be drawn; specifically that sodium is present in the inkjetted m:PEDOT:PSS, that contact with glass in its liquid state can increase the

sodium content of the PEDOT:PSS and that under the application of an electric field this sodium will migrate within the sample to the cathode.

## *6.9 Concluding summary*

This chapter provides details of the inkjet printing of m:PEDOT:PSS across an insulating gap between thermally evaporated aluminium electrodes. A potential step was applied to the samples and the I-t response measured which showed charging/discharging transients. AFM was used to investigate the topography of the printed structures and their cross-sectional area which together with the current data provided estimates for the conductivity of the polymer.

Due to the complex three dimensional geometries of the inketted polymer it was difficult to predict the expected surface potential distribution across the sample. The AFM data was used as the basis for computer modelling so as to provide a comparison for SKPM data. Modifications were made to the models to incorporate interfacial layers and to investigate the effects of these on the surface potential plots.

SKPM was used to provide images of surface potential across the inkjetted bridge between the electrodes. Significant potential drops were seen at the outer boundaries of the polymer bridge with the larger drop appearing at the anode. The slow scan axis of the SKPM was then disabled allowing time resolved SKPM data to be collected. The SKPM tip was traced from one electrode to the other over the center of the polymer bridge at a frequency of 1Hz. From this it could be seen that two electrode polarisation effects, one fast and one slow, were in action. The first was attributed to poor hole injection/extraction at the interfaces resulting in the accumulation of holes at the cathode. Due to the high mobility of holes the potential distortion due to the space charge accumulation occurred prior to the capture of the first line of SKPM data. The second, slower process was attributed to the migration of ions from the bulk of the polymer to the electrodes. As a result of this, further distortion of the potential distribution across the sample occurred and due to the lower mobility of ions in comparison to holes this process could be viewed in the time resolved SKPM plots.

To further the investigation of the charge distribution within the polymer Raman spectroscopy was used to investigate possible structural changes. Work by Garreau et.al. [72] and Lapowski and Pron [73] provided Raman spectra at different stages of doping as determined by electrochemical methods. By relating the changes seen in their spectra to the changes seen in the spectra presented in this work it was possible to identify a dedoping of the polymer at the anode and in

the channel and a possible increase in doping at the cathode. This confirming the conclusions drawn from the SKPM data.

Finally EDX analysis was used to show that even the low ion content PEDOT:PSS (Baytron P CH8000) had a sodium content and that this was increased by contact with glass when in solution. Therefore this confirmed the presence of at least sodium in the polymer as the basis for sodium ions ($Na^+$) which could migrate under the applied fields.

# 7. RESULTS ON ITO ELECTRODES

## *7.1 Introduction*

It was seen in chapter 6 that the aluminium proved an inefficient injector/extractor of charge into PEDOT:PSS. ITO is a well known hole injecting contact for polymers including PEDOT:PSS [24] so the aluminium electrodes were replaced with ITO to provide comparison.

The electrodes were patterned on glass pre-coated with ITO by photolithography and etched using hydro-bromic acid. The electrode separation was measured as $74\pm2\mu m$. The inkjetted lines were fabricated using the same method and parameters as previously.

In order to remove the effects of contact resistance the same structure as used in sample 2 in chapter 6 was adopted for all measurements. DC, AFM, SKPM and Raman analysis were all performed on the samples.

## *7.2 Sample fabrication*

Figures 7.1 and 7.2 show 2D and 3D Tapping mode AFM images of the inkjet printed line crossing between the two ITO electrodes. The AFM data was flattened using a 2nd order fit based on the exposed glass substrate and a spot cleaner was used to remove excessively large spikes in the image due to extraneous particles. Additionally a line cleaner was used to remove bad scan lines. The listed thickness of the ITO was 150nm and measured as 146nm by cross-sectional analysis of the AFM data. As was expected from the results in chapter 4 the m:PEDOT:PSS formed a continuous printed line of droplets from one electrode to the other.

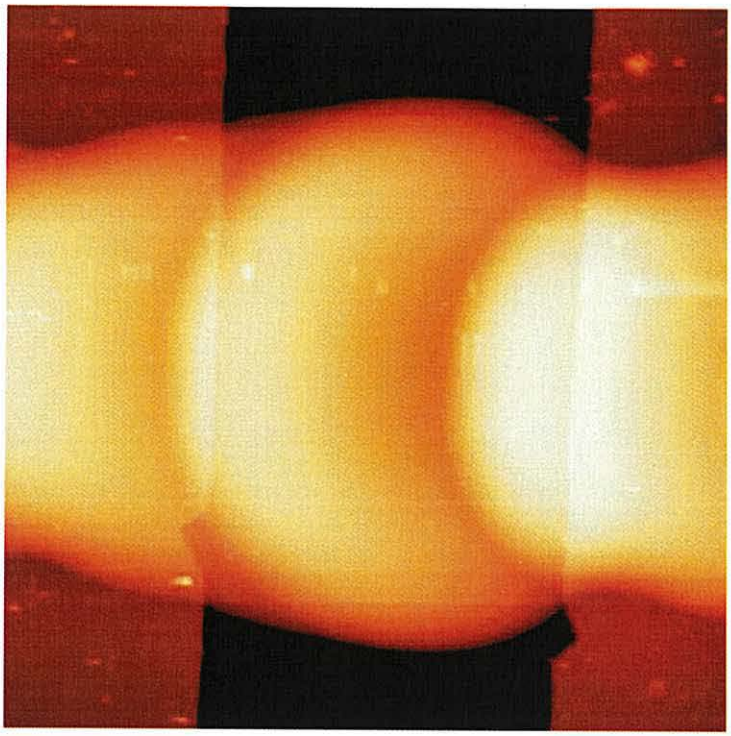

**Fig. 7.1:** 2D AFM image of inkjet printed m:PEDOT:PSS bridging two ITO electrodes.

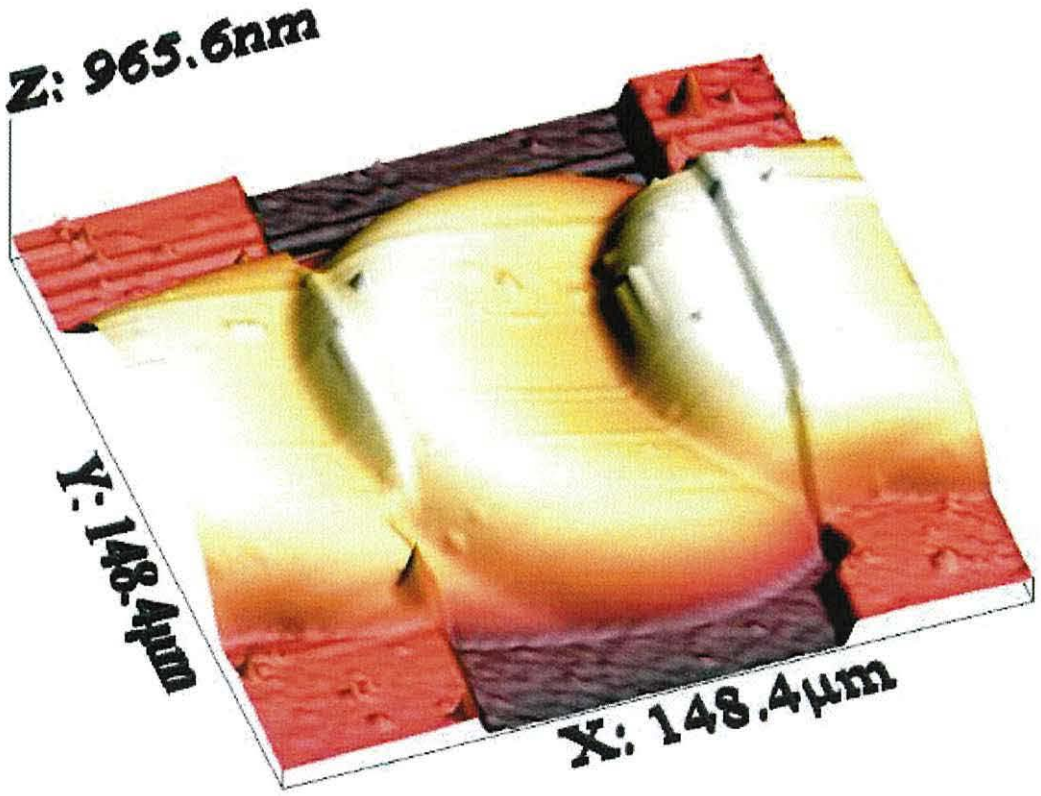


**Fig. 7.2:** 3D AFM image of inkjet printed m:PEDOT:PSS bridging two ITO electrodes.

## 7.3 DC results

The Keithley 237 was used to apply a potential step of 5V to a sample while measuring the current over time. The resulting I-t plot for ITO showed similar current transients as seen with the aluminium samples. The steady state current was measured as $1.5\text{x}10^{-9}$A. Using this value, the resistance of the sample was calculated using Ohms law to be $3.34\text{x}10^{9}\Omega$.

## 7.4 Cross-sectional analysis

Cross-sectional analysis of electrode-polymer-electrode structures was performed on the AFM data shown in figures 7.1 and 7.2 and the results shown in figure 7.3. The edges of the electrodes have been marked on the plot by lines and the point of least cross-sectional area between the electrodes by an X.

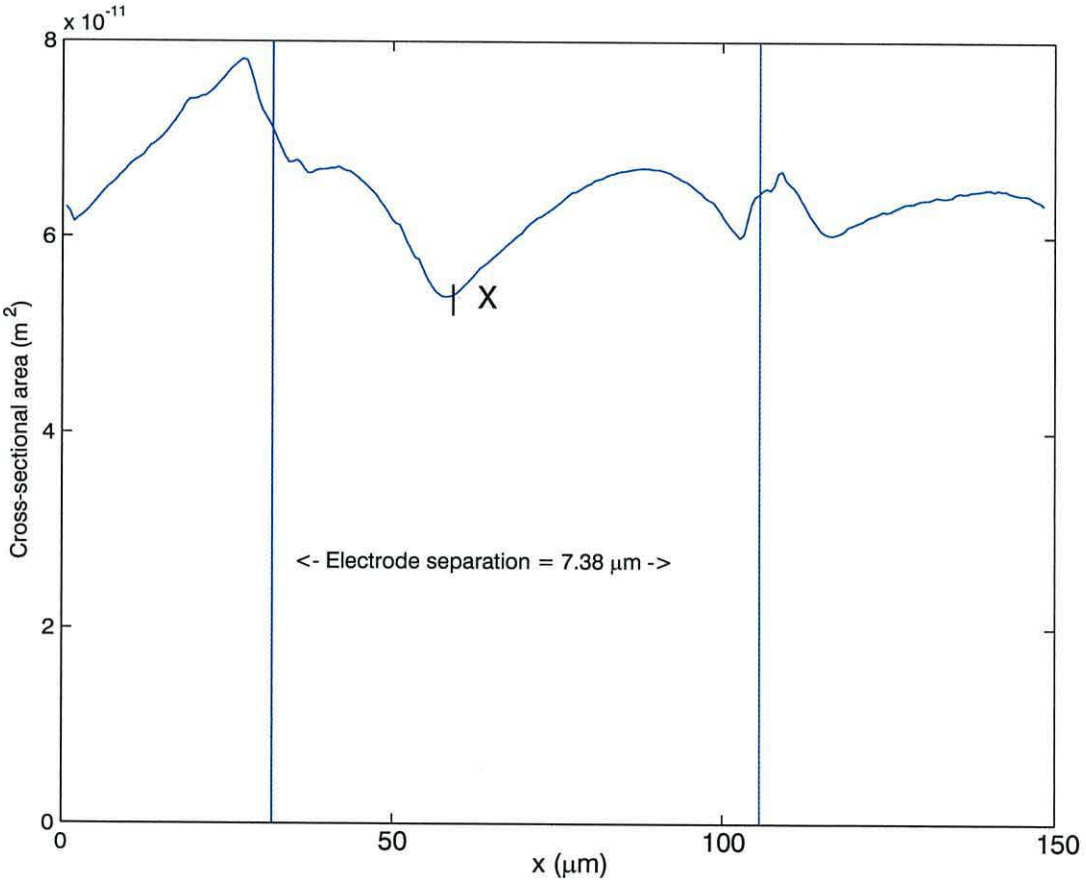


**Fig. 7.3:** Plot of cross-sectional area against distance along the length of the polymer bridge.

The minimum cross-sectional area was derived from figure 7.3 as $5.39\text{x}10^{-11}\text{m}^2$ and the electrode separation as $7.4\text{x}10^{-5}$m. Given the measured resistance of

$3.34x10^9\Omega$ in section 7.3 the resistivity of the polymer was calculated to be 2.40K$\Omega$m using the same method as in chapter 6. The Bayer data sheets list the resistivity of Baytron P as 0.01$\Omega$m and Baytron P CH8000 as 1K$\Omega$m while when aluminium electrodes were used it was measured as 262K$\Omega$m. The calculated value of the conductivity of the m:PEDOT:PSS is close to that listed in the Bayer data sheets indicating good charge transfer between the polymer and ITO, as would be expected from the literature [24].

## *7.5 SKPM results*

### *7.5.1 Work function difference*

A tapping mode AFM image was taken, with SKPM data taken on the retrace at a lift height of 200nm with both electrodes grounded. The AFM height image was identical to that shown in figures 7.1 and 7.2 so has not been repeated here. The surface potential image is shown in figure 7.4 with the blue line indicating the path of the cross-section shown in figure 7.5, the green lines indicating the boundaries of the polymer droplet.

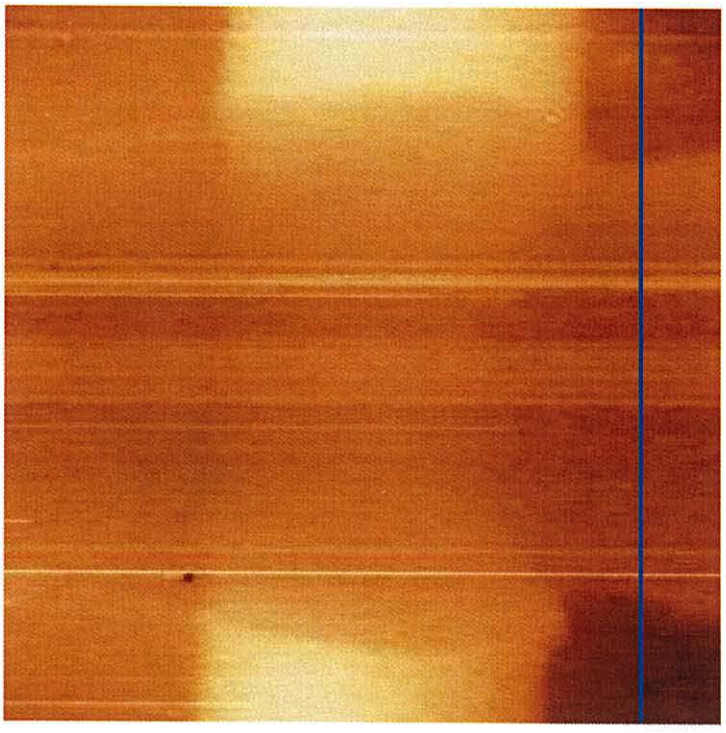

**Fig. 7.4:** Image showing surface potential of sample with both electrodes grounded (image 150x150$\mu m$). The blue line indicates the path of the cross-section shown in figure 7.5.

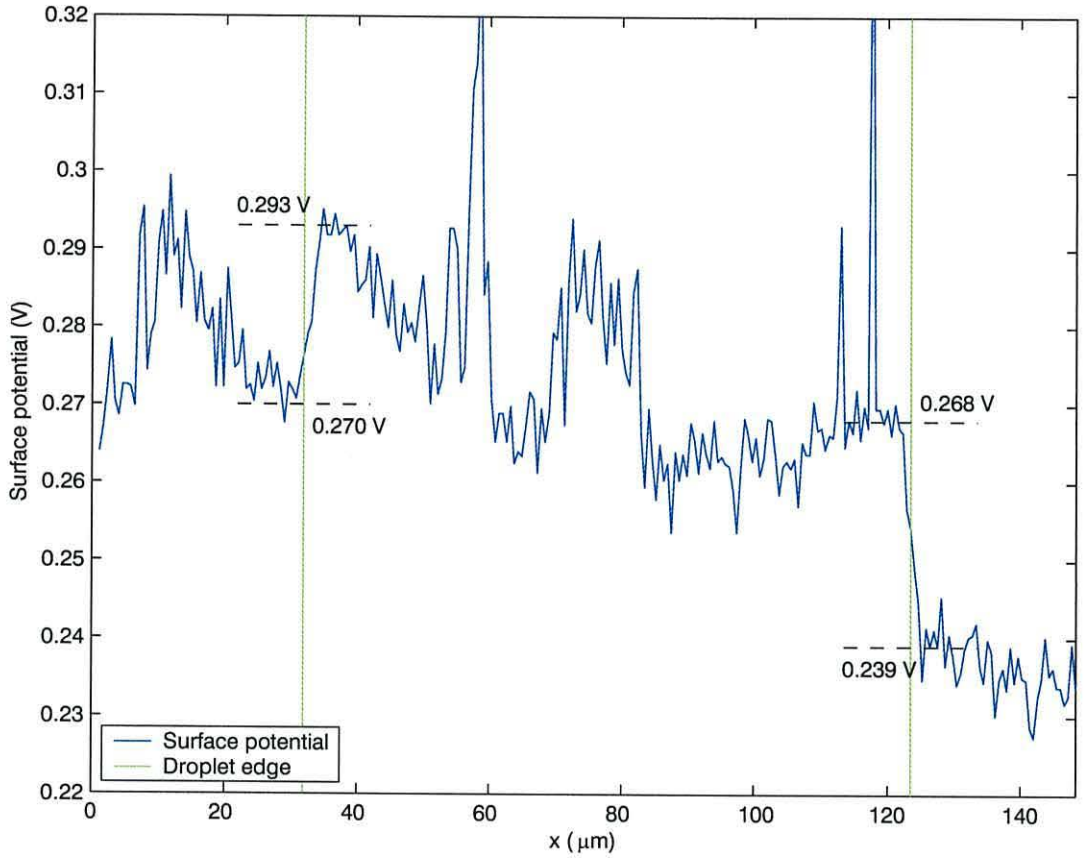


**Fig. 7.5:** Plot of surface potential against distance along cross-section for sample with both electrodes grounded.

The plot of surface potential in figure 7.5 does not show two level areas corresponding to the work function of ITO and to the work function of m:PEDOT:PSS. However two distinct steps can be seen at each polymer edge so the height of these steps was used to give a value for the work function of m:PEDOT:PSS being between 0.023V or 0.029V lower than ITO.

As with aluminium electrodes, the work function of ITO can vary considerably and by more than the 0.023 to 0.029V difference shown. Therefore it is difficult to make comparisons between the measured work function difference and the literature. Of note though is that the potential on the aluminium electrodes was lower than that of the polymer while the potential on the ITO electrodes is higher than that of the polymer.

This confirms that which would be expected from the theory of the Schottky barrier (see section 2.6.1), when a metal and semiconductor are contacted the case where $\Phi_M > \Phi_S$ an ohmic contact is formed between the two, as is the case with the ITO electrodes.

### *7.5.2 Potential distribution across the sample*

The same measurements were then repeated with +1V applied to the right hand electrode while the left hand electrode remained grounded. A delay of 5 minutes between applying the potential and taking the SKPM measurement was allowed so as to ensure that the sample was in its steady state. The resulting surface potential image is shown in figure 7.6 with the blue line indicating the path of the cross-section shown in figure 7.7, the green lines indicating the boundaries of the polymer droplet and the red lines indicating the electrode edges.

It can be seen from figure 7.6 that the cross-sectional path is not straight from one electrode to the other, but follows three connected paths. This allows the cross-section to show the potential of each electrode as well as the polymer line.

The SKPM image shows a scan line, probably due to a dust particle, three quarters of the way down the image. This can be seen in the surface potential plot as small peaks just inside the droplet edge boundary (green line) however it does not cause too much concern regarding the accuracy of the SKPM data.

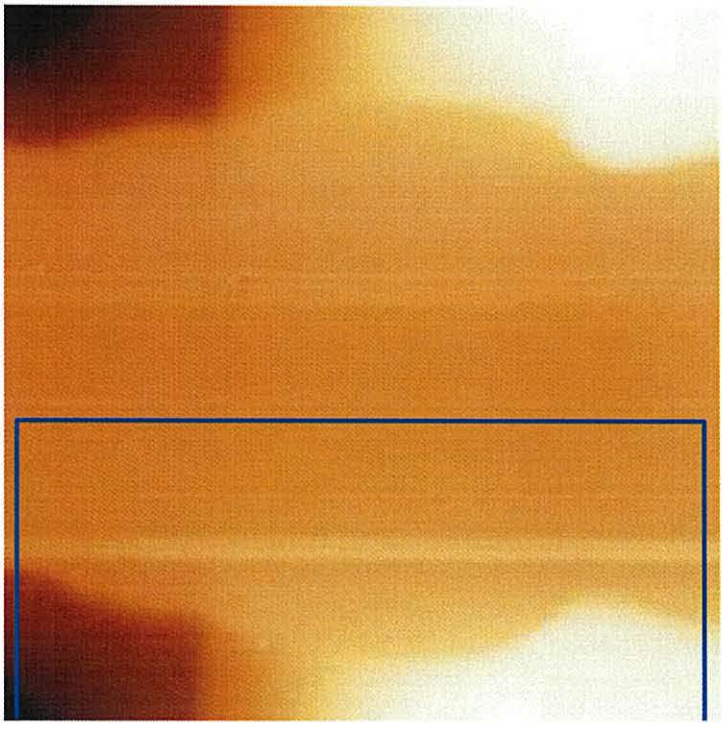

**Fig. 7.6:** Image showing surface potential of sample with the left hand electrode grounded and the right hand electrode at +1V (image 150x150$\mu m$). The blue line indicates the path of the cross-section shown in figure 7.7.

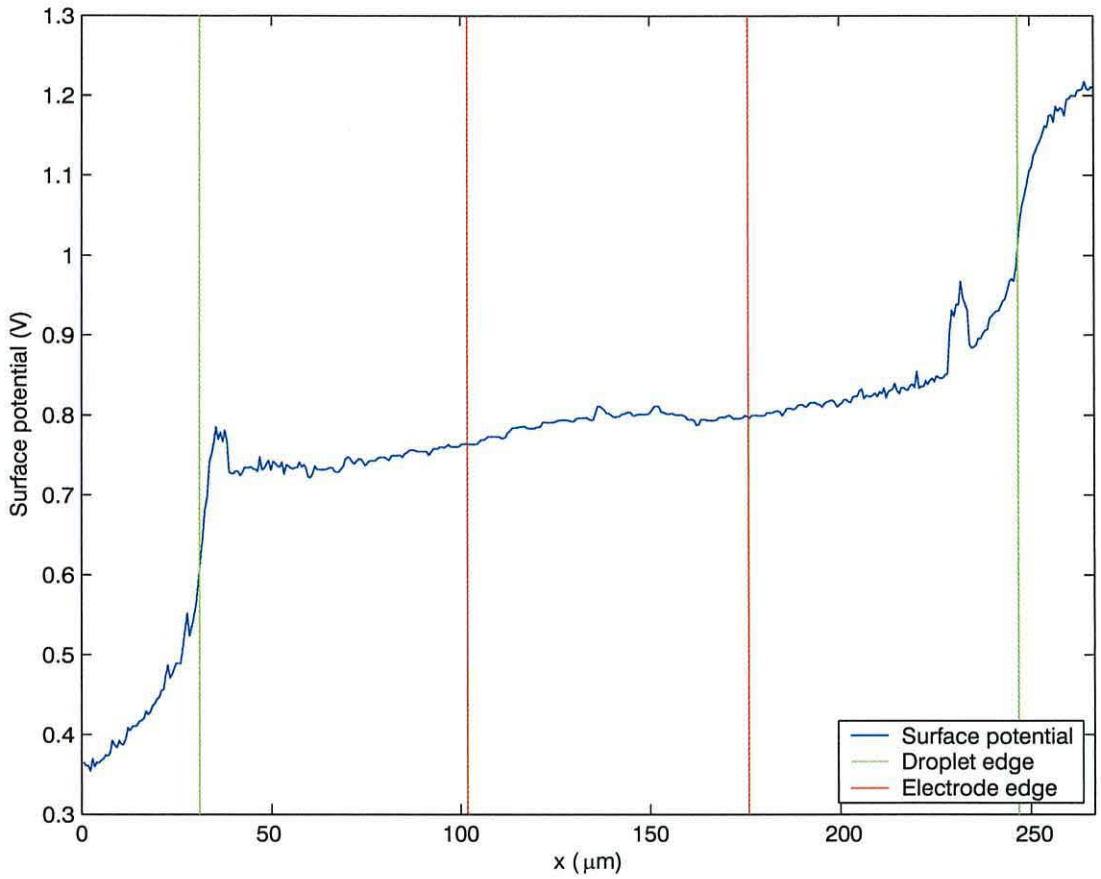


**Fig. 7.7:** Plot of surface potential against distance along cross-section for sample with the left hand electrode grounded and the right hand electrode at +1V.

Both electrodes were then grounded for 5 minutes and -1V applied to the right hand electrode while the left hand electrode remained grounded. The resulting SKPM image is shown in figure 7.8 with the blue line indicating the path of the cross-section shown in figure 7.9, the green lines indicating the boundaries of the polymer droplet and the red lines indicating the electrode edges.

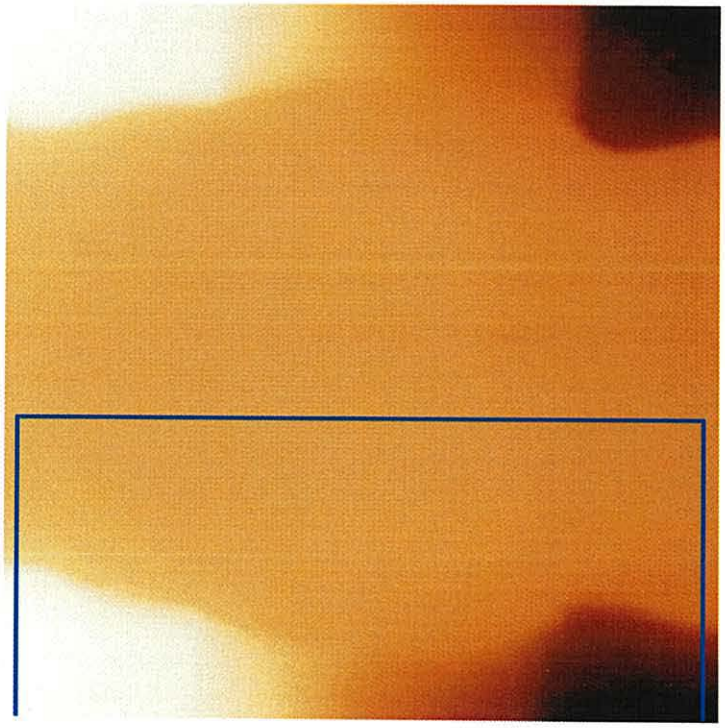

**Fig. 7.8:** Image showing surface potential of sample with the left hand electrode grounded and the right hand electrode at -1V (image 150x150$\mu m$). The blue line indicates the path of the cross-section shown in figure 7.9.

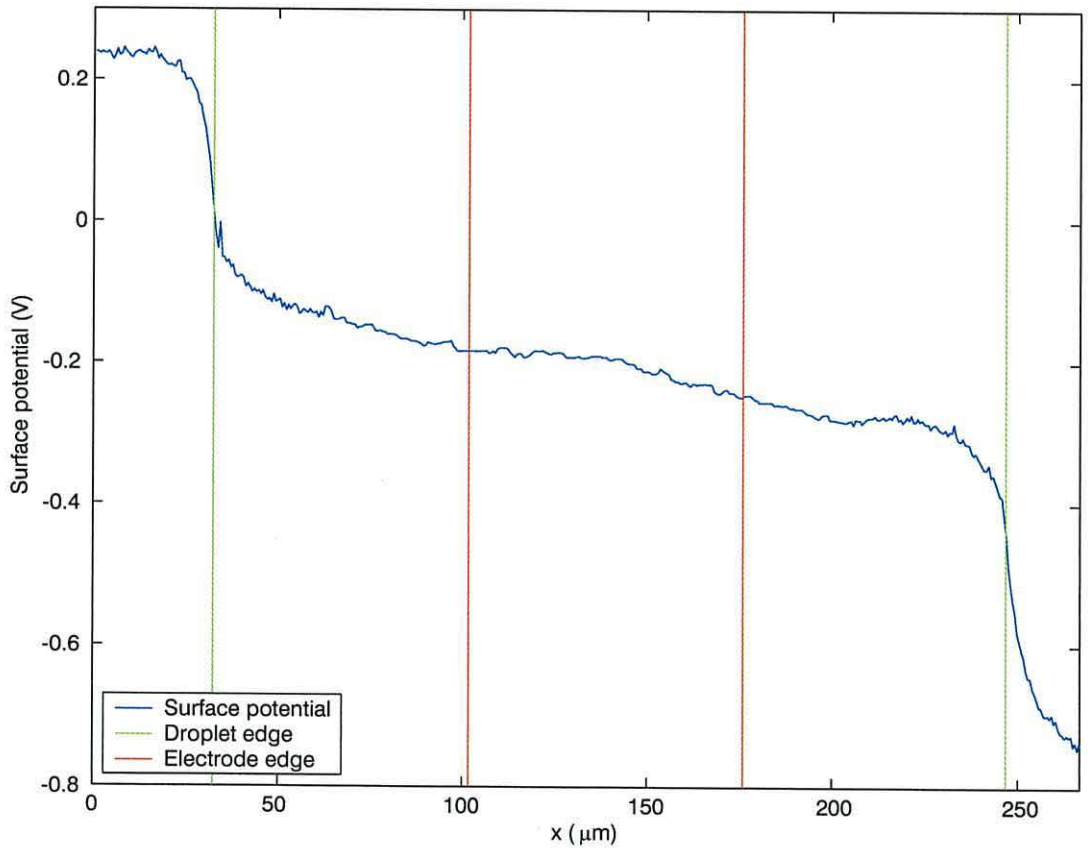


**Fig. 7.9:** Plot of surface potential against distance along cross-section for sample with the left hand electrode grounded and the right hand electrode at -1V.

Figures 7.7 and 7.9 show the potential distribution across the sample for two bias polarities. Again, due to the low measured work function difference between the polymer and the electrode no attempt was made to correct the data.

As with the sample with aluminium electrodes there are large potential steps located at the edges of the polymer line (indicated by the green lines in the plots). Again a comparatively greater potential is dropped across the electrode-polymer interfaces than is across the length of the conducting polymer between the electrodes. However in the case of the ITO electrodes, for both bias polarities, the potential step across the anode is approximately equal to that over the cathode.

Without taking into account the presence of ions within the polymer this result would not be expected of ITO. The I-t/cross-sectional area analysis provides an estimate of the conductivity which concurs with that seen in the Bayer literature thereby implying that the ITO electrodes make good contact with the polymer and that the potential dropped across the sample would be entirely due to the bulk conductivity of the polymer. However, this is not the case as the static SKPM shows large potential drops across the electrode-polymer interface.

### *7.5.3 Time resolved SKPM*

The slow scan axis of the AFM was disabled in order to capture the time evolution of the surface potential across the sample. A pulsed 1V potential difference was applied to the right hand electrode (while the left hand electrode remained grounded) using the Keithley 237 (as shown in figure 7.10). The fast scan axis rate of the AFM was 2Hz giving a total scan of 256s. The time resolved surface potential plot is shown in figure 7.11.

It should be noted that this scan rate is twice as fast as used for the aluminium electrode based samples. The purpose of this was to try and catch the initial potential evolution across the sample in more detail. Therefore care must be taken when directly comparing the time resolved SKPM data for the two different electrode materials.

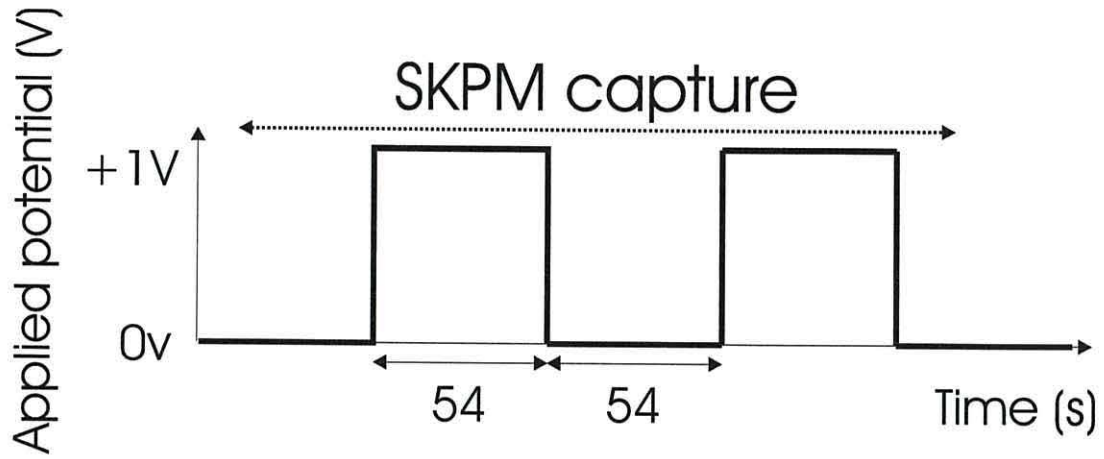


**Fig. 7.10:** Diagram showing applied potential with respect to time for the time resolved SKPM.

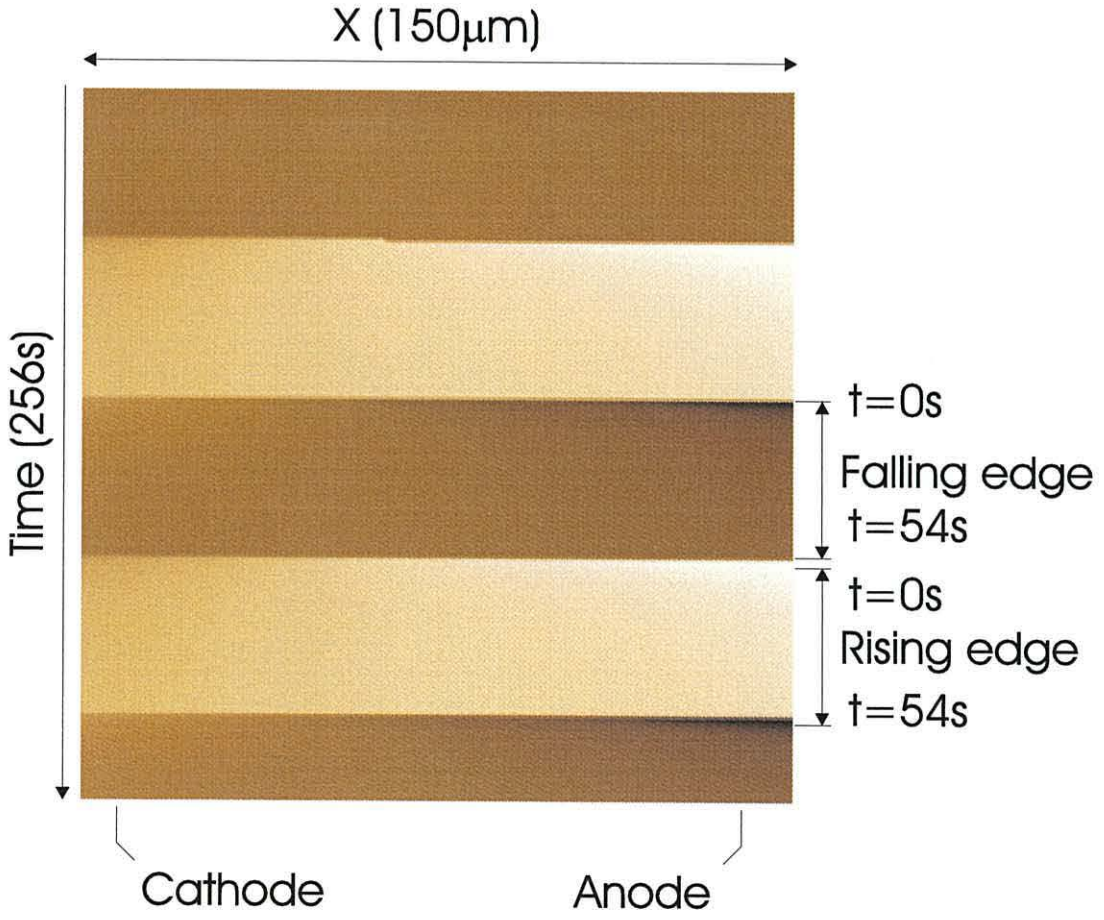


**Fig. 7.11:** Image showing time resolved surface potential of sample with the left electrode grounded and a pulsed potential applied to the right hand electrode (image 139$\mu m$x256s).

### *7.5.3.1 Cross-sections taken with respect to lateral position*

Two pairs of horizontal cross-sections representing the surface potential profile across the polymer from one electrode to the other were taken in the same manner as for the samples with aluminium electrodes. The falling and rising edge data is shown in figure 7.12, due to the increased scan speed the data is presented for t=0s and t=54s.

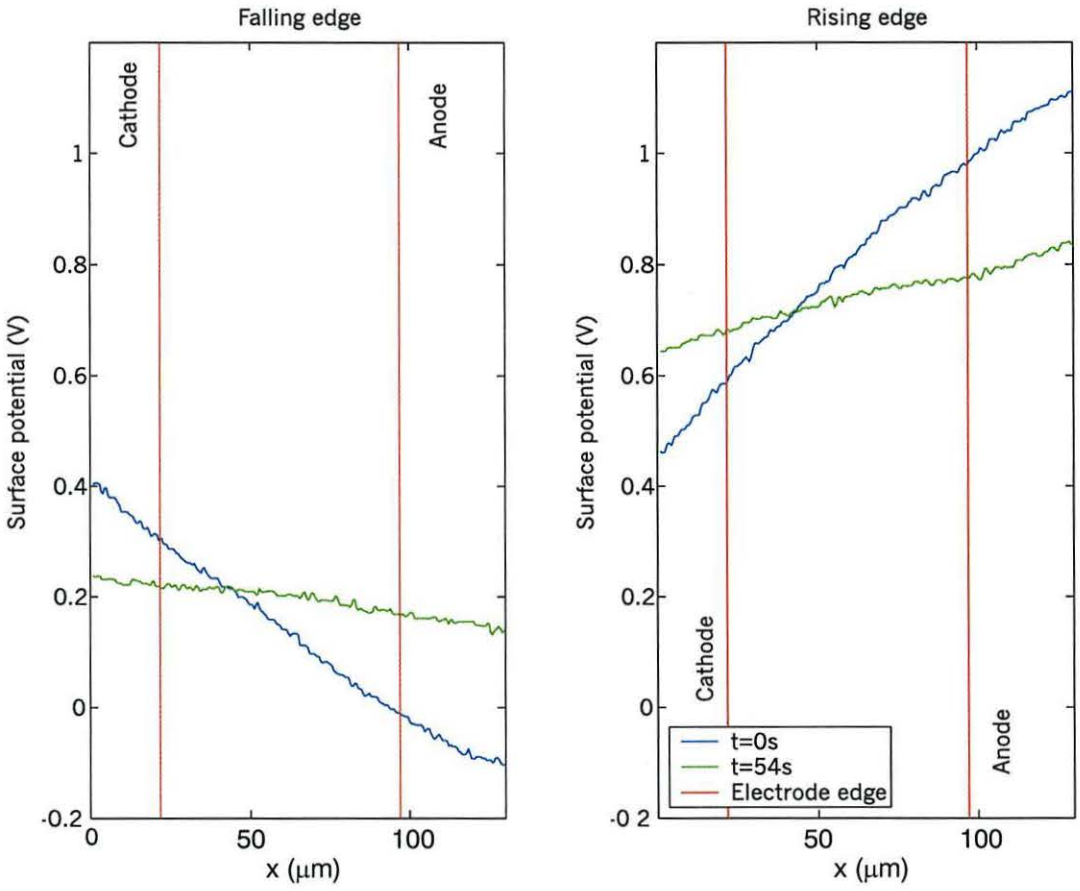


**Fig. 7.12:** Surface potential profiles of falling and rising edges obtained immediately after the voltage change (t=0s) and 54s later.

A significant difference exists between the presentation of the data for the aluminium and ITO electrodes. The time resolved SKPM cross-section taken from the polymer bridge over the aluminium electrodes included at either end a region of aluminium electrode. Therefore the potential drop across the electrode-polymer interface could be viewed. In order to remove the effect of the contact area resistance the isolated bridge structure was replaced with a long continuous line of polymer printed across the ITO electrodes. Therefore it was not possible to directly view the potential drop across the electrode-polymer interface with a single time resolved cross-section.

It was possible to overcome this by taking three time resolved SKPM cross-sections; (i) the first as with the aluminium electrodes traces from one electrode to

the other along the length of the line providing the time resolved potential distribution between them. (ii) and (iii) are across the anode and cathode respectively. These two cross-sections trace parallel to the electrode gap, across the electrode and polymer line, providing a measure of the potential drop across the interface with time.

Only the data for the trace from one electrode to the other is presented for the ITO electrodes as it presented a sufficiently clear explanation of the evolution of the potential across the sample. When analysing time resolved SKPM data for the continuous inkjetted lines across the aluminium electrodes it was necessary to view all three cross-sections as the situation involved two electrode polarisation effects with different timescales with the potential drop across the line barely changing with time, the majority of the changes occurring across the interfaces.

An examination of the potential distribution across the sample immediately following the application of a potential to the sample (see figure 7.12, rising edge, t=0s) shows a near-linear drop from one electrode to the other indicating good charge transfer at the electrodes. However, it can be seen that the full applied 1V is not dropped entirely between the electrode edges, that the potential gradient does not level out at each electrode edge, some potential being dropped over the polymer at the electrodes. This is likely due to the inability of the SKPM to capture the potential evolution at very fast timescales. As a result some ionic accumulation had already occurred at the interface thereby distorting the potential distribution.

It is possible to see part of this effect by a close examination of the potential drop across the anode immediately following the application of the potential (see figure 7.12, rising edge, t=0s). The SKPM data was taken on the retrace meaning that the SKPM tip was traced from right to left so the potential was measured from the anode to the cathode. It can be seen that the gradient of the potential on the anode is slightly less than that between the electrodes. This is an artifact of the measurement process with the potential on the sample changing as the SKPM tip was tracing from one electrode to the other.

Alternatively it is possible that there still exists a low conductivity interfacial layer between the ITO and polymer resulting in the potential gradient on the electrodes at t=0s. However the conductivity of this layer is not as low as that seen with the aluminium electrodes as the potential drops at the ITO electrodes do not significantly distort the potential distribution across the channel (see section 6.5.2).

The plot after 54s (see figure 7.12, rising edge, t=54s) shows that the potential

gradient across the sample has reduced to nearly zero indicating a similar effect attributable to ions migrating to the electrodes as seen with the aluminium based samples. This effect would be expected regardless of the electrode material assuming that the ions were intrinsic to the polymer rather than as a result of the electrodes.

The potential distribution at 54s still has some gradient due to the sample not having attained to steady state. In addition it should be noted that the potential on the sample with no potential on it is not 0V but 0.2V. This can be explained by the data having been saved by the Nanoscope controller with an offset on it. This offset is constant across the data set so can be disregarded when interpreting the time evolution of the data.

On removal of the potential the gradient of the potential across the sample reverses as would be expected as a result of the accumulated ions at the electrodes (see figure 7.12, falling edge, t=0s). When the ions migrate to the electrodes they create electric fields opposite in direction to the applied field. On removal of the applied field these charges are still present resulting in the potential distribution being opposite to that seen immediately on application of the potential (see figure 7.12, rising edge, t=0s). Under this opposite electric field the ions migrate back into the bulk of the polymer to assume an even distribution and the potential across the whole sample returns to zero (actually 0.2V as explained previously).

The SKPM results shown here clearly show the difference between the charge injection properties of electrodes of aluminium and ITO into PEDOT:PSS. In addition to the charge injection properties of the electrodes a second effect due to ions accumulating at the electrodes can be seen and is present for both electrode types indicating it is as a result of the polymer rather than the electrodes. This is further explored in chapter 8.

#### *7.5.3.2 Cross-sections taken with respect to time*

Given that the time-resolved SKPM was performed on a single scan line tracing the polymer line from one electrode to the other, the time evolution of the surface potential of the ITO electrodes has not been shown. Therefore only two vertical cross-sections were taken from the time resolved SKPM, one from the polymer on the cathode, the other from the polymer on the anode. These are shown in figure 7.13 and are comparable to the plot shown in figure 6.21, "Polymer behaviour".

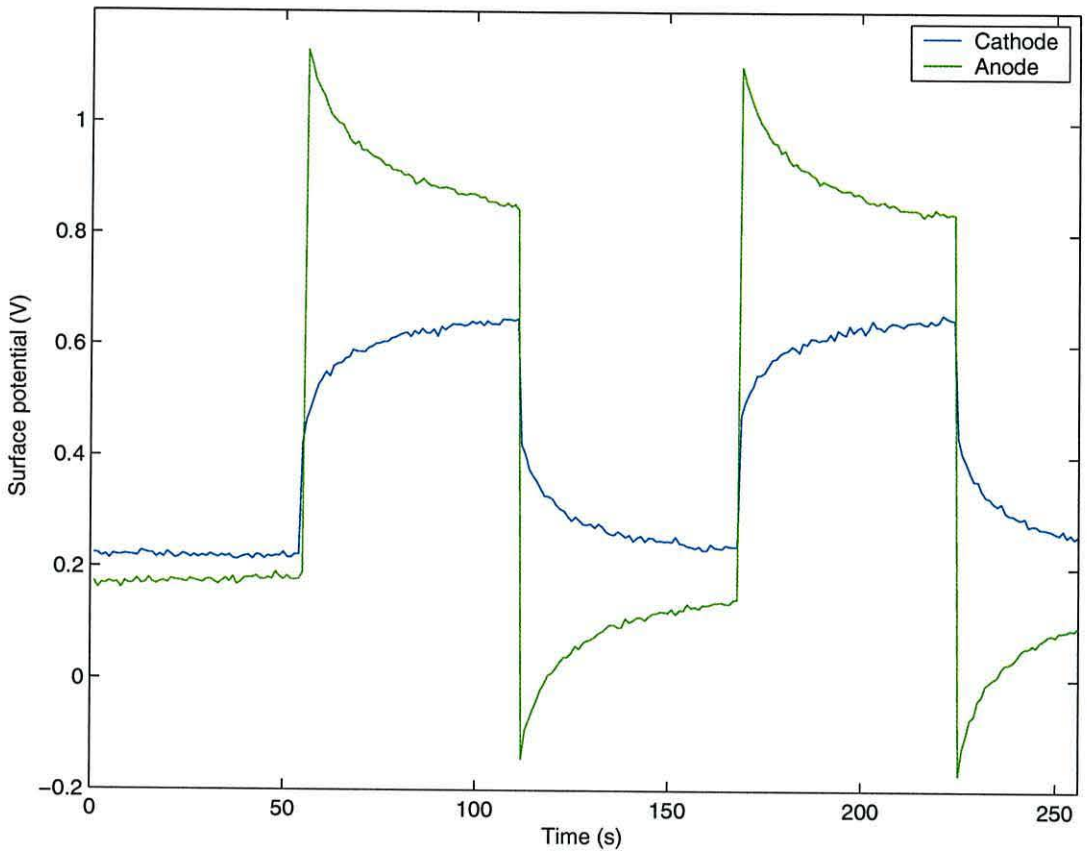


**Fig. 7.13:** Time evolution of the surface potential on the polymer on the cathode and on the polymer on the anode.

The cross-sections with respect to time confirm the behaviour discussed in section 7.5.3.1 showing that the potential difference between the electrodes initially starts at approximately 1V but as the ions migrate to the electrodes they create electric fields which oppose the applied field. As a result the potential drop across the channel is reduced to approximately 0.2V however this would decrease slightly as the sample had not achieved steady state in the plots above.

As a result of this two effects should be seen in the I-t plot; (i) a charging/discharging transient due to the movement of ionic charge to the electrodes and (ii) a decrease in the current with time as the movement of ions depletes the potential across the bulk of the polymer. This is further explored in chapter 8.

## *7.6 Raman spectroscopy and optical images*

### *7.6.1 Experimental sequence*

A slightly different experimental sequence to that in chapter 6 was used, in which three identical samples were fabricated. A sample was then placed under the

Raman spectroscope and spectra taken from the same location on the sample before, during and after current was injected into it. This process was repeated on a new sample with a different location examined. In this way, Raman spectra were taken from the anode, channel and cathode with each set of spectra being taken from a sample having not had current injected prior to the first spectrum.

Initially a Raman spectrum was collected from the sample prior to the application of any electric bias. A constant current of 1nA was then injected into the sample using the Keithley 237. The sample was left under electrical bias for 5 minutes prior to collecting a second Raman spectrum. The injected current was then set to zero (open circuit) and left for one hour before a third Raman spectrum was collected. In addition, optical images were captured before, during and after the application of electrical bias.

### *7.6.2 Optical images*

Figure 7.14 shows optical images of a sample before and after the application of 1nA. The image taken after the application of 1nA shows a light coloured patch in the polymer over the edge of the cathode. The light coloured patch appeared slowly after the current was applied. On removal of the electrical bias the light patch remained.

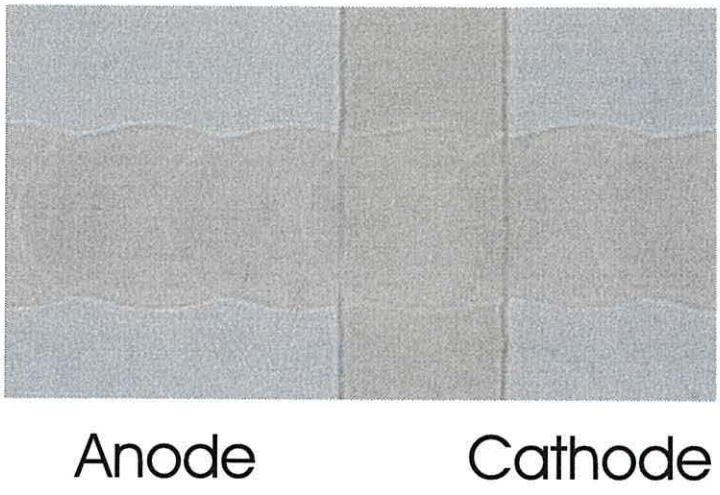


(a) Prior to the application of current

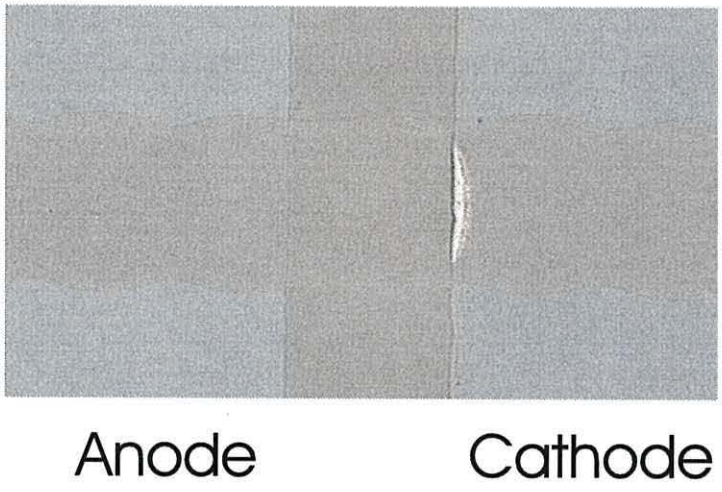


(b) After 1nA was injected into the sample

**Fig. 7.14:** Optical images taken using x20 microscope objective. The width of the images is approximately $350\mu m$ and the height $200\mu m$.

The optical images of the aluminium-based sample following electrical stress showed changes to the polymer at the cathode, and to a lesser degree at the anode. Again changes are seen here at the cathode, but not at the anode. In the case of the aluminium electrodes a dark patch appeared over the cathode whereas in the case of the ITO electrodes a light patch can be seen. This is most likely attributable to the difference in transparency of the electrodes and the lighting method used by the microscope.

This confirms the conclusions drawn in chapter 6 which attributed the colouration change to ionic accumulation. If these changes were due to chemical processes between the aluminium and polymer then it is unlikely they would have been seen in the ITO results too.

### *7.6.3 Comparison of Raman spectra*

Raman spectra were captured from three different locations on the samples; (i) before the application of electrical bias, (i) while 1nA was being injected in to the sample and (iii) 1 hour after the electrical bias was removed. The spectra were captured over the range 200 to 2000cm$^{-1}$ with 10 accumulations of 5s and the cosmic filter was on and a 50%filter was used.

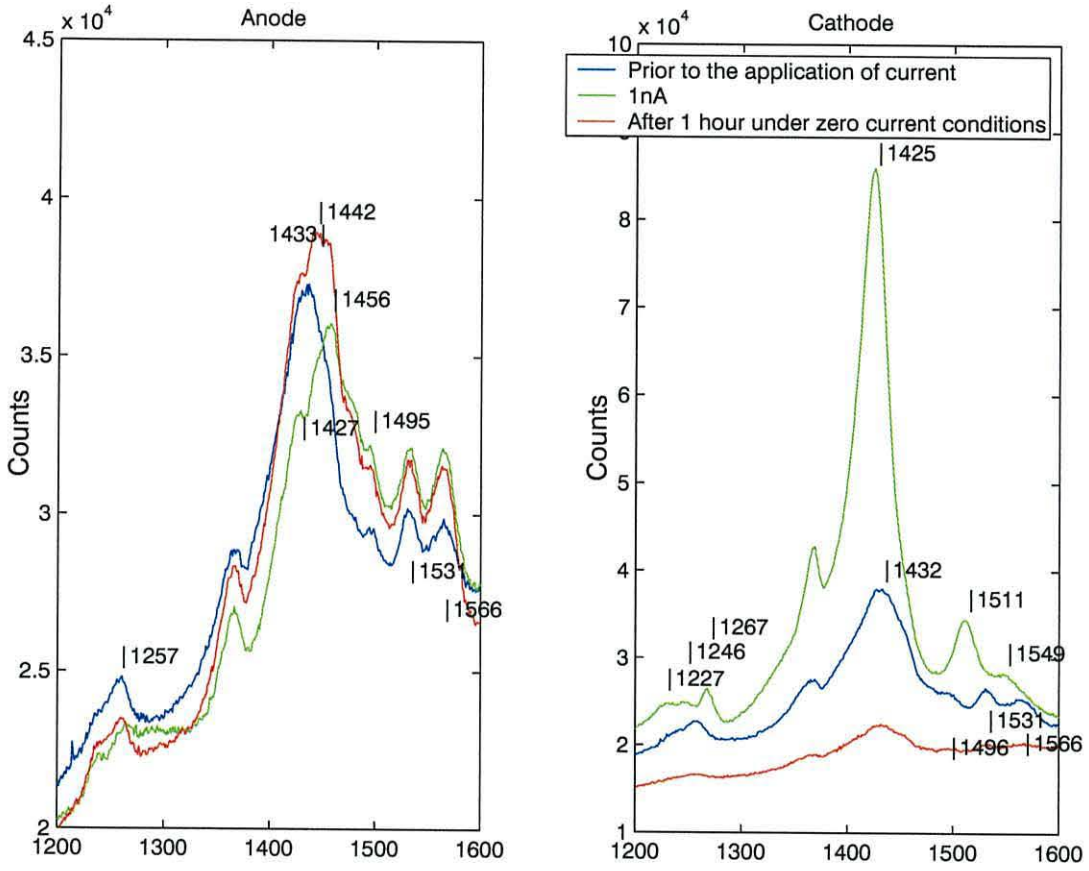


**Fig. 7.15:** Current induced changes in Raman spectra over the range 1200 to 1600cm$^{-1}$ for (i) the anode and (ii) the cathode.

The electrically induced changes in the Raman spectra occurred primarily in the wavenumber range 1200 to 1600cm$^{-1}$ and are shown for the anode and cathode in figure 7.15. It can be seen that there is a significant difference in the Raman spectra of the sample when 1nA is passed through it, depending on the location of the Raman spectra. The changes that occurred in the spectra on the sample with ITO electrodes were similar to those seen on the sample with aluminium electrodes except in reverse. The spectral changes seen on the aluminium anode and channel were seen on the ITO cathode while the spectral changes seen on the aluminium cathode were seen on the ITO anode and channel. While the behaviour of the anode and cathode reversed depending on the electrode material, the channel always showed the same behaviour as the anode.

The changes in the spectrum for the ITO anode were comparable to those of the aluminium cathode except that they showed a more pronounced change in the main 1428cm$^{-1}$ peak. Instead of appearing as a broadening and upwards shift to 1431cm$^{-1}$, the peak appeared as three conjoined peaks at 1428, 1456 and 1478cm$^{-1}$.

While the aluminium anode and channel show identical changes in their spectra, the spectrum for the ITO channel showed a less significant change in the main 1428cm$^{-1}$ band than the ITO anode.

The changes in the spectrum for the ITO cathode were near-identical to those of the aluminium anode with the broad peak at 1257cm$^{-1}$ splitting into three at 1227, 1246 and 1267cm$^{-1}$ and the three peaks at 1496, 1531 and 1566cm$^{-1}$ changing to two at 1511 and 1549cm$^{-1}$.

In the case of the aluminium electrodes charge transfer across the interfaces was poor resulting in the bulk polymer transporting holes away from the anode faster than they could be injected. This resulted in the polymer becoming dedoped at that location which was seen in the Raman spectra. The SKPM for the ITO electrodes indicate that there is good hole transfer across the interfaces. The effect of this is that holes can be injected into the bulk at the anode faster than they can be transported away thereby producing a higher concentration of holes at the anode. At the cathode holes can be extracted from the polymer at the interface faster than they can be transported to the interface thereby depleting the polymer of holes there. This effect is confirmed by the Raman spectra which show that the polymer at the anode is more highly doped than would be expected and the polymer at the cathode has been dedoped.

## *7.7 Concluding summary*

This chapter provides details of the inkjet printing of m:PEDOT:PSS across an insulating gap between ITO electrodes. A similar set of experiments as in chapter 6 were performed on the samples and the results compared with those obtained from the aluminium based samples.

The I-t analysis of the samples again showed charging/discharging transients, however the currents were an order of magnitude higher. From the I-t/cross-sectional area analysis the conductivity of the polymer was calculated and concurred with the values stated in the Bayer data. This confirmed that there was little potential drop across the ITO-PEDOT:PSS interface. The time resolved

SKPM showed the same characteristics attributed to an ionic electrode polarisation effect but showed that the electrodes were good charge injectors/extractors.

Raman spectroscopy confirmed the injection properties of the electrodes with the anode becoming highly doped by easy injection of holes while the cathode became dedoped by the extraction of holes. The optical images taken of the sample under electrical stress showed the same colouration of the polymer at the cathode confirming the ionic accumulation effect was not electrode dependent and most likely due to the sodium ions in the polymer or substrate.

# 8. FURTHER ANALYSIS AND DISCUSSION OF I-T DATA

## *8.1 Introduction*

In light of the current transients in the I-t data and the ionic migration seen in the time-resolved SKPM data, further analysis of the I-t data was undertaken to compare the behaviour for both electrode materials. The difference between the charging and discharging transients were examined followed by an analysis of the time decay law.

## *8.2 Steady state current due to DC conductivity*

As described in section 6.3.1 the application of a potential to the sample causes the ions in the bulk polymer to migrate to the electrodes. Unlike electrons and holes they cannot be discharged resulting in a polarisation field in the bulk opposing the applied field. On removal of the applied field the ions at the electrodes migrate back into the bulk of the polymer as a result of the polarisation field.

Therefore application of a potential step to the sample will result in a charging current which then decays to yield a steady state value due to the DC conductivity of the polymer. On removal of the potential the sample will discharge producing a discharging current in the opposite direction which decays to zero. This should be the mirror image of the charging current without the steady state current. This can be shown by equation 8.1 and assumes that the *law of superposition* holds [79].

$$-I_d(t) = I_c(t) - I_s \tag{8.1}$$

where $I_d(t)$ is the current seen on removal of the potential step, $I_c(t)$ is the current seen on application of the potential step and $I_s$ is the steady state current due to the DC conductivity .

Equation 8.1 assumes that the charging current is equal to the discharging current, i.e. that all of the charge stored upon charging is released under discharge. Deviations from this can be caused by irreversible changes occurring in the polymer such as the ions becoming fixed at the electrodes [77].

From equation 8.1 it can be seen that $I_s = I_c(t) + I_d(t)$ therefore plotting $I_s$ with respect to time should yield a line of zero gradient. This is shown along with the $I_c(t)$ and $I_d(t)$ in figure 8.1 for both electrode materials. The aluminium data was based on sample 1 (see section 6.2) which consisted of electrodes separated by $80\mu m$ with an inkjetted bridge over the gap with limited contact area to the electrodes. The ITO based electrodes consisted of electrodes separated by $74\mu m$ with the inkjetted line consisting of 20 droplets separated by $60\mu m$ and the same potential step but applied for 250s.

Most significantly neither sample was in its virginal state at the start of the I-t data collection. Both samples had had various I-t runs performed on them and the aluminium based sample had been used for SKPM data capture. Therefore care should be taken when drawing conclusions from the data.

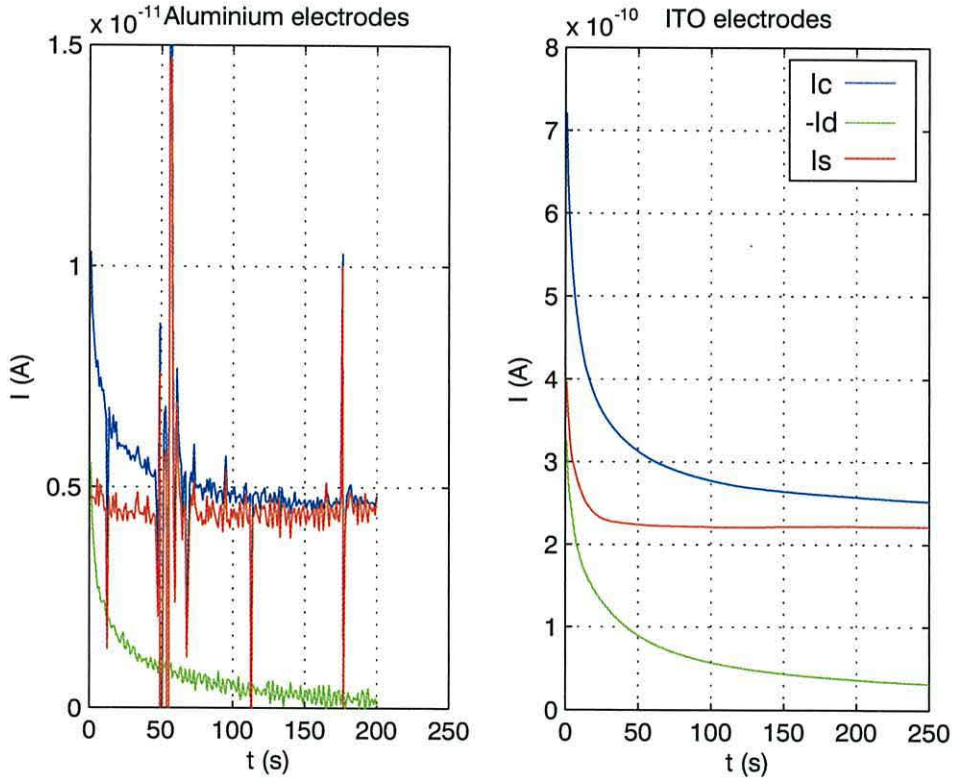


**Fig. 8.1:** I-t data for aluminium and ITO based samples plotted on a lin-lin scale for the charging, discharging and steady state currents.

It appears from figure 8.1 that the steady state current term ($I_s$) for the aluminium based sample is constant with time whereas that of the ITO based sample is not. In that case it shows that more charge is flowing into the sample under charging than is returned on the discharge. Alternatively, slow changes are occuring at the electrodes or that dopant is moving out of/being neutralised in the

bulk.

This effect was further investigated by repeating the same potential step measurement and plotting the steady state current term for successive cycles of the measurement. In the case of the aluminium sample the steady state current remained constant over time following the potential step and also remained constant over successive steps. The ITO on the other hand continued to show the change in the steady state current with time following the potential step (as seen in figure 8.1) but also decreased in magnitude over successive cycles. Similar behaviour was seen by Moller et.al. except, due to using a transverse device structure, the changes were seen over far shorter timescales [76].

Additionally it should be noted though that when taking the SKPM and Raman data, a decrease in the magnitude of the current was seen over successive runs in both types of sample, although this was observed incidentally so no comparison between the rates of decrease for them can be made.

It is difficult to directly attribute the differences in the steady state current behaviour to the difference in the electrode materials as the experimental procedure was not identical in both cases. This included the difference in the previous history of the samples, the time for which the potential step was applied and the electrode contact area. It was seen that the ITO was undergoing some sort of charging process possibly as a result of ions becoming fixed at the interfaces but that this process was reducing in magnitude with successive cycles of measurement. This was not observed in the aluminium sample but it is possible that this process had already occurred during earlier runs.

Optical changes seen at the electrodes, specifically at the cathode, were tentatively attributed to the chemical bonding of the ions at the interface (see section 6.7.5). As a result, on removal of the applied potential, not all of the ions redistributed back into the bulk of the polymer but some remained chemically bonded at the interface. This was seen for both electrode materials though the optical changes seen were different, probably due to the difference in electrode transparency and the microscope lighting method. As a result the loss of ions at the interface cannot be directly related to the difference in steady state current behaviour as there is no directly linked I-t and optical data, however it is likely that the two effects are somehow linked.

Clearly further investigation is required to quantify the steady state current behaviour especially with respect to the different electrode materials. More rigorous

experimental practice would be needed, with directly comparable I-t sequences, sample geometries and optical image capture. Further, the effects of environmental conditions could be removed by performing the experiments under vacuum, or by flushing the chamber with wet and dry nitrogen to investigate the effects of oxygen and water, both of which are known to have effects on doping in polymers.

## *8.3 $t^{-n}$ current decay*

It was found that by plotting the I-t data on a $\log_{10} - \log_{10}$ scale (see figure 8.2) near-straight line graphs were found. This indicated a $t^{-n}$ behaviour in the current transients as shown by equations 8.2 and 8.3 i.e.

$$I = At^{-n} \tag{8.2}$$

so that;

$$\log_{10} I = -n \log_{10} t + \log_{10} A \tag{8.3}$$

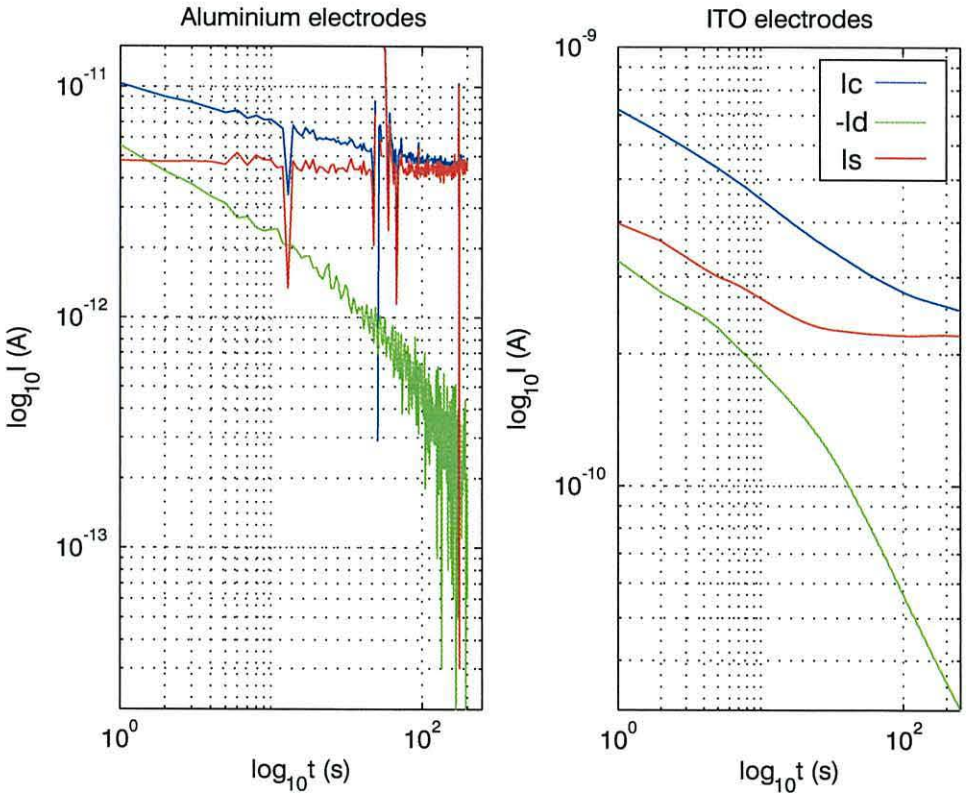


**Fig. 8.2:** I-t data for aluminium and ITO samples shown in figure 8.1 plotted on log-log scale.

Again it was difficult to compare the data as the ITO sample was still undergoing

some form of change. As expected the steady state current for the aluminium sample is constant with respect to time. It can be seen that the steady state current ($I_s$) for the ITO sample settles down to zero gradient after approximately 40s. At this point the gradient of the $-I_d$ line also achieves a constant gradient, possibly showing that this is the true value of n for the discharging response. Taking the gradients of the $-I_d$ lines for both electrode types after 40s gives near identical values of -0.677. However, the noise due to the lower current measurements for the aluminium sample makes it difficult to be more certain of the gradient. This provides indication that the step response current transients are as a result of some process in the polymer as the n values are the same regardless of the electrode material.

Care should be taken with the above interpretation as while the gradients are equal (after 40s) the current varies by orders of magnitude. Further analysis of the $t^{-n}$ behaviour of the current decay is required. A variety of mechanisms can be responsible for it, including, dipole relaxation, hopping conduction, electron tunnelling to empty traps, charge injection resulting in space charge accumulation and electrode, interfacial or bulk polarisation [77].

## *8.4 Concluding summary*

This chapter aims to shed further light on the current transients seen in the I-t data and then to link it back into some of the SKPM and optical results seen in chapters 6 and 7. The aluminium data showed a constant steady state value with respect to time and with respect to successive cycles, this was attributed to the DC conductivity. The ITO data showed that the steady state current varied with time and with successive cycles.

# 9. CONCLUSIONS AND FURTHER WORK

## *9.1 Conclusions*

The foregoing chapters have described pioneering work in which time resolved SKPM and Raman spectroscopy were used to identify electronic and ionic processes occuring at the interface between inkjetted PEDOT:PSS and electrodes of aluminium and ITO.

In order to fabricate experimental structures for investigation, an inkjet printing system was required capable of inkjetting various polymer solutions. This was primarily an engineering challenge, with sufficient care having to be taken to ensure that the system was capable of printing a variety of polymer solutions and solvents with specific accuracy and including optical alignment to surface features.

Following the completion of the inkjet printing system the inkjetting of PEDOT:PSS on various substrates had to be characterised. Initially this was performed on glass and the effects of different droplet pitches and drying delays were examined. This was then followed by AFM analysis which allowed the cross-sectional area of the various printed lines to be calculated along their length. This is a valuable tool as it provides a measure of the likely resistance of a printed line.

Three electrode materials commonly used with polymers are aluminium, gold and ITO, and were investigated in terms of success of making inkjetted contacts to them. This required an understanding of the interaction between the surface tension of the inkjetted droplet and the surface energy of the substrates to be printed on. Due to the oleophilic nature of gold, adsorbed hydrocarbons on its surface reduced its surface energy resulting in unsuccessful inkjetted contacts. Aluminium and ITO on the other hand made good contacts, attributed to the higher surface energy of their oxide surfaces, as a result of which the experimental samples fabricated for this investigation were based on these two materials.

Following the inkjetting of lines of PEDOT:PSS across 45 to 80$\mu m$ gaps between electrodes of aluminium and ITO a series of experimental investigations were made so as to determine the electrical and spectral behaviour of the samples including,

(i) I-t step response, (ii) SKPM and time resolved SKPM measurements of the surface potential across the samples, (iii) Raman spectroscopy of the polymer under electrical bias. Additional measurements were made and included the optical appearance of the samples and EDAX analysis of the polymer to determine its ion content.

The I-t step response of the samples showed significant charging/discharging transients which were attributed to electrode polarisation, with ions moving to the electrodes but not being discharged. Following the decay of the charging current transient a steady state current was seen with that in the ITO sample being at least an order of magnitude greater than in the aluminium for comparable sample structures. However it should be noted that during successive I-t cycles the "steady state" current component decreased.

The time decay of the current transients followed a $t^{-n}$ decay law, with an n value of 0.677 for both electrode materials. This was initially taken to indicate that the transients were the result of the bulk properties of the materials, however it was then noted that while the n values were equal, the currents varied by an order of magnitude.

AFM analysis of the inkjetted structures provided a measure of their cross-sectional area which together with the steady state current values found previously enabled an estimate of the polymers conductivity to be made and compared with the listed Bayer data. It was found that the conductivity of the aluminium samples was between one and two orders of magnitude less than expected while that of the ITO was the same as that shown by Bayer indicating the likelihood of inefficient charge transfer with aluminium.

As a prelude to the SKPM work the AFM data was used to create computer models so as to predict the likely potential distribution across the inkjetted samples. This was felt necessary as the irregular 3D nature of the polymer lines were not conducive to intuitive interpretation of the results as might be the case if the structures were formed from regular 3D blocks of material.

Initially the AFM data was used directly to form high resolution 3D models of the inkjetted structures in Femlab, however due to the memory constraints of the Windows operating system it was not possible to solve these models. Following this a different program, CFD-ACE, was used to model simpler 2D cross-sections through the length of the inkjetted structures which were solved using Laplace's equations and the surface potential plotted. The model was modified to include

low-conductivity interfacial layers at the electrodes. The conductivity of these layers was varied over several orders of magnitude, the effect being to induce large potential drops at the polymer-electrode boundary.

SKPM data was taken from samples under applied biases of different polarities. In comparison to the predicted modelled data both samples showed significant potential drops over the polymer-electrode boundary indicating the presence of an interfacial layer. To further investigate the nature of the potential drops the slow scan axis of the SKPM was disabled so as to allow time resolved SKPM data to be acquired. As a result of this it could be seen that the aluminium and ITO samples behaved in different manners. The aluminium showed the presence of charge injection barriers at the interfaces at early times which were then superseded by ionic accumulation at the electrodes as time progressed, which further distorted the potential distribution. The ITO sample showed good charge injection with a near linear potential drop between the electrodes at early times, followed by distortion of the potential by a subsequent ionic accumulation at the electrodes.

The use of SKPM as a tool to identify charge injection "bottle necks" in polymer devices has already been demonstrated [66][35][67], however a recent literature survey has not revealed the use of time resolved SKPM to show the time response of the surface potential in polymer structures. The work contained in this thesis then presents a significant advance in the application of SKPM in polymer electronics. Time resolved SKPM in the present study has identified the contrasting injecting properties of the aluminium and ITO electrodes as well as the presence of mobile ion induced distortions to the potential distribution at the interface.

The work was furthered by the use of Raman spectroscopy as a complementary method to the SKPM for identifying charge distributions in the polymer samples and is believed that this is the first instance of their combined use to investigate the electrical properties of polymer devices.

By comparing the spectra taken by Garreau et.al. [72] and Lapkowski and Pron [73] of PEDOT in an electrochemical cell at various stages of doping it was possible to qualitatively identify the level of doping of the polymer at various points in the inkjetted electrode-polymer-electrode structure. This confirmed the SKPM data to show that in the aluminium sample, the poor injection of of holes over the interface resulted in a dedoping of the polymer at the anode as charge was transported away from the interface more efficiently than it could be injected, while the polymer at the cathode became more heavily doped as holes accumulated there as a result of poor charge extraction. Conversely, in the ITO sample the polymer at the

anode became more heavily doped as charge was injected more efficiently than it could be transported away, while the polymer at the cathode became dedoped as charge was extracted more efficiently than it could be transported to the interface.

Optical images taken of the polymer at different stages of biasing showed that under the application of bias, the appearance of the polymer at the cathode changed. This was attributed to ionic accumulation with some of the ions chemically bonding with the polymer and changing its appearance. EDX analysis confirmed the presence of sodium in the polymer ink solution and showed that storage in a glass container increased that content. Therefore it is likely that one of the mobile ionic impurities in the polymer was sodium and originated from the solution or the glass substrate. Similar results were found by Rep et.al. [78] who suggested SKPM as a method for identifying the effects of these impurities.

These results have implications for the use of PEDOT:PSS especially the lifetime of manufactured devices. The presence of mobile ionic impurities indicates the the electrical stability of devices could vary with time and that the presence of the ions could lead to their eventual breakdown.

## *9.2 Further work*

The inkjet printing system was completed successfully, however in developing the system, further issues were highlighted for future development and included (i) two optical systems so as to allow optical alignment of the head over surface features and side-viewing to allow the droplet formation to be viewed without disassembling the first camera, (ii) an automated cleaning process whereby the inkjet printing nozzle can be moved over a solvent filled sump and/or cleaning pad and (iii) additional development of the GUI to allow more complex inkjet patterns to be formed, which could be based on a CAD/G-code interpreter.

There is scope for advancing the work on modelling electrical conduction through irregular 3D structures derived from AFM data. The primary limitation to the work presented in this thesis was that of memory allocation by the Windows operating system. This could be overcome by a variety of means, including using a different operating sytem or adjusting the resolution and meshing process so as to reduce the memory requirements. A matched set of AFM data is produced when taking SKPM data allowing the measured surface potential data to be compared with predicted computer modelled data and as such is a useful tool for SKPM analysis.

The I-t step response data clearly requires further investigation with care being taken to compare identical sample structures under more rigorous experimental conditions. The current transients themselves can provide further information on the different behaviour of the electrodes and the bulk properties while further investigation of the effects causing the steady state current to vary are necessary.

There is definite scope to further the SKPM and Raman investigations. The surface potential plots shown in this work were taken at single bias potentials, further information as to the behaviour of the interface between aluminium and PEDOT:PSS can be derived from varying the applied bias and observing the charge injection barriers. The effects of the cantilever and its interaction with the sample have not been addressed in detail in this investigation. It has been shown that the use of I-t, SKPM and Raman provide complementary results and the use of optically transparent SKPM tips with a combined AFM/SKPM/Raman and fast Raman capture would allow synchronised time resolved data to be captured simultaneously .

*Appendix A*

# ELECTRODE FABRICATION

## *A.1 Aluminium electrodes*

1. Clean glass microscope slide (Gerhard Menzel Super Premium plain extra white glass).
   (a) Swab slide repeatedly with fingertip dipped in decon 90 (Decon Laboratories Limited) ensuring entire surface of slide has been scrubbed.
   (b) Rinse slide in hot free flowing tap water (hot water removes decon 90 more effectively than cold water).
   (c) Rinse slide in UPW (filtered and deionised water (Millipore Milli Ro 60 system)).
   (d) Air dry using blown hot dry air.
2. Vacuum evaporate aluminium using Balzers TSH 170 vacuum chamber.
   (a) Cut 10mm length of aluminium wire (BDH, 99.99% pure, 1mm diameter).
   (b) Clean wire using decon 90, rinse in hot water then UPW, air dry.
   (c) Wrap aluminium around conducting tungsten wire.
   (d) Load slide into chamber.
   (e) Evacuate chamber to $10^{-6}$Torr.
   (f) Apply sufficient DC potential to tungsten wire so as to slowly evaporate aluminium.
3. Photolithographically pattern photoresist (Shipley S1818).
   (a) Spin coat photoresist at 4000rpm for 60s.
   (b) Bake on hotplate at 116°C for 60s.
   (c) Expose to UV light through photolithographic mask for 30s.
   (d) Remove exposed resist using developer (Shipley MF319).
4. Etch aluminium

(a) Immerse slide in etch (3 parts phosphoric acid, 1 part nitric acid, 1 part water).

(b) Agitate until unprotected aluminium disappears.

(c) Rinse in UPW.

(d) Rinse in acetone/Shipley SVC-175 to remove remaining resist.

(e) Rinse in UPW, air dry using blown hot dry air.

## *A.2 Gold electrodes*

1. Clean glass microscope slide (Gerhard Menzel Super Premium plain extra white glass).

   (a) Swab slide repeatedly with fingertip dipped in decon 90 (Decon Laboratories Limited) ensuring entire surface of slide has been scrubbed.

   (b) Rinse slide in hot free flowing tap water (hot water removes decon 90 more effectively than cold water).

   (c) Rinse slide in UPW (filtered and deionised water (Millipore Milli Ro 60 system)).

   (d) Air dry using blown hot dry air.

2. Vacuum evaporate 10nm chromium adhesion layer followed by 100nm of gold in Edwards 306 Turbo evaporator.

3. Photolithographically pattern photoresist.

   (a) Spin coat photoresist at 4000rpm for 60s.

   (b) Bake on hotplate at 116°C for 60s.

   (c) Expose to UV light through photolithographic mask for 30s.

   (d) Remove exposed resist using developer.

4. Etch gold then chromium

   (a) Immerse slide in aqua regia (3 parts hydrochloric acid, 1 part nitric acid).

   (b) Agitate until unprotected gold disappears.

   (c) Rinse in UPW.

   (d) Immerse slide in chrome etch (15gm serric ammonia nitrate, 3.5mL acetic acid, 100mL water).

   (e) Agitate until unprotected chrome disappears.

   (f) Rinse in acetone/Shipley SVC-175 to remove remaining resist.

   (g) Rinse in UPW, air dry using blown hot dry air.

## *A.3 ITO electrodes*

1. Clean precoated ITO glass substrate (CG-1IN-1515, Delta-technologies Ltd.).
   (a) Swab slide repeatedly with fingertip dipped in decon 90 (Decon Laboratories Limited) ensuring entire surface of slide has been scrubbed.
   (b) Rinse slide in hot free flowing tap water (hot water removes decon 90 more effectively than cold water).
   (c) Rinse slide in UPW (filtered and deionised water (Millipore Milli Ro 60 system)).
   (d) Air dry using blown hot dry air.
2. Photolithographically pattern photoresist.
   (a) Spin coat photoresist at 4000rpm for 60s.
   (b) Bake on hotplate at 116°C for 60s.
   (c) Expose to UV light through photolithographic mask for 30s.
   (d) Remove exposed resist using developer (Shipley MF319).
3. Etch ITO
   (a) Heat etch (hydrobromic acid) to 50°C on a hotplate.
   (b) Immerse substrate in etch.
   (c) Keep on heat for 5 minutes.
   (d) Rinse in UPW.
   (e) Rinse in acetone/Shipley SVC-175 to remove remaining resist.
   (f) Rinse in UPW, air dry using blown hot dry air.

*Appendix B*

# PROGRAM FOR INKJET PRINT SYSTEM

```
function varargout = l25icam(varargin)
% L25ICAM Application M-file for l25icam.fig
%    FIG = L25ICAM launch l25icam GUI.
%    L25ICAM('callback_name', ...) invoke the named callback.

% Last Modified by GUIDE v2.0 31-Mar-2003 18:45:40

if nargin == 0  % LAUNCH GUI

fig = openfig(mfilename,'reuse');

% Use system color scheme for figure:
set(fig,'Color',get(0,'defaultUicontrolBackgroundColor'));

% Generate a structure of handles to pass to callbacks, and store it.
handles = guihandles(fig);

    %create serial port object
    handles.s = serial('COM1','Terminator','CR');
    fopen(handles.s);

    %set to absolute mode
    fprintf(handles.s,'1MA');
    fprintf(handles.s,'2MA');

    % X configure homing, home and set yposst to zero
    fprintf(handles.s,'1ARM1');
    fprintf(handles.s,'1HOME1(+,0,-5,100,2)');

    fprintf(handles.s,'1ON');
    fprintf(handles.s,'1GH');

    handles.xposval = 0;
    set(handles.xposet,'string', handles.xposval);

    % Y configure homing, home and set yposst to zero
    fprintf(handles.s,'2ARM1');
    fprintf(handles.s,'2HOME1(+,0,-5,100,2)');

    fprintf(handles.s,'2ON');
    fprintf(handles.s,'2GH');

    handles.yposval = 0;
    set(handles.yposet,'string', handles.yposval);

    %configure drop, eject and delay handles
    handles.dropnumval = 0;
    set(handles.dropnumet,'string', handles.dropnumval);

    handles.ejectspval = 0;
    set(handles.ejectspet,'string', handles.ejectspval);

    handles.delayval = 5;
    set(handles.ejectdelayet,'string', handles.delayval);

    set(handles.xoffet,'string',24.9);
    set(handles.yoffet,'string',1.3);
```

```
    %create cancel variable
    global cancel;
    cancel = 0;

    % Generate a structure of handles to pass to callbacks, and store it.
guidata(fig, handles);

if nargout > 0
varargout{1} = fig;
end

elseif ischar(varargin{1}) % INVOKE NAMED SUBFUNCTION OR CALLBACK

try
if (nargout)
[varargout{1:nargout}] = feval(varargin{:}); % FEVAL switchyard
else
feval(varargin{:}); % FEVAL switchyard
end
catch
disp(lasterr);
end

end


% --------------------------------------------------------------------
function varargout = pushbutton15_Callback(h, eventdata, handles, varargin)
%To run code in "run code block" button, place it below

%get start point
xstart = str2double(get(handles.xposet,'string'));
ystart = str2double(get(handles.yposet,'string'));

finalxpos = xstart - 1.1;
while (finalxpos < 0) | (finalxpos > 80);
errordlg('Final position lies outside limits of stage');
return;
end;

finalypos = ystart - 1.1;
while (finalypos < 0) | (finalypos > 25);
errordlg('Final position lies outside limits of stage');
return;
end;

%create data matrix
%no of droplets, separation(um), delay(s), ystart(mm), xstart(mm)
data = [50 -20 1 0 0;
    25 -40 1 -0.22 0;
    17 -60 1 -0.44 0;
    13 -80 1 -0.66 0;
    10 -100 1 -0.88 0;
    9 -120 1 -1.1 0;
    25 -20 4 0 -1.3;
    13 -40 4 -0.22 -1.3;
    9 -60 4 -0.44 -1.3;
    7 -80 4 -0.66 -1.3;
    5 -100 4 -0.88 -1.3;
    5 -120 4 -1.1 -1.3];

for line = 12:-1:7
    %number of drops
    dropnumval = data(line, 1);
    %drop spacing in um
    ejectspval = data(line, 2);
    ejectspval= ejectspval / 1000;
    %drop delay in sec
    delayval = data(line, 3);

    %move to start of line
    %convert mm to steps
```

```
    xpos = xstart + data(line, 5);
    xentry = xpos * 4000;

    %update xposition register
    set(handles.xposet,'string', xpos);

    %create control string and send
    fprintf(handles.s,'1A100');
    fprintf(handles.s,'1V5');
    xentry = int2str(xentry);
    xmovestring = ['1D',xentry];
    fprintf(handles.s,xmovestring);
    fprintf(handles.s,'1G');

    %convert mm to steps
    ypos = ystart + data(line, 4);
    yentry = ypos * 4000;

    %update xposition register
    set(handles.yposet,'string', ypos);

    %create control string and send
    fprintf(handles.s,'2A100');
    fprintf(handles.s,'2V5');
    yentry = int2str(yentry);
    ymovestring = ['2D',yentry];
    fprintf(handles.s,ymovestring);
    fprintf(handles.s,'2G');

    %pause for move
    pause(1);

    %print the line
    for n = 1:1:dropnumval;
    %eject droplet
    fprintf(handles.s,'1O(X1)');
    pause(0.1);
    fprintf(handles.s,'1O(X0)');

%add eject spacing to current position
    nextxpos = xpos + (n * ejectspval);

    %update xposition register
    set(handles.xposet,'string', nextxpos);

    %convert mm to steps
    nextxpos = nextxpos * 4000;

    %create control string and send
    fprintf(handles.s,'1A100');
    fprintf(handles.s,'1V5');
    nextxpos = int2str(nextxpos);
    xmovestring = ['1D',nextxpos];
    fprintf(handles.s,xmovestring);
    fprintf(handles.s,'1G');

    %pause for move
    pause(delayval);
    end

end;


% --------------------------------------------------------------------
function varargout = homebn_Callback(h, eventdata, handles, varargin)
%go home then set static text box (xposst) to zero
fprintf(handles.s,'1GH');

handles.xposval = 0;
set(handles.xposet,'string', handles.xposval);

%go home then set static text box (yposst) to zero
```

```
fprintf(handles.s,'2GH');

handles.yposval = 0;
set(handles.yposet,'string', handles.yposval);

% --------------------------------------------------------------------
function varargout = xhomebn_Callback(h, eventdata, handles, varargin)
%go home then set static text box (xposst) to zero
fprintf(handles.s,'1GH');

handles.xposval = 0;
set(handles.xposet,'string', handles.xposval);

% --------------------------------------------------------------------
function varargout = yhomebn_Callback(h, eventdata, handles, varargin)
%go home then set static text box (yposst) to zero
fprintf(handles.s,'2GH');

handles.yposval = 0;
set(handles.yposet,'string', handles.yposval);

% --------------------------------------------------------------------
function varargout = xmovebn_Callback(h, eventdata, handles, varargin)
%get user entry in microns and check for numeric value type and range
xentry = str2double(get(handles.xposet,'string'));

if isnan(xentry);
    errordlg('Enter numeric value');
    return;
end;

while (xentry < 0) | (xentry > 80);
    errordlg('Enter value between 0 and 80mm');
    return;
end;

%update xposition register
set(handles.xposet,'string', xentry);

%convert mm to steps
xentry = xentry * 4000;

%create control string and send
fprintf(handles.s,'1A100');
fprintf(handles.s,'1V5');
xentry = int2str(xentry);
xmovestring = ['1D',xentry];
fprintf(handles.s,xmovestring);
fprintf(handles.s,'1G');

% --------------------------------------------------------------------
function varargout = xposet_Callback(h, eventdata, handles, varargin)

% --------------------------------------------------------------------
function varargout = ymovebn_Callback(h, eventdata, handles, varargin)
%get user entry in microns and check for numeric value type and range
yentry = str2double(get(handles.yposet,'string'));

if isnan(yentry);
    errordlg('Enter numeric value');
    return;
end;

while (yentry < 0) | (yentry > 25);
    errordlg('Enter value between 0 and 25mm');
    return;
end;

%update y position register
set(handles.yposet,'string', yentry);

%convert mm to steps
yentry = yentry * 4000;
```

```
%create control string and send
fprintf(handles.s,'2A100');
fprintf(handles.s,'2V5');
yentry = int2str(yentry);
ymovestring = ['2D',yentry];
fprintf(handles.s,ymovestring);
fprintf(handles.s,'2G');

% --------------------------------------------------------------------
function varargout = yposet_Callback(h, eventdata, handles, varargin)

% --------------------------------------------------------------------
function varargout = figure1_CloseRequestFcn(h, eventdata, handles, varargin)
%disconnect and clean up
fprintf(handles.s,'1OFF');
fprintf(handles.s,'2OFF');
fclose(handles.s)
delete(handles.s)
clear handles.s

%issue close request
closereq

% --------------------------------------------------------------------
function varargout = ejectbn_Callback(h, eventdata, handles, varargin)
%set programmable output 1 to logic 1 for 1 seconds then return to logic 0
fprintf(handles.s,'1O(X1)');
fprintf(handles.s,'1T1');
fprintf(handles.s,'1O(X0)');

% --------------------------------------------------------------------
function varargout = xlineposbn_Callback(h, eventdata, handles, varargin)
global cancel;
cancel = 0;

%get number of drops and drop separation in um
%check droplet number entry is numeric in format
dropnumval = str2double(get(handles.dropnumet,'string'));

if isnan(dropnumval);
errordlg('Enter numeric value for number of droplets');
return;
end;

%check eject spacing is numeric in format, convert to mm
ejectspval = str2double(get(handles.ejectspet,'string'));
ejectspval= ejectspval / 1000;

if isnan(ejectspval);
errordlg('Enter numeric value for droplet spacing');
return;
end;

%check delay time is numeric in format and greater than 1s (to allow stage to move)
delayval = str2double(get(handles.ejectdelayet,'string'));

if isnan(delayval);
errordlg('Enter numeric value for delay time');
return;
end;

while (delayval < 1);
    errordlg('Enter value greater than 1s');
    return;
end;

%get current xposition and work out final line position then check within limits
xpos = str2double(get(handles.xposet,'string'));
finalxpos = (ejectspval * dropnumval) + xpos;

while (finalxpos < 0) | (finalxpos > 80);
errordlg('Final position lies outside limits of stage');
```

```
return;
end;

%create for loop
for n = 1:1:dropnumval;

    %check that cancel variable isn't 1
    if cancel == 1;
        break;
    end;

    %eject droplet
    fprintf(handles.s,'1O(X1)');
    pause(0.1);
    fprintf(handles.s,'1O(X0)');

%add eject spacing to current position
    nextxpos = xpos + (n * ejectspval);

    %update x position
    set(handles.xposet,'string',nextxpos);

    %confirm xpos is still within stage limits
    while (nextxpos < 0) | (nextxpos > 80);
    errordlg('Error:  Stage outside limits');
    return;
    end;

    %convert mm to steps
    nextxpos = nextxpos * 4000;

    %create control string and send
    fprintf(handles.s,'1A100');
    fprintf(handles.s,'1V5');
    nextxpos = int2str(nextxpos);
    xmovestring = ['1D',nextxpos];
    fprintf(handles.s,xmovestring);
    fprintf(handles.s,'1G');

    %pause for move
    pause(delayval);

end;

% --------------------------------------------------------------------
function varargout = ylinenegbn_Callback(h, eventdata, handles, varargin)
global cancel;
cancel = 0;

%get number of drops and drop separation in um
%check droplet number entry is numeric in format
dropnumval = str2double(get(handles.dropnumet,'string'));

if isnan(dropnumval);
errordlg('Enter numeric value for number of droplets');
return;
end;

%check eject spacing is numeric in format, convert to mm
ejectspval = str2double(get(handles.ejectspet,'string'));
ejectspval= ejectspval / 1000;

if isnan(ejectspval);
errordlg('Enter numeric value for droplet spacing');
return;
end;

%check delay time is numeric in format and greater than 1s (to allow stage to move)
delayval = str2double(get(handles.ejectdelayet,'string'));

if isnan(delayval);
errordlg('Enter numeric value for delay time');
return;
```

```
end;

while (delayval < 1);
    errordlg('Enter value greater than 1s');
    return;
end;

%get current yposition and work out final line position then check within limits
ypos = str2double(get(handles.yposet,'string'));
finalypos = ypos - (ejectspval * dropnumval);

while (finalypos < 0) | (finalypos > 25);
errordlg('Final position lies outside limits of stage');
return;
end;

%create for loop
for n = 1:1:dropnumval;

    %check that cancel variable isn't 1
    if cancel == 1;
        break;
    end;

    %eject droplet
    fprintf(handles.s,'1O(X1)');
    pause(0.1);
    fprintf(handles.s,'1O(X0)');

%add eject spacing to current position
    nextypos = ypos - (n * ejectspval);

    %update y position
    set(handles.yposet,'string',nextypos);

    %confirm ypos is still within stage limits
    while (nextypos < 0) | (nextypos > 25);
    errordlg('Error:  Stage outside limits');
    return;
    end;

    %convert mm to steps
    nextypos = nextypos * 4000;

    %create control string and send
    fprintf(handles.s,'2A100');
    fprintf(handles.s,'2V5');
    nextypos = int2str(nextypos);
    ymovestring = ['2D',nextypos];
    fprintf(handles.s,ymovestring);
    fprintf(handles.s,'2G');

    %pause for move
    pause(delayval);

end;

% --------------------------------------------------------------------
function varargout = ylineposbn_Callback(h, eventdata, handles, varargin)
global cancel;
cancel = 0;

%get number of drops and drop separation in um
%check droplet number entry is numeric in format
dropnumval = str2double(get(handles.dropnumet,'string'));

if isnan(dropnumval);
errordlg('Enter numeric value for number of droplets');
return;
end;

%check eject spacing is numeric in format, convert to mm
ejectspval = str2double(get(handles.ejectspet,'string'));
```

```
ejectspval= ejectspval / 1000;

if isnan(ejectspval);
errordlg('Enter numeric value for droplet spacing');
return;
end;

%check delay time is numeric in format and greater than 1s (to allow stage to move)
delayval = str2double(get(handles.ejectdelayet,'string'));

if isnan(delayval);
errordlg('Enter numeric value for delay time');
return;
end;

while (delayval < 1);
    errordlg('Enter value greater than 1s');
    return;
end;

%get current yposition and work out final line position then check within limits
ypos = str2double(get(handles.yposet,'string'));
finalypos = (ejectspval * dropnumval) + ypos;

while (finalypos < 0) | (finalypos > 25);
errordlg('Final position lies outside limits of stage');
return;
end;

%create for loop
for n = 1:1:dropnumval;

    %check that cancel variable isn't 1
    if cancel == 1;
        break;
    end;

    %eject droplet
    fprintf(handles.s,'1O(X1)');
    pause(0.1);
    fprintf(handles.s,'1O(X0)');

%add eject spacing to current position
    nextypos = ypos + (n * ejectspval);

    %update y position
    set(handles.yposet,'string',nextypos);

    %confirm ypos is still within stage limits
    while (nextypos < 0) | (nextypos > 25);
    errordlg('Error:  Stage outside limits');
    return;
    end;

    %convert mm to steps
    nextypos = nextypos * 4000;

    %create control string and send
    fprintf(handles.s,'2A100');
    fprintf(handles.s,'2V5');
    nextypos = int2str(nextypos);
    ymovestring = ['2D',nextypos];
    fprintf(handles.s,ymovestring);
    fprintf(handles.s,'2G');

    %pause for move
    pause(delayval);

end;

% --------------------------------------------------------------------
function varargout = xlinenegbn_Callback(h, eventdata, handles, varargin)
global cancel;
```

```
cancel = 0;

%get number of drops and drop separation in um
%check droplet number entry is numeric in format
dropnumval = str2double(get(handles.dropnumet,'string'));

if isnan(dropnumval);
errordlg('Enter numeric value for number of droplets');
return;
end;

%check eject spacing is numeric in format, convert to mm
ejectspval = str2double(get(handles.ejectspet,'string'));
ejectspval= ejectspval / 1000;

if isnan(ejectspval);
errordlg('Enter numeric value for droplet spacing');
return;
end;

%check delay time is numeric in format and greater than 1s (to allow stage to move)
delayval = str2double(get(handles.ejectdelayet,'string'));

if isnan(delayval);
errordlg('Enter numeric value for delay time');
return;
end;

while (delayval < 1);
    errordlg('Enter value greater than 1s');
    return;
end;

%get current xposition and work out final line position then check within limits
xpos = str2double(get(handles.xposet,'string'));
finalxpos = xpos - (ejectspval * dropnumval);

while (finalxpos < 0) | (finalxpos > 80);
errordlg('Final position lies outside limits of stage');
return;
end;

%create for loop
for n = 1:1:dropnumval;

    %check that cancel variable isn't 1
    if cancel == 1;
        break;
    end;

    %eject droplet
    fprintf(handles.s,'1O(X1)');
    pause(0.1);
    fprintf(handles.s,'1O(X0)');

%add eject spacing to current position
    nextxpos = xpos - (n * ejectspval);

    %update x position
    set(handles.xposet,'string',nextxpos);

    %confirm xpos is still within stage limits
    while (nextxpos < 0) | (nextxpos > 80);
    errordlg('Error:  Stage outside limits');
    return;
    end;

    %convert mm to steps
    nextxpos = nextxpos * 4000;

    %create control string and send
    fprintf(handles.s,'1A100');
    fprintf(handles.s,'1V5');
```

```
    nextxpos = int2str(nextxpos);
    xmovestring = ['1D',nextxpos];
    fprintf(handles.s,xmovestring);
    fprintf(handles.s,'1G');

    %pause for move
    pause(delayval);

end;

% --------------------------------------------------------------------
function varargout = ejectspet_Callback(h, eventdata, handles, varargin)

% --------------------------------------------------------------------
function varargout = dropnumet_Callback(h, eventdata, handles, varargin)

% --------------------------------------------------------------------
function varargout = ejectdelayet_Callback(h, eventdata, handles, varargin)

% --------------------------------------------------------------------
function varargout = cancelbn_Callback(h, eventdata, handles, varargin)

% --------------------------------------------------------------------
function varargout = xpos01_Callback(h, eventdata, handles, varargin)
%get current xposition
xpos = str2double(get(handles.xposet,'string'));

%add move
nextxpos = xpos + 0.1;

%confirm xpos is still within stage limits
while (nextxpos < 0) | (nextxpos > 80);
    errordlg('Error:  Stage outside limits');
return;
end;

%update x position
set(handles.xposet,'string',nextxpos);

%convert mm to steps
nextxpos = nextxpos * 4000;

%create control string and send
fprintf(handles.s,'1A100');
fprintf(handles.s,'1V5');
nextxpos = int2str(nextxpos);
xmovestring = ['1D',nextxpos];
fprintf(handles.s,xmovestring);
fprintf(handles.s,'1G');

% --------------------------------------------------------------------
function varargout = xneg01_Callback(h, eventdata, handles, varargin)
%get current xposition
xpos = str2double(get(handles.xposet,'string'));

%add move
nextxpos = xpos - 0.1;

%confirm xpos is still within stage limits
while (nextxpos < 0) | (nextxpos > 80);
    errordlg('Error:  Stage outside limits');
return;
end;

%update x position
set(handles.xposet,'string',nextxpos);

%convert mm to steps
nextxpos = nextxpos * 4000;

%create control string and send
fprintf(handles.s,'1A100');
fprintf(handles.s,'1V5');
```

```
nextxpos = int2str(nextxpos);
xmovestring = ['1D',nextxpos];
fprintf(handles.s,xmovestring);
fprintf(handles.s,'1G');

% --------------------------------------------------------------------
function varargout = ypos01_Callback(h, eventdata, handles, varargin)
%get current yposition
ypos = str2double(get(handles.yposet,'string'));

%add move
nextypos = ypos + 0.1;

%confirm ypos is still within stage limits
while (nextypos < 0) | (nextypos > 80);
    errordlg('Error:  Stage outside limits');
return;
end;

%update y position
set(handles.yposet,'string',nextypos);

%convert mm to steps
nextypos = nextypos * 4000;

%create control string and send
fprintf(handles.s,'2A100');
fprintf(handles.s,'2V5');
nextypos = int2str(nextypos);
ymovestring = ['2D',nextypos];
fprintf(handles.s,ymovestring);
fprintf(handles.s,'2G');

% --------------------------------------------------------------------
function varargout = yneg01_Callback(h, eventdata, handles, varargin)
%get current yposition
ypos = str2double(get(handles.yposet,'string'));

%add move
nextypos = ypos - 0.1;

%confirm ypos is still within stage limits
while (nextypos < 0) | (nextypos > 80);
    errordlg('Error:  Stage outside limits');
return;
end;

%update y position
set(handles.yposet,'string',nextypos);

%convert mm to steps
nextypos = nextypos * 4000;

%create control string and send
fprintf(handles.s,'2A100');
fprintf(handles.s,'2V5');
nextypos = int2str(nextypos);
ymovestring = ['2D',nextypos];
fprintf(handles.s,ymovestring);
fprintf(handles.s,'2G');

% --------------------------------------------------------------------
function varargout = xneg05_Callback(h, eventdata, handles, varargin)
%get current xposition
xpos = str2double(get(handles.xposet,'string'));

%add move
nextxpos = xpos - 0.5;

%confirm xpos is still within stage limits
while (nextxpos < 0) | (nextxpos > 80);
    errordlg('Error:  Stage outside limits');
return;
```

```
end;

%update x position
set(handles.xposet,'string',nextxpos);

%convert mm to steps
nextxpos = nextxpos * 4000;

%create control string and send
fprintf(handles.s,'1A100');
fprintf(handles.s,'1V5');
nextxpos = int2str(nextxpos);
xmovestring = ['1D',nextxpos];
fprintf(handles.s,xmovestring);
fprintf(handles.s,'1G');

% --------------------------------------------------------------------
function varargout = xpos05_Callback(h, eventdata, handles, varargin)
%get current xposition
xpos = str2double(get(handles.xposet,'string'));

%add move
nextxpos = xpos + 0.5;

%confirm xpos is still within stage limits
while (nextxpos < 0) | (nextxpos > 80);
    errordlg('Error:  Stage outside limits');
return;
end;

%update x position
set(handles.xposet,'string',nextxpos);

%convert mm to steps
nextxpos = nextxpos * 4000;

%create control string and send
fprintf(handles.s,'1A100');
fprintf(handles.s,'1V5');
nextxpos = int2str(nextxpos);
xmovestring = ['1D',nextxpos];
fprintf(handles.s,xmovestring);
fprintf(handles.s,'1G');

% --------------------------------------------------------------------
function varargout = yneg05_Callback(h, eventdata, handles, varargin)
%get current yposition
ypos = str2double(get(handles.yposet,'string'));

%add move
nextypos = ypos - 0.5;

%confirm ypos is still within stage limits
while (nextypos < 0) | (nextypos > 80);
    errordlg('Error:  Stage outside limits');
return;
end;

%update y position
set(handles.yposet,'string',nextypos);

%convert mm to steps
nextypos = nextypos * 4000;

%create control string and send
fprintf(handles.s,'2A100');
fprintf(handles.s,'2V5');
nextypos = int2str(nextypos);
ymovestring = ['2D',nextypos];
fprintf(handles.s,ymovestring);
fprintf(handles.s,'2G');

% --------------------------------------------------------------------
```

```
function varargout = ypos05_Callback(h, eventdata, handles, varargin)
%get current yposition
ypos = str2double(get(handles.yposet,'string'));

%add move
nextypos = ypos + 0.5;

%confirm ypos is still within stage limits
while (nextypos < 0) | (nextypos > 80);
    errordlg('Error:  Stage outside limits');
return;
end;

%update y position
set(handles.yposet,'string',nextypos);

%convert mm to steps
nextypos = nextypos * 4000;

%create control string and send
fprintf(handles.s,'2A100');
fprintf(handles.s,'2V5');
nextypos = int2str(nextypos);
ymovestring = ['2D',nextypos];
fprintf(handles.s,ymovestring);
fprintf(handles.s,'2G');

% --------------------------------------------------------------------
function varargout = ypos1_Callback(h, eventdata, handles, varargin)
%get current yposition
ypos = str2double(get(handles.yposet,'string'));

%add move
nextypos = ypos + 1;

%confirm ypos is still within stage limits
while (nextypos < 0) | (nextypos > 80);
    errordlg('Error:  Stage outside limits');
return;
end;

%update y position
set(handles.yposet,'string',nextypos);

%convert mm to steps
nextypos = nextypos * 4000;

%create control string and send
fprintf(handles.s,'2A100');
fprintf(handles.s,'2V5');
nextypos = int2str(nextypos);
ymovestring = ['2D',nextypos];
fprintf(handles.s,ymovestring);
fprintf(handles.s,'2G');

% --------------------------------------------------------------------
function varargout = xneg1_Callback(h, eventdata, handles, varargin)
%get current xposition
xpos = str2double(get(handles.xposet,'string'));

%add move
nextxpos = xpos - 1;

%confirm xpos is still within stage limits
while (nextxpos < 0) | (nextxpos > 80);
    errordlg('Error:  Stage outside limits');
return;
end;

%update x position
set(handles.xposet,'string',nextxpos);

%convert mm to steps
```

```
nextxpos = nextxpos * 4000;

%create control string and send
fprintf(handles.s,'1A100');
fprintf(handles.s,'1V5');
nextxpos = int2str(nextxpos);
xmovestring = ['1D',nextxpos];
fprintf(handles.s,xmovestring);
fprintf(handles.s,'1G');

% --------------------------------------------------------------------
function varargout = yneg1_Callback(h, eventdata, handles, varargin)
%get current yposition
ypos = str2double(get(handles.yposet,'string'));

%add move
nextypos = ypos - 1;

%confirm ypos is still within stage limits
while (nextypos < 0) | (nextypos > 80);
    errordlg('Error:  Stage outside limits');
return;
end;

%update y position
set(handles.yposet,'string',nextypos);

%convert mm to steps
nextypos = nextypos * 4000;

%create control string and send
fprintf(handles.s,'2A100');
fprintf(handles.s,'2V5');
nextypos = int2str(nextypos);
ymovestring = ['2D',nextypos];
fprintf(handles.s,ymovestring);
fprintf(handles.s,'2G');

% --------------------------------------------------------------------
function varargout = xpos1_Callback(h, eventdata, handles, varargin)
%get current xposition
xpos = str2double(get(handles.xposet,'string'));

%add move
nextxpos = xpos + 1;

%confirm xpos is still within stage limits
while (nextxpos < 0) | (nextxpos > 80);
    errordlg('Error:  Stage outside limits');
return;
end;

%update x position
set(handles.xposet,'string',nextxpos);

%convert mm to steps
nextxpos = nextxpos * 4000;

%create control string and send
fprintf(handles.s,'1A100');
fprintf(handles.s,'1V5');
nextxpos = int2str(nextxpos);
xmovestring = ['1D',nextxpos];
fprintf(handles.s,xmovestring);
fprintf(handles.s,'1G');

% --------------------------------------------------------------------
function varargout = capturebn_Callback(h, eventdata, handles, varargin)

framecount = 1;
image = vfm('grab',framecount);
imwrite(image, 'image.bmp', 'bmp');
```

```
% --------------------------------------------------------------------
function varargout = ptocbn_Callback(h, eventdata, handles, varargin)
%get offset entry in mm and check for numeric value type and range
xoff = str2double(get(handles.xoffet,'string'));
if isnan(xoff);
    errordlg('Enter numeric value');
    return;
end;

%get current xposition
xpos = str2double(get(handles.xposet,'string'));
nextxpos = xoff + xpos;

%confirm xpos is still within stage limits
while (nextxpos < 0) | (nextxpos > 80);
    errordlg('Error:  Stage outside limits');
return;
end;

%get offset entry in mm and check for numeric value type and range
yoff = str2double(get(handles.yoffet,'string'));
if isnan(yoff);
    errordlg('Enter numeric value');
    return;
end;

%get current yposition
ypos = str2double(get(handles.yposet,'string'));
nextypos = yoff + ypos;

%confirm ypos is still within stage limits
while (nextypos < 0) | (nextypos > 80);
    errordlg('Error:  Stage outside limits');
return;
end;

%update x position
set(handles.xposet,'string',nextxpos);

%convert mm to steps
nextxpos = nextxpos * 4000;

%create control string and send
fprintf(handles.s,'1A100');
fprintf(handles.s,'1V20');
nextxpos = int2str(nextxpos);
xmovestring = ['1D',nextxpos];
fprintf(handles.s,xmovestring);
fprintf(handles.s,'1G');

%update y position
set(handles.yposet,'string',nextypos);

%convert mm to steps
nextypos = nextypos * 4000;

%create control string and send
fprintf(handles.s,'2A100');
fprintf(handles.s,'2V5');
nextypos = int2str(nextypos);
ymovestring = ['2D',nextypos];
fprintf(handles.s,ymovestring);
fprintf(handles.s,'2G');

% --------------------------------------------------------------------
function varargout = ctopbn_Callback(h, eventdata, handles, varargin)

%get offset entry in mm and check for numeric value type and range
xoff = str2double(get(handles.xoffet,'string'));
if isnan(xoff);
    errordlg('Enter numeric value');
    return;
end;
```

```
%get current xposition
xpos = str2double(get(handles.xposet,'string'));
nextxpos = xpos - xoff;

%confirm xpos is still within stage limits
while (nextxpos < 0) | (nextxpos > 80);
    errordlg('Error:  Stage outside limits');
return;
end;

%get offset entry in mm and check for numeric value type and range
yoff = str2double(get(handles.yoffet,'string'));
if isnan(yoff);
    errordlg('Enter numeric value');
    return;
end;

%get current yposition
ypos = str2double(get(handles.yposet,'string'));
nextypos = ypos - yoff;

%confirm ypos is still within stage limits
while (nextypos < 0) | (nextypos > 80);
    errordlg('Error:  Stage outside limits');
return;
end;

%update x position
set(handles.xposet,'string',nextxpos);

%convert mm to steps
nextxpos = nextxpos * 4000;

%create control string and send
fprintf(handles.s,'1A100');
fprintf(handles.s,'1V20');
nextxpos = int2str(nextxpos);
xmovestring = ['1D',nextxpos];
fprintf(handles.s,xmovestring);
fprintf(handles.s,'1G');

%update y position
set(handles.yposet,'string',nextypos);

%convert mm to steps
nextypos = nextypos * 4000;

%create control string and send
fprintf(handles.s,'2A100');
fprintf(handles.s,'2V5');
nextypos = int2str(nextypos);
ymovestring = ['2D',nextypos];
fprintf(handles.s,ymovestring);
fprintf(handles.s,'2G');

% --------------------------------------------------------------------
function varargout = xoffet_Callback(h, eventdata, handles, varargin)

% --------------------------------------------------------------------
function varargout = yoffet_Callback(h, eventdata, handles, varargin)
```

*Appendix C*

# CROSS-SECTIONAL AREA OF INKJETTED LINES

## *C.1 Matlab m-file for calculating cross-sectional area of inkjet printed lines along their length*

```
disp('All units in meters or meters^2')
%matlab m file to take in an ascii matrix file via the import wizard
%the lines pass horizontally
%the program scans colums and finds the total area below it, the height of
%the glass is estimated then subtracted from each line

%use imhist(hn) on the normalised hn data and pixval on to estimate the glass height
glass = 0.035

%xy plot size:  xy = 256 bits
%z plot height:  z = hmax - hmin
xy = 0.000163
z = 0.0000005
%therefore 1 bit = xy/256 and 1V = z/(hmax-hmin)

h = data;
[r, c] = size(h);

%normalize data to start at zero and place in hn
hmin = 1000;
hmax = -1000;
for i = 1:r
    for j = 1:c
        if h(i, j) < hmin
            hmin = h(i, j);
        end
        if h(i, j) > hmax
            hmax = h(i, j);
        end
    end
end

hn = h - hmin;
imhist(hn)
pixval on

%calculate area of each line
area = zeros(c, 1);

for i = 1:c
    area(i, 1) = area(i, 1) - (glass * c);
    for j = 1:r
        area(i, 1) = area(i, 1) + (hn(j, i));
    end
end

%scale area
areascale = area * (xy / 256) * (z / (hmax - hmin));
figure, plot(areascale);

%find max and min values of area and plot
areamin = 1000;
areamax = -1000;
```

```
for i = 1:c
    if areascale(i, 1) < areamin
        areamin = areascale(i, 1);
    end
    if areascale(i, 1) > areamax
        areamax = areascale(i, 1);
    end
end

areamax
areamin

axis([0 c 0 areamax])
```

## *C.2 m-file for calculating cross-sectional area of inkjet printed lines along their length that cross electrode gaps*

```
%assume height data in workspace variable h

%size h
%------
[r c] = size(h);

%calculate scaling factors
%-------------------------
%256 bits = xy meters
xy = 148.2E-6
%hmax - hmin = z meters
hmax = max(h);
hmax = max(hmax);
hmin = min(h);
hmin = min(hmin);
hrange = hmax - hmin;
z = 1.07E-6

onebit = xy / 256;
onevolt = z / hrange;

%normalise image to zero
%-----------------------
h = h - hmin;

%select area from which to take glass baseplane and calculate its average
%height in meters
%-----------------------------------------------------------------------
baseplane = imcrop(h);
meanbaseplane = mean(baseplane);
meanbaseplane = mean(meanbaseplane);
meanbaseplane = meanbaseplane * onevolt;

%calculate crossectional area for each column
%--------------------------------------------

%crosssectional area of each columns baseplane
baseplanecolumnarea = meanbaseplane * onebit;

%crosssectional area of each column
columnarea = sum(h);
columnarea = columnarea * onebit * onevolt;
columnarea = columnarea - baseplanecolumnarea;

%show point of minimum crosssectional area and electrode edges
%-------------------------------------------------------------
[mincrosssectionalarea, minlocation] = min(columnarea);
minlocation = minlocation * onebit;
imagesc(h);
[electrodes, fubar] = ginput;
electrodes = electrodes * onebit;
maxcrosssectionalarea = max(columnarea);
```

```
%plot results
%------------
for i = 1:c
    index(i) = i * onebit;
end

plot(index, columnarea);
xlabel('x (m)');
ylabel('Cross-sectional area (m^2)');

%electrode locations
line([electrodes(1) electrodes(1)], [0 maxcrosssectionalarea]);
line([electrodes(2) electrodes(2)], [0 maxcrosssectionalarea]);

%point of minimum crosssectional area
minxcstring = num2str(mincrosssectionalarea);
minxcstring = ['|  ', minxcstring, ' m^2'];
text(minlocation, mincrosssectionalarea, minxcstring, 'horizontalalignment', 'left');

%electrode separation
electrodeseparation = electrodes(2) - electrodes(1);
electrodelocation = (electrodeseparation / 2) + electrodes(1);
elecsepstring = num2str(electrodeseparation);
elecsepstring = ['<- Electrode separation = ', elecsepstring, ' m ->'];
text(electrodelocation, mincrosssectionalarea / 2, elecsepstring, 'horizontalalignment', 'center');
```

# BIBLIOGRAPHY


[1] T. Ito, H. Shirakawa, and S. Ikeda. *J. Polym. Sci. Polym. Chem. Ed.*, 12:11, 1974.

[2] H. Shirakawa, E. Louis, A. McDiarmid, C. Chiang, and A.J. Heeger. Synthesis of electrically conducting organic polymers: Halogen derivatives of polyacetylene, $(ch)_x$. *J. Chem. Soc. Chem. Commun*, page 578, 1977.

[3] A. Tsumura, H. Koezuka, and T. Ando. Macromolecular electronic device: Field-effect transistor with a polythiophene thin film. *Applied Physics Letters*, 49:1210–1212, 1986.

[4] H. Tomozawa, D. Braun, S. Phillips, A.J. Heeger, and H. Kroemer. Metal-polymer schottky barriers on cast films of soluble poly(3-alkylthiophenes). *Synthetic Metals*, pages 63–69, 1987.

[5] J.H. Burroughes, D.D.C Bradley, A.R. Brown, R.N. Marks, R.H. Friend, and P.L. Burns. *Nature*, 347:539, 1990.

[6] A.A. Darhuber, S.M. Troian, J.M Davis, S.M. Miller, and S. Wagner. Selective dip-coating of chemically micropatterned surfaces. *Journal of Applied Physics*, 88:5119–5126, 2000.

[7] R. Osterbacka, G. Juska, K. Arlauskas, A.J. Pal, K.M. Kallman, and H. Stubb. Electric field redistribution and electroluminescence response time in polymeric light-emitting diodes. *Journal of Applied Physics*, 84:3359–3363, 1998.

[8] D. Meyerhofer. Characteristics of resist films produced by spinning. *Journal of Applied Physics*, 49(3993-3997), 1978.

[9] T. R. Hebner, C. C. Wu, D. Marcy, M. H. Lu, and J. C. Sturm. Ink-jet printing of doped polymers for organic light emitting devices. *Applied Physics Letters*, 72:519–521, 1998.

[10] H. Sirringhaus, T. Kawase, R.H. Friend, T. Shimoda, M. Inbasekaran, W. Wu, and E.P. Woo. High-resolution inkjet printing of all-polymer transistor circuits. *Science*, 290:2123–2126, 2000.

[11] P. Calvert. Inkjet printing for materials and devices. *Chemistry of Materials*, 13:3299–3305, 2001.

[12] J.A. Rogers, Z. Bao, A. Dodabalapur, and A. Makhija. Organic smart pixels and complementary inverter circuits formed on plastic substrates by casting and rubber stamping. *IEEE Electron Devices Letters*, 21:100–103, 2000.

[13] Z. Bao, Y. Feng, A. Dodabalapur, V.R. Raju, and A.J. Lovinger. High-performance plastic transistors fabricated by printing techniques. *Chemistry of Materials*, 9:1299–1301, 1997.

[14] J.M. Xu. Plastic electronics and future trends in microelectronics. *Synthetic Metals*, 115:1–3, 2000.

[15] S. Molesa, D.R. Redinger, D.C. Huang, and V. Subramanian. High-quality inkjet-printed multilevel interconnects and inductive components on plastic for ultra-low-cost rfid applications. *Materials research society symposia proceedings*, 769:253–259, 2003.

[16] R.A. Street, M. Mulato, R. Lau, J. Ho, J. Graham, Z. Popovic, and J. Hor. Image capture array with an organic light sensor. *Applied Physics Letters*, 78:4193–4195, 2001.

[17] A.A. Darhuber, S.M. Troian, S.M. Miller, and S. Wagner. Morphology of liquid microstructures on chemically patterned surfaces. *Journal of Applied Physics*, 87:7768–7775, 2000.

[18] K. Kargupta and A. Sharma. Templating of thin films induced by dewetting on patterned surfaces. *Physical Review Letters*, 86:4536–4539, 2001.

[19] WO0146987, 2001.

[20] M.P. de Jong, L.J. van Ijzendoorn, and M.J. de Voigt. Stability of the interface between indium-tin-oxide and poly(3,4-ethylenedioxythiophene)/poly(styrenesulfonate) in polymer light-emitting diodes. *Applied physics letters*, 77(14):2255–2257, 2000.

[21] K.W. Wong, H.L. Yip, K.Y. Wong, W.M. Lau, K.H. Low, H.F. Chow, Z.Q. Gao, W.L. Yeung, and C.C. Chang. Blocking reactions between ito and pedot:pss with a self-assembly monolayer. *Applied Physics Letters*, 80:2788–2790, 2002.

[22] T.M. Brown and F. Cacialli. Energy level line up in polymer light-emitting diodes via electroabsorption spectroscopy. *IEE Proc. Optoelectron.*, 148:74–80, 2001.

[23] A.J. Campbell, D.D.C. Bradley, and H. Antoniadis. Quantifying the efficiency of electrodes for positive carrier injection in to poly(9,9-dioctylfluorene) and representative copolymers. *Journal of Applied Physics*, 89:3343–3351, 2001.

[24] M.B. Khalifa, D. Vaufrey, A. Bouazizi, J. Tardy, and H. Maaref. Hole injection and transport in ito/pedot/pvk/al diodes. *Materials Science and Engineering C*, 21:277–282, 2002.

[25] J.S. Kim. Polymer light-emitting diodes. Master's thesis, University of Cambridge, 2000.

[26] M.K. Fung, S.L. Lai, S.W. Tong, M.Y. Chan, C.S. Lee, S.T. Lee, W.W. Wu, M. Inbasekaran, and J.J. O'Brien. Anode modification of polyfluorene-based polymer light-emitting devices. *Applied Physics Letters*, 81:1497–1499, 2002.

[27] EP440957, 1991.

[28] EP564911, 1994.

[29] Y. Kudoh, K. Akami, and Y. Matsuya. Solid electrolytic capacitor with highly stable conducting polymer as counter electrode. *Synthetic Metals*, 102:973–974, 1999.

[30] W.H. Kim, A.J. Makinen, N. Nikolov, R. Shashidhar, H. Kim, and Z.H. Kafafi. Molecular organic light-emitting diodes using highly conductive polymers as anodes. *Applied Physics Letters*, 80:3844–3846, 2002.

[31] L. Groenendaal, F. Jonas, D. Freitag, H. Pielartzik, and J.R. Reynolds. Pedot and its derivatives, past, present and future. *Advanced Materials*, 12:481–494, 2000.

[32] A.W. Denier van der Gon, J. Birgerson, M. Fahlman, and W.R. Salaneck. Modification of pedot-pss by low-energy electrons. *Organic Electronics*, 3:111–118, 2002.

[33] H.O. Jacobs, P. Leuchtmann, O. J. Homan, and A. Stemmer. Resolution and contrast in kelvin probe force microscopy. *Journal of Applied Physics*, 84(3):1168–1173, 1998.

[34] D.M. Taylor. Developments in the theoretical modelling and experimental measurement of the surface potential of condensed monolayers. *Advances in Colloid and Interface Science*, 87:183–203, 2000.

[35] J.A. Nichols, D.J. Gundlach, and T.N. Jackson. Potential imaging of pentacene organic thin-film transistors. *Applied physics letters*, 83(12):2366–2368, 2003.

[36] S. Garreau, G. Louarn, J.P. Buisson, G. Froyer, and S. Lefrant. In situ spectroelectrochemical raman studies of poly(3,4-ethylenedioxythiophene) (pedt). *Macromolecules*, 32:6807–6812, 1999.

[37] J.L. Duvail, P. Retho, S. Gareau, G. Louarn, C. Godon, and S. Demoustier-Champagne. Transport and vibrational properties of poly(3,4-ehtylenedioxythiophene) nanofibers. *Synthetic Metals*, 131:123–128, 2002.

[38] EP339340, 1998.

[39] A.J. Heeger. Semiconducting and metallic polymers: the fourth generation of polymeric materials. *Synthetic Metals*, 125:23–42, 2002.

[40] A.G. MacDiarmid. Synthetic metals: a novel role for organic polymers. *Synthetic Metals*, 125:11–22, 2002.

[41] L.A.A. Pettersson, S. Ghosh, and O. Inganas. Optical anisotropy in thin films of pedot:pss. *Organic Electronics*, 3:143–148, 2002.

[42] K.E. Aasmundtveit, E.J. Samuelsen, L.A.A. Pettersson, O. Inganas, T. Johansson, and R. Freidenhans. Structure of thin films of pedot. *Synthetic Metals*, 101:561–564, 1999.

[43] G. Greczynski, T. Kugler, and W.R. Salaneck. Characterization of the pedot-pss system by means of x-ray and ultraviolet photoelectron spectroscopy. *Thin Solid Films*, 354:129–135, 1999.

[44] S.K.M. Jonsson, J. Birgerson, X. Crispin, G. Greczynski, W. Osikowicz, A.W. Denier van der Gon, W.R. Salaneck, and M. Fahlman. The effects of solvents on the morphology and sheet resistance in poly(3,4-ethylenedioxythiophene)polystyrenesulfonic acid (pedotpss) films. *Synthetic Metals*, 139:1–10, 2003.

[45] L.S. Hung, C.W. Tang, and M.G. Mason. Enhanced electron injection in organic electroluminescence devices using an al/lif electrode. *Applied Physics Letters*, 70:152–154, 1997.

[46] J.S. Kim, M. Granstrom, R.H. Friend, N. Johansson, W.R. Salaneck, R. Daik, W.J. Feast, and F. Cacialli. Indiumtin oxide treatments for single- and double-layer polymeric light-emitting diodes: The relation between the anode physical, chemical, and morphological properties and the device performance. *Journal of Applied Physics*, 84:6859–6870, 1998.

[47] F. Nuesch, L.J. Rothberg, E.W. Forsythe, Q.T. Le, and Y. Gao. A photoelectron spectroscopy study on the indium tin oxide treatment by acids and bases. *Applied Physics Letters*, 74:880–882, 1999.

[48] H. Peisert, M. Knupfer, F. Zhang, A. Petr, L. Dunsch, and J. Fink. Charge transfer doping at organic/organic interfaces. *Applied Physics Letters*, 83:3930–3932, 2003.

[49] H. Ishii and K. Seki. Energy level alignment at organic/metal interfaces studied by uv photoemission: Breakdown of traditional assumption of a common vacuum level at the interface. *IEEE Transactions on Electron Devices*, 44:1295–1301, 1997.

[50] N. Koch, A. Kahn, J. Ghijsen, J.J. Pireaux, J. Schwartz, R. L. Johnson, and A. Elschner. Conjugated organic molecules on metal versus polymer electrodes: Demonstration of a key energy level alignment mechanism. *Applied Physics Letters*, 82:70–72, 2003.

[51] X. Crispin, V. Geskin, A. Crispin, J. Cornil, R. Lazzaroni, W.R. Salaneck, and J. Bredas. Characterization of the interface dipole at organic/metal interfaces. *Journal of the American Chemical Society*, 124:8131–8141, 2002.

[52] A. Rajagopal and A. Kahn. Photoemission spectroscopy investigation of magnesiumalq3 interfaces. *Journal of Applied Physics*, 83:355–358, 1998.

[53] R. Lazzaroni, J.L. Bredas, P. Dannetun, C. Fredriksson, S. Stafstrom, and W.R. Salaneck. The chemical and electronic structure of the interface between aluminium and conjugated polymers. *Electrochimica Acta*, 39:235–244, 1994.

[54] B.G. Levi. New printing technologies raise hopes for cheap plastic electronics. *Physics Today*, 54:20, 2001.

[55] P. Cooley, D. Wallace, and B. Antohe. Applications of ink-jet printing technology to biomems and microfluidic systems. *Proc. SPIE Microfluidics and BioMEMS Conf.*, October 2001.

[56] S.K.Volkman, S. Molesa, B. Mattis, P.C. Chang, and V. Subramamian. Inkjetted organic transistors using a novel pentacene precursor. *Mat. Res. Soc. Symp. Proc.*, 769:369, 2003.

[57] S.E. Burns, P. Cain, J. Mills, J. Wang, and H. Sirringhaus. Inkjet printing of polymer thin-film transistor circuits. *Materials research society bulletin*, pages 829–834, November 2003.

[58] T. Shimoda, K. Morii, S. Seki, and H. Kiguchi. Inkjet printing of light-emitting polymer displays. *Materials research society bulletin*, pages 821–827, November 2003.

[59] L.T. Creagh and M. McDonald. Design and performance of inkjet print heads for non-graphic arts applications. *Materials research society bulletin*, pages 807–811, November 2003.

[60] L. Do, D. Hwang, H. Chu, S. Kim, J. Lee, H. Park, and T. Zyung. The initial state of dark spots in degradation of polymer lighting-emitting diodes. *Synthetic Metals*, 111-112:249–251, 2000.

[61] J. Bharathan and Y. Yang. Polymer electroluminescent devices processed by inkjet printing: I. polymer light-emitting logo. *Applied Physics Letters*, 72:2660–2662, 1998.

[62] S. Chang, J. Bharathan, Y. Yang, R. Helgeson, F. Wudl, M.B. Ramey, and J. R. Reynolds. Dual-color polymer light-emitting pixels processed by hybrid inkjet printing. *Applied Physics Letters*, 73:2561–2563, 1998.

[63] Y. Yang, S. Chang, J. Bharathan, and J. Liu. Organic/polymeric electroluminescent devices processed by hybrid ink-jet printing. *Journal of Materials Science: Materials in Electronics*, 11:89–96, 2000.

[64] T.R. Hebner and J.C. Sturm. Local tuning of organic light-emitting diode color by dye droplet application. *Applied Physics Letters*, 73:1775–1777, 1998.

[65] Lord Kelvin. *Phil. Mag.*, 46:82–120, 1898.

[66] L. Burgi, H. Sirringhaus, and R.H. Friend. Noncontact potentiometry of polymer field-effect transistors. *Applied physics letters*, 80(16):2913–2915, 2002.

[67] K.P. Puntambekar, P.V. Pesavento, and C.D. Frisbie. Surface potential profiling and contact resistance measurements on operating pentacene thin-film transistors by kelvin probe force microscopy. *Applied Physics Letters*, 83:5539–5541, 2003.

[68] K. Seshadri and C.D. Frisbie. Potentiometry of an operating organic semiconductor field-effect transistor. *Applied Physics Letters*, 78:993–995, 2001.

[69] K. Kaneto, M. Nakagawa, and W. Takashima. Direct probing of potential distribution in al/poly(3-hexylthiophene)/au schottky diode. *Synthetic Metals*, 135-136:25–26, 2003.

[70] G. Koley, M.G. Spencer, and H.R. Bhangale. Cantilever effects on the measurement of electrostatic potentials by scanning kelvin probe microscopy. *Applied Physics Letters*, 79:545–547, 2001.

[71] H. Sugimura, Y. Ishida, K. Hayashi, O. Takai, and N. Nakagiri. Potential shielding by the surface water layer in kelvin probe force microscopy. *Applied Physics Letters*, 80:1459–1461, 2002.

[72] S. Garreau, J.L. Duvail, and G. Louarn. Spectroelectrochemical studies of poly(3,4-ethylenedioxythiophene) in aqueous medium. *Synthetic Metals*, 125:325–329, 2002.

[73] M. Lapkowski and A. Pron. Electrochemical oxidation of poly(3,4-ethylenedioxythiophene) - "in situ" conductivity and spectroscopic investigations. *Synthetic Metals*, 110:79–83, 2000.

[74] R.W. Vest, E.P. Tweedell, and R.C. Buchanan. Inkjet printing of hybrid circuits. *International journal for hybrid microelectronics*, 6:261–267, 1983.

[75] J.S. Kim, B. Lagel, E. Moons, H. Johansson, I.D. Baikie, W.R. Salaneck, R.H. Friend, and F. Cacialli. Kelvin probe and ultraviolet photoemission measurements of indium tin oxide work function: a comparison. *Synthetic Metals*, 111-112:311–314, 2000.

[76] S. Moller, C. Perlov, W. Jackson, C. Taussig, and S.R. Forrest. A polymer/semiconductor write-once read-many-times memory. *Nature*.

[77] I.A. Noble. Electrical conduction in n-octadecane. Master's thesis, University of Wales, Bangor, 1979.

[78] D.B.A. Rep, A.F. Morpurgo, W.G. Sloof, and T.M. Klapwijk. Mobile ionic impurities in organic semiconductors. *Journal of Applied Physics*, 93:2082–2090, 2003.

[79] A. Von Hippel. *Dielectrics and waves*. John Wiley, New York, 1954.

## PUBLICATIONS ARISING FROM WORK

1. D.M. Taylor and D. Morris. Engineering challenges for polymer electronics. 2001 International symposium on electrical insulating materials (ISEIM 2001), November 2001.

2. D.J. Morris, D.M. Taylor, and J.A. Cambridge. Electrical conductors from inkjet printed pedot:pss. 7th European conference on molecular electronics, September 2003. Poster presentation.

3. D.M. Taylor, D.J. Morris, and J.A. Cambridge. Time evolution of the electrical field at electrode interfaces with conducting polymers. *Applied Physics Letters.* Accepted, due for publication 06th December 2004.